TENSILE-STRAINED GERMANIUM QUANTUM DOTS GROWN ON INDIUM ALUMINUM ARSENIDE (111)A AND (110) BY MOLECULAR BEAM EPITAXY

by

Kathryn Eva Sautter

A dissertation

submitted in partial fulfillment

of the requirements for the degree of

Doctor of Philosophy in Materials Science and Engineering

Boise State University

May 2021

BOISE STATE UNIVERSITY GRADUATE COLLEGE

DEFENSE COMMITTEE AND FINAL READING APPROVALS

of the dissertation submitted by

Kathryn Eva Sautter

Dissertation Title: Tensile-Strained Germanium Quantum Dots Grown on Indium Aluminum Arsenide (111)A and (110) by Molecular Beam Epitaxy

Date of Final Oral Examination: 16 April 2021

The following individuals read and discussed the dissertation submitted by student Kathryn Eva Sautter, and they evaluated their presentation and response to questions during the final oral examination. They found that the student passed the final oral examination.

Paul J. Simmonds, Ph.D.	Chair, Supervisory Committee
Eric Jankowski, Ph.D.	Member, Supervisory Committee
Christian Ratsch, Ph.D.	Member, Supervisory Committee
Michael Scheibner, Ph.D.	Member, Supervisory Committee

The final reading approval of the dissertation was granted by Paul J. Simmonds, Ph.D., Chair of the Supervisory Committee. The dissertation was approved by the Graduate College.

DEDICATION

To my relentlessly supportive and ever-loving parents, Dave and Terri Sautter, and my forever best friend & sister, Lizzie Sautter— without you, I could not have possibly made it this far. I love you.

ACKNOWLEDGMENTS

First and foremost, I wish to thank my advisor, Dr. Paul Simmonds. I firmly believe that I am a better scientist, engineer, writer, and professional because of his guidance and support. Graduate school is a long uphill battle, and Paul has always supported me through this journey. I hope that some day I can be as fantastic a mentor for someone else, just as Paul has been for me. Throughout the ups and downs of graduate school, I knew I could always count on Paul's unwavering support. Thank you, Paul, for always steering me in the right direction, and I hereby put this in writing now that I think I owe Paul a beer.

I am grateful to my committee members, Dr. Eric Jankowski, Dr. Christian Ratsch, and Dr. Michael Scheibner, for their support of both me and my work in graduate school. You each have played an important role in my education here at Boise State University, especially through our insightful conversations, and of course through your careful attention on the work within this dissertation.

Many collaborators have contributed to my work. Dr. Kevin Grossklaus, Dr. Eric Jankowski, Dr. Mike Henry, Dr. Baolai Liang, Dr. Aaron Muhowski, Dr. Daniel Wasserman, and Dr. Paul Davis, to name a few. I want to thank them for their expertise and perspectives on the science we do in the Collaboratory for the Epitaxy of Nanomaterials (CEN) laboratory, particularly on the work within this dissertation. I am grateful to have learned a great deal from them as a result of our many conversations. We

have done some fantastic science together, and I hope I get the chance to work with them again in the future. Thank you for supporting me in my research and in my career.

I also wish to thank Dr. Peter Müllner. Working with him helped me discover that I love teaching. He gave me the space to creatively explore my own teaching style, while giving me the opportunity to learn about pedagogy as well as myself and what I want in my future career. Thank you for your mentorship, Dr. Müllner.

Many thanks to the Micron School of Materials Science and Engineering (MSMSE) at Boise State University for your help throughout my time here. I particularly want to thank Jessica Economy for helping me with class scheduling and for answering my numerous questions. The MSMSE staff are all wonderful people and I appreciate how much they genuinely care about their students.

I want to thank all the past and present CEN lab members. Dr. Chris Schuck is a good friend and has taught me a lot about the many components of being an MBE scientist. Kevin Vallejo is witty, and I always appreciate his quips— not to mention, he is super reliable and has always been an enormously helpful person in the lab. Trent Garrett was the maestro behind the majority of our atomic force microscopy work, and I always find him a very healing person to talk to— a great listener, a kind and supportive friend— he always believes in me. Ariel Weltner is another wonderful friend I made in the lab. She gave me a home when I most needed it during my experiences here at Boise State University, and I will always be grateful to her for that. Kevin Saythavy, Hunter Coleman, Matthew Abramson, Alessia Molino, Patrick Eusepi, and Maddy Drake also helped me and the CEN succeed, and I thank you all for your hard work and companionship.

I want to thank my immediate and extended family for their endless love and support. I especially want to thank my parents and sister to whom this dissertation is dedicated. I would not have been able to do this without them. Everyone's support means the world to me. I am the first in my family to get a doctorate degree, and I know that they are all very proud of me. I also know that both my grandpas would be really proud of me and my achievements. I miss them and I wish they were here to celebrate this chapter of my life with me.

I live far from my family, so my friends are my chosen family here in Boise. They have made up my support network during my graduate school experience, and I am extremely grateful for them and the memories we made together. In my time here, I have met some amazing people. In no particular order, I want to say thank you to Dr. Sumedha Gandharava Dahl, Florent Muramutsa, Dr. Tony Varghese, Meriya Sanchez, Kshama Lakshmi Ranganatha, Ruth Romero, Bravyn Stutzman, Patrick Eusepi, Roberta Russell, Ciera Partyka-Worley, Heidi Muramutsa, and many more. I am grateful for all of you—not only have you all given me boundless support during my time here at Boise State University, but you all have made Boise my home.

One friend whom I know will always be "home" for me is Naqsh Mansoor. She has made this whole graduate student experience joyful, and for that I will always be grateful—without her, graduate school would not have been the same. Naqsh, if you are reading this, I promise that no matter what happens in life, you will always find a friend in me.

Finally, I want to acknowledge the unceded, ancestral territory of the Shoshone-Bannock tribe on which I have lived and worked here at Boise State University. This is

their native land, despite many hundreds of years of colonial violence and theft. It is my hope that those reading this will take time to learn which indigenous lands they currently live on and acknowledge the history that came before.

ABSTRACT

Molecular beam epitaxy (MBE) enables the growth of semiconductor nanostructures known as tensile-strained quantum dots (TSQDs). The highly tunable nature of TSQD properties means that they are of interest for a wide variety of applications including for infrared (IR) lasers and light-emitting diodes (LEDs), improved tunnel junction efficiency in multijunction solar cell technology, quantum key encryption, and entangled photon emission. In this project, I focus on one of the most technologically important materials, germanium (Ge). Ge has a high gain coefficient, high electron mobility, and low band gap: all excellent properties for optoelectronic applications. Until recently, these technological advantages were unattainable for light-emitting purposes due to Ge's indirect band gap.

Placing Ge under tensile strain changes this semiconductor's fundamental electronic structure by turning its indirect band gap into that of either a direct band gap semiconductor or a semimetal, depending on the choice of surface orientation. However, it is extremely difficult to use bulk Ge, because the propensity for dislocation formation and strain relaxation is high under the tensile strains required for this band gap transition. In contrast, we can store large amounts of tensile strain in TSQDs without detrimental effects on the crystal quality. The primary objective of this dissertation is therefore to explore whether we can use tensile-strained self-assembly to synthesize Ge TSQDs under large tensile strains, and in doing so, transform the fundamental properties of this technologically important element.

In this project I used TSQD self-assembly to create Ge TSQDs on two non-traditional (i.e. non-(001)) surface orientations: (111)A and (110). My research explores the first known Ge TSQDs on these systems. Because of this, I wrote much of this dissertation trying to understand the impact of MBE parameters on Ge TSQD growth/formation and how the properties of Ge TSQDs compare to other quantum dot (QD) systems. I focus on this, because TSQD self-assembly is one of the only ways in which we can induce the very large tensile strains needed for dramatic changes to Ge's band structure without producing crystalline defects, making it a new and exciting area of study. Additionally, TSQD self-assembly is a recent advancement, leaving this area of science relatively unexplored. For the first time, I am able to report light emission from tensile-strained Ge(110) TSQDs, suggesting that we have transformed this important semiconductor into a direct band gap material with efficient light emission.

In Chapter 1, I provide the background needed to understand the work within this dissertation. I describe the motivation for the work, the basics of MBE growth, the characterization tools I employed, the relevant crystallography of these structures, the mechanisms for TSQD self-assembly, and finally the optoelectronic background needed to better understand Ge TSQDs.

In Chapter 2, I expand on many of the concepts from Chapter 1. Chapter 2 was an invited paper, wherein we wrote a tutorial-style guide for quantum dot (QD) growth by MBE and provide methodologies for many different QD self-assembly systems commonly investigated in literature. We discuss the premise for QD development, where it fits into quantum applications, how QD self-assembly works, how to grow various compressively strained systems, and finally how to grow tensile-strained systems. This

particular paper was designed as an introduction to new QD growers, helping them by giving all the information they would need to start growing QDs in general, but particularly TSQDs. Since TSQDs are still a relatively new field, gathering all the information about how to grow several different materials systems all in one place and providing clear, step-by-step instructions about how to grow them is valuable. This Chapter is thus a guidebook for other researchers.

In Chapter 3, I apply this background information and use it to create the first self-assembled Ge TSQDs on InAlAs(111)A. I provide a comprehensive study of how the structural properties of Ge/InAlAs(111)A TSQDs change with growth parameters, providing a robust platform for future work in embedded, low-resistivity tunnel junctions and contacts. I discovered an extremely unusual phase transition for these Ge/InAlAs(111)A TSQDs from a Stranski-Krastonov (SK) growth mode at low temperatures, to a Volmer-Weber (VW) growth mode at higher temperatures. This characteristic is highlighted in the paper, because this work provides the clearest evidence to-date of the ability to switch between different growth modes for quantum dot self-assembly based simply on MBE parameters. Being able to choose between mixed one- and three-dimensional (3D) quantum confinement (e.g., from the wetting layer and QDs in the SK growth mode) or just 3D quantum confinement (e.g., QD-only VW growth) with a high degree of tunability opens up the door to new electronic device applications.

In Chapter 4, I compare Ge/InAlAs(111)A TSQDs to an analogous purely III-V TSQD system: namely GaAs/InAlAs(111)A TSQDs. These two TSQD systems, while seemingly similar from both a surface (InAlAs(111)A) and a strain perspective (both have ~3.7% tensile strain), have entirely different shapes, nucleation behaviors, and areal

densities. We use potential energy surfaces, radial distribution scaling, and island scaling analyses to compare the two TSQD systems. In the process, we obtain a much deeper understanding of the kinetic behavior during self-assembly for both Ga and Ge adatoms on an InAlAs(111)A surface. This will allow us to more effectively tailor these TSQDs for specific optoelectronic applications.

In Chapter 5, I demonstrate growth of the first Ge(110) TSQDs grown on InAlAs. The (110) surface is essential to this project, because theory suggests that tensile strain should produce a direct band gap transition in the Ge, transforming it into an efficient light-emitting semiconductor. I use a variety of experimental techniques and surface symmetry/diffusion anisotropy arguments to explain the unusual shapes of the resulting TSQDs. Initial photoluminescence data indicates strong light emission from Ge(110) TSQDs for the first time, indicating that a strain-driven indirect-to-direct transition has occurred. This breakthrough could enable the future use of these nanostructures for an entirely new type of IR light emitter.

In Chapter 6, I discuss several avenues for researchers to continue this project. The light emission I report in Chapter 5 needs to be investigated in greater detail. Once we learn more about the light emission properties of Ge(110) TSQDs, we can make LED and lasing devices out of them, optimizing their growth for these purposes and test their overall performance. We can also investigate the possible topological insulating characteristics of Ge/(111)A TSQDs and test how they change tunnel junction efficiency. Additionally, there are several other surface orientations that could work for defect-free tensile-strained Ge growth, either from the point of known, successful surface orientations (i.e. (111)B) or from the perspective of antiphase-domain (APD)-free

capping on (211) surfaces. Tensile-strained self-assembly on miscut (111)B surfaces often leads to quantum wire formation, which in the case of Ge would enable novel quantum wires for embedded semimetallic tunnel junctions, contacts, and even topological insulators. Meanwhile, the tensile-strained self-assembly on the (211) surface is entirely untouched, remaining a vast area for exploration in tunable, tensile-strained self-assembly for the development of novel electronic devices.

I discovered proper growth conditions for the first-ever reported Ge TSQDs grown on InAlAs(111)A and (110). During this process, I not only found an unusual growth mode transition for Ge/(111)A TSQDs, but I also increased the body of knowledge on the fundamental kinetics behind their growth. This knowledge will be a boon for future electronic device development using semimetallic Ge TSQDs. I also proved efficient, direct band gap light-emission from Ge(110) TSQDs and provided a robust methodology for their successful growth.

TABLE OF CONTENTS

LIST OF TABLES

LIST OF FIGURES

LIST OF ABBREVIATIONS

a	Width of potential well
a_i	Constant in island scaling for a given *i* value
A_1, A_2, A_3	Energy minima for adatom absorption
ADF	Annular dark field
AFM	Atomic force microscopy
Al	Aluminum
AlGaN	Aluminum gallium nitride
AlN	Aluminum nitride
APB	Anti-phase boundary
APD (Chapter 2)	Avalanche photodiode
APD (else)	Anti-phase domain
As	Arsenic
As_2	Dimeric arsenic
As_4	Tetrameric arsenic
Be	Beryllium
BEP	Beam equivalent pressure
BF TEM	Bright field transmission electron microscopy
BL	Bilayer
C	Carbon
Cd	Cadmium

C_i	Constant in island scaling for a given *i* value
CdS	Cadmium sulfide
CdSe	Cadmium selenide
CdTe	Cadmium telluride
$D_{[\bar{1}10]/[001]}$	Orthogonal adatom diffusion coefficient
D_0	Adatom diffusion constant
DC	Diamond cubic
DE	Droplet epitaxy
D(E)	Density of states
DFT	Density functional theory
d_{hkl}	Distance between (hkl) planes
E	Energy
e	Elementary charge ($1.60217662 \times 10^{-19}$ coulombs)
E_C	Conduction band energy
E_D	Energy barrier for surface diffusion
EELS	Electron energy loss spectroscopy
E_F	Fermi energy
E_n	Quantum well energy at an integer level
Er	Erbium
ErAs	Erbium arsenide
ES	Ehrlich-Schwoebel
E_V	Valence band energy
eV	Electron volt

FCC	Face-centered cubic
FHI-aims	Fritz Haber Institute *ab initio* molecular simulations
f_i	Scaling function
$f_i(u)$	Island size scaling function
FM	Frank-van der Merwe (layer-by-layer growth)
$g(r/\langle R \rangle)$	Radial distribution function (RDF)
$g^{(2)}(\tau)$	Second order autocorrelation function
Ga	Gallium
GaAs	Gallium arsenide
GaN	Gallium nitride
GaP	Gallium phosphide
GaPSb	Gallium phosphorous antimonide
GaSb	Gallium antimonide
GaTe	Gallium telluride
Ge	Germanium
GeSi	Germanium silicon alloy
H (Chapter 1)	Monolayers (Figure 1.17)
H (else)	Hydrogen
HAADF	High angle annular dark field
HBT	Hanbury Brown and Twiss
(hkl)	Crystallographic notation for a crystal plane
{hkl}	Crystallographic notation for a family of crystal planes
[hkl]	Crystallographic notation for a crystal direction

<hkl>	Crystallographic notation for a family of crystal directions
HRTEM	High-resolution transmission electron microscopy
i	Critical cluster size: one atom fewer than needed to stabilize an island nucleus
In	Indium
InAlAs	Indium aluminum arsenide, typically with InP lattice-matching: In ~ 52%, Al ~48%
InAs	Indium arsenide
InGaAs	Indium gallium arsenide, typically with InP lattice-matching: In ~ 53%, Al ~47%
InGaN	Indium gallium nitride
InGaP	Indium gallium phosphide
InGaSb	Indium gallium antimonide
InN	Indium nitride
InP	Indium phosphide
InPSb	Indium phosphorous antimonide
InSb	Indium antimonide
IR	Infrared
k	Momentum
K	Kelvin
k_B	Boltzmann constant (~ 8.617×10^{-5} eV/K)
kMC	Kinetic Monte Carlo
LED	Light-emitting diode

LN_2	Liquid nitrogen
m	Mass of carrier
MBE	Molecular beam epitaxy
MEE	Migration-enhanced epitaxy
Mg	Magnesium
MgSe	Magnesium selenide
MgTe	Magnesium telluride
ML	Monolayer
n	Integer (i.e., 1, 2, 3…) level in quantum well or in wavelength
N	TSQD areal density
N (Chapter 2)	Nitrogen
NH_3	Ammonia
nm	Nanometer (1×10^{-9} m)
NN	Nearest neighbor
N(r)	Scaling relation as a function of distance between QDs, r
N_s	Number of islands of size s
O	Oxygen
P	Phosphorous
P_2	Diphosphorous
PBN	Pyrolytic boron nitride
PES	Potential energy surface
PID	Proportional-integral-derivative
PL	Photoluminescence

r	Separation distance between two QD centers
r_0	Average TSQD radius
$\langle R \rangle$	Average distance between TSQDs
RDF	Radial distribution function
RDS	Radial distribution scaling
RGA	Residual gas analyzer
RHEED	Reflection high-energy electron diffraction
RMS	Root mean square
R_q	Root mean square roughness
S	Sulfur
s	Second
s	Size of island
$\langle s \rangle$	Average island size
|s|	Fine structure splitting
SAQD	Self-assembled quantum dot
Sb	Antimony
Sb_4	Tetrameric antimony
Se	Selenium
Si	Silicon
SiC	Silicon carbide
SK	Stranski-Krastanov (islands on layer growth)
SL	Superlattice
SQS	Special quasirandom structure

STEM	Scanning transmission electron microscopy
T	Temperature
t	Thickness of a layer
T_1, T_2	Adatom transition site energy
TA	Thermal annealing
t_c	Wetting layer thickness
TC	Thermocouple
T_{cell}	Effusion cell temperature
Te	Tellurium
TEM	Transmission electron microscopy
T_{SUB}	Substrate temperature
TSQD	Tensile-strained quantum dot
u	$s/\langle s \rangle$
V_{BI}	Built-in potential voltage
QD	Quantum dot
QKD	Quantum key distribution
QW	Quantum well
QWr	Quantum wire
VW	Volmer-Weber (island growth)
WL	Wetting layer
XC	Exchange correlation
XPS	X-ray photoelectron spectroscopy
XRD	X-ray diffraction

XTEM	Cross-sectional transmission electron microscopy
$\|XX\rangle$	Bound exciton state
ZB	Zinc-blende
Zn	Zinc
ZnSe	Zinc selenide
ZnTe	Zinc telluride
0D, 1D, 2D, 3D	Zero-, one-, two-, and three-dimensional
°C	Degrees Celsius
Å	Angstrom (1×10^{-10} m)
$\hbar$	Reduced Planck constant
α-Al_xO_3	Sapphire
γ_e	Epilayer free energy
γ_i	Interface (epilayer-surface) free energy
γ_s	Surface free energy
ΔE	Radiative homogenous linewidth
θ	Surface coverage; also x-ray angle of diffraction
λ	Wavelength
μm	Micrometer (1×10^{-6} m)
τ	Resolved uniaxial stress tensor; also delay time between successive photon detection events

CHAPTER ONE: BACKGROUND & MOTIVATION OF GERMANIUM TENSILE-STRAINED QUANTUM DOTS

1.1 Motivation

The electronics industry is undeniably a powerhouse in today's economy; the consumer electronics market alone was valued at $1 trillion US dollars in 2019 and is expected to increase 7% by 2026.[1] The existence of this industry is only possible because of semiconducting materials, which are materials that contain a relatively small energy gap of <2 eV between the valence and conduction bands.[2,3] There are two types of semiconductors: direct and indirect band gap semiconductors.[3]

In a direct band gap semiconductor, the conduction band minimum and valence band maximum align in momentum (k) space (Figure 1.1).[4,5] This means that no momentum change is needed for electrons to transition between the conduction and valence bands.[4,5] Therefore, the absorption or emission of a photon is sufficient for an electron to transition from the valence to the conduction band or vice-versa.[5]

In contrast, electrons in an indirect band gap semiconductor require a change in both energy and momentum to move between the valence and conduction bands.[4,5] This is due to a k space offset between the conduction band minimum (L or X valley) and the valence band maximum (Figure 1.1).[4,5] Photon absorption or emission allows us to change the electron energy, but a transition from the conduction to valence band also requires interactions with phonons (quantized lattice vibrations) to change electron momentum.[3] The probability of this "three-particle" process occurring is

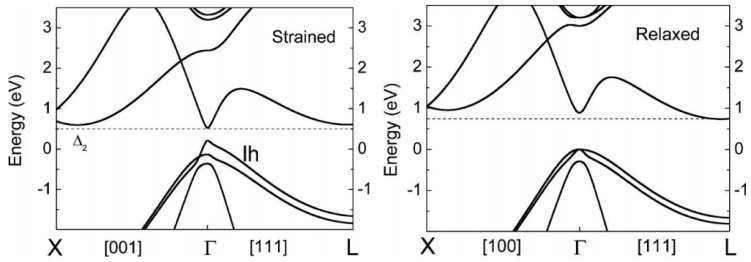

Figure 1.1 Computationally-derived band structures for (left) strained and (right) unstrained Ge. From Reference [6].

extremely small and so indirect band gap materials, like silicon (Si) and germanium (Ge), are very inefficient light-emitters.[5,7] Ge is a technologically important semiconductor widely used in industry for transistors and infrared detectors.[7] Ge works well for these devices due to its high gain coefficient, high electrical mobility, and narrow band gap.[7] However, its indirect band structure means that Ge is not useful for optoelectronic devices such as lasers and light-emitting diodes.

Computational modelling suggests a possible solution to this problem: bulk Ge should become a direct band gap semiconductor when grown on (001) and (110) surfaces, under ~1.6% and ~3% biaxial tensile strain respectively (see also Figure 1.2(a)(b)).[4,6,8,9] The band gap of (111)-oriented Ge should shrink to zero at ~4% tensile strain, turning it into a semimetal (Figure 1.2(c)).[4,8] In each case, the tensile strain causes dramatic changes to Ge's band structure, producing band gaps lower than that of unstrained, bulk Ge.[4,6] These changes to the band structure have important implications for optoelectronic applications that seek to take advantage of Ge's high gain coefficient and low band gap, or as a possible route to future topological materials based on conventional semiconductors.[6,8,10,11]

Researchers have adopted a number of different approaches for inducing tensile strain in Ge, ranging from nanomembranes, microdisks, and nanowires under mechanical

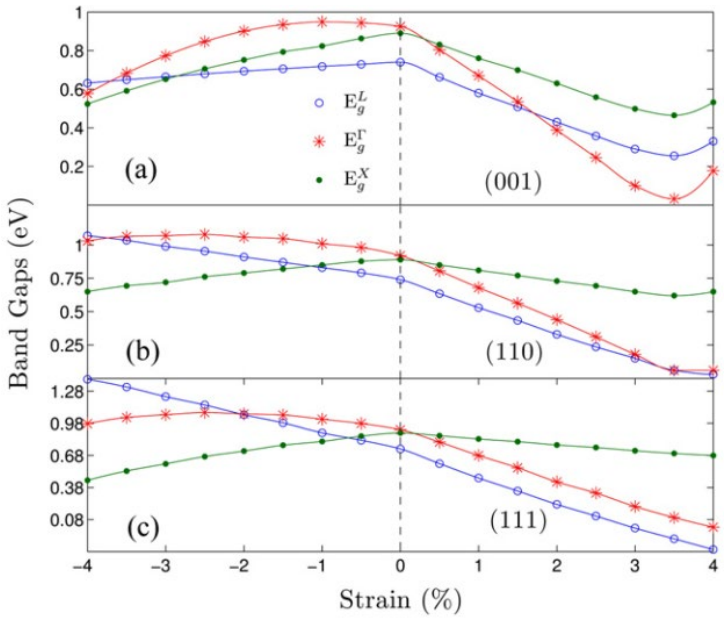

Figure 1.2 Band minima points as a function of biaxial strain on the (a) (001), (b) (110), and (c) (111) surfaces for Ge. The red, starred points indicate the calculated Γ valley band gap while the blue, open points indicate the L valley band gap. Green, solid points indicate the X valley band gap. Conceptually, wherever the red, starred points are below the green and blue points is where there is a direct band gap. From Reference [4].

stress, to self-assembled Ge/InAlAs and Ge/AlAs nanocomposites.[12–16] Although these are all ingenious methods, mechanically straining bulk Ge to the required tensile strains can cause plastic (irreversible) deformations in the material.[12,14] The self-assembled nanocomposite approaches rely on phase separation, which reduces the amount of control in the system.[13,16] Therefore in terms of scalability and future device compatibility, a simple, tunable technique that can accommodate large tensile strains without generating defects would be preferable.

Recent research has provided just this solution: self-assembled tensile-strained quantum dot growth. Tensile-strained self-assembly is a device-compatible, scalable, tunable, one-step process that produces defect-free structures with large tensile strains.[17–19] As a proof of concept, we extended this self-assembly growth technique to create

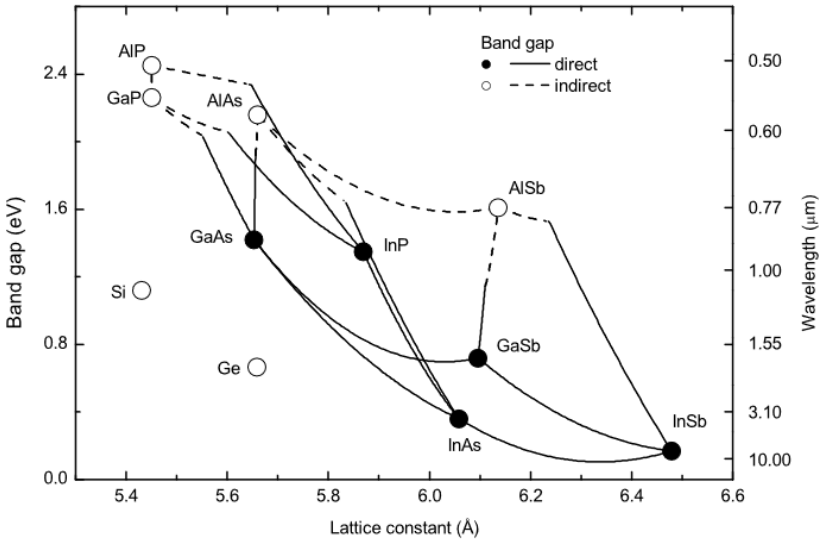

Figure 1.3 Lattice constants vs. band gap energy/wavelength for several common III-V and group IV semiconductors. From Reference [20].

highly tensile-strained, defect-free GaAs quantum dots under 3.7% tensile strain on $In_{0.52}Al_{0.48}As$(111)A and (110) surfaces.[21–25] Figure 1.3 shows the similarities between GaAs and Ge lattice constants, which means that replacing GaAs with Ge in $In_{0.52}Al_{0.48}As$ (lattice-matched to InP) is a direct substitution.[20,26] Recently, researchers used tensile-strained self-assembly to grow Ge tensile-strained quantum dots (TSQDs) on InAlAs(001) lattice-matched to InP, resulting in successful light emission.[27] Tensile-strained self-assembly is therefore essential to this research, and a detailed discussion of how this process works is provided in Section 1.2.4.2 and Chapter 2 in this dissertation.

1.2 Background

I use this background section to discuss the basics of molecular beam epitaxy (MBE); characterization techniques for this project; zinc-blende and diamond cubic structures, including their impact on antiphase domains; heteroepitaxial growth and self-assembly; and band structure, quantum confinement, and tensile strain effects.

I designed and carried out experiments to deconvolve the effects of growth temperature, growth rate, and capping to understand their contributions to Ge tensile-strained quantum dot (TSQD) nucleation and growth on each substrate orientation. We created comprehensive matrices of samples to ensure that we mapped out the growth parameter phase space (i.e. temperature, growth rate, and deposition amount) to help us easily interpret how changes impact TSQD growth. In other words, certain aspects of the growths (i.e. temperature, growth rate, and deposition amount) acted as independent variables. For example, we designed experiments that kept the same growth temperatures and rates but varied the deposition amount, allowing us to reliably discern growth effects.

1.2.1 Molecular Beam Epitaxy (MBE)

MBE is an important tool for precise sample growth in both research and industry. It uses a pristine environment consisting of an ultra-high vacuum ($<10^{-9}$ Torr) and ultra-pure (>99.999%) elemental sources. The ultrahigh vacuum and source purity in the MBE chamber is essential for minimizing impurities. This is because background levels of unwanted atoms/molecules in the chamber and source impurities can incorporate into the growing crystal, creating point defects.[28] These impurities act as scattering centers or charge carrier traps,[28] reducing the electronic and optical properties of the material we grow. For this reason, we use ion gauges and a residual gas analyzer to monitor the chamber pressure and elemental partial pressures, respectively, and identify any leaks.

Figure 1.4 illustrates a simplified MBE machine with many of the same components discussed in this section. The MBE we use is slightly different than the one depicted in Figure 1.4. We use a Veeco Gen 930 model MBE, and the following source elements are available: Ge, Ga, Al, In, As, Sb, Si, Be, and GaTe, many of which are

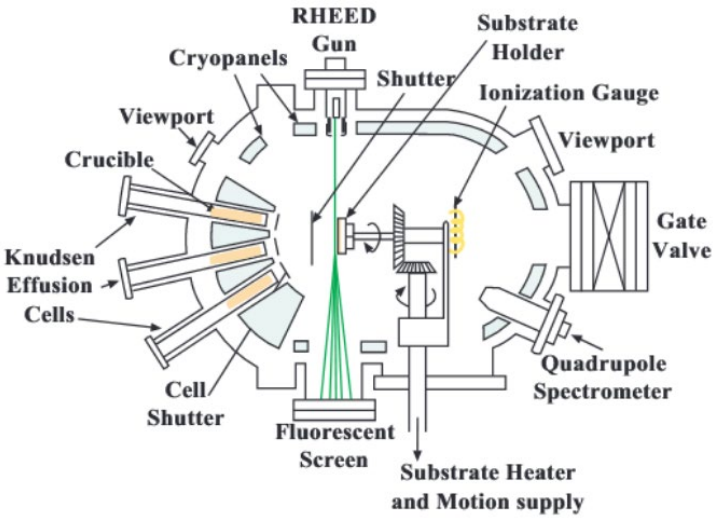

Figure 1.4 Simple schematic of a typical MBE machine. From Reference [29]. While the MBE used in our lab is different (there is no Quadrupole Spectrometer or extra shutter in front of the substrate), the key components (i.e. Knudsen effusion cells, cell shutters, RHEED gun, etc.) are similar.

essential for this project. Effusion cells containing these molecular/atomic sources are temperature-controlled by heaters and thermocouples. The hotter the effusion cell, the more atoms/molecules evaporate, creating a beam of atoms/molecules directed at a heated substrate. These atoms move across the substrate surface until they find a low energy bonding site, at which point they bond to the substrate and the crystal grows, one layer of atoms at a time. Before sample growth, we measure the flux of each relevant source using a retractable ion gauge to measure beam equivalent pressures (BEPs) in front of the substrate. To calibrate BEPs, we determine growth rates as a function of effusion cell temperatures. MBE growth rate is low (μm/hour or monolayers (ML) or bilayers (BL) per second). With low growth rates and pneumatic shutters that control the amount of time the substrate is exposed to the beam of atoms/molecules, we precisely control layer thickness down to the atomic scale.

We monitor substrate temperature with a thermocouple and an optical pyrometer, calibrated against known temperatures where the crystallographic surface reconstruction

changes for a given substrate. We detect these changes using reflection high-energy electron diffraction (RHEED). For example, some of the important transition points that we look at on GaAs(001) substrates are the thermal desorption of the native oxide at 580 °C and the transition between the (2 × 4) and c(4 × 4) surface reconstructions at 525 °C.[30]

1.2.2 Characterization

Here I describe the various experimental techniques that I used during the course of my project to understand the growth rates for each source and the structural and optoelectronic properties of Ge TSQDs.

1.2.2.1 Growth Rate Determination

This section investigates the methods used to determine source growth rates. I used reflection high-energy electron diffraction (RHEED) to find the growth rates of the In, Al, and Ga sources, while I used transmission electron microscopy (TEM) and ellipsometry to determine the Ge growth rate. In future work, I recommend using ellipsometry over TEM for determining the Ge growth rate, since it is faster, cheaper, and simpler to use compared to TEM without sacrificing accuracy.

1.2.2.1.1 Reflection high-energy electron diffraction (RHEED)

A high energy (~14 kV, 1.4 A) electron beam diffracts off the sample at a low-angle of incidence during MBE growth. A phosphorescent screen captures the resulting RHEED diffraction pattern, which is digitized using a high-resolution camera for software analysis. Streaks, also known as reciprocal lattice rods or “rel-rods,” appear on the screen, indicating a smooth surface.[31] The brightness of a streak in the RHEED pattern can be measured at the onset of growth.[31,32] During growth, the streak’s intensity will oscillate (see Figure 1.5(b)).[31,32] When the surface is smooth (i.e. when there is one

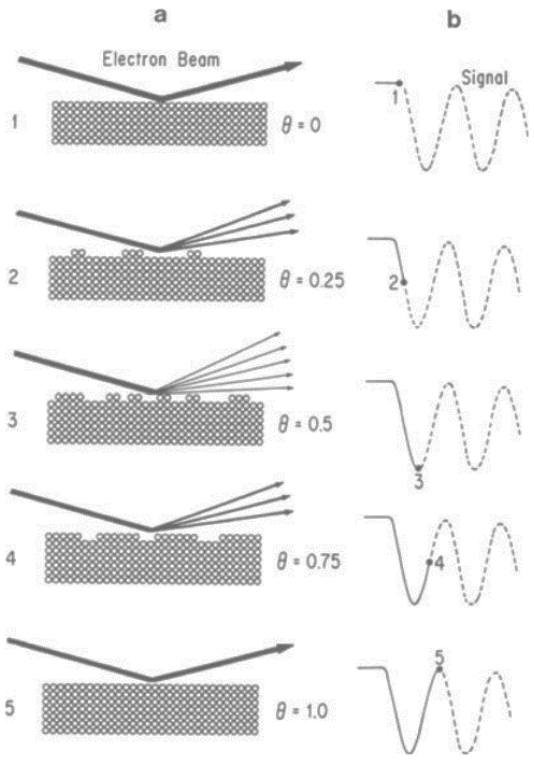

Figure 1.5 (a) These diagrams are cross-sectional surface representations showing the growth progression of a single monolayer, with the RHEED beam (initial and reflected) represented as solid black arrows and the surface coverage amount, θ. These show the relationship between surface coverage and reflected electron beam (b) These plots are the accompanying RHEED intensity for each diagram in (a). From Reference [33].

complete layer of growth with minimal-to-no island formation) (Figure 1.5(a)), the brightness is at its highest (Figure 1.5(b).[31,32] When half a monolayer is complete, there are many islands that scatter the electron beam, so brightness is at its lowest (see Figure 1.5).[31–34] The oscillation period of the RHEED intensity is hence a direct measure of the time taken to grow a complete atomic monolayer (ML) on the sample.[31–34] This means that the growth rate of a material in ML/s can be accurately measured during MBE growth using RHEED.[31,32,34] If we know the lattice constant, we can convert the units from ML/s either to nm/s or μm/hr. We also use RHEED to see how the surface morphology reconstructs with changing conditions (i.e. substrate temperature, oxide

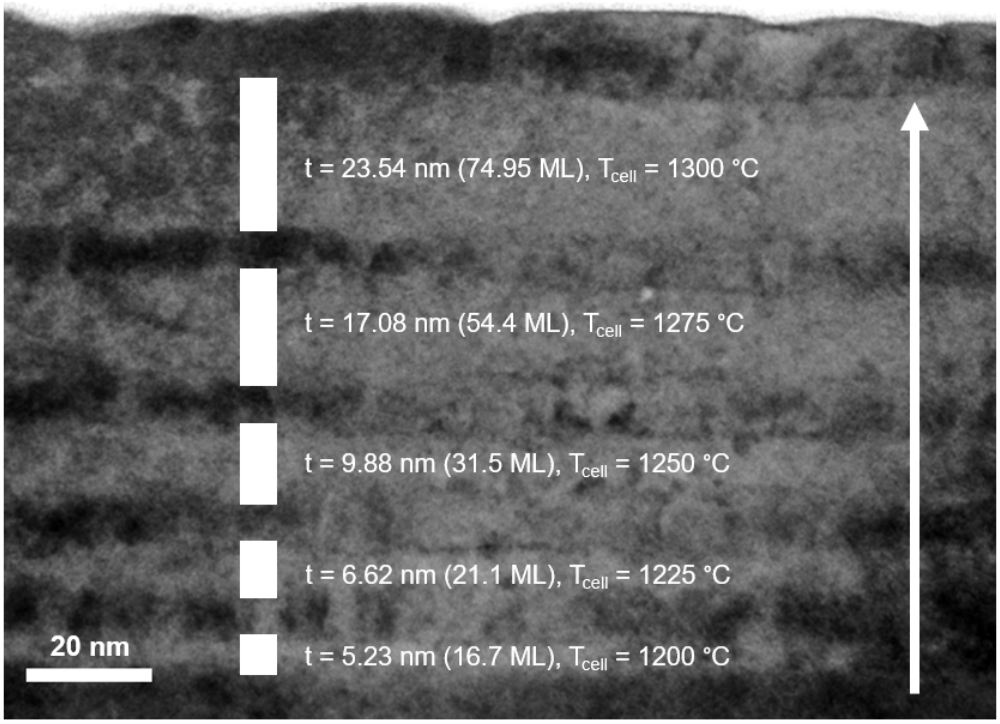

Figure 1.6 Cross-sectional TEM image showing Ge layers of different thicknesses, separated by darker AlGaAs layers. The white arrow shows the growth direction. In this diagram, *t* is the layer thickness and T_{cell} is the Ge cell temperature.

desorption, quantum dot deposition).[31] RHEED thus allows the grower to know the surface conditions in real time so that they can adjust growth accordingly.

1.2.2.1.2 Transmission Electron Microscopy (TEM)

Unlike other elements in our MBE system, Ge does not easily form RHEED intensity oscillations.[26] This is why we used TEM in Chapter 3 to determine the growth rate.[26]

TEM uses the diffraction of an electron beam through a mechanically thinned sample (<100 nm thick) to image the internal crystal structure of a sample at the atomic-scale.[35] To measure Ge's growth rate, we deposited multiple Ge layers between ~10 nm AlGaAs marker layers on GaAs(001) (Figure 1.6). Each Ge layer was grown for an hour at a different effusion cell temperature. Then a cross-section of the sample was imaged by

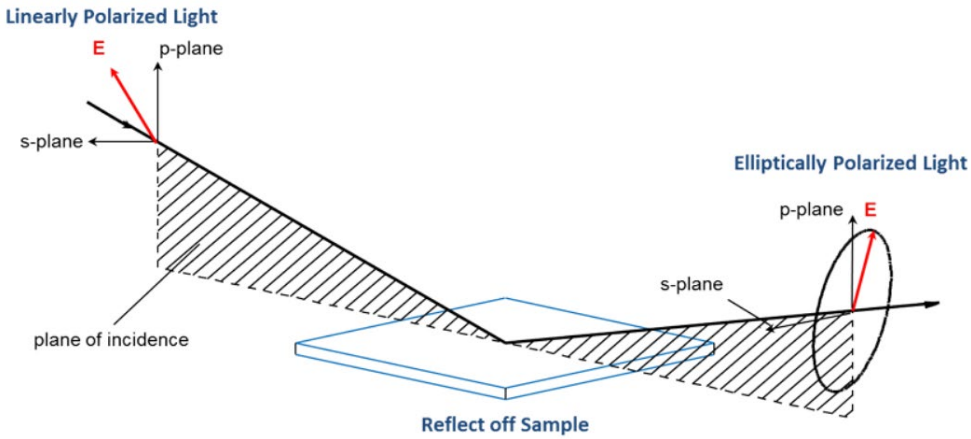

Figure 1.7 Diagram of an ellipsometry setup. The diagram shows how light, reflected off a sample can change its polarization direction, in this case, represented as the light's transverse electric field, E (red), changes direction. This gives us information about film thickness. From Reference [36].

TEM (Figure 1.6). We used ImageJ software to measure the average thickness and standard deviation for each Ge layer in these images. ImageJ is useful for this calculation, because it measures lengths in pixels which we converted to either nanometers or monolayers based on the scalebar.

1.2.2.1.3 Ellipsometry

Although we started the project using TEM to calibrate the Ge growth rate, we discovered we could save time and effort by instead using ellipsometry. We grew three different Ge samples on GaAs(001) for an hour each and used the ellipsometry results to calculate the Ge growth rate. One of the advantages of ellipsometry is that it can measure film thicknesses in the range of 1 nm up to 10 mm.[37] Our samples fit within this range as they were approximately 30 nm thick. Ellipsometry measurements are highly thickness- and material-dependent,[37] which makes it an ideal tool for quickly measuring Ge thin films. Ellipsometry works by beaming a laser at a thin film and measuring the change in light polarization (Figure 1.7).[36,37] This technique is sensitive enough to measure layers thinner than the laser's wavelength.[37]

1.2.2.2 Structural and Chemical Characterization

Once I know the growth rates for each source, I can then grow buffer calibration and TSQD samples with precise layer thicknesses and compositions. In this section, I discuss the tools needed to characterize structures after growing them. We use x-ray diffraction (XRD), high-resolution scanning TEM (STEM), electron energy-loss spectroscopy (EELS), energy dispersive x-ray spectroscopy (EDS), Raman spectroscopy, and atomic force microscopy (AFM) to characterize the sample composition, QD location, QD strain, and QD shape/size.

1.2.2.2.1 X-Ray Diffraction (XRD)

XRD provides information about lattice constants and hence structural composition.[2] Bragg's law (Equation 1.1) says that the incident light will diffract off the material's lattice at specific, allowed angles.[2]

Equation 1.1 $$n\lambda = 2d_{hkl}\sin(\theta)$$

In Equation 1.1, we define the variables as follows: λ is the x-ray's wavelength, θ is the angle of diffraction, d_{hkl} is the distance between (hkl) planes, and n indicates an integer multiple of λ.[2] We can hence calculate lattice constant from the angular position of XRD peaks.[2] Figure 1.8 shows an example of how we analyze peak fitting of an XRD spectra. To determine the composition for a ternary alloy, such as the buffer and barrier layers we use (e.g. InGaAs and InAlAs), we use Vegard's law, which assumes a linear interpolation of lattice constant between the binary end-point compounds.[38] XRD also provides information about the lattice strain or relaxation, which helps us calibrate the growth conditions needed to get compositions required for lattice-matching different materials.

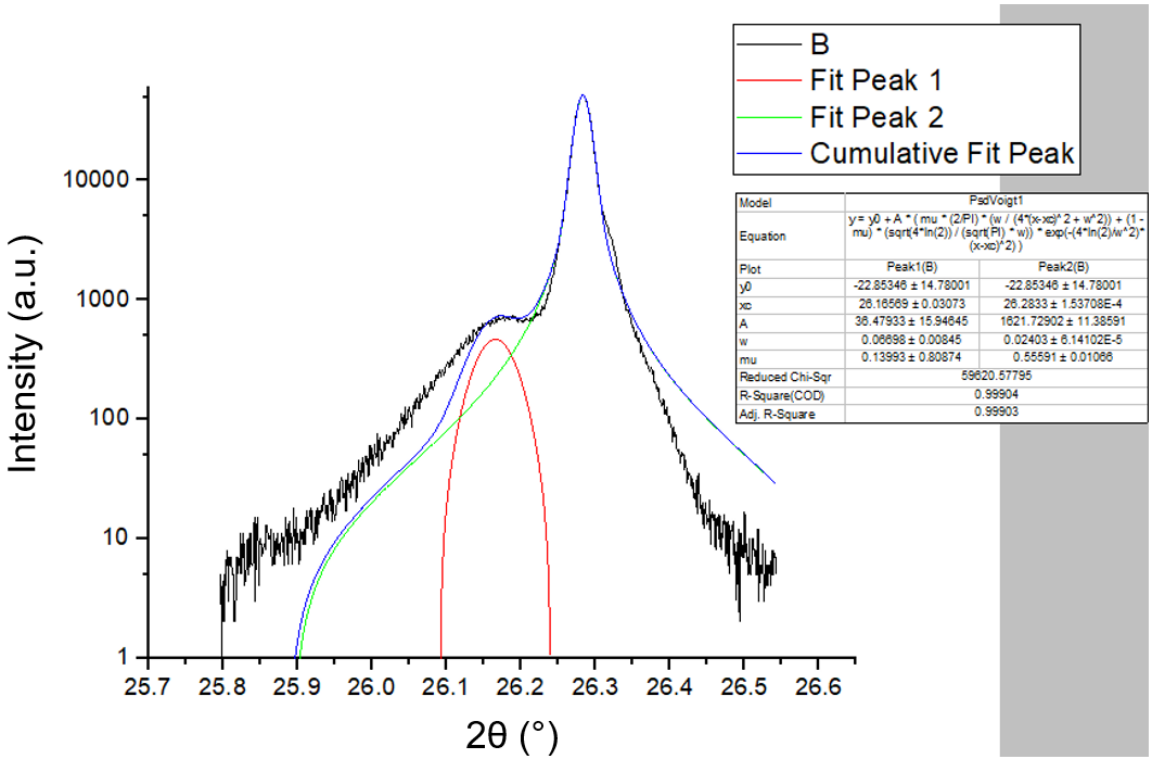

Figure 1.8 XRD spectra showing a peak fitting analysis of an InAlAs(111)A calibration sample, 2θ is twice the diffraction angle, θ. The black spectrum is the original data, the red line fits the InAlAs(111)A peak, the green line fits the InP(111)A substrate, and the blue line is the cumulative peak fit from both the red and green lines. I analyzed this particular sample with a Pseudo Voigt (PsdVoigt1) peak fit, for which the fitting parameters are given in the inset table.

1.2.2.2.2 Scanning transmission electron microscopy (STEM)

STEM, while nearly identical to TEM, is different in that it uses a highly focused beam that scans across a sample, producing a serial signal stream correlated with the beam's position.[35] This technique results in high-resolution images where atoms and defects can easily be seen.[35] STEM has a high enough resolution to see atoms,[26,35] making it a useful tool for analyzing the crystal quality of Ge TSQDs. We also used STEM to image individual dislocations and determine defect type, density, angle, and location. See Chapter 3, Figure 3.2 and Figure 3.5 examples of how we used STEM imaging to analyze our TSQDs.

1.2.2.2.3 Electron Energy-Loss Spectroscopy (EELS)

EELS is used within a STEM and works by plotting the spectrum of energy loss against electron counts.[39] The electrons in the beam lose energy when they interact inelastically with the sample.[39] Inelastic energy loss is caused by electron interaction with inner-shell valence electrons, which occurs at specific loss energies for a given element.[39] We can therefore use EELS with STEM to map a sample's elemental composition with sub-nm resolution.[39] I refer the reader to Figures 3.2 and 3.5 for a good representation of how we used STEM in combination with EELS for our samples.

1.2.2.2.4 Energy Dispersive X-ray Spectroscopy (EDS)

Like EELS, EDS is used within a TEM/STEM for elemental composition mapping.[40] EDS works by using the electron beam to stimulate the emission of x-rays from atoms within a sample.[40] This emission is caused by ejecting an inner-shell electron, causing a higher energy electron to fall into the inner shell, emitting x-rays characteristic of a specific element.[40] An EDS spectrometer measures the energy of the emitted x-rays and plots the intensities of each emitted x-ray as a spectrum or a map with nm resolution.[40] EDS is preferred over EELS for quick scans of elemental distribution in a sample.[40] EELS has higher resolution, and thus is preferred for precise diffusion and TSQD studies.[39] I refer the reader to Figure 3.2 for a good representation of how we used STEM in combination with EDS for our samples.

2.2.2.5 Atomic Force Microscopy (AFM)

I employed tapping mode AFM to image my sample surfaces and confirm the presence of Ge TSQDs. In AFM, a nm-scale tip oscillates across the surface in a raster

scan at the cantilever's resonant frequency.[41] The piezoelectric cantilever adjusts the tip height according to the resulting force displacement in the oscillations.[41] These

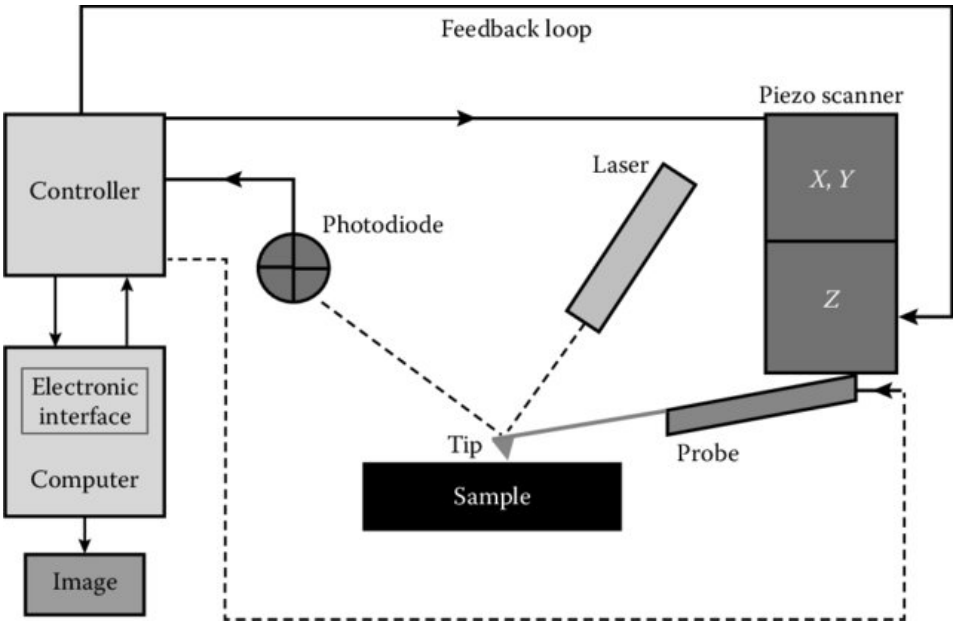

Figure 1.9 Simplified schematic showing a typical AFM setup. From Reference [42].

oscillations are detected by reflecting a laser off of the top of the probe's tip (Figure 1.9) into a photodetector, which sends signals to a computer, resulting in an image.[41,42] This allows a researcher to measure sub-nm differences in height on the sample surface,[41] which is critical for understanding Ge TSQDs. AFM images reveal qualitative and quantitative information about symmetry, height, diameter, and areal density of uncapped (i.e. uncovered) quantum dots.[22,26,43] AFM shows where TSQDs prefer to nucleate, and how much deposition is needed to trigger nucleation, telling us about TSQD growth kinetics and thermodynamics.[43] Additional computational analysis, like radial distribution scaling (RDS), is used on AFM images to understand the preferred TSQD separation distance.

1.2.2.2.6 Raman Spectroscopy

Once Ge TSQD growth was confirmed using the previous structural characterization techniques, we used Raman spectroscopy to determine the amount of

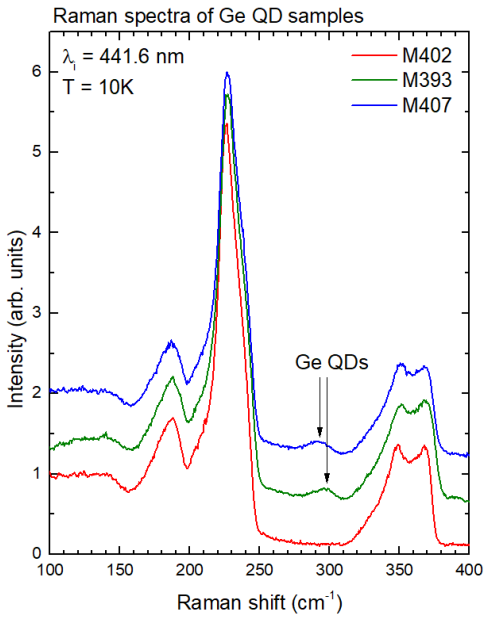

Figure 1.10 Raman spectra showing Ge(110) TSQD peak identification. A more thorough analysis of this spectra, with bulk Ge peak position and InAlAs peaks identified, is provided later in Chapter 5.

strain in our TSQDs. We can do this, because Raman spectroscopy is an optical technique that is highly sensitive to crystal bonding and thus tension or compression between atoms.[44]

Raman spectroscopy relies on the inelastic scattering of light, typically from a laser in the visible or ultraviolet range.[44] Incident light interacts with the crystal's vibrations and changes the energy of the scattered light.[44] An energy shift reveals vibrational information in a crystal,[44] such as biaxial tensile strain.[26] Strain is measured by a negative or positive peak shift from the bulk value.[26,45] With this information and with Ge's strain coefficient (found in literature), we can calculate the tensile strain within

our Ge TSQDs.[26,45] A representative spectra for Raman spectroscopy of Ge TSQDs is shown in Figure 1.10. The data in Figure 1.10 is presented in a different format in Chapter 5 and is explained in detail there.

1.2.2.3 Band Gap Characterization: Photoluminescence Spectroscopy (PL)

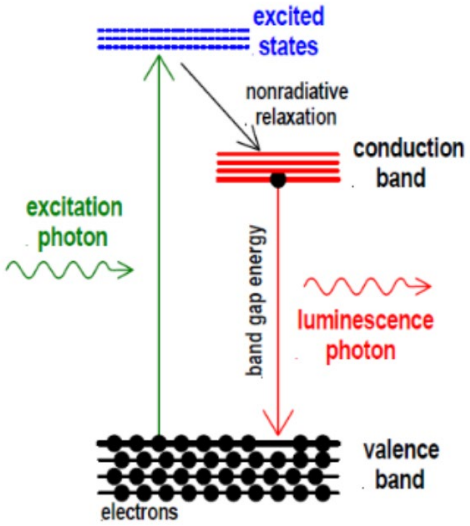

Figure 1.11 Diagram showing the basic principles of PL: electron excitation from the valence band, non-radiative relaxation to the conduction band, and finally the emission of a photon with the semiconductor band gap's energy. From Reference [46].

After confirming the presence of Ge TSQDs, we analyzed the optical properties of buried TSQDs. A wider band gap InAlAs layer above the TSQDs acts as a potential barrier to provide 3D quantum confinement of carriers within the Ge TSQDs (see also Figures 1.2 and 1.3 for a comparison of Ge and $In_{0.52}Al_{0.48}As$ band gaps).[47] In PL, laser light with an energy larger than the band gap of a sample is absorbed and reemitted at a characteristic wavelength corresponding to the semiconductor band gap (Figure 1.11).[48–50] The incident light excites electrons from the valence to the conduction band, leaving behind a hole in the valence band.[2,50] The electron and hole recombine across the band gap and emit a photon (Figure 1.11).[2,50] Measuring the wavelengths of the light emitted

gives us information about sample composition, quantum confinement within TSQD nanostructures, and overall band structure.[9,21,48–50] PL requires a defect-free sample, because defects such as dislocations or impurities create non-radiative recombination centers that suppress PL emission.[28] Overall, PL is a really useful way of identifying whether or not I transformed Ge's band structure from an indirect band gap to a direct band gap, because indirect band gaps do not emit light efficiently whereas direct ones do (see Section 1.1).

1.2.3 Sample Structure and Crystallography

Now that I have described how we calibrate our InAlAs/InGaAs layer compositions and analyze the sample properties, I want to take the time to describe the physical and chemical properties of the relevant materials, Ge, InAlAs, InGaAs, InAs, and GaAs. In this section, I discuss the zinc-blende and diamond cubic crystal structures as well as the challenges related to growing zinc-blende on diamond cubic crystals.

1.2.3.1 Zinc-blende and Diamond Cubic Structures

The zinc-blende (ZB) structures of interest are InAlAs, InAs, and InGaAs, which we use as the buffer and/or capping materials.[26] The substrate that we grow our samples on, InP, is also ZB.[51] GaAs TSQDs, which we use to compare to Ge TSQDs throughout this dissertation but especially in Chapter 4, are also ZB crystals.[43,51] The specific combinations of $In_{0.52}Al_{0.48}As$ and $In_{0.53}Ga_{0.47}As$ that I used are calibrated to be lattice-matched to the InP substrate.[52] We embed the Ge TSQDs, which have a diamond cubic (DC) structure,[51] within InAlAs barrier layers. We use InAlAs to encapsulate Ge TSQDs, because InAlAs has a larger band gap than Ge, which should allow for charge carrier (i.e. electrons and/or holes) confinement within the TSQDs.[20–22,26,47]

The DC structure consists of two interpenetrating face-centered cubic (FCC) lattices of the same elemental species, offset by (¼, ¼, ¼) (see Figure 1.12(a)).[51] The atoms form tetrahedral polygons covalently bonded at each corner.[51] Since there is no charge difference between atoms, the DC crystal structure is nonpolar, meaning there is no electrostatic charge difference between atoms.[53] The ZB structure is a derivative of the

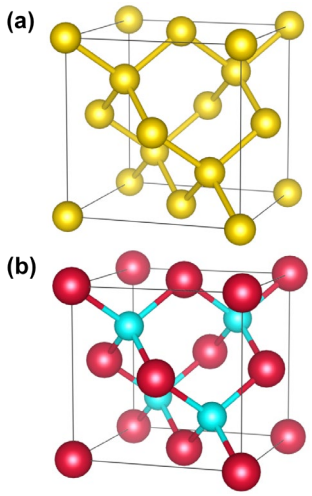

Figure 1.12 (a) Diamond cubic and (b) zinc-blende structures. The thin black lines in each diagram represent one cubic unit cell. I used Vesta Crystallography software to make this diagram.

DC structure.[51] Instead of having all one elemental species, the two interpenetrating FCC sublattices consist of either group III or group V elements (see Figure 1.12(b)).[51] Due to their similar electronegativities, these elements bond covalently into tetrahedral polygons, however electron donation creates a small ionicity.[2,53] This ionization results in a slight structural polarity, since ionic bonding leads to a difference in electrostatic charge between atoms, the atoms will have a slightly positive (group III) or negative (group V) charge.[2,53,54]

1.2.3.2 Monolayers or Bilayers— The Nomenclature Stems from Crystallography

Throughout this dissertation, we use the term "monolayers (ML)" or "bilayers (BL)" depending on the crystal structure and surface orientation used. Figure 1.13 illustrates this concept. For ZB structures, both a group III and group V element make up each monolayer, but for a DC structure, monolayers or bilayers are formed exclusively by a group IV element.[51,53]

When growing on (001), ZB structures have two equally-spaced monolayers per unit cell (see Figure 1.13(a)). This equal spacing between monolayers persists regardless

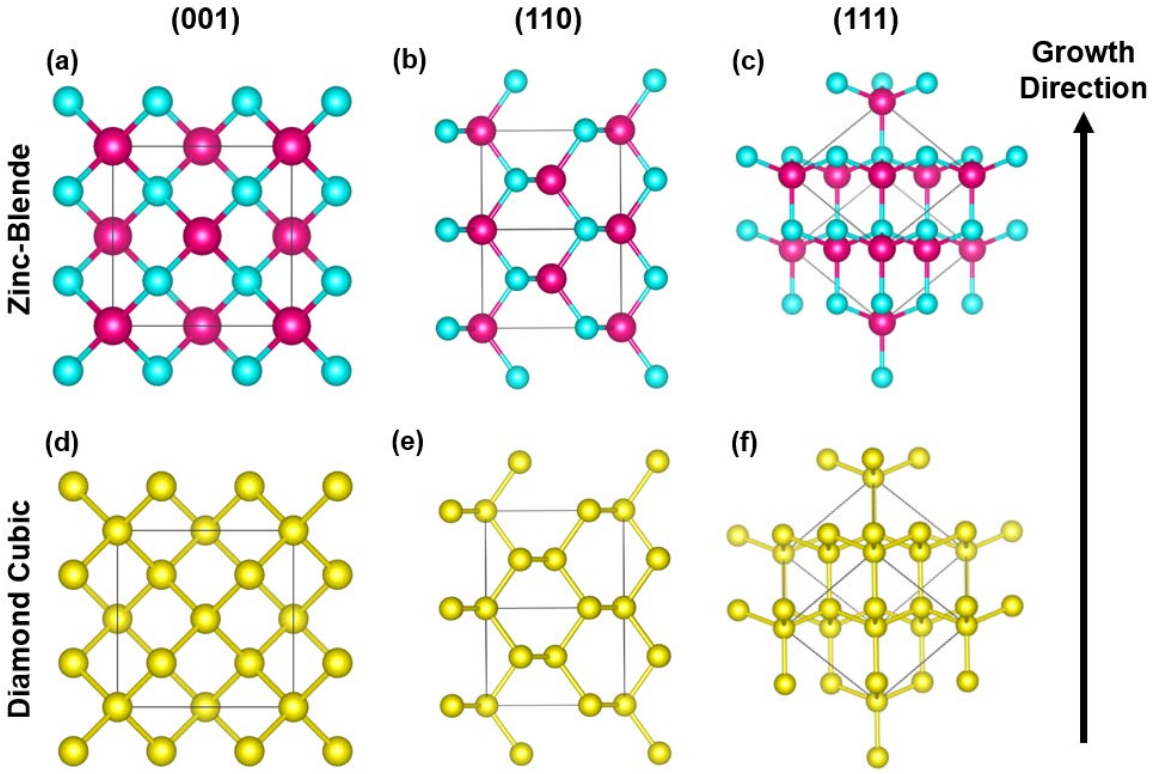

Figure 1.13 (a)-(c) Zinc-blende and (d)-(f) diamond cubic structures rotated to show the growth direction along (a),(d) (001); (b),(e) (110); and (c),(f) (111). The thin black lines in each diagram represent the cubic unit cell. I used Vesta Crystallography software to make this diagram.

of growth direction for ZB structures (Figure 1.13 (a)-(c)). Even on the (111) surface, ZB monolayers are equally separated (Figure 1.13(c)). In this case, as with each ZB growth

direction investigated here, one monolayer is defined as a complete layer composed of equal parts group III and group V. Figure 1.13(c) also reveals that a ZB (111) monolayer is layered so that all group III align along one direction in the (111) plane and vice versa for the group V element. For ZB (111) structures, we denote the (111) surface with an A or a B to signify that the surface is group III or group V terminated, respectively.[19] For example, InP(111)A is In-terminated at its surface, and InP(111)B is P-terminated at its surface.[19]

DC structures differ in that there are four complete, equally spaced monolayers per lattice constant on (001) instead of two monolayers for ZB (Figure 1.13(d)). Because of this equal spacing, we use the term monolayers for Ge(001) growths. Equal spacing between group IV layers also occurs on the (110) surface, hence why we use monolayers to describe (110) growths (Figure 1.13(e)). The term "bilayer" is used for diamond cubic materials grown on (111), because the spacing between each layer of atoms is not the same (Figure 1.13(f)). Instead, there is a shorter bilayer of atoms separated by the elemental bond length (Figure 1.13(f)). Because all atoms are the same element in a DC structure, it would be incorrect to write "Ge(111)A," so we instead must write "Ge grown on InAlAs(111)A" or "Ge/(111)A" to describe the surface symmetry and chemistry.

1.2.3.3 Challenges in Ge TSQD Capping

This project involves the growth of Ge with a DC structure within a III-V semiconductor crystal with a ZB structure. These different structures, while similar, are not entirely compatible with one another. This makes integrating Ge in III-V semiconductors such as InAlAs challenging for several reasons, which I address in this section.

1.2.3.3.1 Anti-Phase Domains (APDs)

The polarity difference between the ZB and DC structures means that combining them can lead to APDs.[53,55–58] A crystal without APDs has the same structure seen in Figure 1.13(a)-(c) where only III-V bonds are present.[53] When an APD exists, III-III and V-V bonds form a two-dimensional structural defect called an antiphase boundary (APB), as depicted in Figure 1.14(a).[53] The fundamental difference between APDs and APBs is found in their terminologies. APDs are "bounded" by APBs, resulting in crystal

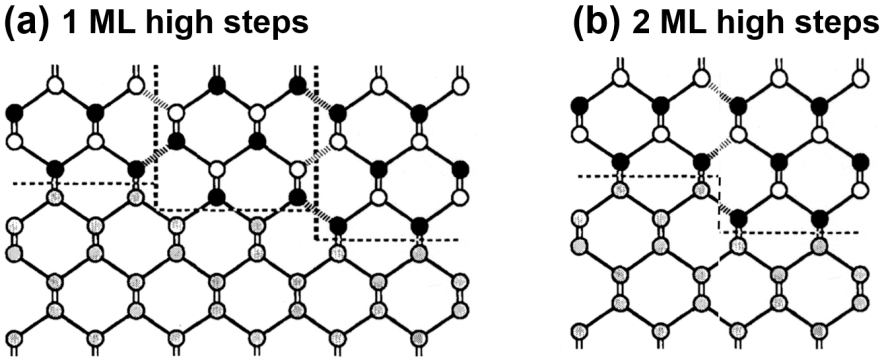

Figure 1.14 2D crystal representations showing a III-V material (black and white atoms) grown on a diamond cubic structure's (001) interface (grey atoms). In general, the dashed lines represent interfaces, but in (a), the vertical dashed lines separate APDs. (b) shows how increasing the step height from one to two monolayers (ML) eliminates APDs. Adapted from Reference [53].

"domains" where the ordering is different relative to the rest of the crystal.[53] Defects generated at APBs include stacking faults and twin boundaries that degrade a crystal's optoelectronic properties.[58] Therefore, preventing APD formation is a priority when we cap Ge TSQDs (DC) with InAlAs (ZB), which is necessary to form the top barrier for quantum confinement.

These APBs tend to form along single step edges on the (001) surface (Figure 1.14(a)).[53] Since real materials will have step edges, it is important to understand how to eliminate or reduce the possibility of APDs. Two possible methods exist: change the

crystallographic orientation and/or use a substrate whose surface is intentionally offcut at some angle.[53,55–57]

Although (001) is the most common surface orientation used in semiconductor devices, it suffers from significant APD formation during polar-on-nonpolar epitaxy (i.e. III-V ZB, a polar structure, on a nonpolar DC structure).[59,60] To avoid the APD formation shown in Figure 1.14(a), this surface requires either a perfect doubling of every step edge's height via the use of offcut substrates[53] (see Figure 1.14(b)), or using migration-

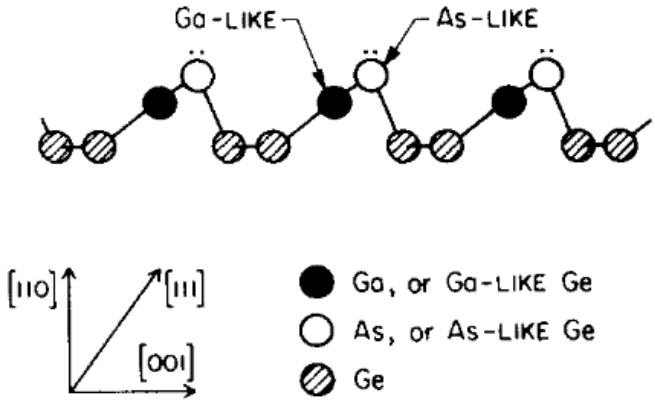

Figure 1.15 A 2D crystal diagram showing the surface reconstruction of Ga- and As-like sites on a Ge(110) substrate. From Reference [59].

enhanced epitaxy (MEE).[58] MEE alternates group III and group V depositions between short (~1 s) pauses, allowing for long adatom diffusion lengths that lead to smoother, less-defected surfaces.[61]

Alternatively, the (110) surface may be particularly favorable for Ge TSQD growth, because for this orientation the ZB structure is pseudo-nonpolar.[59,60] Kroemer *et al*. mention that electrical neutrality exists because of the (110) surface's geometry, which is composed of equal parts III and V atoms.[59] This pseudo-nonpolarity can be illustrated by looking at the horizontal planes of atoms (perpendicular to growth

direction) in Figure 1.13(a)-(c). There are an equal number of III and V atoms on a (110) plane (Figure 1.13(b)), compared to either III- or V-terminated (001) and (111) planes (Figure 1.13(a),(c)). Additionally, Kroemer *et al*. explains that regardless of the starting Ge surface reconstruction, the number of available valence electrons in the Ge lends itself to either a III-like or V-like chemistry that is consistent across the crystal surface (see Figure 1.15).[59] This means that APDs are avoided simply by the chemical properties of a (110) DC surface.[59] Thus, a pseudo-nonpolar structure grown on a nonpolar interface will have suppressed APD formation. In Chapter 5, I confirm that the InAlAs(110) cap above Ge(110) TSQDs is APD-free.

Another good orientation for suppressed APD formation is the (111) surface. Although the ZB (111) surface's polarity would indicate APD formation without sufficient substrate offcut angles,[59] successful attempts of growing zinc-blende GaAs on diamond cubic Ge (111) exist using MEE.[60] As I will show in Chapter 3, by growing samples with traditional MBE techniques, I was able to successfully grow Ge TSQDs on InAlAs(111)A free of APDs without the use of MEE.[26]

1.2.3.3.2 Minimizing Interdiffusion

APD formation was an issue I avoided in this dissertation, but it was not the only problem I successfully averted. I anticipated that interdiffusion of Ge, In, and Al atoms between the TSQDs and the surrounding InAlAs matrix would be a potential challenge for this project, but as is discussed in Chapters 3 and 5, no interdiffusion was found. Interdiffusion is a process where atoms from one crystal diffuse into a different crystal.[2,62,63] Specifically for the purposes of this dissertation, Ge is a common dopant in III-V compounds, and III-V compounds can easily diffuse into Ge.[62,63] In both cases, the

foreign atoms likely act as substitutional dopant species, which may complicate nanostructure optoelectronic behavior.[57,63] Hence, we used EELS to check for interdiffusion from Ge TSQDs into the surrounding InAlAs crystal after deposition.[26]

If interdiffusion were to occur, there are a few ways to minimize it via interface control methods. Examples such as MEE and/or low temperature growth are known to help the Ge and III-V atoms stay where we want them.[57,64] During MEE, layers grow via alternating fluxes (i.e. depositing some Ga then some Al to grow AlGaAs) with brief annealing pauses, resulting in atomically smooth surfaces even for difficult growths.[65,66] We did not use MEE within the scope of this work, because it takes more time than our current, standard MBE growths. However, even without MEE, we found that Ge interdiffusion effects were negligible on both InAlAs(111)A and (110) under the MBE conditions we used (see Chapters 3 and 5).[26]

We speculate that we did not see interdiffusion due to the growth modes present in the samples investigated. The VW and SK growth modes are explained in greater detail in Section 1.2.4.1. In short, the samples we imaged with EELS/STEM (Ge/InAlAs(111)A grown at 535 °C and Ge/InAlAs(110) grown at 525 °C) grow via the Volmer-Weber (VW) growth mode,[26] which does not rely on interdiffusion processes.[67–69] In contrast, the Stranski-Krastanov (SK) growth mode often depends on interdiffusion processes.[67–69] For example, Chapter 2, Section 2.5.2 and Figure 2.10 show how interdiffusion plays an important role in InAs/GaAs(001) QD formation.[67] This is because adatom-adatom interactions are stronger than adatom-surface interactions, reducing the chances of intermixing.[68,70,71] We did not look at the SK Ge/InAlAs(111)A

TSQDs under EELS/STEM, so this paragraph is purely speculative. I suggest that future work investigate SK Ge/InAlAs(111)A TSQDs to determine this conclusively.

1.2.4 Heteroepitaxy: Growth Kinetics and Thermodynamics

Now that I discussed the two different types of crystal structures used in this project, DC and ZB, I will describe the processes of combining these materials in MBE. MBE researchers call this process heteroepitaxy, which is the layer-by-layer, single-crystal growth of one material on top of another.[58,72] In this section, I provide the reader with a fundamental look at the growth kinetics and thermodynamics in heteroepitaxy. I

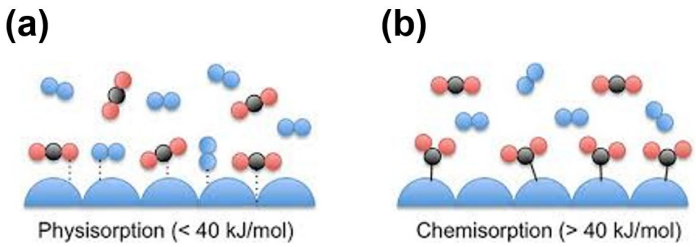

Figure 1.16 Diagrams showing (a) physisorption and (b) chemisorption of carbon dioxide molecules to a surface. The dashed lines represent electrostatically attracted adatoms, while the solid black lines represent adatoms that bonded to the surface. From Reference [73].

discuss how epitaxy works, how heteroepitaxy growth modes enable QD self-assembly, how self-assembly changes with strain sign, and finally I describe two techniques I used to understand Ge TSQD growth.

In discussing kinetics and thermodynamics of MBE growth, it is first important to understand how epitaxy works. In MBE, as the beams of atoms/molecules reach the sample surface, epitaxial growth involves physisorption and surface diffusion, concluding with either chemisorption or desorption.[74] Physisorption is what happens when an incident atom initially sticks to the surface: the atom is electrostatically attracted to the surface but not technically bonded to the surface (Figure 1.16(a)).[73,74] Once on the

surface, the atom, now called an adatom, can travel along the surface until it chemisorbs or desorbs.[74] Chemisorption describes the process of adatom bonding,[73,74] which forms a new layer or participates in island (QD) nucleation (Figure 1.16(b)).[74]

This MBE growth is often modelled by kinetic Monte Carlo (kMC) simulations of atomic interactions and density functional theory (DFT) calculations of surface energy.[34,43,75–77] There is experimental consistency with these modelling techniques when comparing with annealed-surface scanning tunneling microscopy (STM) and *in-situ* RHEED patterns.[68] That said, heteroepitaxial modelling is complicated by the non-equilibrium atomic interactions present during experiments: low substrate temperatures and continuous atomic fluxes during MBE growth reduce thermodynamic control.[68] Thermodynamic control increases with higher growth temperatures and lower atomic fluxes.[68] Both higher growth temperature and slower growth rates maximize adatom diffusion, pushing the MBE process towards equilibrium.[68] This increases the challenges faced by computational modelling. That said, modelling can be done over a wide range of parameters, even if we cannot realize those parameters experimentally.

1.2.4.1 Growth Modes

I use this section to describe the different ways heteroepitaxy manifests based on capillarity arguments, which occurs for both compressively-strained and tensile-strained systems.[21,26,78]

Heteroepitaxy occurs via one of three growth modes: Frank-van-der-Merwe (FM), Volmer-Weber (VW), and Stranski-Krastanov (SK).[68] VW and SK growths can grow via Ostwald ripening once enough material is deposited at a given temperature.[26,68,78] Ostwald ripening is the process of smaller islands coming together to form bigger ones

(Figure 1.17).[78] Figure 1.17 represents each growth mode and includes a corresponding phase diagram for a compressively strained system, where *H* is the number of monolayers and ε is the biaxial strain in the epitaxial layer.[78] I chose to show a compressively strained system in this example, because research on tensile-strained self-assembly shows similar results,[21,22,26] making this a comparable study.[68] Since the literature is so thorough on compressively-strained systems, it offers a good place to start when comparing to tensile-strained self-assembly processes.

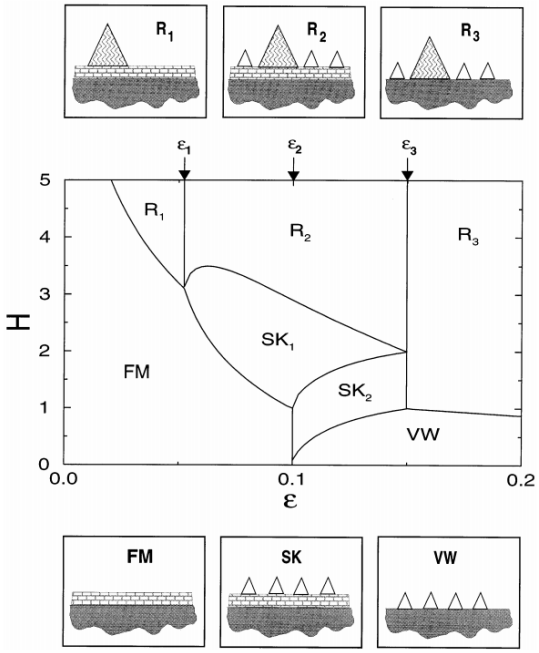

Figure 1.17 An equilibrium phase diagram showing growth modes as a function of deposition coverage, H, and compressive strain, ε. The small diagrams represent a cross-sectional look at the surface after depositing material with a certain growth mode. Large, shaded triangles represent ripened islands while small, white islands represent un-ripened, stable islands. From Reference [78].

FM growth proceeds via smooth, layer-by-layer deposition; VW grows via islands/QDs; SK_1 forms QDs on an FM layer; SK_2 forms a wetting layer around VW islands; and *R* represents Ostwald ripening, FM occurs at low *H* and low ε; VW occurs at

low H and high ε; SK occurs between the FM and VW phases; and R occurs at high H (Figure 1.17).[78]

These growth modes are a function of both strain and the substrate/epilayer interface free energy (γ_i), surface potential energy (γ_s), and epilayer potential energy (γ_e).[70,79,80] The capillarity model uses Young's equation to quantify each growth mode: FM growth occurs when $\gamma_s = \gamma_i + \gamma_e$; VW proceeds when $\gamma_s < \gamma_i + \gamma_e$; and SK happens when $\gamma_s > \gamma_i + \gamma_e$.[70,79] This means that VW islands will form when an epilayer has higher energy than the interface or surface energy, and an FM wetting layer will occur when the epilayer has equivalent or lower energy than the surface.[68,70] SK occurs due to an increase in strain with increasing wetting layer thickness.[68,70] This increase in strain with thickness is due to several factors. In particular, intermixing of new epitaxial atoms with surface atoms changes the entropy and strain percentage of the wetting layer.[69,80] This changes the wetting potential until the lattice mismatch strain reaches a critical thickness, causing SK islanding.[68–70] Both VW and SK growth modes lead to the self-assembly of defect-free QDs and a high degree of tunability in optoelectronic properties.[68,70,81,82]

Researchers have heavily explored growth modes in heteroepitaxial systems under compressive strain, but heteroepitaxy in tensile-strained systems remains largely unstudied. Research in our group recently showed that GaAs/InAlAs(111)A TSQDs form via an anomalous SK growth mode, where the wetting layer continues to grow even after formation.[82] This change is likely due to the presence of tensile strain and a change in relative TSQD/barrier surface energies on the (111)A surface.[82] Since the deposited adatoms preferentially grow the wetting layer instead of the TSQDs, there is likely only a small reduction in the free energy compared to typical SK growth.[78,82] Because the

wetting layer acts as a quantum well (QW) and the islands act as QDs, a tunable wetting layer thickness has important implications for possible QD and coupled QD-QW devices.[82–85] This tells us that tensile strain enables the defect-free growth of tunable QWs and QDs.

1.2.4.2 Self-assembly: Compressive vs. Tensile Comparison

The principles behind self-assembly not only depend on capillarity arguments, but also the sign of strain and surface orientation.[19] By convention, tensile strain takes

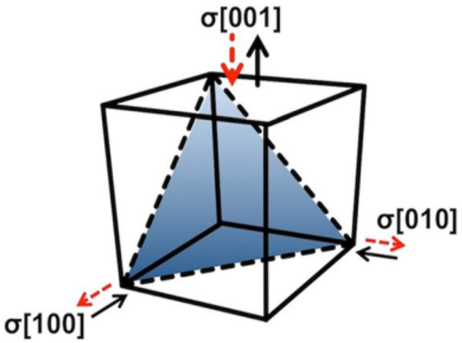

Figure 1.18 A representation showing how the biaxial compression (black arrows) and tension (red arrows) become a uniaxial tensor along [001]. The shaded triangle is a {111} glide plane in a face-centered cubic unit cell. From Reference [19].

positive values, while compressive strain takes negative values.[2] In this section, I focus on how these growth modes change based on the strain sign and surface orientation.

In biaxially strained materials, elastic processes (e.g. island formation) and plastic processes (e.g. dislocation nucleation and glide) compete to relax the strain.[19,86] Depending on the application, researchers typically prefer either plastic or elastic relaxation. For example, controlled plastic relaxation is essential when growing high-quality metamorphic buffers to produce virtual substrates with a desirable lattice constant.[87] In contrast, elastic strain relief is preferred for QD self-assembly, because

plastic relaxation manifests as defects such as dislocations, which act as mid-band gap carrier traps for non-radiative recombination.[19,28,68,88]

Elastic processes reduce the system's strain through the self-assembly of 3D islands and the accompanying increase in free surface area.[19,68,70] The sign of strain and the surface orientation allow researchers to choose between these two relaxation types.[17–19] The structure of both the DC and ZB structures allows the resolution of biaxial strain into a uniaxial shear stress along the {111} glide planes (Figure 1.18).[19]

I want to quickly point out the differences between 60° total dislocations and 90° and 30° partial dislocations, since they are important for this discussion. Figure 1.19

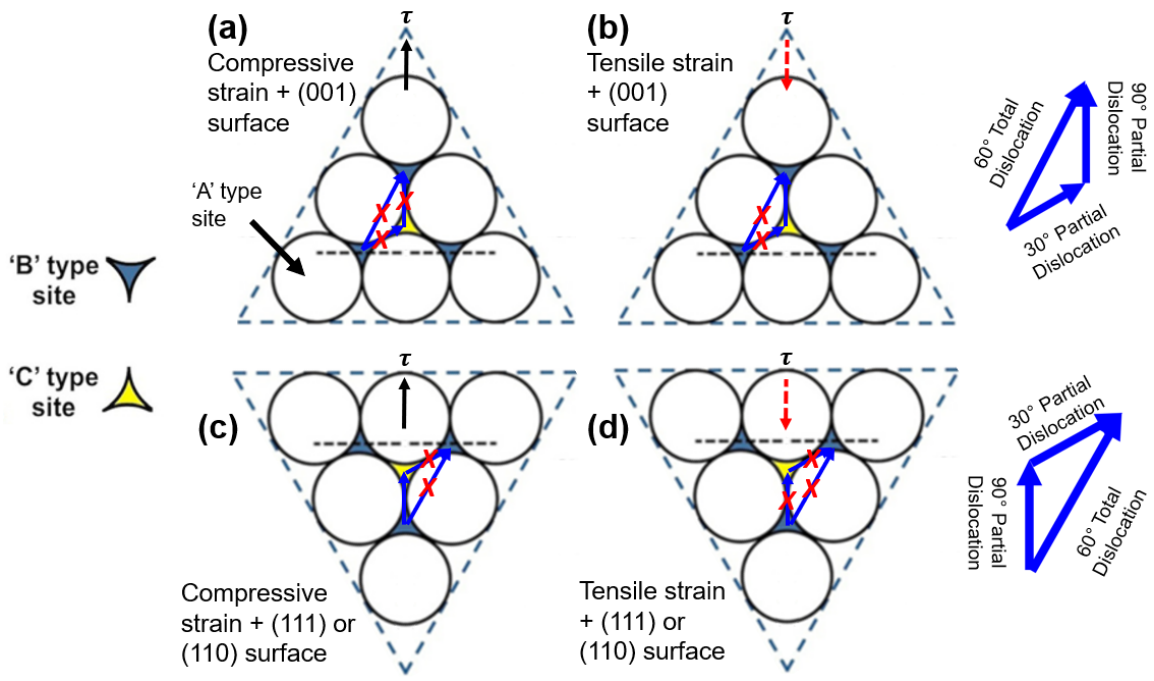

Figure 1.19 Diagrams showing the {111} glide planes (dashed, navy blue lines forming equilateral triangles) for a face-centered cubic unit cell, rotated to match up with (a),(b) (001) and (c),(d) (111) and (110) biaxially strained growths. The solid black and dashed red arrows represent the direction of the resolved uniaxial shear stress (τ). The solid black arrow (a),(c) represents the compressive τ, while the dashed red arrow (b),(d) represents tensile τ. The solid blue arrows that point to/from 'B' and/or 'C' type sites indicate where an atom laying on a 'B' type site moves to form 30° and 90° partial, and 60° total dislocations. The dashed black line helps the eye define the total and partial dislocation angles. The red X on any blue arrow indicates which dislocations are energetically unlikely. Adapted from Reference [19].

shows {111} planes with white circles representing atoms at 'A' type sites and filled in blue or yellow site locations representing the layer sitting directly above the 'A' layer: either 'B' (blue) or 'C' (yellow) locations.[19] Figure 1.19 shows us that 60° total dislocations occur between two 'B' type sites, towards the resolved uniaxial shear stress, τ.[19] A 30° partial dislocation instead occurs when an atom from a 'B' type site moves to the middle 'C' type site (Figure 1.19).[19] A 90° partial dislocation occurs when an atom moves from a 'B' type site to a 'C' type site or vice-versa directly parallel to τ (Figure 1.19).[19] For both 30° and 90° partial dislocations, atomic movement is only energetically

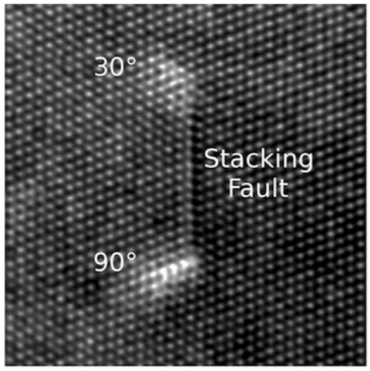

Figure 1.20 A high-resolution TEM image showing 30° and 90° partial dislocations connected by a stacking fault. From Reference [19].

favorable when τ's direction does not oppose this movement (Figure 1.19).[19] Conceptually, Figure 1.19 also shows us that regardless of surface orientation and sign of strain, 60° total dislocations require more energy, because they are the combined vector sum of 30° and 90° partial dislocations.[19] This means that 60° total dislocations require more energy to distort/move through the crystal, as is true for substitutional diffusion.[2]

While these dislocations are discussed in detail by Simmonds & Lee,[19] I summarize their discussion here. Simmonds & Lee present a thorough discussion on the effect of strain sign and crystal orientation on relaxation type.[19] They show that biaxial compressive strain on the (001) surface preferentially leads to elastic strain relief instead of higher-energy 60° total dislocations (Figure 1.19(a)).[19] This agrees with the well-understood self-assembly of compressively strained nanostructures on (001).[68,70,81] As I mentioned before, both 30° and 90° partial dislocations are energetically favorable if τ's direction does not oppose atomic diffusion along those angles.[19] Figure 1.19(a) shows that for compressive strain on (001), 30° and 90° partial dislocations are highly unlikely due to τ's direction.[19]

However, when tensile strain is applied to the (001) surface, the uniaxial strain tensor reverses direction on the {111} glide plane (Figure 1.19(b)).[19] This means that an atom can easily move 'downwards' from a 'B' type site to a 'C' site (Figure 1.19(b)) causing a 90° partial dislocation.[19] This 90° partial dislocation experiences a larger resolved shear stress than either the 30° partial or 60° total dislocation.[19] A stacking fault connects the 30° and 90° partial dislocations (Figure 1.20).[19] The energy for this process is lower and thus more favorable for a 90° partial dislocation than any other type of dislocation.[19] Dislocation nucleation rate, a kinetically driven process, is proportional to $\exp[-E_{nuc90°}/kT]$, which means strain relief rapidly occurs via plastic processes.[19] Experimental results of tensile-strained materials on (001) confirm this idea: these heterostructures form flat, extensively dislocated layers.[19,68,88]

This same, plastic relaxation occurs when compressive strain is added in combination with a (110) or (111) surface (Figure 1.19(c)).[19,68] Using the Thompson tetrahedron model for FCC crystals, we can define the (110) and (111) surfaces as rotationally equivalent, so dislocation nucleation and glide properties should be the same on these two surfaces.[19,89] I illustrate this rotational equivalency on the (110) and (111) surfaces by rotating Figure 1.19(a),(b) 60°, as is suggested by the Thompson tetrahedron model.[19,89] Like with tensile strain on (001) surfaces, compressive strain on (110) or (111) points τ in a direction which allows the movement of atoms from 'B' type sites to 'C' type sites as a 90° partial dislocation (Figure 1.19(c)).[19] Experimental results also show that compressive strain on the (111) surface form 30° and 90° partial dislocations connected by stacking faults.[68]

Luckily for the purposes of this project, there is a window within which tensile strain on (110) and (111) can relax elastically. Dislocation nucleation behavior for tensile-strained crystals grown on (110) or (111) are analogous to compressively-strained crystals grown on (001).[19] Figure 1.19(a) and Figure 1.19(d) are equivalent.[19] This is because τ opposes 90° and 30° partial dislocations, and 60° total dislocations are energetically unfavorable for all cases (Figure 1.19(d)).[19] Elastic relief is therefore preferred for tensile materials grown on (110) and (111) even though plastic relaxation is preferred for compressively strained materials grown on these surfaces.[19,68]

Therefore, the self-assembly of dislocation-free TSQDs on these surfaces is possible. In fact, defect-free TSQDs have already been demonstrated on both (110) and (111) surfaces, and their growth is analogous to well-studied compressively-strained QDs on (001).[17–19,21,26] Like compressively-strained QDs, TSQD size is highly tunable with MBE parameters and thus we have excellent control over the light emission wavelength.[21,22,82] Additionally, because tensile strain reduces the band gap below bulk values, new low-band gap devices (e.g. infrared detectors and emitters) are possible.[21,22,25,90] This is a key motivator for this work: we can use tensile strain to produce defect-free TSQDs on (111) and (110),[21,22] and the tensile strain we use in our systems should be large enough to transform Ge's band structure.[4]

1.2.4.3 Island Scaling Theory

In this section, I describe island scaling theory, a technique we use in Chapter 4 to better understand tensile-strained heteroepitaxy kinetics. Specifically, I used island scaling theory to better understand Ge and GaAs TSQD growth kinetics and predict QD size distributions (see Chapter 4).[43] We use it to compare the self-assembly process in

TSQD samples with varying deposition thicknesses, growth rates, and temperatures.[18,43,76,91] We used Equation 1.2, from the work of Bartelt and Evans,[92] in order to perform our island scaling analysis,

Equation 1.2 $$f_i\left(\frac{s}{\langle s\rangle}\right) = \frac{N_s\langle s\rangle^2}{\theta}$$

where f_i is the scaling function, N_s is the number of islands of size s, θ is the surface coverage, and $\langle s\rangle$ is the average island size.[43,76,91,92] This equation allows researchers to describe the critical cluster size, i, which is one less than the number of atoms required to form the smallest stable island.[76,91] The critical cluster size can be found by fitting the scaled distributions found by Equation 1.2 with integer values of i plugged into Equation 1.3 (from the analysis of Amar and Family[91]) and comparing the fits to determine the most likely value for i (Figure 1.21).[43,91] In Equation 1.3, $f_i(u)$ is the island size scaling function, which satisfies the condition $\int_0^\infty f_i(u)\,du = \int_0^\infty f_i(u)u\,du = 1$, u is simply $s/\langle s\rangle$, and C_i and a_i are constants for a given i value.[91] The resulting shape is shown in the solid curves seen in Figure 1.21.

Equation 1.3 $$f_i(u) = C_i u^i \exp\left[-ia_i u^{\frac{1}{a_i}}\right]$$

Systems that obey scaling theory are only sensitive to mono/bilayer coverage, deposition flux, and the adatom diffusion constant.[76,91] For this reason, we used island scaling theory to better understand the underlying kinetic processes during MBE growth.[43] In particular, this technique helps us understand how Ge adatoms form islands and the islands' size uniformity for a particular distribution.[43] Generally, the larger i is, the narrower the scaled distribution and thus the greater the island size uniformity (see Figure 1.21).[43,91] See Chapter 4, Section 4.4.3 for a more detailed description.

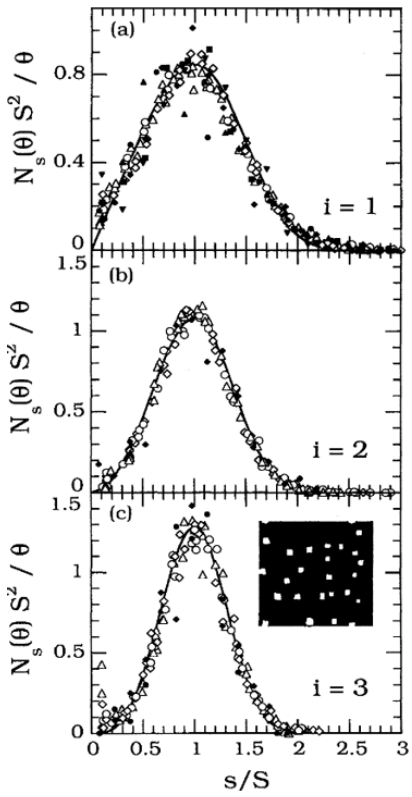

Figure 1.21 An example of island scaling plots. These show how, as *i* increases (from (a) to (c)), the distribution of island sizes narrows. From Reference [91].

1.2.4.4 Radial Distribution Scaling/Functions (RDS, RDFs) and Linear Distribution Functions (LDFs)

Like with island scaling theory, we can use RDS, RDF, and LDF to interpret heteroepitaxial self-assembly growth kinetics, with a particular focus on identifying whether TSQDs form at some preferred separation.[43] We selected RDS, RDF, and LDF depending on our needs. In this section, I describe the basic principles behind RDS, RDF, and LDF, how we used each to determine preferred adatom diffusion lengths, and how each is different.

The key difference between the terms “Function” and “Scaling” stems from whether the data was scaled in a particular way or not. Generally, we use the term “Scaling” in Chapter 4, and “Function” in Chapter 5. In Chapter 4, it was more

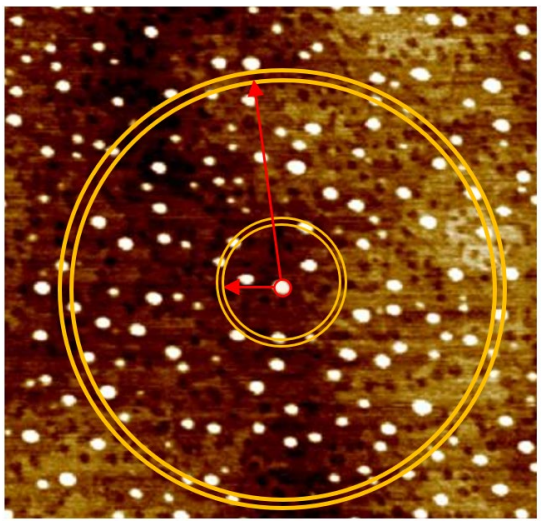

Figure 1.22 Schematic representing a smaller and a larger radial distance from a TSQD center, *r* (red arrows). The yellow circles provide an eye's guide two selected *r*. This shows how there are more TSQDs the larger *r* becomes. The arrows and circles overlay an AFM image of Ge/InAlAs(111)A TSQDs.

convenient to normalize all the plotted data (i.e. scale/compress the data by dividing the distance between QDs, *r*, with the average distance between TSQDs, $\langle R \rangle$), making comparison simple;[43] the magnitude of the peak was more important than interpreting nearest-neighbor correlations along one direction or another. In Chapter 5, the opposite was true, so Dr. Eric Jankowski, Alessia Molino, and I used RDFs and LDFs instead of RDS in that chapter.

Dr. Jankowski, Dr. Mike Henry, and Trent Garrett wrote programs to identify TSQD centers from AFM images, from which spatial correlations are calculated. For each technique, detailed methodologies are described in Chapters 4 and 5. We interpreted the data we received from these programs.

Figure 1.22 illustrates how RDF plots are created: as *r* increases, more TSQDs are detected at that radius until the probability of detecting a TSQD becomes 1.[43,72,92] Figure 1.22 demonstrates this by showing two 'rings' of radii a distance *r* away from the

highlighted TSQD. The RDF approaches 1 when the TSQD density at *r* is the average areal density.

In RDS, we find the position of TSQDs in an AFM image so that we can calculate the distances between each dot and every other dot. From these interdot separations we can plot their scaling relation, N(*r*) as a function of *r*.[43,72,92] A radial distribution function (RDF), $g(r/\langle R \rangle)$, is the normalized probability for finding a TSQD center with a distance *r* away from another TSQD.[43,72,92] For these RDS plots, we use Equation 1.4.

Equation 1.4 $$g\left(\frac{r}{\langle R \rangle}\right) = \frac{N(r)}{N}$$

We calculate $\langle R \rangle$, the preferred adatom diffusion length, from the sample's areal density, then we use $\langle R \rangle$ to scale *r* for RDS plots.[43,72,92] $\langle R \rangle$ is calculated by taking the inverse square root of the average areal density.[43,72,92] We can calculate $\langle R \rangle$ from areal density, because adatom length and TSQD areal density are inherently tied: as areal density increases, the adatom length decreases because the TSQDs are closer together.[26,43] When $g(r/\langle R \rangle)$ exceeds 1, the probability of seeing a TSQD at a distance of $r/\langle R \rangle$ is larger than the areal density.[43,72,92] A large local maximum for $g(r/\langle R \rangle)$ indicates a preferred separation distance.[43,72,92] Below this highly probable separation distance is considered the TSQD capture zone.[43] RDS analysis provides quantification of how the TSQDs are distributed, which can inform our hypotheses about how they may have nucleated, and it allows comparison of multiple growth conditions across several materials and their surface orientations.[43] Indeed, we used RDS analysis in Chapter 4 to compare the differences between Ge and GaAs TSQDs grown on InAlAs(111)A.

While RDFs are useful for finding the preferred separation distance for highly symmetrical TSQDs, its spherical symmetry obscures any anisotropies in spatial

distribution. To solve this, Dr. Jankowski developed a program to find LDFs. LDFs use the same principles as RDFs, but instead of finding *r* radially, we find *r* in specific linear directions. We use this to investigate Ge(110) TSQD anisotropy in Chapter 5.

1.2.5 Band Structure, Quantum Confinement, and Tensile Strain Effects

Understanding the effects of heteroepitaxial growth kinetics and TSQD self-assembly helps researchers tailor QDs for specific optoelectronic applications. Understanding how optoelectronic properties change with TSQD growth is equally important for the purposes of this dissertation. Thus, this section provides a fundamental look into this project's relevant physics, such as band structure, quantum confinement, and strain effects on band gap.

Heteroepitaxial growth has many purposes, but they are primarily created to form abrupt band structure changes. When we create semiconductor structures with several materials, we can confine carriers and construct junctions useful in electronic devices.[3] One example of a heteroepitaxial device includes the high electron mobility transistor (HEMT), which uses a 2D electron gas formed within a quantum well (QW).[93] Another example is a multijunction solar cell, which consists of two or more junctions between materials with different band gaps.[94] These multijunction solar cells thus absorb multiple parts of the solar spectrum.[94] In this project, the heteroepitaxy of the low band gap Ge TSQDs within wider band gap InAlAs barriers will ensure that carriers in the TSQDs experience quantum confinement.[47]

These structures require knowing more about how we can use band structure, doping, and quantum confinement to create effective devices. As was mentioned in Section 1.1, the semiconductor band gap separating the valence and conductance bands

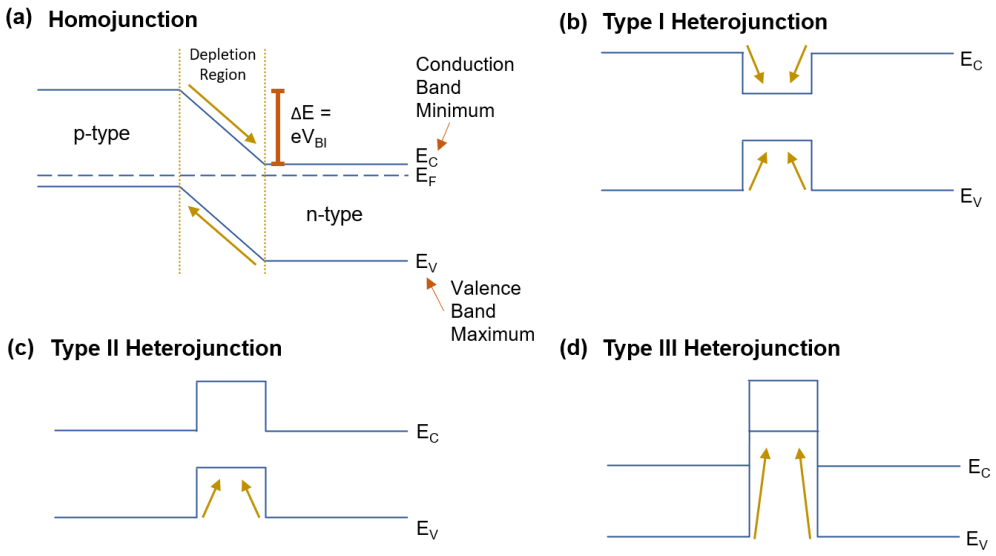

Figure 1.23 Band diagrams for a (a) p-n homojunction, and (b) type I, (c) type II, and (d) type III heterojunctions. Yellow arrows indicate the movement of holes in the valence band (E_V) and electrons in the conduction band (E_C). The E_C labelled here is the conduction band minimum, while E_V is the valence band maximum. (a) The change in conduction band energy (ΔE) equals the elementary charge (e) multiplied by the built-in Voltage (V_{BI}). The Fermi energy (E_F) is labelled in the homojunction diagram. I created this figure using PowerPoint.

can be direct or indirect.[3] Band structure can be tuned by material choice, strain, and QD size.[21,22,95,96] We can create a wide variety of useful electronic junctions by combining different materials and/or dopants.[3]

When a semiconductor material has p-type (hole dominant) and n-type (electron dominant) sections placed together, the result is a p-n junction.[2,3] This junction can be made of one or two types of semiconductors: a p-n junction with one semiconductor material is called a homojunction (Figure 1.23(a)) while two different semiconductors form a p-n heterojunction.[3] A homojunction is made of one material, but each side of the junction has different majority carriers.[3] In all p-n junctions, different majority carriers create a difference in Fermi energies between each side of the junction.[2,3] To minimize the system's energy, electrons and holes recombine near the homojunction, effectively equating the Fermi energies and creating a depletion region free of charge carriers

(Figure 1.23(a)).[2,3] Instead, the immobile ionized dopant atoms in the depletion region give rise to a built-in potential barrier that opposes the flow of electrons and holes in one direction while allowing them to move freely in the other.[2,3]

Researchers can also make heterojunctions by combining two semiconductor materials without adding dopants (Figure 1.23(b)-(d)).[3] This contrasts homojunctions, which require dopants.[3] Instead, an undoped heterojunction creates a potential barrier from the conduction band minimum and valence band maximum differences between the two materials (Figure 1.23(b)-(d)).[3] When charge carriers meet a junction, a few different things can happen: they can move across the junction or they cannot due to a barrier, they can tunnel through a junction barrier (i.e., at an upwards potential step), or they are reflected at a downwards step in the potential.[97] Generally, electrons prefer to cross a junction in the direction where the conduction band energy, E_C, is lower (e.g. electrons "sink"), while holes prefer crossing in the direction where the valence band energy, E_V, is higher (e.g. holes "float") (Figure 1.23(b)-(d)).[2,3,97] When one material is sandwiched between a different material, a band well or barrier forms for the electrons and/or holes (Figure 1.23(b)-(d)).[3] Energy quantization occurs when a structure is small enough that its dimensions approach a carrier's de Broglie wavelength.[3] Depending on the materials used in a heterojunction, the confinement of carriers can be selectively chosen. In general, all QDs, regardless of strain type, can be type I, type II, or type III.[3] Type I QDs confine charge carriers in both the conduction and valence bands (Figure 1.23(b)), but type II QDs confine either the electrons or the holes (Figure 1.23(c)) while creating a barrier to the motion of the opposite carrier type.[3] Type III heterojunctions (Figure

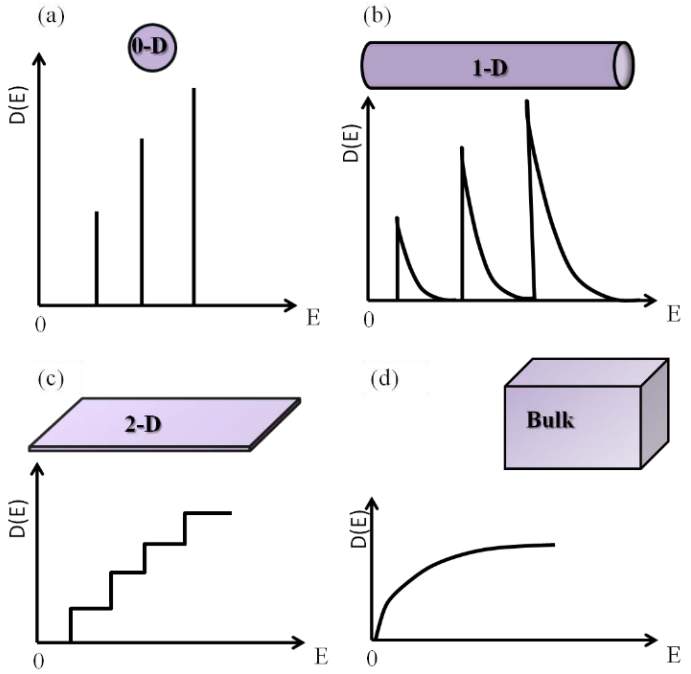

Figure 1.24 Electron energy (E) vs density of states (D(E)) plots comparing (a) 0D (b) 1D (c) 2D and (d) 3D structures. From Reference [98].

1.23(d)) occur when the bands are offset so that the valence band energy of one material is above the conduction band energy of another material.[3]

Quantum confinement in one or more dimensions changes the density of states (Figure 1.24).[3,98,99] The density of states is the number of available energy states as a function of energy that a charge carrier can occupy within a structure.[3] When we plot the density of states as a function of energy, each type of quantum confinement will have a different dependency on energy: a (0D) QD's density of states corresponds to a delta-function (Figure 1.24(a)); a (1D) quantum wire has a density of states proportional to $E^{-1/2}$ (Figure 1.24(b)); a (2D) QW's density of states is independent of E and instead acts as a step function with increasing energy (Figure 1.24(c)); and a bulk (3D) material's density of states is proportional to $E^{1/2}$ (Figure 1.24(d)).[3,98,99]

The delta-function for a QD's density of states means that charge carriers can occupy only discrete energy states (Figure 1.24(a)).[3,98,99] In other words, a QD behaves in

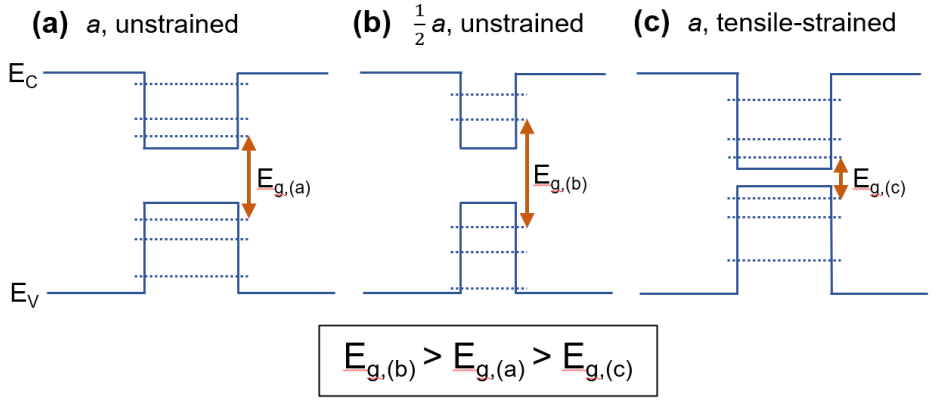

Figure 1.25 Band diagrams depicting Type I quantum well heterostructures. The dashed lines represent quantized energy levels. (a) represents an unstrained heterostructure with a well width, *a*. (b) represents the same heterostructure as in (a) but with half the original *a*. (c) shows (a) under tensile strain. The effective band gaps, $E_{g,(a)}$, $E_{g,(b)}$, $E_{g,(c)}$, for each respective diagram are emphasized with arrows, and the outlined box at the bottom of the figure compares the effective band gaps. I created this figure using PowerPoint.

some ways like an artificial atom with discrete electron states (orbitals) separated by forbidden energy gaps.[3,98,99] Since QDs have tunable sizes, unlike an atom, their density of states is tunable.[3,98,99] This is because quantum confinement is dependent on the width of the region occupied by a carrier, so tuning the QD size changes the confined states energy.[3,21,22,98] Quantum confinement is thus extremely useful for optoelectronic devices designed to emit or absorb photons with very specific wavelengths/energies.

Quantum confinement increases the energy needed for an electron to transition from the valence to the conduction band (or vice versa) compared to the same semiconductor's bulk band gap (Figure 1.25(a)).[3,99] The confined energy levels of a quantum well, E_n, are related to the width of that well, a, by Equation 1.5,

Equation 1.5 $$E_n = (n\pi\hbar)^2/(2ma^2) \quad \text{where } n = 1, 2, 3, \ldots$$

where ħ is the reduced Planck's constant, and m is the charge carrier's mass.[3,99] Therefore, as a increases, the energy of the first energy state ($n = 1$) decreases, and so the transition energy redshifts (Figure 1.25(b)).[3,21,99] This equation also tells us why we

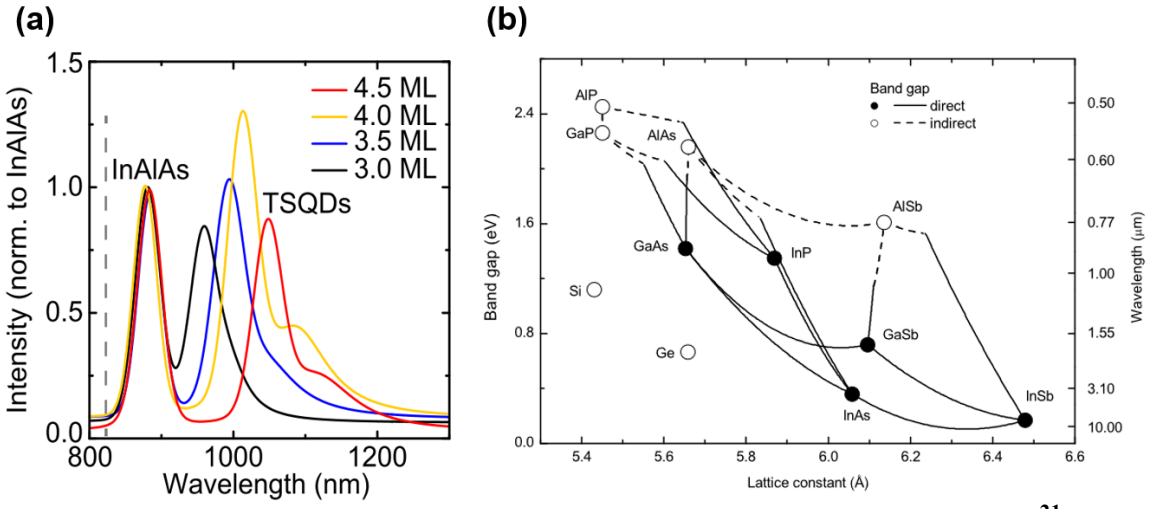

Figure 1.26 (a) PL emission from GaAs(111)A TSQDs. From Reference [21]. (b) Diagram showing several elemental and binary compound semiconductor's bulk band gaps as a function of lattice constant. From Reference [20].

should care about QD shape: an elongated or asymmetrical QD will likely have different energy emission along different directions. In contrast, highly symmetrical TSQDs whose confined states in different directions are degenerate have potential applications in entangled photon emission.[21]

In contrast to compressive strain, tensile strain reduces a semiconductor's band gap below its bulk value (Figure 1.25(c)).[4,6,8,9] This red-shifts (i.e. increases the wavelength), the emitted light below the unstrained materials' bulk band gap energy.[4,6,8,9] There is a push-pull interplay between quantum confinement and tensile strain. Even though quantum confinement naturally blue-shifts the effective band gap, we have found the red-shift from tensile strain tends to be larger, and so the combined effect is a reduction in the photon energy relative to the bulk band gap.[21,22] We see that this is true in GaAs(111)A TSQDs: Figure 1.26(a) shows that GaAs(111)A TSQDs emit above 950 nm, whereas Figure 1.26(b) shows that bulk GaAs emits at about 850 nm.[20,21,100] This means that GaAs(111)A TSQD light emission is red-shifted from the bulk GaAs band

gap despite quantum confinement (compare Figure 1.26(a) and Figure 1.26(b)).[20,21] This interplay opens up new possibilities for light emitting technology.

1.2.5.1 The Ge Band Structure

Unstrained Ge has an indirect band gap of 0.67 eV at 302 K.[100] Tensile or compressive strain changes the band gap by stretching or compressing bonds along certain directions.[4] This changes the orientations of the bonds and thus the orbitals' interactions, which varies the heavy and light hole energy.[4] The conduction band also changes, since this process forces hybridized sp^3 orbitals to reshape.[4] The type of strain and the direction of the biaxial tensile strain affects these orbitals in different ways.[4] This leads to a heavily orientation-dependent variation in the valence and conduction band maxima/minima.[4] Thus, the band gap changes in this way (see Figure 1.27).

Figure 1.27 shows how compressive (negative) and tensile (positive) strains affect the Ge band structure. In Figure 1.27, a direct band gap transition occurs when the Γ valley dips below the L and X valleys.[4] In Figure 1.27, compressive strain decreases the Γ valley below the L valley on each surface orientation, but the X valley becomes the new, indirect band gap.[4] Therefore, compressive strain never results in a direct band gap or semimetal transition, because an indirect valley always has the lowest conduction band energy and never approaches 0 eV.[4]

In contrast, Figure 1.27 shows that Ge will become a direct band gap semiconductor on the (001) and (110) surfaces at ~1.6% and ~3% biaxial tensile strain respectively.[4,6,8,9] Although large tensile strains on the (001) surface tend to result in plastic strain relief via dislocation nucleation and glide, on the (110) surface we should be able to achieve elastic strain relief via TSQD self-assembly (see Section 1.2.4.2).[17,19,59]

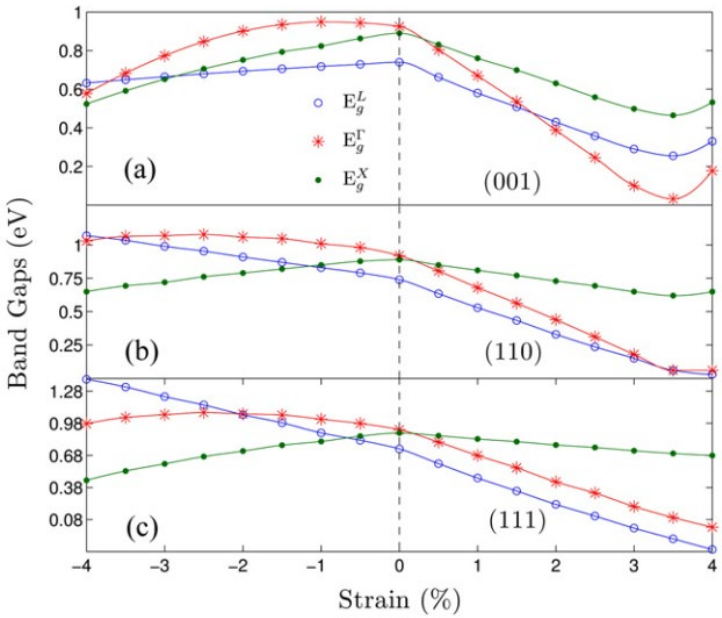

Figure 1.27 Band minima points as a function of biaxial strain on the (a) (001), (b) (110), and (c) (111) surfaces for Ge. The red, starred points indicate the calculated Γ valley band gap while the blue, open points indicate the L valley band gap. Green, solid points indicate the X valley band gap. Conceptually, wherever the red, starred points are below the green and blue points is where there is a direct band gap. From Reference [4].

Later in Chapter 5, we demonstrate that not only can we grow Ge TSQDs on InAlAs(110), but we may also see direct band gap light emission.

Chapters 3 and 4 focus on Ge grown on InAlAs(111)A, which leads us to talk about Ge's band structure changes on (111) surfaces. On the (111) surface, even though the Γ valley never dips below the L valley under tensile strain, the band gap reaches 0 eV at ~4% tensile strain, which means Ge turns into a semimetal (Figure 1.27(c)).[4,8]

Semimetals have zero-band gap in certain directions in k-space but have a band gap in others.[101] This allows for the easy flow of electrons and holes between the valence and conduction bands.[101] Semimetallic Ge could potentially be used to explore a new area in topological materials based on conventional semiconductors, which is why the (111) surface is of interest to this project.[10] Additionally, turning a resistive semiconductor into

a conductive semimetal could be useful for tunnel junctions or low-resistance contact layers.[102–104]

1.3 Conclusions

We are interested in using tensile-strained self-assembly to produce defect-free Ge QDs on InAlAs(110) and (111)A orientations. On these surfaces, we anticipate that 3-4% tensile strain will allow us to transform Ge into either a direct band gap semiconductor or a semimetal. These are two outcomes that would be extremely interesting, both from the point of view of fundamental materials science, but also for the potentially novel optoelectronic applications they would enable.

This introductory section helps build upon the knowledge needed to successfully complete and continue the project in this dissertation. Understanding how the crystal properties and growth kinetics relate to optoelectronic properties is key to continued success in the future. The next few chapters go into more depth on many of the topics discussed in Chapter 1.

CHAPTER TWO: STRAIN-DRIVEN QUANTUM DOT SELF-ASSEMBLY BY MOLECULAR BEAM EPITAXY

Kathryn E. Sautter,[1] Kevin D. Vallejo,[1] and Paul J. Simmonds[1,2,a)]

[1] Micron School of Materials Science & Engineering, Boise State University, 1910 University Drive, Boise, ID 83725

[2] Department of Physics, Boise State University, 1910 University Drive, Boise, ID 83725

[a)] Corresponding author: paulsimmonds@boisestate.edu

Paper published as part of the special topic on Materials for Quantum Technologies: Computing, Information, and Sensing MQT2020.

Reprinted from K.E. Sautter, K.D. Vallejo, and P.J. Simmonds, J. Appl. Phys. **128**, 031101 (2020), doi: 10.1063/5.0012066, with the permission of AIP Publishing.

Abstract

Research into self-assembled semiconductor quantum dots (QDs) has helped advance numerous optoelectronic applications, ranging from solid-state lighting to photodetectors. By carefully controlling molecular beam epitaxy (MBE) growth parameters, we can readily tune QD light absorption and emission properties to access a broad portion of the electromagnetic spectrum. Although this field is now sufficiently mature that QDs are found in consumer electronics, research efforts continue to expand into new areas. By manipulating MBE growth conditions and exploring new combinations of materials, substrate orientations, and the sign of strain, a wealth of opportunities exist for synthesizing novel QD nanostructures with hitherto unavailable properties. As such, QDs are uniquely well positioned to make critical contributions to the development of future quantum technologies. In this tutorial, we summarize the history of self-assembled QDs, outline some examples of quantum optics applications based on QDs, discuss the science that explains the spontaneous formation of QDs, and provide recipes for successful QD growth by MBE for some of the most commonly used semiconductor materials systems. We hope that compiling this information in one place will be useful both for those new to QD self-assembly and for experienced researchers, ideally supporting the community's efforts to continue pushing the boundaries of knowledge in this important field.

2.1 Introduction and Background

For the last 30 years, epitaxial quantum dots (QDs) have been the subject of intense research interest across physics, materials science, and electrical engineering. QDs represent a highly tunable platform for research driven by fundamental scientific

questions and technological applications alike. We can think of a QD as a quantum well that confines charge carriers in all three spatial dimensions. When the size of the QD approaches the electron's de Broglie wavelength, the resulting energy quantization produces a density of states that approximates a series of discrete delta functions. Viewed from this perspective, the quantum states of an individual QD are very similar to the electron orbitals of an atom. The key difference is that an atom's position in the periodic table dictates the specific energies of its electron orbitals. In contrast, the confined energy states of a QD are inherently tunable. By controlling their size, we can design and create QDs that emit or absorb light at very specific wavelengths.

In the 1970s, researchers used a new technology, molecular beam epitaxy (MBE),[105] to synthesize the first quantum wells with one-dimensional quantum confinement.[106,107] However, going further, to produce nanostructures that offered two-dimensional or three-dimensional quantum confinement was, at the time, a huge technological challenge. By the early 1990s, researchers had developed two techniques for achieving three-dimensional confinement, both based on the initial growth of a quantum well.

The first approach used top-down processing to fabricate narrow pillars with diameters of a few tens of nanometers. Each pillar contained a small disc of the quantum well, with in-plane confinement offered by the pillar's sidewalls (Figure 2.1(a)).[49,108] Indeed, this was the approach used in the paper that coined the term "quantum dots" to describe nanostructures with three-dimensional confinement.[109]

The second approach grew out of quantum point contact research,[110–113] where electrostatic gates on the sample surface lower the Fermi level to deplete carriers from

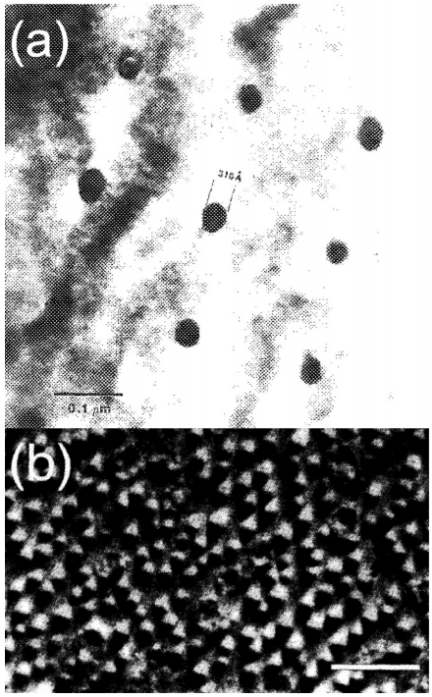

Figure 2.1 (a) Transmission electron microscope (TEM) image showing early examples of QDs created by electron beam lithography and ion beam milling. The average width of these InGaAs/InP QDs is ~30 nm. Reprinted with permission from Temkin *et al.*, Appl. Phys. Lett. 50, 413–415 (1987). Copyright 1987 AIP Publishing LLC.[5] (b) Plan-view TEM image of self-assembled InAs QDs in a GaAs matrix (scalebar = 100 nm). Reprinted with permission from Grundmann *et al.*, Phys. Rev. Lett. 74, 4043 (1995). Copyright 1995 American Physical Society.[114]

specific regions of the underlying quantum well. In this way, researchers produced small, discrete disks or "puddles" within the quantum well, each of which offered three-dimensional confinement.[115–117]

These two approaches both permit the synthesis of arrays of QDs at precise locations, making it easy to subsequently build devices around them. One can also tune the diameter of gate-defined QDs after fabrication, simply by controlling the gate voltage applied. These approaches do, however, share some disadvantages. Both require extensive post-growth processing, which can be expensive and time-consuming. What is more, the maximum areal QD density that can be practically achieved with these

approaches is ~10^8 cm^{-2}, which is lower than the >10^{10} cm^{-2} needed for efficient QD-based light emitters.

The discovery of self-assembled QDs around 1990 presented researchers with a straightforward synthesis approach for QDs that required no post-growth processing and could easily provide areal densities >10^{10} cm^{-2} (Figure 2.1(b)). The development of self-assembled QDs came about almost by accident. Since the early 1980s, researchers had known that certain combinations of materials began growth in a smooth, layer-by-layer growth mode. However, once some critical thickness was reached, a spontaneous transition to 3D island formation occurred, consistent with the Stranski–Krastanov (SK) growth mode.[118,119] Island growth was typically associated with materials systems such as Ge on Si(001) and $In_xGa_{1-x}As$ on GaAs(001) that have large differences in lattice constants and/or surface energies.[118–120] Considerable efforts were invested in understanding and suppressing the self-assembly of these undesirable 3D islands.[121–125]

The breakthrough came when researchers recognized first that during the initial stages of growth, these 3D islands are actually dislocation-free,[70,125–127] and second that their heights and diameters are close to the electron de Broglie wavelength in these semiconductors.[81,128] When islands consisting of a narrow bandgap semiconductor were embedded within a wider bandgap semiconductor, they behaved as optically active QDs.[114,128–132] Carrier confinement in quantized energy states was confirmed using photoluminescence (PL) spectroscopy.[133–136]

Once these facts were established, the floodgates opened, and self-assembled QDs became the subject of intense research activity. Self-assembled QDs have since been demonstrated in a range of materials systems, including Ge/Si, $In_xGa_{1-x}As$/GaAs, In_xGa_{1-}

$_x$Sb/GaAs,[137,138] $In_xGa_{1-x}P$/GaAs,[139–141] InAs/InP,[142–144] $In_xGa_{1-x}As$/GaP,[139,145] GaN on AlN,[146,147] $In_xGa_{1-x}N$ on GaN,[148,149] CdSe on ZnSe,[150,151] and CdTe on ZnTe.[152,153] The features that unite all of these materials systems are growth on a (001)-oriented substrate and the presence of compressive strain.

More recently, QDs on (110)- and (111)-oriented surfaces have also been achieved by using tensile rather than compressive strain to drive the self-assembly process.[17–19,21–23,25,154] Tensile-strained self-assembly has now been demonstrated in the GaP/GaAs, GaAs/$In_{0.52}Al_{0.48}As$, and Ge/$In_{0.52}Al_{0.48}As$ materials systems on both (110) and (111) substrate orientations.

Compressive strain increases a semiconductor's bandgap, while tensile strain reduces it.[155] In conjunction with the size of the bulk bandgap and quantum size effects, we can, therefore, use the sign and magnitude of strain in a QD to achieve exquisite control over the transition energy between electron and hole ground states. Together with their discrete density of states, these characteristics mean that laser diodes built around QDs exhibit exceptionally low-threshold currents and excellent temperature stability.[156–158] QDs will continue to drive innovations in optoelectronic research.

2.2 Quantum Dots for Quantum Technologies

It is the unique properties of QDs for quantum information and communication applications that is of most relevance to this special topic collection.[23,159–162] QDs are ideally suited for use as single-photon emitters, as single-photon detectors, and as sources of entangled photons, all of which are key components in various quantum information systems.[159,161–166]

2.2.1 QD Single-Photon Emitters

An electron and a hole confined within a single QD will experience electrostatic attraction and can form a bound state known as an exciton. When the electron recombines with the hole, a photon is emitted whose energy corresponds to the transition between the electron and hole ground states of the QD. We can create excitons in a QD device structure by either optical or electrical means. Since one exciton can only produce one photon, we can, therefore, use a QD to generate single photons on demand.[167] A QD placed within an optical cavity, such as a photonic crystal, can hence be used as an efficient single-photon emitter.[48,166,168]

We use photon correlation measurements to verify that a QD is indeed behaving as a quantum emitter of single photons. Quantum emitters exhibit a property known as photon antibunching, which means that the probability of more than one photon being emitted within some time window is essentially zero.[169,170] In other words, a QD that is truly a quantum light source can only emit a single photon at a time. To check for photon antibunching, we use a Hanbury Brown and Twiss (HBT) setup.[171] Using a monochromator, we spectrally filter the QD emission and then pass it through a non-polarizing 50:50 beam splitter. Each arm goes to a high-sensitivity, low-noise single-photon detector. These two detectors are connected to a timer whose resolution is typically a few 100s of picoseconds. This timer provides the delay time (τ) between successive photon detection events, allowing one to plot the second-order autocorrelation function $g^{(2)}(\tau)$.[172] Photon anti-bunching, and hence single-photon emission from a QD, is characterized by a dip in the second-order autocorrelation function at zero time delay,

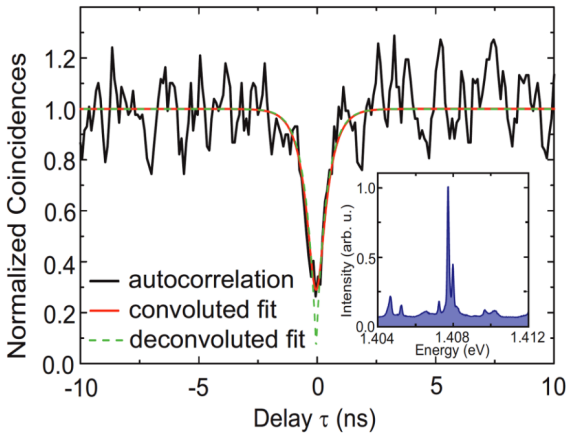

Figure 2.2 Autocorrelation of a QD emission line shown in the inset. The dip at $\tau \sim 0$ ns extends below 0.5 confirming single-photon emission. The dashed line shows a deconvoluted fit to these data from which a value of $g^{(2)}(0) = 0.05^{+0.17}_{-0.05}$ is extracted. Reprinted with permission from Unsleber *et al.*, Opt. Express 24, 23198–23206 (2016). Copyright 2016 The Optical Society.[172]

where $g^{(2)}(0) < 0.5$ (Figure 2.2). Using pulsed laser excitation, we can use this approach to demonstrate triggered single-photon emission.[167,170,172]

High-quality single-photon emitters are in great demand for various quantum technologies,[165] including quantum key distribution (QKD),[159,173] true random number generation,[174] and quantum metrology for sensing below the shot-noise limit.[175]

2.2.2 QD Single-Photon Detectors

The ability to detect single photons is clearly central to the HBT setup described above for confirming single-photon emission. However, single-photon detection is also critical in its own right to the success of various quantum technologies, perhaps most notably for QKD applications.[163,176]

Although single-photon detectors based on Si avalanche photodiodes (APDs) and superconducting nanowires are in wide-spread use,[165,177–179] QD-based single-photon detectors offer several advantages.[178,180–185] These include a III–V semiconductor device architecture compatible with QD single-photon emitters, infrared detection beyond the

band edge of Si (for example, at fiber-optic wavelengths), very low dark count rates, and the lack of problems with after pulse noise seen in InGaAs APDs that result from the avalanche process.[178,180–185]

For single-photon detection, QDs are placed close to the channel of a field-effect transistor[181,182,184] or the double barriers of a resonant tunneling diode.[183,185,186] The capture of a single photon by a QD generates an electron–hole pair, which in turn produces a measurable change in the device current, and the single photon is detected.

2.2.3 QD Entangled Photon Sources

According to quantum mechanics, a pair of quantum entangled photons exhibits a superposition of all polarization states and can be described by a single wavefunction. These entangled photons exhibit the counterintuitive property that even if some arbitrarily large distance separates them, their polarizations remain physically linked. Measuring the polarization of one photon instantaneously causes its counterpart to assume the opposite polarization. Entangled photons are essential for various quantum communication technologies.[162,164,187,188] As a result, research groups have explored various means to create entangled photons, including non-linear optical effects, single atoms or atomic ensembles, and nitrogen color vacancies in diamond.[189–193] However, the generation of entangled photon pairs in semiconductor QDs has some distinct advantages. As we have seen, QDs are compact, tunable, and we can electrically trigger them to emit photons on-demand.[167,194,195]

We can use a QD to generate entangled photons via the biexciton–exciton cascade (Figure 2.3).[196–198] Two electrons and two holes within a QD form a bound biexciton state $|XX\rangle$. For the biexciton to decay to the ground state $|0\rangle$, the two electron–hole pairs must

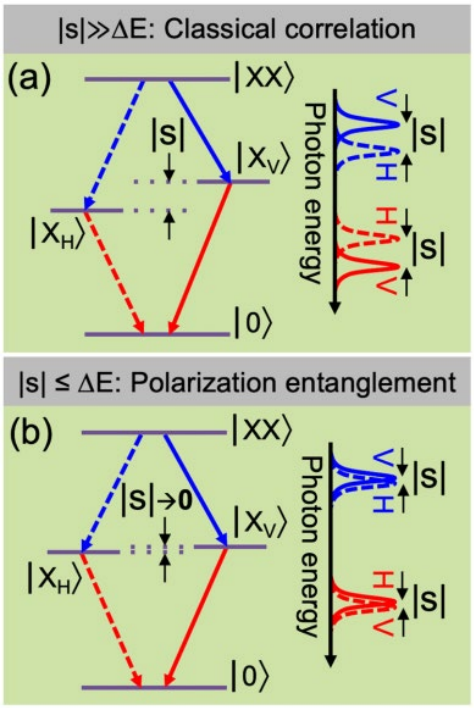

Figure 2.3 Biexciton–exciton cascades with corresponding photon emission spectra. (a) For large fine-structure splitting |s|, the two decay paths are distinguishable, leading to classically correlated photon polarizations. (b) As |s| → 0, the two paths become indistinguishable and emitted photons are polarization entangled (after Ref. [198]).

recombine, releasing two photons in the process. The key is that the first exciton recombination event puts the remaining exciton in one of two states, $|X_H\rangle$ or $|X_V\rangle$, which are orthogonally polarized. If we cannot say which of the two intermediate exciton states the cascade passed through, then the polarization of the two photons emitted will be entangled.

The key to remaining ignorant of this "which-path" information, and so to obtaining entangled photons, is the difference in energy |s| between the two intermediate exciton states. When |s|, referred to as the fine-structure splitting, is larger than the radiative homogeneous linewidth (ΔE), we can distinguish between the two decay paths, destroying the entanglement (Figure 2.3(a)). However, when |s| is reduced, ideally to zero so that $|X_H|$ and $|X_V|$ are degenerate, then the two decay paths are indistinguishable, and

the two emitted photons will be polarization entangled (Figure 2.3(b)). Testing for photon entanglement involves polarization-resolved second-order cross-correlation measurements using an HBT setup with rotatable λ/2 and λ/4 plates. In this way, one can populate the two-photon density matrix, where strong off-diagonal elements signify photon entanglement.[196,198]

In practice, however, synthesizing QDs with $|s| \sim 0$ is not trivial. Self-assembled QDs grown on the traditional (001) surface suffer from structural anisotropy and piezoelectric effects[160] so that $|s|$ can be tens or hundreds of μeV.[199,200] However, various techniques, including thermal, electrical, and magnetic tuning, enable researchers to systematically reduce $|s|$ to zero.[196,199,201,202] In this way, entangled-photon light-emitting diodes (LEDs) have been demonstrated.[96,203]

An alternative approach is to choose a QD system that has an instrinsically low fine-structure splitting. Self-assembled QDs grown on (111)-oriented substrates exhibit vanishingly small values of $|s|$ due to the high symmetry of this surface.[160] QD formation on (111) surfaces can be achieved with either droplet epitaxy (see Section 2.4.3) or tensile-strained self-assembly (see Section 2.4.6), with both methods showing promise for future quantum technology applications.[23,204]

In the remainder of this tutorial, we seek to provide an overview of the fundamental principles and techniques relating to the growth of self-assembled QDs by MBE. Clearly, an exhaustive review of every study of self-assembled QDs is beyond the scope of this tutorial. Rather, we have aimed to summarize the typical MBE parameters widely used to grow QDs in some of the more commonly encountered QD materials systems. It is our hope that this information will be sufficient for someone unfamiliar

with QD self-assembly to get started and to begin growing optically active QDs by MBE for quantum information applications.

2.3 Approaches to QD Growth by MBE

The technological potential of QDs quickly pushed research toward the phenomenological design of processes that produce uniform, high-density, defect-free QD arrays. For device applications, the ability to reliably tailor QD size, shape, and spacing was essential. QD self-assembly meets these requirements without the need for pre-growth substrate patterning and can be accomplished in two ways: via induced nucleation through droplet epitaxy[205] or through strain-driven processes, which are the focus of this tutorial.[206] These techniques rely on stochastic nucleation events so that the resulting self-assembled QDs are distributed randomly across the substrate. For an excellent review of efforts to engineer QD arrays with specific placement, see Ref. [207].

Droplet epitaxy (DE) enables the growth of QDs, even in unstrained materials systems.[205,208,209] DE growth of III–V QDs is a three-step process. (1) Grow a smooth III–V buffer surface and close the group V source(s) and wait for the background pressure to become negligibly low. (2) Open the group III source(s) to deposit a few monolayers of pure metal to form liquid nanodroplets. (3) Reopen the group V source(s), crystallizing the liquid nanodroplets into III–V semiconductor QDs. By removing the requirement for strain, this method increases the possible combinations of materials from which we can synthesize QDs.[210] Researchers have also grown QD molecules, quantum rings, and quantum holes by DE.[210–212] References [213] and [214] provide more information on DE. The rest of this tutorial concentrates solely on the self-assembly of strained QDs.

2.4 Strain-Driven QD Self-Assembly

2.4.1 Thermodynamics and Kinetics in MBE

As with other epitaxial growth techniques, MBE depends on thermodynamic and kinetic contributions. The rates of various processes, the strain in a given material system, and the relative magnitudes of the surface energies are all critical factors in determining the outcome of a given growth. Researchers use thermodynamic wetting arguments to explain and predict the growth mode for a given material system.[68,215,216] The three relevant parameters are the surface free energies of the epilayer–vacuum interface γ_e, the epilayer–substrate interface γ_i, and the substrate–vacuum interface γ_s. In addition, if the epilayer's lattice constant is larger (smaller) than that of the substrate, the epilayer will experience compressive (tensile) strain due to the Poisson effect.[217]

Classifying growth modes based solely on surface energy and strain considerations is valid only if we assume the system is close to thermodynamic equilibrium. MBE is a far-from-equilibrium growth technique,[216] although annealing can provide sufficient time for effects such as Ostwald ripening to occur, where larger QDs grow at the expense of smaller QDs.[218] Whether growth occurs or not is also a function of the relevant rates of various processes including atomic arrival, desorption, diffusion, and bonding. There are numerous interactions between adatoms and terraces, steps, kinks, and surface defects (Figure 2.4). At typical atomic fluxes and substrate temperatures, growth by MBE is, therefore, limited by kinetics rather than thermodynamics.

During MBE, the interplay between thermodynamics and kinetics gives rise to three growth modes. First is the Frank–van der Merwe (FM) growth mode, which

proceeds either via 2D layer-by-layer (Figure 2.4(a)) or step-flow crystal growth (Figure 2.4(b)). On surfaces where the average adatom diffusion length is less than the distance

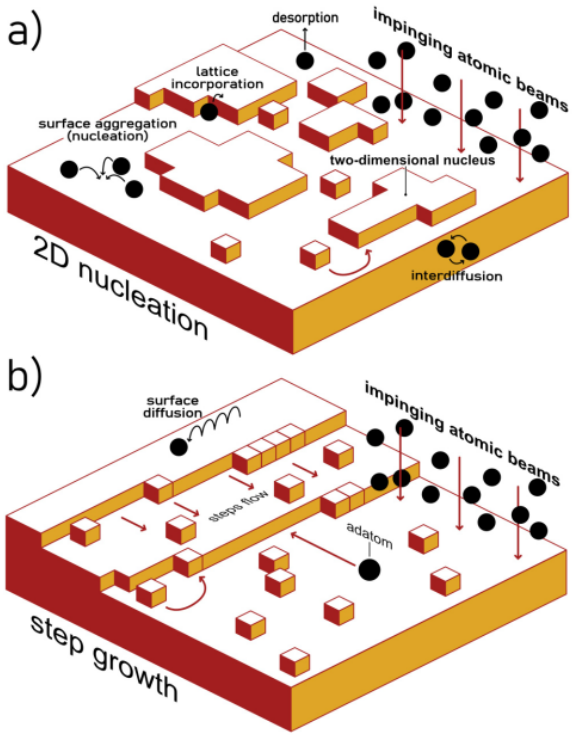

Figure 2.4 Kinetic processes present during the nucleation and growth of 2D thin films via (a) layer-by-layer growth and (b) step-flow growth.

between neighboring step-edges, crystal growth will tend to proceed via layer-by-layer growth. On surfaces where the average adatom diffusion length is greater than the distance between neighboring step-edges, crystal growth will tend to proceed via step-flow growth.

During layer-by-layer growth, low mobility adatoms will locally nucleate into 2D islands that eventually merge to form complete single-crystal layers (Figure 2.4(a)).[219] If adatom diffusion is very low (for example, if the substrate temperature is too low), multi-layer growth (i.e., roughening) can occur. Adatoms landing on top of existing 2D islands have insufficient energy to overcome the Ehrlich–Schwoebel (ES) barrier and descend to

the main epitaxial surface. ES potential barriers exist at the top of step-edges and prevent low energy adatoms from moving down to the terrace below.[220] The ES barrier occurs because as the adatom passes over the top of the step-edge, it sees a "missing" atom and so it has fewer bonding sites (has lower coordination) than an adatom on the smooth terrace. The result of the ES barrier is that low energy adatoms may coalesce to form a new island on top of an existing island before the full 2D layer is completed.[215]

In contrast, for high mobility adatoms whose diffusion lengths exceed the average terrace width, step-flow growth may occur instead (Figure 2.4(b)). An adatom on the lower terrace that is able to reach the bottom of a step-edge will encounter a potential well.[220] This potential well occurs because of the increase in adatom coordination due to the opportunity for bonding with step-edge atoms as well as those on the terrace itself. The result of this potential well is that most adatoms will join the growing crystal at the step-edges (Figure 2.4(b)). The step-edges grow out at the same rate and the surface morphology is essentially preserved.

For more detail on ES barriers, and crystal growth kinetics in general, we direct the reader to Refs. [221] and [222].

FM growth typically occurs in materials systems where strain is low. When $\gamma_e + \gamma_i < \gamma_s$, it is energetically favorable for the epi-layer to completely wet the substrate surface, giving rise to the FM growth mode (Figure 2.5(a)). It follows that the spontaneous formation of 3D QDs does not arise naturally from this growth mode.

2.4.2 Volmer-Weber Growth

The second growth mode we must consider is the Volmer–Weber (VW) growth mode, which produces discrete, 3D islands (Figure 2.5(b)). For VW growth, the condition

$\gamma_e + \gamma_i > \gamma_s$ must be met, resulting in dewetting of the epilayer so that 3D islanding occurs. In situations close to thermodynamic equilibrium, the contact angle between the VW islands and the substrate surface is given by $\cos\theta = (\gamma_s - \gamma_i)/\gamma_e$.[215] In practice, the VW

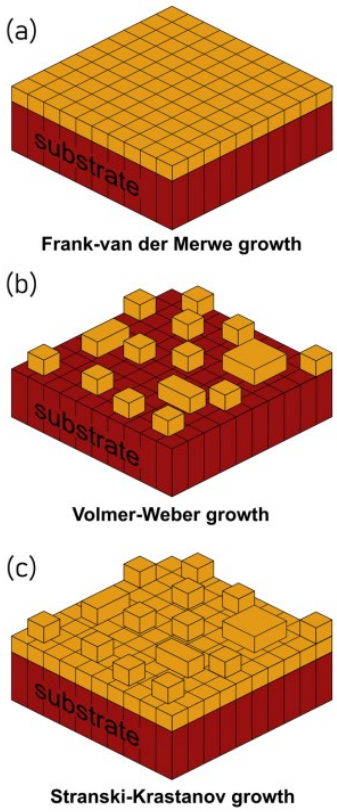

Figure 2.5 Different growth modes during MBE growth resulting from a thermodynamic interaction of surface energies: (a) the FM layer-by-layer growth mode, (b) the Volmer–Weber (VW) growth mode, which produces 3D islands directly on a substrate; and (c) the SK growth mode in which 3D islands form on top of a complete 2D wetting layer.

growth mode is rarely encountered among the semiconductors of interest for QD-based optoelectronics. Typically, only very thin layers of materials under extremely high strains (>10%) self-assemble via the VW growth mode, for example, in the InPSb/InP, GaPSb/GaP, and InN/GaN QD systems.[78,223,224]

That being said, QD self-assembly by the VW mode does occur under lower strains in some hybrid group V/III–V semiconductor systems.[26,225–229] VW-based self-

assembly has also been reported for tensile-strained systems such as GaP/GaAs(110) and Ge/InAlAs(111)A, where QD formation is mediated by step-edges on the substrate surface.[17,26] If the potential well associated with the ES barrier is sufficiently deep, adatoms will not cross from one terrace to another but instead preferentially accumulate at the bottom of the step-edges.[17] This means that locally, the adatom density can quickly become high enough to trigger island nucleation, even when the total amount of material deposited is ≪1 monolayer. The result is the preferential self-assembly of QDs at the step-edges (Figure 2.6), in contrast to the randomly distributed QDs we typically see during strain-driven self-assembly.

2.4.3 Stranski-Krastanov Growth

The third growth mode we must consider is the Stranski–Krastanov (SK) growth mode, where initial 2D growth transitions into the self-assembly of 3D islands (Figure 2.5(c)). SK growth typically occurs for intermediate levels of compressive or tensile strain, say 2.5%–10%. During the initial stages of SK growth, the various surface free energies are such that the epilayer wets the substrate surface. The group III adatom diffusion length is sufficiently high that we initially obtain layer-by-layer growth of a 2D wetting layer.[230] However, as the wetting layer gets thicker, the strain energy builds up, and a competition between plastic and elastic strain relief mechanisms comes into play.[19,86] Depending on the specific combination of sign of strain and substrate orientation, this strain energy will be relieved either plastically by dislocation nucleation and glide, or elastically by surface roughening.[19] For compressive strain on a (001) substrate or tensile strain on a (110) or (111) substrate, elastic strain relief is energetically

favorable, and a morphological change can occur from 2D to 3D growth. This transition is the hallmark of the SK growth mode.

Due to its propensity to surface segregate, the presence of indium in certain QD systems can further complicate the picture. The archetypal example of this is in the self-

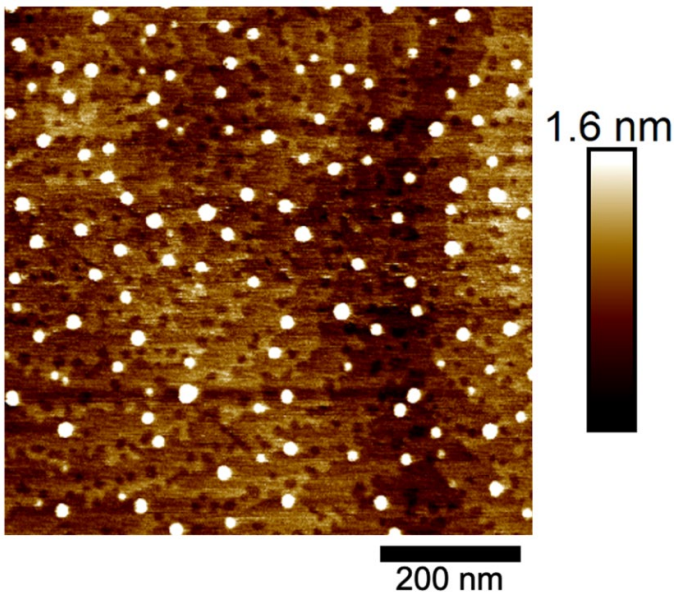

Figure 2.6 Atomic force microscope (AFM) image of tensile Ge/InAlAs(111)A QDs that self-assemble via the VW growth mode. Most of the Ge QDs form at the step-edges of the InAlAs surface.

assembly of InGaAs/GaAs(001) QDs. In–Ga intermixing at the epilayer–substrate interface dilutes the indium composition of the InGaAs epilayer below its nominal value (Figure 2.10).[231,232] However, indium also undergoes strain-driven vertical segregation, which enriches indium content at the InGaAs surface.[231] Once this surface indium concentration reaches 80%–85%,[231] the strain is large enough for the SK transition from 2D to 3D growth to occur.[86,233] As we reduce the nominal indium composition of the deposited InGaAs, we lower the strain, but we also lower the amount of indium available. This means that the wetting layer will grow thicker before this critical surface indium concentration is achieved, and self-assembly begins.

It is interesting to note that reversing the situation, so that indium is present in the matrix material but not in the QDs, can lead to some unusual effects such as SK growth with a tunable wetting layer thickness (see Section 2.4.6.1).[154]

Once the critical thickness has been reached, SK growth proceeds via the formation of discrete 3D islands on top of the 2D wetting layer. As discussed above, either compressive or tensile strain can be used to drive SK growth as long as a substrate with the correct crystallographic orientation is used: [compressive + (001); tensile + (111) or (110)].[19,21,154,230] For these specific combinations, the resulting 3D islands will be elastically strained and free from dislocations, provided the total amount of material deposited is less than some maximum amount, typically a few monolayers (ML). Exceeding this maximum will allow the accumulated strain energy in the wetting layer and QDs to overcome the energy barrier to dislocation nucleation, and plastic strain relief will take place.

Although the SK growth mode is much more frequently encountered, we can take advantage of both the SK and VW growth modes to produce 3D self-assembled QDs with high areal densities.[234] Indeed, for Ge QDs grown on InAlAs(111)A (Figure 2.6), Sautter *et al*. showed that it may be possible to move between the VW and SK growth modes through careful choice of MBE parameters.[26]

As we have seen, the resulting characteristics of these self-assembled QDs depend on both thermodynamic and kinetic factors, with atomic deposition rate, adsorption, and adatom surface diffusion of particular importance. In the remainder of this tutorial, we look at systems where compressive and tensile strain are the driving forces for the formation of QD self-assembly. Given their much earlier discovery, the body of literature

concerning compressively strained QD systems is more extensive and covers a wider variety of materials. In contrast, tensile-strained QDs are still in the comparatively early stages of research but represent a fertile area for the development of novel QD systems.

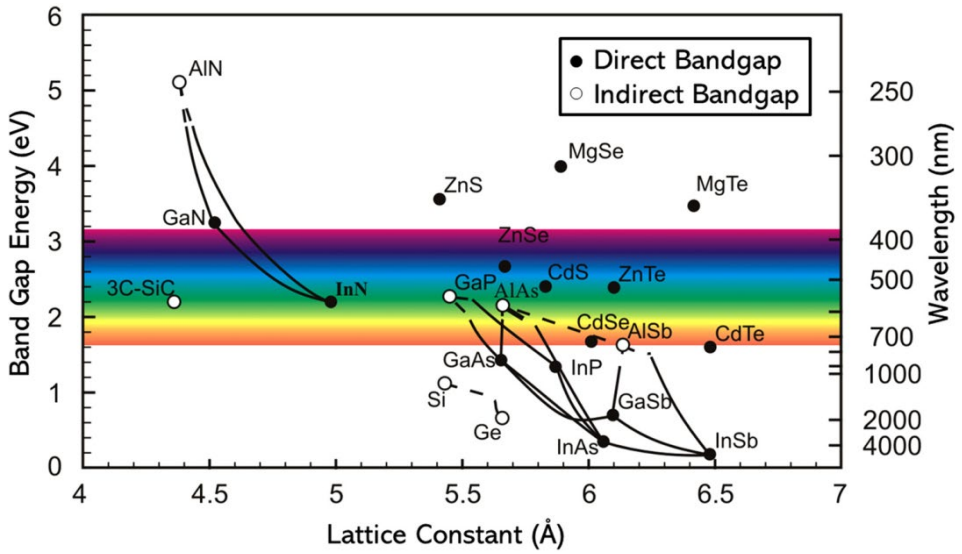

Figure 2.7 Room-temperature bandgaps of various elemental and binary compound semiconductors as a function of lattice constant. Reprinted with permission from Fornari, "Epitaxy for energy materials," in *Handbook of Crystal Growth*, 2nd ed., Handbook of Crystal Growth, edited by T. F. Kuech (North-Holland, Boston, 2015), pp. 1–49. Copyright 2015 Elsevier.

2.5 Compressively Strained Quantum Dots

Research into epitaxial QDs began with materials systems under compressive strain. Compressive strain occurs when the lattice constant of the QD material is larger than that of the surrounding matrix. Since the lattice constant of most semiconductors relates inversely to their bandgap (Figure 2.7), this situation lends itself well to producing quantum confinement of carriers in the QD.

The critical thickness for the SK transition from 2D to 3D growth is dictated by the accumulated compressive strain in the wetting layer. For materials systems under high strain, the critical thickness will, therefore, tend to be lower. For example, InAs/InP

QDs (3.2% strain) have a critical thickness of 2.5 ML,[235,236] while InAs/GaAs QDs (7.2% strain) and GaSb/GaAs QDs (7.8% strain) have critical thicknesses of 1.6 ML and 1.2 ML, respectively.[237] As well as driving the self-assembly process, compressive strain has the effect of increasing the semiconductor bandgap (Figure 2.8(a)) and hence blue-shifting the light the QDs emit or absorb. In addition, we see that compressive strain breaks the valence band degeneracy, pushing the heavy-hole band above the light-hole band. We can control the strain by changing the composition and hence the lattice constant of the QD and/or the surrounding matrix. In doing so, we can fine-tune the QD band structure, for example, to select light absorption or emission at a specific wavelength. Further tunability is possible by manipulating QD size, shape, and areal density, all of which one can tailor during self-assembled growth by MBE.

The compressively strained materials systems we discuss below represent some of the most widely studied self-assembled QDs, providing an excellent starting point for understanding the newer field of tensile-strained QD self-assembly in Section 2.4.6.

2.5.1 Ge or Ge_xSi_{1-x} on Si(001)

Due to the dominance of Si in the electronics industry, Ge_xSi_{1-x} on Si(001) is one of the most heavily studied diamond-cubic heteroepitaxial systems. By combining the elemental semiconductors Si and Ge, researchers created alloys whose composition allowed them to manipulate both the band structure and, via lattice constant, the strain (Figure 2.7). There is a ~4.2% lattice mismatch between Si and Ge (see Figure 2.7).[121,238–240] Not only did strain-relaxed 2D buffers of Ge_xSi_{1-x} alloys lead to important developments in electronic device design,[241,242] they also helped researchers better understand homo- and heteroepitaxy from a kinetic and thermodynamic perspective.

In general, compressively strained Ge_xSi_{1-x} self-assembles into rectangular-based "huts" on Si(001) with {105} facets under typical MBE growth conditions.[238,239,243–245] For further information, several detailed studies of Ge_xSi_{1-x} QD shapes/facets exist.[238,239,243–245] While researchers have explored Ge_xSi_{1-x} self-assembly on Si(001) substrates with a 0°–8° miscut toward the [110] direction,[239,246,247] most studies focus on miscuts of <2°.[239,246,247] Interestingly, exceeding a 4° miscut angle can change the growth mode from SK to VW.[247]

To remove the native oxide before MBE, Si substrates are typically heated to a "flash-clean" temperature of 1050–1255 °C and held there for 40 s[239,243,246,248] or may be first annealed at 900 °C for 3 min before flash-cleaning the Si substrate.[248] The substrate is then cooled to 500–700 °C for Si deposition.[238,240,247–249] At this growth temperature, Si(001) grows with a (2 × 1) surface reconstruction in a step-flow growth mode.[238] Typical growth rates for Si homoepitaxy are from 0.005 to 0.74 ML/s, with 0.044–0.405 ML/s the most common.[240,247–249] A Si buffer layer of ~100 nm is grown to act as a bottom potential barrier for the Ge_xSi_{1-x} QDs. The sample may be annealed at 1100 °C for 10 min and then cooled to the desired temperature for Ge_xSi_{1-x} QD growth.[249]

Researchers have demonstrated Ge_xSi_{1-x} QD self-assembly at substrate temperatures from 300 to 750 °C, but 450–600 °C is typical.[70,238–240,243,247–249] The Ge_xSi_{1-x} growth rate can range from 0.0008 to 0.707 ML/s, but we recommend 0.001–0.083 ML/s based on the most common rates in the literature. [70,238,240,243,248,249]

For deposition of pure Ge (i.e., x = 1) on Si(001), the wetting layer initially grows via the step-flow mode, with Si/Ge intermixing at substrate temperatures ≥500 °C.[238,248,249] After 3 ML Ge deposition, the reflection high-energy electron diffraction

(RHEED) pattern changes from streaky to spotty, indicative of the SK growth mode transition from 2D growth to 3D island self-assembly.[238–240,243,248,249] For Ge_xSi_{1-x}/Si(001) studies, typical QD deposition amounts are 3–8 ML.[70,238–240,249] Individual layers of Ge_xSi_{1-x} QDs are separated by at least 10 nm of Si and finally capped with ~100 nm of Si to act as the top potential barrier and provide confinement.[70,240]

Surfactants can help delay the SK transition to 3D islanding, thus increasing the critical thickness and red-shifting the energy of the quantum confined states in the wetting layer.[248] Example surfactants are As_4 and Sb_4, with As providing a more stable (i.e., thicker) Ge wetting layer than Sb.[248]

2.5.2 $In_xGa_{1-x}As$ on GaAs(001)

As the earliest optically active QD system, self-assembled $In_xGa_{1-x}As$/GaAs(001) QDs are the most extensively studied in the literature. Together with Ge_xSi_{1-x}/Si(001), $In_xGa_{1-x}As$/GaAs(001) QDs gave researchers an opportunity to study MBE growth kinetics and thermodynamics in great detail and opened the door to materials design through strain-engineering. $In_xGa_{1-x}As$/GaAs QD self-assembly is driven by a compressive lattice mismatch of ~7.2% between InAs and GaAs, but despite this large strain, the QDs are free from dislocations.[67,68,118,250,251] A direct bandgap (Figure 2.8) and strong type-I carrier confinement (Figure 2.9), mean that $In_xGa_{1-x}As$/GaAs(001) QDs are well suited to a range of optoelectronic devices.[114]

Here, we describe the MBE conditions most widely used to grow self-assembled $In_xGa_{1-x}As$/GaAs QDs. The native oxide is thermally removed from GaAs(001) substrates under a flux of As_2 or As_4 at anywhere from 580 to 650 °C.[19,251–253] A homoepitaxial GaAs(001) buffer of several hundred nanometers is then grown at a

substrate temperature of 550–600 °C (typically closer to 600 °C).[19,68,81,114,137,211,251–256] The GaAs growth rate for the buffer is 0.3–1.0 μm/h (often at the higher end of this range). [19,68,114,137,211,251–256] GaAs(001) growth typically occurs on the (2 × 4) As-

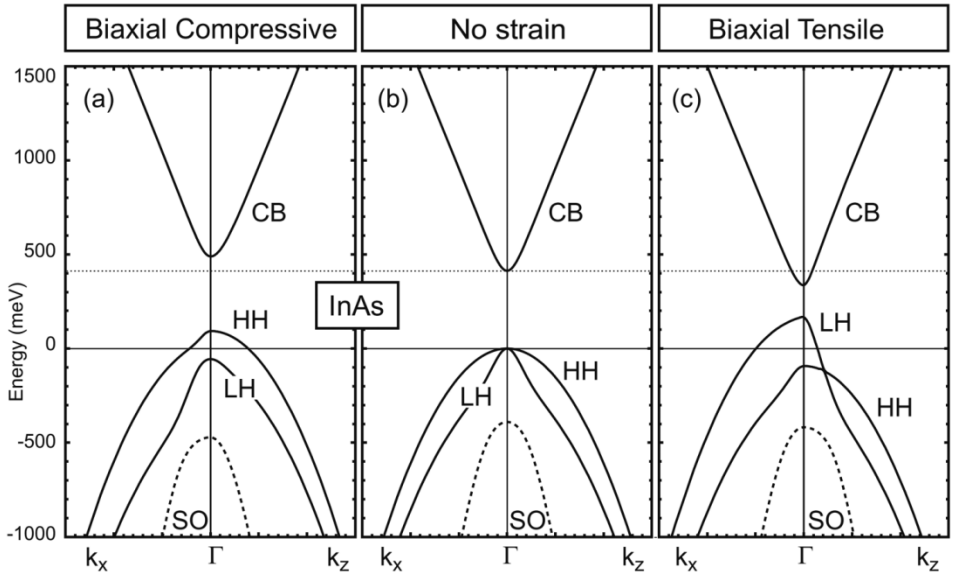

Figure 2.8 Calculated band structures for InAs in the presence of (a) biaxial compressive strain, with strain components $\varepsilon_{xx} = \varepsilon_{yy} < 0$ and $\varepsilon_{zz} > 0$, (b) no strain, and (c) biaxial tensile strain, with $\varepsilon_{xx} = \varepsilon_{yy} > 0$ and $\varepsilon_{zz} < 0$. Reprinted with permission from Schliwa *et al.*, "Electronic properties of III-V quantum dots," in *Multi-Band Effective Mass Approximations*, Lecture Notes in Computational Science and Engineering (Springer, Cham, 2014), Vol. 94, pp. 57–85. Copyright 2014 Springer Nature.[257]

stabilized surface reconstruction, in part because this surface comprises the largest part of the GaAs(001) flux–temperature phase diagram for a given As flux.[68,81,252]

For the growth of binary InAs QDs, the substrate temperature is typically reduced to 400–490 °C.[114,251,252,254,255,258,259] Unless care is taken to reduce the As overpressure during cooling, the GaAs(001) surface will undergo a phase change to the c(4 × 4) surface reconstruction at around 520 °C.[68,251] As a result, most $In_xGa_{1-x}As$/GaAs(001) QDs undergo self-assembly on this c(4 × 4) surface. The$In_xGa_{1-x}As$ is deposited at 0.018–0.3 ML/s, and typical deposition amounts range from 1.4 to 2.7 ML.[67,68,114,251,252,254,258]

Once the InAs critical wetting layer thickness of 1.6–1.7 ML is reached, the RHEED pattern rapidly changes. Consistent with the SK transition from 2D to 3D growth, the streaky c(4 × 4) pattern of the wetting layer gives way to a spotty pattern, with spots and

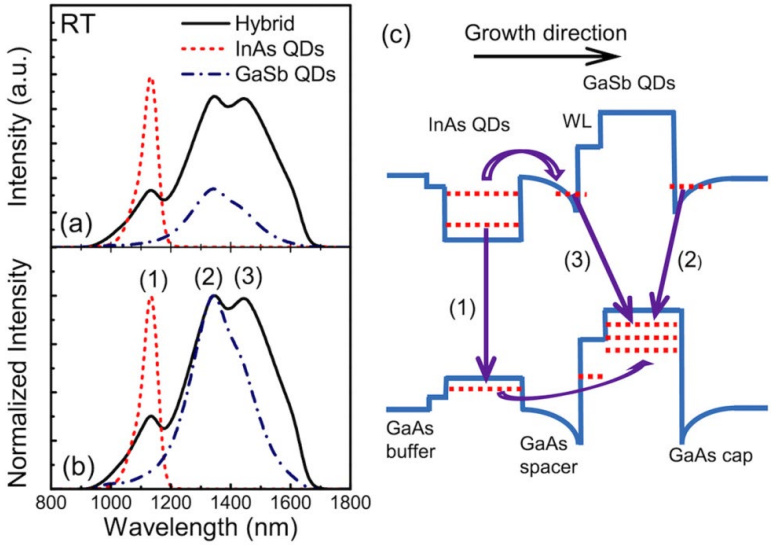

Figure 2.9 (a) Room-temperature PL spectra for InAs/GaAs(001) QDs, GaSb/GaAs(001) QDs, and an InAs–GaSb hybrid QD structure. (b) These same spectra normalized to the maximum intensity. (c) The band diagram for this hybrid structure explains the origin of the three peaks and shows the type-I and type-II band alignments of the InAs and GaSb QDs, respectively. Reprinted with permission from Ji *et al.*, Appl. Phys. Lett. 106, 103104 (2015). Copyright 2015 AIP Publishing LLC.[254]

chevrons forming along the [110] and [$\bar{1}$10] azimuths, respectively.[67,68,114,254] The result of this step is the self-assembly of InAs QDs. Cation intermixing naturally occurs at the InAs–GaAs interface to form an $In_xGa_{1-x}As$ alloy.[68,81,231] This alloy extends up into the QDs and generally becomes more In-rich with increased deposition (Figure 2.10). [68,81,231] The concentration of In in both the wetting layer and the QDs increases with a decrease in the InAs growth rate.[68]

Some studies suggest adding an anneal step of 5 min at 580 °C before and/or after depositing the $In_xGa_{1-x}As$.[254,255] The use of a surfactant, such as Te, can increase the

critical wetting layer thickness up to 6 ML.[258] Houzay *et al*. were also able to obtain a critical wetting layer thickness of 6 ML by depositing 0.5–1 ML InAs, pausing "several" minutes, and continuing the deposition at 0.05 ML/s.[251] The authors also show that it is

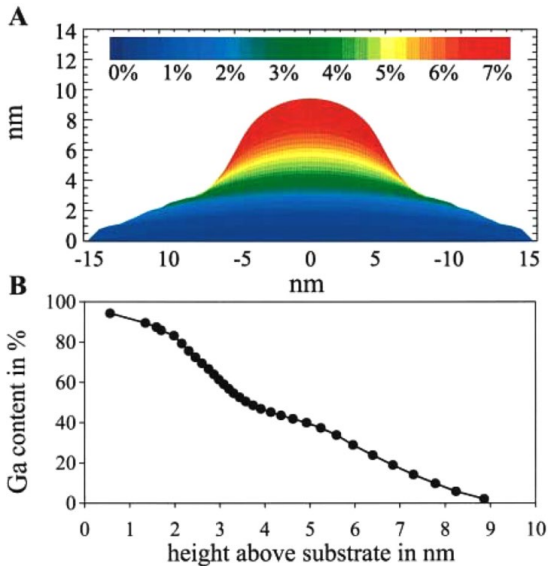

Figure 2.10 Experimental results for the InAs/GaAs QD system. (a) Deviation of the lateral lattice parameter due to compositional variation in a QD compared to GaAs. (b) Ga-content of the $In_{1-x}Ga_xAs$ alloy in a QD as a function of vertical position. Reprinted with permission from Kegel *et al.*, Phys. Rev. Lett. 85, 1694 (2000). Copyright 2000 American Physical Society.[67]

possible to increase the wetting layer critical thickness to 3 ML by increasing the As overpressure during InAs growth.[251]

Ternary $In_xGa_{1-x}As$ QDs (i.e., $x < 1$) are often grown at slightly higher substrate temperatures of 505–530 °C.[81,253] Note that above ~530–540 °C, the sticking coefficient of indium falls rapidly to zero, placing an upper limit on the substrate temperature for QD growth.[260] For $x = 0.5$, the critical wetting layer thickness for $In_xGa_{1-x}As$ QD self-assembly increases to 4–5 ML.[81,253] An increase in the critical thickness is consistent both with the lower strain and the reduced availability of indium, meaning that it takes longer

to reach the critical surface concentration for the transition to 3D growth (see Section 2.4.3).[231]

When capping $In_xGa_{1-x}As$ QDs with GaAs to create the top barrier, it only takes ~5 nm for the streaky RHEED pattern to recover, indicating planar growth.[81] Typically, at least the first ~5–10 nm of the GaAs cap is grown at the QD growth temperature. This prevents indium-desorption when the sample is heated to the optimal substrate temperature for growth of the GaAs cap. We recommend growing a total GaAs cap thickness of at least 25 nm. However, if multiple layers of QDs are to be stacked in a given structure, tuning the spacer layer thickness may be required to prevent carrier tunneling or vertical alignment of QDs (if these effects are undesirable).[81,253,261] For further reading, the paper by Joyce and Vvedensky offers a comprehensive discussion of both GaAs homoepitaxy and InAs/GaAs heteroepitaxy.[68] The authors present information on surface reconstructions and demonstrate how substrate orientation impacts homo- and heteroepitaxy. In addition, the study by Jacobi provides a thorough discussion of InAs/GaAs QD facets and QD sizes.[259]

2.5.3 GaSb on GaAs(001)

GaSb QDs embedded within a GaAs matrix experience 7.8% lattice mismatch and exhibit a type-II band alignment offering hole confinement (Figure 2.9).[137,211,254,256,262,263] QDs with type-II band alignments may be preferable for applications where low carrier recombination rates/long radiative lifetimes are required.[256,262,263] What is more, unlike type-I QDs, the emission energy from type-II QDs is tunable, blue-shifting as the cube root of the laser excitation density.[264,265]

We summarize our recommendations for growing GaAs(001) homoepitaxial buffers in Section 2.5.2. Once the GaAs buffer layer is complete, the substrate is cooled to 450–530 °C (we recommend 450–490 °C) while closing off the As flux (or dramatically reducing it).[137,211,256,262] We recommend exposing the GaAs buffer to a beam equivalent pressure (BEP) Sb_2 flux of ~1×10^7 Torr for 60 s prior to opening the Ga shutter.[211]

To grow the QDs, deposit 1.4–5 ML GaSb at a rate of 0.2–0.73 ML/s, with a V/III flux ratio of 1–2. [137,211,254,256,262] Once the critical wetting layer thickness of ~1.2 ML is reached,[237] the RHEED pattern transforms from streaky to spotty, indicating a transition to 3D self-assembly.[254,256] The result is defect-free GaSb(001) QDs.

Sun *et al*. show that to maintain GaSb QD quality, care during growth of the top barrier, or cap, is critical. After QD growth, increasing the substrate temperature above 500 °C results in "an immediate disappearance" of the spotty RHEED pattern.[256] The authors show that for GaSb QDs grown above 460 °C, the spotty RHEED pattern is maintained only if the substrate temperature is reduced to 460 °C under an Sb flux. [256] Once at 460 °C, the Sb valve can be closed, and the As valve opened.

Growth of a 50–100 nm GaAs cap can then take place. [256] It is common to deposit the first 10–15 nm GaAs at the GaSb QD growth temperature, before interrupting the growth and finishing the cap at standard GaAs growth temperatures close to 600 °C. [137,211,256,262] For a droplet epitaxy method for growing GaSb/GaAs(001) QDs by MBE, see Liang *et al*.[211]

2.5.4 InAs on $In_{0.52}Al_{0.48}As$, $In_{0.53}Ga_{0.47}As$, or InP(001)

The compressive lattice mismatch of 3.2% between InAs and InP(001) (and its lattice-matched alloys $In_xAl_{1-x}As$ and $In_xGa_{1-x}As$) is considerably lower than the 7.2% mismatch InAs experiences on GaAs(001) (see Figure 2.7). Because compressive strain serves to increase the semiconductor bandgap energy (Figure 2.8), the lower strain in InAs/InP-based QDs means that their light emission/absorption is significantly red-shifted compared with similar QDs grown on GaAs. This red-shift means that InAs/InP-based QDs allow us to access the telecom-relevant "O" and "C" bands, centered at wavelengths of 1.3 μm and 1.55 μm, respectively.[266–270] These wavelengths correspond to minima in the absorption spectrum of standard silica optical fibers, where light transmission is more efficient. As a result, considerable research efforts have gone into obtaining room-temperature light emission from InAs QDs in these materials systems.[236,266–272]

An unusual feature of InAs self-assembly in these InP-based systems is the ability to synthesize either discrete QDs or elongated quantum wires (QWrs) depending on the MBE conditions, specific choice of buffer materials, or substrate offcut. [236,269,271–275] The InAs QWrs tend to line up parallel to the $[\bar{1}10]$ direction due to the anisotropic relaxation of strain (Figure 2.11).[273,276] García *et al*. show that the group V stabilized (2 × 4) surface reconstruction gives rise to QWr formation in heteroepitaxial systems involving different group V elements.[276] Similar QWr formation effects have been reported in other mixed-group V systems, including InAs/AlAsSb(001).[265,277] In all cases, the QWrs form parallel to the dimer rows of the (2 × 4) reconstruction, which are aligned along $[\bar{1}10]$.[276]

Differences in QWr (or QD) morphology and light emission characteristics are observed when InAs is deposited on InP, $In_xAl_{1-x}As$, or $In_xGa_{1-x}As$.[236,266–272,278]

To grow self-assembled InAs QWr's or QDs, the InP(001) substrate oxide is desorbed at 500 °C for 10 min.[279] Regardless of the buffer material used, a 200–400 nm smoothing layer suffices for QD growth.[267–272,278]

For an InP buffer, we recommend growing at 1 μm/h and 400 °C under a P_2/In flux ratio of 20.[267,268,270–272,278] For $In_{0.53}Ga_{0.47}As$ or $In_{0.52}Al_{0.48}As$ buffers, a growth temperature of 460–525 °C is more common.[236,268,269,272] We recommend annealing the

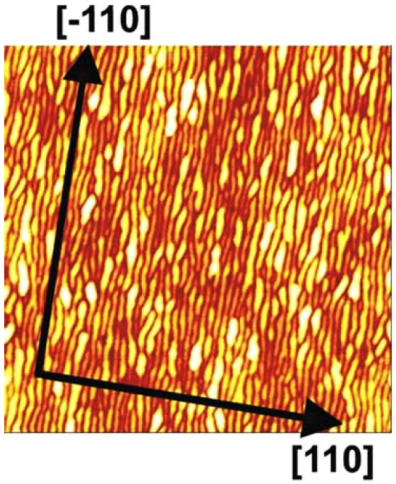

Figure 2.11 1×1 μm^2 AFM image of self-assembled InAs/InAlAs QWrs, showing their alignment parallel to [$\bar{1}$10]. Reprinted with permission from Simmonds *et al.*, J. Vac. Sci. Technol. B 25, 1044–1048 (2007). Copyright 2007 American Vacuum Society.[236]

buffer at its growth temperature for 10 min under either an As or P flux depending on the buffer's group V element.[268,269]

The InAs QD growth temperature is typically 400–495 °C on InP[269–271,278] and 460–525 °C on $In_{0.52}Al_{0.48}As$ or $In_{0.53}Ga_{0.47}As$.[236,268,269,272] Typical InAs growth rates are 0.1–0.5 ML/s under an As-rich overpressure where the V/III ratio is 30–35.[236,268–272,278]

The critical thickness for the SK growth mode transition is ~2.5 ML,[236,268–272] which is a result of the lower strain in this system compared to InAs/GaAs QDs (see Section 2.4.3).

To tune QD size and areal density, some authors recommend annealing the self-assembled InAs after deposition for 30–120 s under the same substrate temperature and As flux.[268–272,278]

If growing more than one layer of self-assembled InAs, we recommend using 25–50 nm spacer layers grown under the same conditions as the bottom barrier.[266,272] Depending on requirements, a surface capping layer of 50–300 nm is sufficient to form a top potential barrier.[268–272]

2.5.5 InP on $In_xGa_{1-x}P$/GaAs(001)

InP QDs on $In_xGa_{1-x}P$/GaAs(001), with a maximum lattice mismatch of 7.2%, present an interesting opportunity to achieve highly organized, 2D arrays of QDs without substrate pre-patterning.[280–283] For x = 0.51, $In_xGa_{1-x}P$ is lattice-matched to GaAs, resulting in a 3.7% compressive lattice mismatch in the InP QDs. InP deposited onto lattice-matched $In_xGa_{1-x}P$/GaAs(001) can self-assemble into quantum rings.[284] Slightly straining the $In_xGa_{1-x}P$ with respect to the GaAs substrate can produce QDs with spatial alignment along the [100] and [010] directions (Figure 2.12).[281,282] Many studies of this material system investigate the effect of the buffer composition on SK growth, QD elongation, and QD shape.[280–283,285] There is evidence that the 2D wetting layer in this system is unstable. Corrosion of the wetting layer likely increases QD size.[282]

The initial steps for QD growth in this system involve the native oxide removal and the initial buffer growth of GaAs(001), which is described in Section 2.5.2. Typically, a 200–300 nm GaAs buffer is grown to smooth the surface, followed by the

$In_xGa_{1-x}P$ bottom barrier.[127,280–285] 150–500 nm $In_xGa_{1-x}P$ is deposited at 0.5–1.0 ML/s, at a substrate temperature of 415–550 °C, under a P_2/III flux ratio of 10–32.[127,280–283,285] Smooth $In_xGa_{1-x}P$ buffers exhibit a streaky (2 × 1) RHEED pattern.[281–283]

Once the $In_xGa_{1-x}P$ growth is complete, the substrate temperature is adjusted for growth of the InP QDs, typically 410–540 °C.[127,280–283,285] InP QDs are deposited at 0.16–1.6 ML/s, usually at the lower end of that range.[280–285] The critical wetting layer thickness of the QDs is 1.5–3 ML, depending on the $In_xGa_{1-x}P$ buffer composition, and hence the amount of compressive strain in the InP. The 2D-to-3D SK transition is identifiable in RHEED from the telltale change from a streaky to spotty pattern.[280,283,285] The QDs are

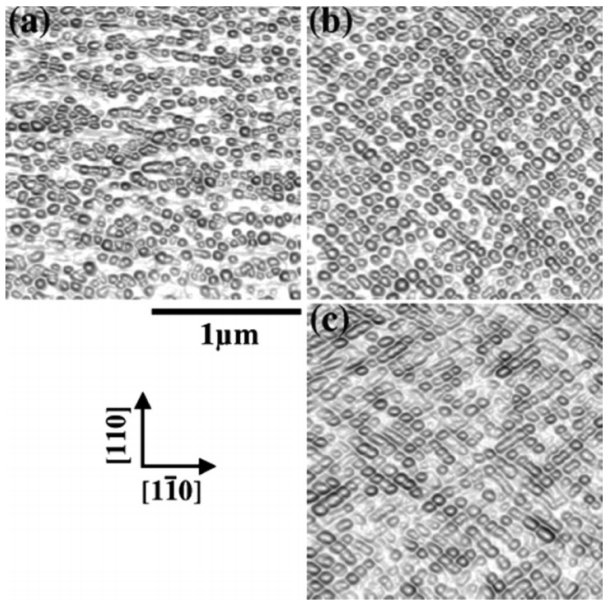

Figure 2.12 AFM images of InP QDs grown on InGaP (a) lattice-matched to on-axis GaAs(001), (b) 0.60% lattice-mismatched to on-axis GaAs(001), and (c) 0.60% lattice-mismatched to GaAs(001) miscut by 2° toward <111>A. Darker regions correspond to steeper facets. Reprinted with permission from Bortoleto *et al.*, Appl. Phys. Lett. 82, 3523–3525 (2003). Copyright 2003 AIP Publishing LLC.[282]

then capped with 10–100 nm of $In_xGa_{1-x}P$ to form the top barrier. Usually, the same MBE conditions are used in the top barrier as for the bottom barrier, although some groups suggest using migration-enhanced epitaxy for the first 10 nm of the $In_xGa_{1-x}P$ cap.[284]

2.5.6 $In_xGa_{1-x}As$ and $In_xGa_{1-x}P$ on GaP(001)

The growth of self-assembled QDs on GaP is of particular relevance to the integration of III–V semiconductors with Si. The ability to grow light emitters on a CMOS-silicon platform would have far-reaching technological implications. GaP is almost lattice-matched to Si and so is the natural substrate choice for developing suitable III–V semiconductor QDs such as $In_xGa_{1-x}As$ and $In_xGa_{1-x}P$.[139,145,286,287]

Although researchers struggled for many years to develop anti-phase domain-free GaP on Si, recent advances have minimized this deleterious effect.[286,287] In fact, high-quality GaP/Si substrates are now commercially available.[286,287]

Here, we provide recommendations for $In_xGa_{1-x}As$ and $In_xGa_{1-x}P$ QDs grown on GaP(001) nominally on-axis substrates.[139,140,145] These two materials systems boast maximum lattice mismatches of 7.7% for InP/GaP and 11.1% for InAs/GaP.[139,141,145] Both QD systems can emit light in the visible spectrum, in the range of 1.8–2.1 eV at ~80 K.[140,141,145] The lower bandgaps of $In_xGa_{1-x}As$ compared with $In_xGa_{1-x}P$ mean that InGaAs QDs embedded within GaP will have stronger carrier confinement, an advantage for reliable operation at room temperature.[145] In addition, for $x < 0.3$, $In_xGa_{1-x}P$ is an indirect bandgap semiconductor rendering it incapable of light emission for these compositions (see Figure 2.7).[140]

As for the previous examples of QDs made from ternary alloys, lattice mismatch in the $In_xGa_{1-x}(As,P)$/GaP systems is tunable by controlling the composition. For

example, $In_xGa_{1-x}As$/GaP QDs with $0.07 < x < 0.5$ correspond to lattice mismatch in the range of 4%-7%. Since we can use compressive strain to widen the bandgap (Figure 2.8), composition enables precise tuning of QD emission wavelength.[145]

For GaP(001) substrates, native oxide desorption occurs at 650 °C.[139,145] The GaP(001) substrate reveals a streaky, (2 × 4) RHEED pattern (Figure 2.13).[139,141,145] To grow smooth GaP buffers, the substrate temperature is reduced to 560–620 °C.[139–141,145] The P_2/Ga flux ratio is ~10,[145] and the growth rate is 0.4–0.7 ML/s.[140,145] We recommend a buffer thickness of at least 150–250 nm.[139,141,145]

To grow the $In_xGa_{1-x}(As,P)$/GaP QDs, one cools the substrate to 490–510 °C, and either As_2 or P_2 is used for the QD deposition,[139,141,145,287] at a V/III flux ratio of ~40.[145] QD growth rates of 0.013–0.2 ML/s are typical.[139,145]

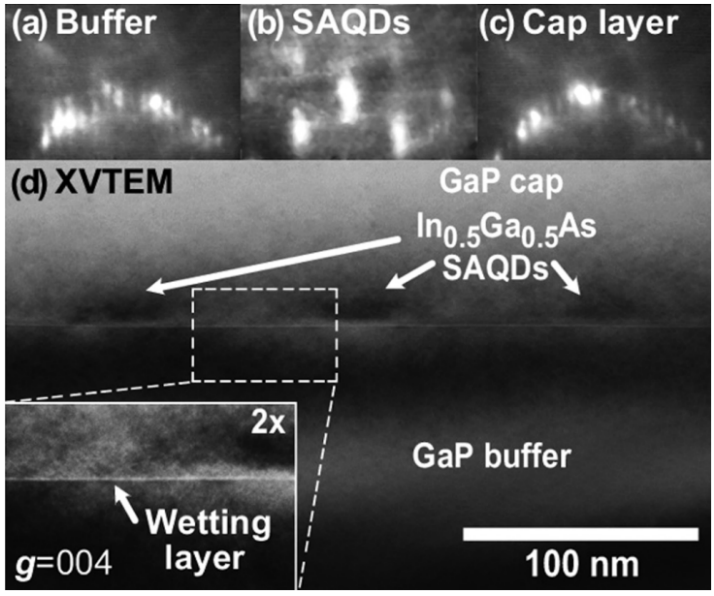

Figure 2.13 (a)–(c) RHEED images showing the (2 × 4) pattern (a) before, (b) immediately after growth of 1.9 ML $In_{0.5}Ga_{0.5}As$ self-assembled QDs (SAQDs), and (c) after capping the QDs with GaP. (d) shows a cross-sectional TEM image of InGaAs SAQDs with an inset confirming the presence of a wetting layer and hence SK growth. Reprinted with permission from Song *et al.*, Appl. Phys. Lett. 97, 223110 (2010). Copyright 2010 AIP Publishing LLC.[145]

For $In_{0.5}Ga_{0.5}As$ self-assembly via the SK growth mode, the critical wetting layer thickness is 1.9 ML.[145] For InAs/GaP QDs, however, there is evidence that the very high compressive strain leads to a VW growth mode.[139] For InP on GaP, the critical wetting layer thickness is 1.8–2.9 ML.[139,141] In all cases, the onset of 3D growth is accompanied by the transition from a streaky to a spotty RHEED pattern (Figure 2.13).[139,141,145] The GaP cap should be grown under the buffer growth conditions.[139]

2.5.7 (Al)GaN on AlN

The InN, GaN, and AlN semiconductor family offers a wide range of bandgaps and lattice constants (Figure 2.7), allowing researchers to engineer devices that can emit light from the visible to the ultraviolet parts of the spectrum. In the III-As materials system, the compounds GaAs and AlAs have almost identical lattice constants ruling out strain-driven GaAs QD self-assembly. In contrast, there is a 2.5% lattice mismatch between GaN and AlN, which is just sufficient to enable the self-assembly of compressively strained GaN QDs on AlN via the SK growth mode.

For many years, the lack of free-standing III–N substrates meant that the majority of nitride growth was carried out on sapphire (α-Al_xO_3), 6H-SiC(0001), and 3C-SiC(001).[146] Researchers have used SiC substrates to integrate III–N LED technology with current Si electronics.[146,147] Growth on 3C-SiC(001) permits the growth of zinc-blende GaN.[148]

Damilano *et al*. showed the growth of GaN QDs on Si(111)substrates.[288] The lack of a native substrate meant that III–N samples suffered from very high threading dislocation densities. Thick buffer layers were hence needed to achieve high-quality epitaxy without effects from the substrate.[146,289] Low-defect, free-standing, and template

III–N substrates are now commercially available, however, which has allowed researchers to achieve significantly improved epitaxial quality.[289]

Depending on the substrate material and the nitrogen source being used (e.g., N plasma or NH_3 gas), certain cleaning, annealing, and nitridating steps will be required.[146,148] For example, in the case of an rf source, some groups expose sapphire substrates to the N plasma for 1 h at 870 °C to form a reactive $Al_xO_{1-x}N$ surface layer.[146] Plasma powers are typically around 300 W, with N flow rates of ~1 sccm.[224] After this process, a 10–30 nm layer of AlN is grown at 650–730 °C, with an optional step of growing 2 μm of GaN. Following this step, a further 0.2–1.5 μm of AlN can be grown at 500–550 °C.[146] The GaN QDs can then be grown on top of this buffer.

Depositing the GaN at substrate temperatures below 620 °C results in the smooth, FM growth mode; it is only at higher temperatures that we see the transition to self-assembly of GaN QDs via the SK growth mode.[146] GaN/AlN QDs are, therefore, grown at substrate temperatures of 680–730 °C by depositing 2–4 ML of GaN.[146] Gačević *et al*. used a growth rate of 0.3 ML/s at a substrate temperature of 720 °C.[290] The 2.5% lattice mismatch between GaN and AlN means that the critical thickness of the 2D wetting layer is 2–2.5 ML.[146,224]

Schupp *et al*. grew GaN on a 3C-SiC(001) substrate by growing a 30 nm AlN buffer at 730 °C.[291] Depositing GaN onto the AlN, they report a critical thickness for the 2D-to-3D growth transition of 2 ML.[291] The resulting QDs present an areal density of 5×10^{11} cm^{-2}, with average heights and diameters of 3 nm and 15 nm, respectively.[291]

As *et al*. reported the self-assembly of GaN QDs on a 3C-SiC(001) substrate that had first been chemically etched and then annealed for 10 h at 500 °C.[292] They then

deposited the GaN at 720 °C directly on the SiC substrate.[292] More recently, Bürger *et al.* used a Si substrate, on which they grew a 10 μm 3C-SiC(001) buffer layer.[289] Using a N plasma source, the team used Al flashes to clean the surface at 910 °C before cooling it to 760 °C to grow 30 nm of AlN.[289] Upon completion of the AlN barrier layer, they deposited GaN in different amounts; using PL spectroscopy, they pinpointed the critical thickness for the SK transition at 1.95 ML.[289] They also showed an increase in the average areal density of these QDs from 10^{10} cm^{-2} at 2 ML of deposition to 10^{11} cm^{-2} at 3 ML.[289]

We recommend using these growth conditions established by Bürger *et al.* as they have also been used by Blumenthal *et al.* for a study of the optical characteristics of these GaN QDs.[293]

There is currently considerable research interest in creating mercury-free light emitters operating at ultraviolet (UV) wavelengths. Recent studies propose to create UV-emitting LEDs based on wide-bandgap $Al_yGa_{1-y}N$ QDs grown on $Al_xGa_{1-x}N$ at various concentrations.[95,294] Brault *et al.* grew a low-temperature GaN buffer on a sapphire (0001) substrate followed by 100–150 nm of AlN grown at 950 °C. They then grew 0.8–1 μm of Si-doped $Al_{0.6}Ga_{0.4}N$ at 850–870 °C.[95,294] This layer serves as the bottom barrier for QD nucleation. The researchers decreased the substrate temperature to 720–730 °C and deposited 8–10 ML $Al_yGa_{1-y}N$ with concentrations of y = 0.1 – 0.4. The V/III flux ratio was 0.7 with a growth rate of 0.1–0.4 ML/s. The critical thickness observed for the SK formation of QDs is between 3 and 4 ML.[95,294] The QDs were then annealed in vacuum for 6 min and then heated to 820 °C to improve QD uniformity.[95] A 30 nm top layer of $Al_{0.6}Ga_{0.4}N$ was used to cap the sample. The authors use NH_3 for growing the

GaN and AlGaN layers but switch to a N_2 plasma source for the QD layers.[95,294] The resulting QDs have densities of 1.5–5.4 10^{11} cm^{-2}, heights between 1.5 and 3 nm, and diameters of 5–20 nm.[95,294] Other groups have grown UV LED structures under similar conditions but containing multiple layers of QDs.[295]

It is possible to tune GaN QD size, areal density, and morphology by growing them under either N-rich (N/III flux ratio > 1) or Ga-rich growth (N/III flux ratio < 1) conditions.[146,224,290,296–298] Under N-rich conditions, adatom mobility is reduced, leading to small GaN QDs with high areal density (typically 10^{11}–10^{12} cm^{-2}).[146] Ga-rich conditions increase adatom mobility, resulting in larger GaN QDs whose areal density is 1–2 orders of magnitude lower.[290]

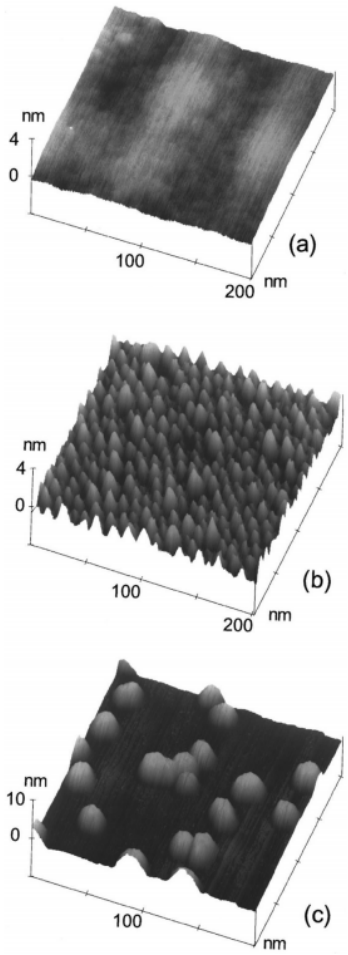

Figure 2.14 AFM scans of (a) a smooth AlN surface, (b) GaN QDs cooled rapidly after growth, and (c) GaN QDs annealed for 50 s in N plasma after growth. Reprinted with permission from Daudin *et al*., Phys. Rev. B 56, R7069 (1997). Copyright 1997 American Physical Society.[296]

Ostwald ripening provides a reliable way to control the areal density (Figure 2.14). At a sufficiently high substrate temperature, annealing the GaN QDs under a N plasma for ~50 s decreases the areal density while increasing the average QD size.[146] Due to the nucleation of QDs on threading dislocations, bimodal distributions of QD size have been reported.[224] QD size uniformity was improved by growing multiple QD layers to form a superlattice.[224] When stacking multiple layers of GaN QDs, a vertical correlation between adjacent QD layers was observed for AlN spacers ≤8 nm thick.[146]

2.5.8 $In_xGa_{1-x}N$ on GaN

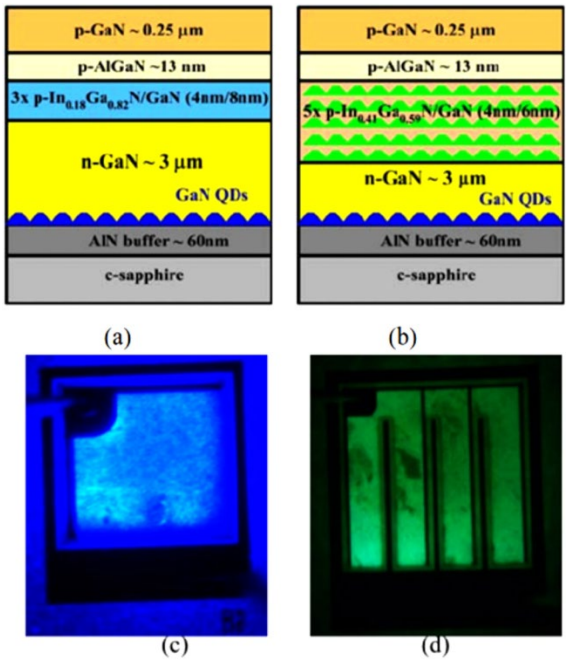

Figure 2.15 (a) and (b) are schematics for the LEDs in (c) and (d), respectively. In (a) and (c), an InGaN/GaN QW is used to emit blue light, whereas in (b) and (d), InGaN/GaN QDs are used to produce green light. Reprinted with permission from Moustakas *et al*., Phys. Status Solidi A 205, 2560–2565 (2008). Copyright 2008 Wiley-VCH Verlag GmbH & Co. KGaA.[224]

Similar to the GaN/AlN system, $In_xGa_{1-x}N$ on GaN offers the possibility of compressively strained QDs with high quantum efficiency for LED applications (Figure 2.15).[146,148] Again, using sapphire as the example substrate, researchers begin by growing a 2 µm GaN buffer.[146] Adelmann *et al*. then deposited an $In_{0.35}Ga_{0.65}N$ layer (lattice mismatch of 3.9%) at 580 °C and noted that the critical thickness for the 2D-to-3D SK transition occurred at 1.7 ML.[149] As the $In_{0.35}Ga_{0.65}N$ deposition amount is raised to 5 ML, the resulting QDs have an areal density of 10^{11} cm^{-2}, with an average diameter and a height of 27 nm and 2.9 nm, respectively.[149] These QDs exhibit strong blue-violet PL, even at 300 K.[149]

Indeed, Damilano *et al*. show that the self-assembly of $In_xGa_{1-x}N$/GaN QDs is possible with indium compositions as low as x = 0.12.[288] As the strain is reduced, the critical thickness for the SK growth mode transition increases accordingly (see Section 2.4.3). For example, for $In_{0.15}Ga_{0.85}N$/GaN QDs grown at 530–570 °C, the critical thickness is 5 ML for x = 0.15, and the resulting QDs have an average areal density of 5×10^{11} cm^{-2}, with an average diameter and a height of 35 nm and 4 nm, respectively.[288]

Gačević *et al*. grew $In_{0.5}Ga_{0.5}N$/GaN QDs at substrate temperatures of 520–580 °C. After completing 12 ML deposition, the researchers annealed the sample for 1 min before cooling. The average QD areal density for this growth is 7×10^{10} cm^{-2}, with an average height and a diameter of 3 and 30 nm, respectively.[290]

Binary InN/GaN QDs (x = 1) self-assemble via the VW growth mode (i.e., no wetting layer) due to the 11% lattice mismatch (see Section 2.4.2).[224] After the usual GaN buffer growth, the substrate was cooled to 425 °C, before depositing 9 ML of InN at a growth rate of 0.05 nm/s. The sample was then annealed under N for 5 min before cooling down.[224] The QD density for this sample was 2×10^9 cm^{-2}, with an average QD diameter and a height of 115 and 15 nm, respectively. The absence of a wetting layer indicates nucleation of InN QDs directly on the GaN threading dislocations.[224] The QDs have a wurtzite structure and are epitaxial to the GaN buffer layer.[224]

2.5.9 CdSe on ZnSe

Self-assembled QDs in the II–VI semiconductors combine all the advantages of QDs mentioned so far (bandgap tunability, enhanced quantum efficiency, limited post-growth processing) but with bandgap energies that correspond to the visible spectrum.[150,151] Similar to the $In_xGa_{1-x}As$/GaAs system (see Section 2.5.2), the lattice

mismatch values for the CdSe/ZnSe and CdTe/ZnTe systems are 6.3% and 5.8%, respectively.[151,299]

The offset in the bandgap between CdSe and ZnSe is comparable to that in archetypal InAs/GaAs QDs, enabling similarly strong quantum confinement of carriers. As a result of the chemical species present in II–VI materials, we can study QD formation in these material systems to deconvolve the contributions to self-assembly from surface energy and strain.

The critical thickness for CdSe/ZnSe QDs is not well established. Indeed, several studies show that the SK growth mode transition has to be induced.[151,300,301]

Xin *et al*. synthesized CdSe QDs on ZnSe by first growing a 2 μm ZnSe buffer at 300 °C on a GaAs(001) substrate.[150] At this point, the RHEED showed a streaky (2 × 1) pattern. The team then increased the substrate temperature to 350 °C and deposited CdSe at a growth rate of 0.4 ML/s. The RHEED pattern became spotty, indicating a transformation from 2D to 3D growth.[150] They buried the CdSe QDs with a 50 nm of ZnSe.[150] The QD areal density in their samples was 2.5×10^9 cm^{-2}, with an average QD diameter of 40 ± 5 nm and a height of 10 ± 3 nm.

Robin *et al*. developed a method to induce the 2D to 3D transition in smooth, strained CdSe layers.[300] After the growth of 3 ML CdSe by atomic layer epitaxy, the sample is cooled below room temperature and an amorphous Se layer is deposited. The substrate temperature is then ramped up to 230 °C to desorb the amorphous Se and achieve a bright spotty RHEED pattern, consistent with 3D self-assembly.[300] The critical thickness found by the researchers is 3 ML; depositions below that produce only undulations on the surface.[300]

CdSe QDs grown on $Zn_{1-x}Mn_xSe$ (with x = 0.05 and 0.10) have a higher areal density and a smaller average size than CdSe/ZnSe QDs due to the reduced compressive strain.[150] Merz *et al*. studied the same system as Xin *et al*., but with a slightly higher substrate temperature and a lower growth rate (370 °C and 0.025 ML/s, respectively). From RHEED, they show that QDs begin to appear after deposition of 3.0–3.5 ML of CdSe,[302] consistent with other groups who place it in the range of 2.5–3.0 ML.[303] These results rule out VW self-assembly.

Researchers capped some CdSe QDs with a 50 nm of ZnSe for PL while doing AFM on uncapped samples within 1 h of unloading to study their morphology.[302] The QDs are relatively circular in shape, with an areal density of 2×10^9 cm^{-2}. AFM scans performed at 48 h intervals show that surface CdSe QDs undergo Ostwald ripening at room temperature, a phenomenon not observed on III–V QD systems (see Figure 2.16). As a consequence, areal density decreases, and the average QD size distribution broadens. The rate of change in the areal density with time shows that the ripening occurs through interface-transfer-mediated growth.[303] Extrapolation shows size uniformity at the moment of deposition. Daruka and Barabási refer to this transition from a wetting layer to islands that ripen as "Regime I."[304] Cooling the samples to 0 °C prevented this ripening effect.[302]

Rabe *et al*. grew 1 μm of ZnSe on GaAs(001) at 310 °C.[305] After growing the buffer, the sample is cooled down to 230 °C under Se-rich conditions. They then deposit a few monolayers of CdSe, which grows in a layer-by-layer mode. Then, while keeping the Se shutter open, they heat the substrate to 310 °C, at which point they observe a transition to 3D self-assembly in the RHEED pattern.[305] Immediately after the CdSe

deposition, samples are capped with 85 nm of ZnSe. Sample analysis using PL showed researchers that the QDs form on top of a 2 ML wetting layer.[305]

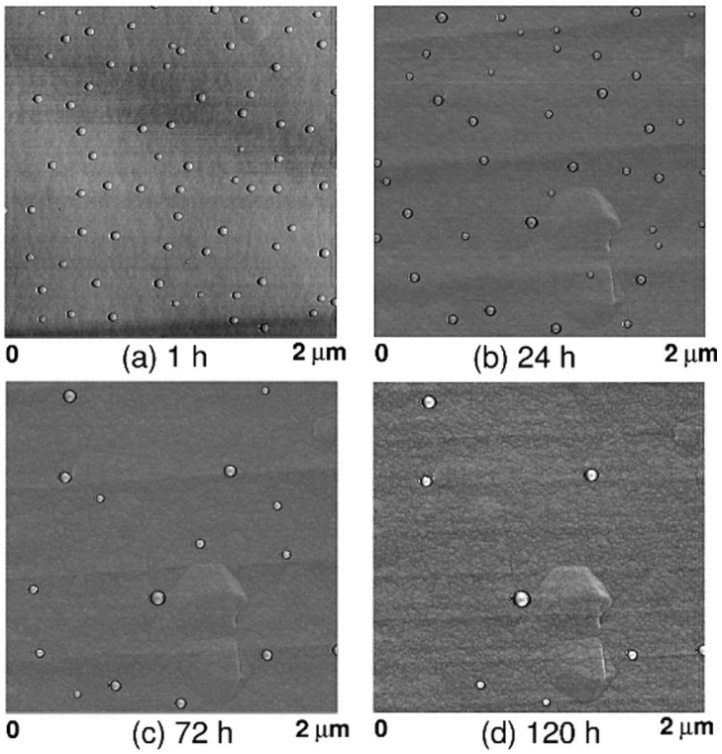

Figure 2.16 Bright-field TEM images of the same region of a sample of CdSe/ZnSe QDs showing room-temperature ripening of the QDs (a) 1 h, (b) 24 h, (c) 72 h, and (d) 120 h after the sample was removed from the MBE chamber. Reprinted with permission from Lee *et al.*, Phys. Rev. Lett. 81, 3479 (1998). Copyright 1998 American Physical Society.[306]

Kratzert *et al.* studied the thermally activated transition of QDs more closely by growing a ZnSe buffer on GaAs(001) at 230 °C, depositing 3 ML of CdSe at the same temperature, and then heating the sample to 310 °C. Surface analysis with ultrahigh vacuum AFM showed reproducible and consistent QDs averaging 1.6 ± 0.3 nm in height and 10 nm in diameter.[307] Maćkowski *et al.* found that doping with Mn atoms affects the emission from these QDs by interacting with the magnetic ions provided as dopants.[308] Kurtz *et al.* showed that when using a CdS source for Cd during the growth of these QDs, the S can act as a surfactant.[309]

2.5.10 CdTe on ZnTe

CdTe/ZnTe QDs are an interesting system for the growth of diluted magnetic materials (DMS), with applications in quantum information technologies.[152] Controlling CdTe QD growth of CdTe QDs is critical to enable the subsequent incorporation of magnetic ions.[152]

Karczewski *et al*. began by growing a 4.5 μm CdTe buffer on GaAs(001) at 420 °C, followed by 100 nm of ZnTe.[153] They deposited 1.5, 2.0, and 2.5 ML CdTe to form thin, QD-like structures, with an average diameter of 3 nm and a density of 10^{12} cm^{-2}. Interestingly, they did not observe a 2D-to-3D transition in the RHEED pattern.[153] After QD growth, they annealed the sample for 20 s and then grew a 100 ML ZnTe top barrier. The authors argue that the PL characteristics of the CdTe QDs suggest enhanced quantum efficiency.[153]

Tinjod *et al*. demonstrate that both strain and surface energy are important factors in CdTe/ZnTe(001) QD formation.[299] They grew CdTe on ZnTe in a layer-by-layer mode at 280 °C. They then covered the samples with amorphous Te at room temperature, before heating the sample back up to 220 °C to desorb the Te, at which point the RHEED pattern is spotty when it reappears.[299] This thermal activation (TA) step promotes QD formation by changing the sample's surface energy and was later adopted by other researchers.[152,310,311] The ionic nature of a Te-rich II–VI surface increases the 2D surface energy, thus decreasing the cost for facet creation and favoring a 3D transition. Using this information, groups grew self-assembled CdTe QDs on a $Zn_{0.8}Mg_{0.2}Te$ alloy with a lower lattice mismatch of 5%.[299]

Wojnar *et al*. studied how to control the properties of CdTe/ZnTe QDs by *in situ* annealing of the QD ensemble before deposition of the cap layer. They showed that QDs and 0D *quasi-islands* form by potential fluctuations at the interfaces of the quasi-wetting layer.[310] They grew 1 μm of ZnTe, followed by 6 ML of CdTe to form the QDs, and then applied the TA step. The researchers annealed the samples under a Te flux, before depositing a 100 nm ZnTe cap. Annealing below 380 °C results in Ostwald ripening of the QDs. Extended annealing at higher temperature causes the RHEED to revert to a streaky 2D pattern.[310]

Sorokin *et al*. demonstrated the growth of CdTe/Zn(Mg)(Se)Te QDs using the TA technique.[311] They grew 200 nm of InAs on InAs(001) at 295–300 °C to obtain a (2 × 4) surface reconstruction. They then deposited 5 ML of ZnTe, followed by 10 nm of $Zn_{0.9}Mg_{0.1}Te$, 20 nm of ZnTe, 3.0–5.5 ML of CdTe, and finally capped the sample with 20 nm of ZnTe. After depositing the CdTe, they carried out the TA step, followed by 30–40 min at 300 °C with and without a Te overpressure. From PL, the authors estimate a QD areal density of 10^{10} cm^{-2}.[311] The same team reported CdTe QDs in barriers of quasi-quaternary ZnMgSeTe in the form of short period superlattice (SL) ZnTe/MgTe/MgSe with 2 nm periods. The structures are composed of 5 ML ZnTe and a 150 nm short period ZnTe/MgTe/MgSe SL, followed by 3 ML CdTe QD layers separated by 3 ML ZnTe spacers, and a 45 nm top barrier consisting of another ZnTe/MgTe/MgSe SL.[312]

2.6 Tensile-Strained Quantum Dots

Research interest in tensile-strained self-assembly has grown steadily since around 2005.[17,313–316] Tensile strain occurs when the lattice constant of the QD material is smaller than that of the surrounding matrix. The lattice constant of most semiconductors

is inversely related to their bandgap (Figure 2.7). Correspondingly, the QD and matrix materials must be selected carefully to achieve quantum confinement. However, this constraint imposed by the limited number of suitable QD-matrix band alignments is relaxed somewhat by the fact that tensile strain has the opposite effect to compressive strain and serves to reduce the bandgap energy (Figure 2.8(c)). Light emitted or absorbed by tensile-strained QDs is hence red-shifted, and as a result, they are optically active below the effective bandgap of the corresponding unstrained material.[22,23,25] In addition, tensile strain pushes the light-hole band above the heavy-hole band (Figure 2.8(c)). The possibility of QDs that naturally exhibit a light-hole exciton ground state is extremely attractive for quantum media conversion and other applications.[317,318]

To ensure defect-free self-assembly, researchers typically grow tensile-strained QDs on (110) and (111) substrates instead of (001).[19] The characteristics of these non-traditional surface orientations give tensile-strained QDs some unusual properties. For example, under sufficient tensile strain, Ge on a (110) surface orientation should become a direct bandgap semiconductor useful for light-emitting infrared devices.[4,6,8,9] (111)-oriented QDs are widely expected to exhibit low fine-structure splitting.[9,139–141,145,160] As we discuss in Section 2.2.3, low fine-structure splitting is essential if a QD is to be used as a source of entangled photons for quantum information applications.

That being said, the growth of high-quality buffers on (110) and (111) surfaces is notoriously difficult. Researchers have invested considerable effort to identify MBE conditions that produce smooth buffer surfaces required for subsequent growth of tensile-strained QDs.[19,21,22,25,26,52,319,320] As a direct result of these efforts, research into tensile-

strained QDs is growing quickly. The relative youth of this field means that there is a great deal still to discover.

2.6.1 GaAs on InAlAs(110) and (111)A

As noted above, self-assembled GaAs QDs with a (111)A orientation exhibit a low fine-structure splitting, suitable for entangled photon emission via the biexciton–exciton cascade.[23] Because of the low bandgap, tensile strain, and type-I band alignment in this system, these QDs on both (111) and (110) substrate orientations could also be used for near-IR optoelectronics.[21–23,154,321] Additionally, the GaAs/InAlAs(111)A QD system presents an unusual opportunity to tune the wetting layer thickness beyond the critical thickness.[23,154]

GaAs(111)A QDs are grown on nominally on-axis InP(111)A substrates, where the tensile lattice mismatch is 3.7% (Figure 2.17).[21,23,154,321] The native oxide is removed by heating the InP substrate to 510 °C for 15 min under an As_4 flux.[26] The substrate temperature is then slightly adjusted to 495–510 °C for the buffer growth.[21,23,26,154,321] A 50 nm $In_{0.53}Ga_{0.47}As$ (hereafter simply InGaAs) buffer is deposited, which promotes surface smoothing.[52] This is followed by 200 nm $In_{0.52}Al_{0.48}As$ (hereafter simply InAlAs) for the bottom barrier. Both the InGaAs and InAlAs are grown at a rate of ~170 nm/h with a high V/III flux ratio of ~160.[21,23,26,154,321]

The substrate is then brought to the desired QD growth temperature, typically between 460 and 540 °C.[21,23,154,321] The As valve is partially closed to reduce the V/III flux ratio to ~75, and GaAs is deposited at a rate of 0.025–0.125 ML/s.[21,23,154,321] The critical thickness for the 2D-to-3D SK transition is 2.5 ML.[21,154] This critical thickness is determined by AFM since the streaky (2 × 2) RHEED pattern does not change during

GaAs deposition.[21,154] We believe that the combination of a low areal density (10^8–10^9 cm^{-2}) and a small height (typically <2 nm) of the QDs means that the interaction between the electron beam and the GaAs in the QDs is insufficient to generate a spotty pattern.

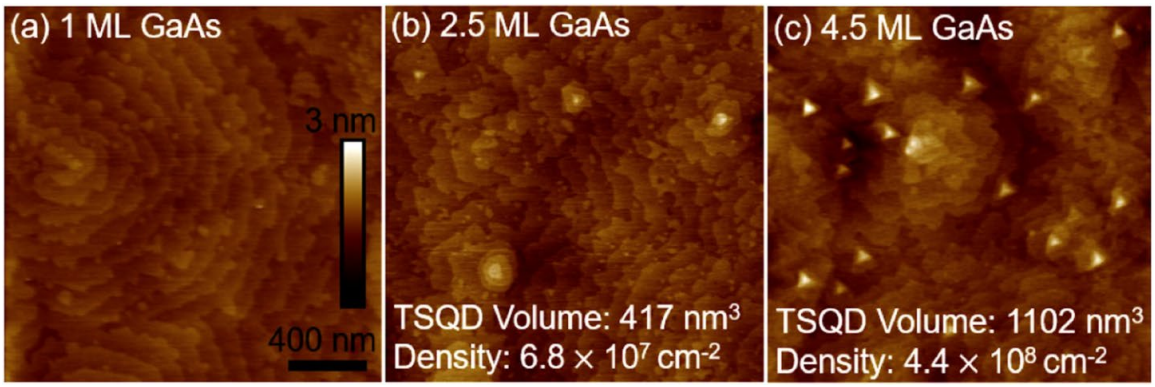

Figure 2.17 2 × 2 µm² AFM images revealing the evolution of GaAs(111)A TSQD morphology with increasing deposition: (a) 1 ML GaAs showing the smooth 2D wetting layer, (b) 2.5 ML GaAs showing the onset of 3D TSQD self-assembly, and (c) 4.5 ML GaAs showing mature TSQD formation. Reprinted from Schuck *et al.*, Sci. Rep. 9, 1–10 (2019). Copyright 2019 Springer Nature.[154]

The streaky RHEED pattern of the smooth tensile-strained GaAs wetting layer between the QDs, therefore, dominates.[21,154]

The QDs are covered by 10 nm of InAlAs, grown at the QD growth temperature.[21,23,154,321] The growth is then interrupted and the substrate is heated back to 495–510 °C to grow the rest of the InAlAs top barrier (another 30–40 nm).[21,23,154,321] The sample is typically completed by growing another layer of GaAs QDs on the surface for morphology studies or with a 5–10 nm InGaAs cap to prevent oxidation of the InAlAs top barrier.[21,23,154,321]

For tensile-strained GaAs(110) QDs, a nominally on-axis InP(110) substrate is degassed at 500 °C for 30 min under an As_4 over-pressure.[22] The substrate temperature is decreased to 300 °C, and 200 nm InAlAs is deposited at 0.5 µm/h, with a V/III flux ratio

of 80.[22] The substrate is then annealed at 500 °C for 15 min.[22] Once the buffer is annealed, GaAs is deposited at 0.1 ML/s, with a V/III flux ratio of 65.[22] The critical thickness for the 2D-to-3D transition is 1.6 ML, which again is established with AFM since the streaky (1 × 1) RHEED pattern of the unreconstructed (110) surface does not change during GaAs deposition [see the discussion of GaAs(111)A QDs above].[22] To cap the QDs, the substrate is cooled back to 300 °C to grow the top InAlAs barrier under an As_4 flux.[22] We recommend a cap thickness of >50 nm, and if not depositing surface QDs, the growth of a thin, 5–10 nm InGaAs cap is to prevent oxidation of the InAlAs top barrier.[22]

2.6.2 Ge on InAlAs(111)A

Recently, researchers have developed a method of growing tensile-strained Ge QDs within an $In_{0.52}Al_{0.48}As$(111)A matrix lattice-matched to InP (Figure 2.18).[26] For a (111) substrate orientation, the 3.7% tensile lattice mismatch between Ge and InP is expected to reduce Ge's bandgap to zero, transforming this well-known semiconductor into a semimetal.[322] Semimetallic Ge(111) QDs could be useful for high-efficiency solar cell tunnel junctions, thermoelectric materials, or even as a novel route to topological insulators.[10,102–104] Unusually, researchers are able to select either SK or VW for tensile-strained Ge QD self-assembly, simply by controlling the substrate temperature.[26]

After removing the InP(111)A oxide, an InGaAs smoothing layer is grown, followed by an InAlAs bottom barrier (see Section 2.6.1).[26] The substrate temperature is then adjusted to 435–560 °C for Ge QD growth, before closing the As valve and shutter.[26] After waiting 60 s for the As overpressure to reduce, they deposited 0.2–1.2

bilayers (BL) of Ge at 0.010–0.025 BL/s.[26] Upon deposition, the RHEED pattern swiftly develops from streaky (2 × 2) to spotty, indicative of 3D self-assembly.[26]

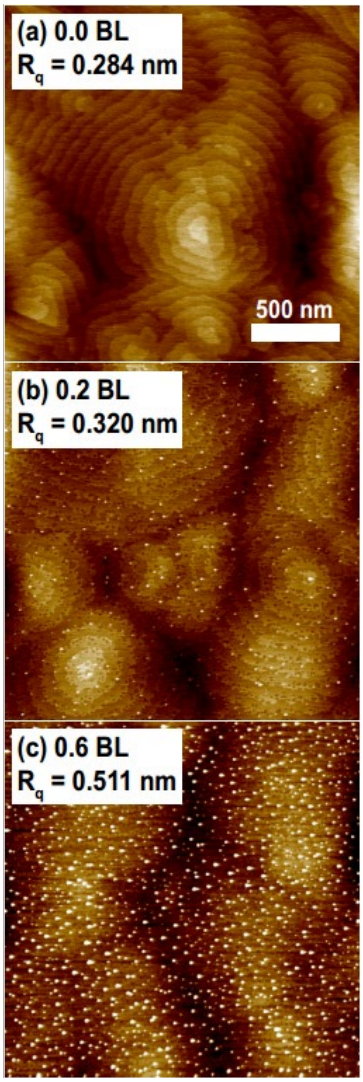

Figure 2.18 2 × 2 μm² AFM images showing the evolution of Ge(111)A TSQD morphology with increasing deposition: (a) 0 BL Ge, i.e., the bare InAlAs(111)A surface, (b) 0.2 BL Ge, and (c) 0.6 BL Ge. The z-scalebar is 2 nm for all images. Reprinted with permission from Sautter *et al.*, J. Cryst. Growth 533, 125468 (2020). Copyright 2020 Elsevier.[26]

Ge QDs grown at substrate temperatures below 510 °C self-assemble via the SK growth mode. An initial 2D wetting layer forms, with a critical thickness for the 2D to 3D transition of 0.6 BL at 435 °C. The critical thickness decreases as the substrate

temperature is raised, until at ≥510 °C, the Ge QDs self-assemble via the VW growth mode (i.e., the critical thickness of 0 BL).[26] After Ge QD growth, the substrate is heated to ~500 °C to grow the top InAlAs barrier, followed by a 5 nm InGaAs cap (if not growing a surface layer of QDs for AFM).[26] A follow-up study of Ge QD self-assembly on InAlAs(110) is under way, for which the InAlAs/InGaAs buffer conditions will be similar to those discussed in Section 2.6.1.

2.6.3 Additional Tensile-Strained Self-Assembly Systems

Although this section discusses self-assembly, not all of the resulting 3D nanostructures are optically active. Some are composed of indirect bandgap semiconductors. For others, the nanostructure bandgap is larger than that of the surrounding matrix, preventing carrier confinement and hence light emission. As a result, they cannot be considered true QDs; therefore, we instead describe them as "nanostructures."

We include this section for historical and practical reasons since the studies described below typically discuss not only how to grow the tensile-strained nanostructures but also the smooth buffer surfaces beneath. These buffers include materials such as Ge(111), GaAs(110), and GaAs(111). Interest in semiconductor systems with non-(001) orientations is growing,[52] and these materials could represent useful starting points from which to investigate new tensile-strained QD systems.

Si on Ge(111) was one of the earliest tensile-strained systems investigated. Researchers demonstrated the self-assembly of tensile-strained defect-free Si nanostructures.[227] They start with 40 nm Ge at 380 °C, followed by 40 nm $Ge_{0.85}Si_{0.15}$ at 500 °C. The substrate is heated to 450–650 °C for Si deposition. After deposition, the

substrate is immediately cooled. The resulting defect-free Si(111) nanostructures form via the VW growth mode, with tunable size and areal density.

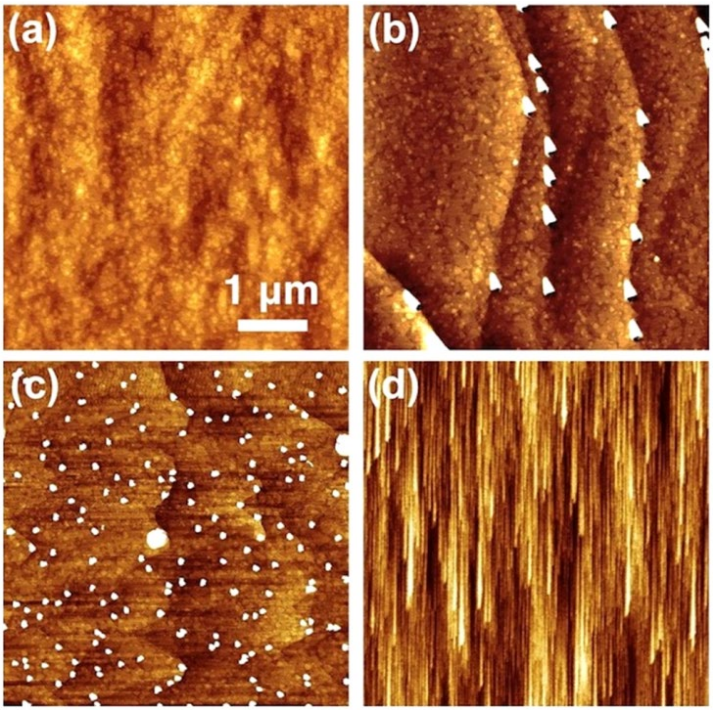

Figure 2.19 5 × 5 μm^2 AFM images showing the results of growing (a) a 4.5 ML GaP film on GaAs(001) (3 nm z-scale), (b) 4.2 ML GaP QDs on GaAs(110) (3 nm z-scale), (c) 1.7 ML GaP QDs on GaAs(111)A (5 nm z-scale), and (d) 3.9 ML GaP QWrs on GaAs(111)B with a 2 miscut (5 nm z-scale). Reprinted with permission from Simmonds and Lee, J. Appl. Phys. 112, 054313 (2012). Copyright 2012 AIP Publishing LLC.[19]

Building on that early report, Simmonds and Lee moved to III–V semiconductors to carry out a comprehensive investigation into the relationship between surface orientation and a sign of strain sign (Figure 2.19).[17–19] They showed that both factors must be considered to predict whether strain relief is elastic (i.e., via 3D nanostructure formation) or plastic (i.e., via dislocation nucleation and glide).[17–19] The result of their study was to predict that defect-free, tensile-strained nanostructures would self-assemble, as long as they were grown on either (110) or (111)-oriented substrates.[17–19]

To test this prediction, they focused on the growth of GaP on GaAs, which experiences a tensile lattice mismatch of 3.7%.[17–19] They showed that when GaP is grown on GaAs(001), the tensile strain is relieved plastically and self-assembly does not occur. However, when GaP is grown on GaAs(110) or (111) surfaces, the tensile strain is relieved elastically, and defect-free 3D GaP nano-structures self-assemble via the VW growth mode.[17–19] Although optically inactive due to GaP's indirect bandgap, the spontaneous formation of these tensile-strained nanostructures confirmed the model's prediction. This result provides a deeper understanding of QD self-assembly: namely, that we can grow QDs with either compressive or tensile strain, provided we select the correct substrate orientation.

For GaP/GaAs(110) nanostructures, the GaAs(110) substrate is first degassed at 610 °C for 20 min under an As_4 overpressure.[17,19] For the GaAs(110) homoepitaxial buffer, the substrate temperature is reduced to 540 °C. The buffer is typically 60 nm thick and is grown at 0.45 μm/h with a relatively high V/III flux ratio of 75.[17,19] The buffer is then annealed for 15 min at 600 °C to promote surface smoothing.[17,19] For GaP/GaAs(111)A nanostructures, the GaAs(111)A substrate is first degassed at 630 °C for 30 min under an As_4 overpressure, and then the substrate temperature is reduced to 540–600 °C for homoepitaxial buffer growth.[18,19] The GaAs(111)A buffer is grown under a V/III flux ratio of 70 and a growth rate of 0.45 μm/h.[18,19] After depositing ~60 nm GaAs(111)A, the substrate is annealed at 640 °C under an As_4 overpressure for 15 min to promote surface smoothing.[18,19]

Both surface orientations use similar GaP growth conditions. After annealing the buffer surface, the substrate temperature is reduced to grow the GaP nanostructures,

typically between 460 and 580 °C, under an As_4 overpressure.[17–19] Once at the desired QD growth temperature, the As valve is closed for 20 s to reduce anion mixing, before opening the Ga and P_2 sources to deposit the GaP.[17–19] 0.2–6.4 ML of GaP is deposited at

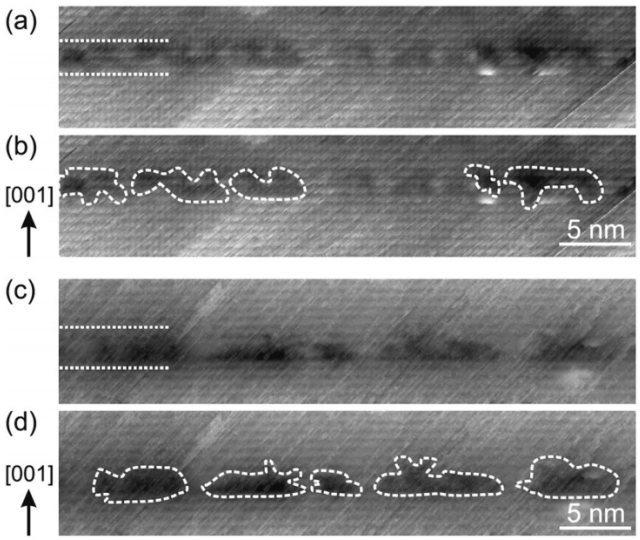

Figure 2.20 Cross-sectional scanning tunneling microscope (XSTM) images of (a) and (b) 1 ML and (c) and (d) 2 ML GaAs/GaSb(001) QDs. (a) and (b) Empty-state and (c) and (d) filled-state XSTM images. In (a) and (c), the height of the GaAs containing layer is indicated by the dotted lines; in (b) and (d), the GaAs nanostructures are indicated by dashed lines. Reprinted with permission from Lenz *et al*., Appl. Phys. Lett. 102, 102105 (2013). Copyright 2013 AIP Publishing LLC.[316]

0.014–0.142 ML/s, with a V/III flux ratio of 10–12.[17–19] Since these nanostructures were mainly used for surface studies, the substrate was then immediately cooled under a P_2 overpressure.[17–19]

A small number of other studies exist in which researchers have explored the use of tensile strain to drive nanostructure self-assembly by MBE. Toropov *et al*. and Meltser *et al*. demonstrate the growth of GaAs/GaSbAs(001) QWs with a 7.5% tensile lattice mismatch. QDs form spontaneously within these QWs as a result of compositional inhomogeneities.[313,314] Taliercio *et al*. demonstrated $In_xGa_{1-x}As$/GaSb(001) quantum wells with some signs of QD formation.[315] Lenz *et al*. studied GaAs/GaSb(001) tensile-

strained nanostructures using cross-sectional scanning tunneling microscopy and showed that tunable, defect-free self-assembly is possible in that system (Figure 2.20).[316] Zhang *et al*. and Huo *et al*. demonstrated Ge(001) QDs grown on various III–V semiconductors, but either did not show if these QDs were defect-free[279] or found that there was anti-phase disorder in the capping layer.[323] Pachinger *et al*. demonstrated Si QDs grown on Ge(001), but these QDs were dislocated.[88] All of these examples demonstrate the breadth of research into developing new, tensile-based QDs for a range of future technologies.

2.7 Conclusions

In this tutorial, we have explored the mechanisms, materials systems, and applications of semiconductor QDs grown by MBE using strain-driven self-assembly. We outlined the history of this field, from the earliest attempts at creating 3D QWs, right up to highly symmetric QDs designed specifically for future quantum information applications. There has been enormous progress made over the last 30 years, but new developments, such as the development of tensile-strained self-assembly, continue to push this important field forward. We hope that this tutorial will serve as an incomplete but useful guide. Perhaps collating some of the most frequently used MBE conditions for QD growth in one place will contribute to future efforts to create novel self-assembled QDs, with unique properties, for new applications.

Authors' Contributions

K.E.S. and K.D.V. contributed equally to this work.

Acknowledgements

Some of the results discussed here are based upon work sup-ported by the National Science Foundation under NSF CAREER Grant No. 1555270 and by the Air Force Office of Scientific Research (AFOSR) under Award No. FA9550-16-1-0278.

Data Availability

The data that support the findings of this study are available from the corresponding author upon reasonable request.

CHAPTER THREE: SELF-ASSEMBLY OF TENSILE-STRAINED Ge QUANTUM DOTS ON InAlAs(111)A

Kathryn E. Sautter,[1,a)] Christopher F. Schuck,[1] Trent A. Garrett,[2] Ariel E. Weltner,[1] Kevin D. Vallejo,[1] Dingkun Ren,[3] Baolai Liang,[4] Kevin A. Grossklaus,[5] Thomas E. Vandervelde,[5] and Paul J. Simmonds[1,2,a)]

[1] Micron School of Materials Science & Engineering, Boise State University, Boise, ID, 83725 USA

[2] Department of Physics, Boise State University, Boise, ID, 83725 USA

[3] Department of Electrical Engineering, University of California, Los Angeles, CA 90095 USA

[4] California NanoSystems Institute, University of California, Los Angeles, CA 90095 USA

[5] Department of Electrical and Computer Engineering, Tufts University, Medford, MA 02155 USA

a) Corresponding authors: katiesautter@boisestate.edu, paulsimmonds@boisestate.edu

Reproduced from K.E. Sautter, C.F. Schuck, T.A. Garrett, A.E. Weltner, K.D. Vallejo, D. Ren, B. Liang, K.A. Grossklaus, T.E. Vandervelde, and P.J. Simmonds, J. Cryst. Growth **533**, 125468 (2020), with the permission of Elsevier publishing.

https://doi.org/10.1016/j.jcrysgro.2019.125468

Abstract

A recently developed growth technique enables the self-assembly of defect-free quantum dots on (111) surfaces under large tensile strains. We demonstrate the use of this approach to synthesize germanium (Ge) quantum dots on $In_{0.52}Al_{0.48}As$(111)A with >3% residual tensile strain. We show that the size and areal density of the tensile-strained Ge quantum dots are readily tunable with growth conditions. We also present evidence for an unusual transition in the quantum dot growth mode from Stranski-Krastanov to Volmer-Weber as we adjust the substrate temperature. This work positions Ge quantum dots as a promising starting point for exploring the effects of tensile strain on Ge's band structure.

3.1 Introduction

Germanium (Ge) is an indirect band gap semiconductor that plays a pivotal role in today's electronics industry. However, theory predicts that tensile strain should cause dramatic changes to Ge's band structure, opening up new possibilities for electronic and optoelectronic applications.[4,6,8,9,11,322] Of particular note is the prediction that for Ge with a (111) crystallographic orientation, ~4% biaxial tensile strain should shrink the band gap to zero, transforming Ge from a semiconductor into a semimetal.[4,8,322,324] High-quality semiconductor materials with a (111) crystallographic orientation are growing in demand, offering unique characteristics that are highly relevant to a range of applications from quantum optics to topological insulators.[23,325–327] Transforming the fundamental properties of a material as widely used as Ge would be in and of itself interesting. However, the ability to create functionalized (111)-oriented heterostructures by embedding semimetallic materials within semiconductor matrices could be useful in areas

ranging from solar cells to thermoelectrics.[102–104] Zero band gap Ge could even have implications for future topological materials based on conventional semiconductors.[10]

As a result of these predictions, researchers have hence explored various approaches to induce tensile strain in Ge, ranging from mechanical stress, to self-assembled Ge nanostructures.[12–16,279,323] As a result, tensile strains as large as 3.8% have been achieved in Ge, leading to the observation of some of the predicted changes in band structure.[13] However, these activities have been almost exclusively limited to (001)-oriented Ge, such that tensile-strained Ge with a (111) orientation remains unexplored. To facilitate research in this area, what is first required is a robust method by which we can synthesize defect-free Ge under large tensile strains on (111)-oriented substrates.

In recent years, tensile-strained self-assembly has been established as a scalable, one-step technique for the growth of tensile-strained quantum dots (TSQDs) by molecular beam epitaxy (MBE).[17–19] The specific combination of tensile strain and a (111) or (110) surface orientation creates an energetic barrier to plastic strain relief by dislocation nucleation and glide.[17,19,21] As a result, a window exists within which elastic strain relief by the self-assembly of dislocation-free 3D islands (TSQDs) can take place. This situation is analogous to the well-known self-assembly of compressively strained QDs on (001) surfaces.[81,254,277] We have previously used this process to synthesize defect-free GaAs TSQDs under 3.7% tensile strain on $In_{0.52}Al_{0.48}As$(111) and (110) surfaces.[21–25] These GaAs TSQDs are optically active, with properties that are readily tunable with MBE growth parameters.[21–24,82]

In this paper, we adapt tensile-strained self-assembly to enable the growth of defect-free Ge nanostructures on InAlAs(111)A. Crucially, the model for tensile-strained

self-assembly is expected to apply to both zinc-blende (e.g., GaAs) and diamond-cubic (e.g., Ge) semiconductors.[19] Since GaAs and Ge have similar lattice constants, substituting Ge for GaAs in the InAlAs-based material system described above should be a direct replacement, at least from the point of view of the tensile strain. We discuss the role that the MBE growth parameters play in controlling the size and areal density of the Ge TSQDs. We also present evidence for a rarely observed transition between the Stranski-Krastanov (SK) and Volmer-Weber (VW) growth modes for TSQD self-assembly with increasing substrate temperature. Robust control over TSQD synthesis establishes these nanostructures as a useful basis for future studies of tensile-strain-engineered Ge.

3.2 Methodology

We used solid-source MBE to grow several series of Ge/$In_{0.52}Al_{0.48}As$/InP(111)A samples under different growth conditions. The InP(111)A substrates were Fe-doped and nominally on-axis (±0.5°). We used standard effusion cells for the ultra-high purity Al, Ga, In, and Ge, and a valved-source for the As_4 with the cracker set to 600 °C. We determined the substrate temperature (T_{SUB}) with a pyrometer and a thermocouple calibrated against known changes in surface reconstruction, observed with reflection high-energy electron diffraction (RHEED). We used a flux monitor to measure the beam equivalent pressure (BEP) for each source at the substrate position.

We found the Al, Ga, and In growth rates using RHEED intensity oscillations, and calibrated ternary alloy compositions using *ex situ* x-ray diffraction. We calibrated Ge growth rate using transmission electron microscopy (TEM) to measure the thicknesses of Ge layers grown for one hour at different cell temperatures.

For sample growth, we removed the substrate surface oxide by heating in the growth chamber at T_{SUB} = 510 °C for 15 min under an As_4 BEP of 1.5×10^{-5} Torr. We reduced T_{SUB} to 495 °C and grew a 50 nm $In_{0.53}Ga_{0.47}As$ (hereafter InGaAs) smoothing layer,[52] followed by a 200 nm $In_{0.52}Al_{0.48}As$ (hereafter InAlAs) bottom barrier, at growth rates of 169 nm/hr. and 175 nm/hr., respectively. We adjusted T_{SUB} to 435–560 °C, closed the As_4 valve and shutter, waited for 60 s, and deposited 0.2–1.2 bilayers (BL) of Ge at growth rates from 0.010–0.025 BL/s. We then either immediately cooled the Ge layer or buried it with a 20 nm InAlAs top barrier, finishing with a 5 nm InGaAs cap to prevent oxidation.

For each T_{SUB} value of 435, 460, 485, 510, 535, and 560 °C, we grew samples with 0.2, 0.4, 0.6 and 1.2 BL of Ge at 0.020 BL/s, to create a 6 × 4 sample matrix. We also grew two additional samples with 0.9 BL Ge at 435 °C and 460 °C to add detail in key areas.

From atomic force microscopy (AFM) scans, we extracted the root-mean-square roughness (R_q) of the uncapped Ge, as well as the heights, diameters, and areal densities of any nanostructures. We mapped the crystal and compositional structure of our samples using scanning TEM (STEM) with electron energy loss spectroscopy (EELS) and energy-dispersive x-ray spectrometry (EDS). We used ImageJ and NanoScope software to analyze EELS maps and AFM images respectively. To measure residual tensile strain in the Ge TSQDs using Raman spectroscopy, we grew a sample at 535 °C containing four layers of 0.6 BL TSQDs separated by 20 nm InAlAs barriers. Taking care to minimize sample heating, we compared Raman spectra from this four-layer Ge/InAlAs TSQD

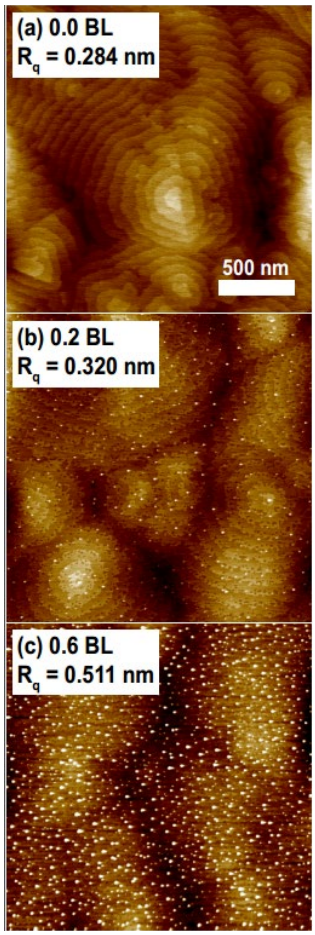

Figure 3.1 2×2 µm^2 AFM images showing evolution of InAlAs(111)A surface morphology and RMS roughness (R_q) with increasing Ge deposition: (a) 0 BL Ge (i.e. InAlAs(111)A buffer), (b) 0.2 BL Ge, and (c) 0.6 BL Ge. Ge deposition rate = 0.020 BL/s, and T_{SUB} = 535 °C. The z-scalebar is 2 nm.

sample to those from two bulk InAlAs(111)A control samples: one uncapped, and one with a 10 nm InGaAs cap.

3.3 Results & Discussion

TSQDs form spontaneously when Ge is deposited onto InAlAs(111)A. Prior to Ge deposition, the InAlAs(111)A buffer surfaces (i.e. 0 BL Ge) are smooth, with monolayer-high steps and R_q = 0.28 nm (Figure 3.1(a)). Once we start to deposit Ge at T_{SUB} = 535 °C, the surface morphology changes abruptly. Upon opening the Ge shutter, the (2 × 2) InAlAs(111)A RHEED pattern changes to (1 × 1), followed rapidly by the

appearance of a bright spotty pattern. AFM reveals 3D Ge TSQDs distributed across the surface, with average height 1.81 ± 0.39 nm (Figure 3.1(b)). Analysis of AFM images such as Figure 3.1(b) shows that more than 80% of Ge TSQDs nucleate at step edges as opposed to on the terraces. As we raise the Ge deposition amount to 0.6 BL, R_q increases from 0.32 nm to 0.51 nm (Figure 3.1(c)), accompanied by an increase in the areal density and size of the Ge TSQDs, with average height 2.21 ± 0.54 nm (Figure 3.1(b),(c)).

High-resolution TEM imaging, combined with STEM/EELS compositional mapping, confirms the presence of discrete, dislocation-free Ge TSQDs embedded within the InAlAs matrix (Figure 3.2 (a),(b)). A survey of multiple Ge TSQDs suggests that 80–85% are dislocation-free, and hence coherently tensile-strained to the InAlAs (Figure 3.5). We do see some evidence of defects in regions of the InAlAs cap, including triple-period ordering, dislocations, twinning, and stacking faults. However, unlike growth of III-Vs on (001)-oriented Ge, we do not see antiphase domains at the non-polar/polar interface.[57,328] Atomic steps that are an odd number of atomic layers high are energetically very unfavorable on a (111) surface, and so antiphase domains are not expected to form.[59] Future work will focus on optimizing nucleation of the InAlAs above the Ge TSQDs.

The EELS maps in Figure 3.2(b) and Figure 3.5 reveal no sign of a Ge wetting layer beneath the TSQD. Diffusion of the Ge from the TSQDs into the surrounding InAlAs also appears to be negligible. Taking profiles through the EELS map in Figure 3.2(b), we determine a TSQD height of 3.2 ± 0.4 nm and diameter of 16.7 ± 1.0 nm (Figure 3.2(c),(d)). These values are similar to AFM profiles of representative uncapped

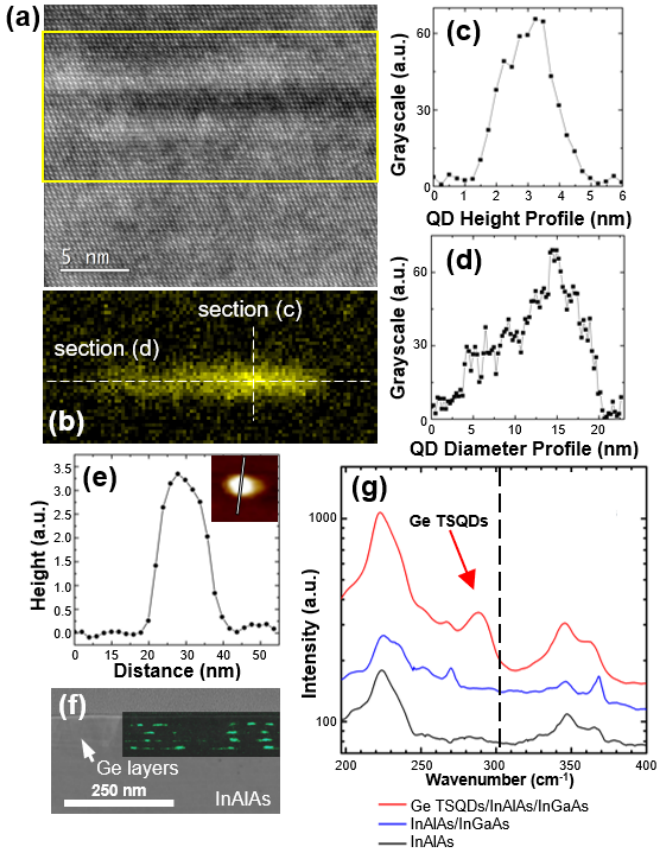

Figure 3.2 (a) Annular dark field STEM image of an individual, capped Ge TSQD. (b) an EELS map of the Ge L signal corresponding to the region enclosed by the yellow box in (a). (c) and (d): grayscale profiles showing TSQD height (c) and diameter (d) cross-sections along the dashed lines on the EELS map in (b). (e) AFM cross-section of a representative Ge TSQD on an InAlAs surface (Inset: the 50 nm × 50 nm AFM image of the TSQD shows the location of the cross-sectional profile (z-scalebar = 4.3 nm)). (f) TEM image overlaid with an EDS elemental map of the Ge Kα1 line. (g) Raman spectra of bulk InAlAs(111)A (black), InAlAs(111)A capped with InGaAs (blue), and InAlAs(111)A containing Ge TSQD layers and capped with InGaAs (red). The black dashed line shows the position of the LO phonon line for unstrained, bulk Ge(111). All samples in this figure were grown from 0.6 BL at 535 °C, with a growth rate of 0.02 BL/s.

TSQDs (Figure 3.2(e)): height = 3.4 ± 0.3 nm; diameter = 18±1 nm. These results suggest minimal alloying of the Ge TSQDs with the surrounding InAlAs matrix.

Figure 3.2(f) shows a TEM image of a sample containing four stacked layers of Ge TSQDs. Consistent with EELS, an EDS elemental map (Figure 3.2(f) inset) shows discrete Ge TSQDs. EDS also reveals vertical alignment of the Ge TSQDs in consecutive

layers. The tensile strain field surrounding each Ge TSQD enhances the probability of another TSQD nucleating directly above it in the next layer, a well-known effect in compressively strained QD systems.[329] This observation provides additional confirmation that the Ge TSQDs are coherently tensile-strained to the InAlAs matrix.

To quantify the amount of tensile strain within the Ge TSQDs, Figure 3.2(g) compares the Raman spectrum from the sample in Figure 3.2(f) with those from InAlAs control samples. The InAs phonon lines at 220 cm^{-1} (TO_1) and 237 cm^{-1} (LO_1), and the AlAs phonon lines at 347 cm^{-1} (TO_2) and 369 cm^{-1} (LO_2), are common to the Raman spectra from all samples (Figure 3.2(g)).[330] The samples containing InGaAs also show InAs-like LO and GaAs-like TO lines at 251 cm^{-1} and 268 cm^{-1} respectively.[331] Unique to the Ge TSQD Raman spectrum is the feature at 288.4 cm^{-1}, corresponding to the LO phonon line of the Ge TSQDs. This line is shifted from 302.4 cm^{-1} where we observe the LO phonon for bulk, unstrained Ge(111) (dashed line). From this Raman shift of –14.0 cm^{-1}, we calculate the tensile strain in the Ge TSQDs to be 3.38 ± 0.36% using a value of –415 ± 40 cm^{-1} for the phonon strain-shift coefficient.[45] Although this calculated tensile strain is a little lower than the 3.7% lattice mismatch between Ge and $In_{0.52}Al_{0.48}As$, they agree to within error. The most likely causes of any discrepancy are elastic strain relief in the Ge TSQDs, and typical run-to-run variations in the composition of the InAlAs layers used in the Raman sample. The asymmetric broadening of the Ge TSQD line towards lower wavenumbers (Figure 3.2(g)) is observed in the Raman spectra of other QD systems, including strain-free Ge QDs, and compressively strained InAs QDs.[16,332] These asymmetric phonon line shapes derive from optical phonon confinement in arrays of QDs with a finite size distribution.[333–335]

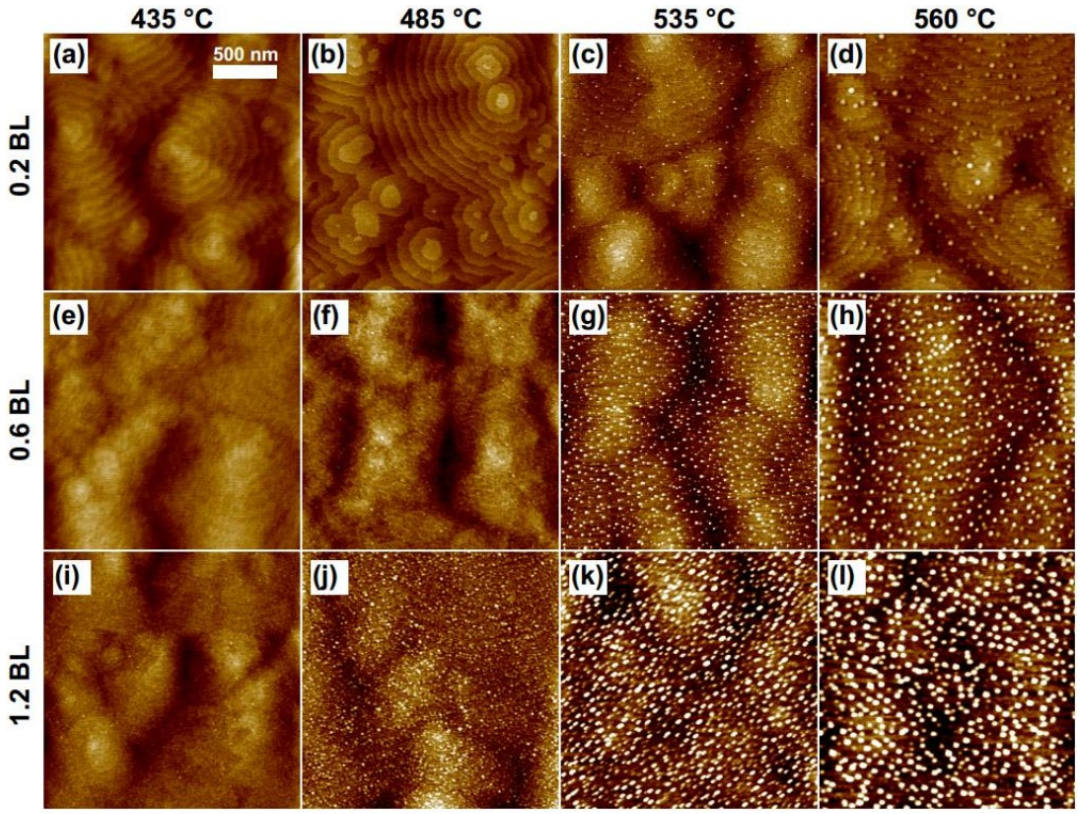

Figure 3.3 2×2 μm^2 AFM images demonstrating control of Ge TSQD size and density as a function of both Ge deposition amount (rows) and T_{SUB} (columns). All samples grown at 0.020 BL/s. The z-scalebar is 2 nm.

We can readily tune TSQD size and areal density by controlling T_{SUB} and Ge deposition during MBE growth. In the interest of space, Figure 3.3 shows only a subset of the full sample matrix. Each row shows the effect of raising T_{SUB}, while each column shows the effect of increasing Ge deposition. To avoid thermal degradation of the InAlAs, we were limited to $T_{SUB} < 560$ °C.

Surprisingly, Figure 3.3 reveals that there are two growth modes responsible for Ge TSQD self-assembly in this sample set. At $T_{SUB} = 435$ °C, there is no TSQD formation for ≤ 0.6 BL Ge (Figure 3.3(a),(e)), indicating that Ge initially grows as a 2D wetting layer. However, for deposition ≥ 0.9 BL, the Ge self-assembles into 3D TSQDs (Figure 3.3(i)). This 2D-to-3D growth transition is consistent with the SK growth mode.

Barabási suggests that there are two kinds of SK growth depending on whether growth is thermodynamically or kinetically limited.[78] The far-from-equilibrium nature of MBE means we observe the kinetically limited version of SK growth here. As T_{SUB} is increased to 485 °C, we again see TSQD self-assembly via the SK mode with a transition from 2D growth (Figure 3.3(b)) to 3D growth (Figure 3.3(f)) as deposition is increased. Interestingly, the critical thickness of 0.6 BL for the 2D-to-3D SK transition is lower than at 435 °C. This observation is consistent with previous studies, which showed reduced SK critical thickness for increased adatom diffusion length:[69,336,337] in our case, by increasing T_{SUB}. From the areal density and average TSQD volume, we calculate that in Figure 3.3(f) only 0.61±0.24% of the total 0.6 BL Ge deposited is contained within the TSQDs, with the remainder in the wetting layer. We therefore estimate the wetting layer is ~0.596 BL thick, and since this value is >0.5 BL (i.e. 1 ML), we conclude that the wetting layer is continuous over the surface, consistent with SK growth.

In contrast, for $T_{SUB} \geq 510$ °C, we see TSQD formation after deposition of just 0.2 BL Ge (Figure 3.3(c),(d)), which is insufficient for a continuous wetting layer to form. Immediate TSQD self-assembly in the absence of a wetting layer indicates that for $T_{SUB} \geq 510$ °C, growth proceeds via the VW mode. Indeed, both EELS and EDS in different samples grown at $T_{SUB} = 535$ °C confirm the absence of a continuous Ge wetting layer (Figure 3.2 and Figure 3.5).

The ability to controllably change the growth mode from SK to VW is very unusual. Although theory predicts that a transition between SK and VW growth modes is possible,[78] experimental evidence is scarce. We have previously seen hints of a crossover from SK to VW growth during GaAs TSQD self-assembly.[21] Other researchers have used

substrate offcut angle to move from SK to VW self-assembly during growth of GeSi on Si(001), which is a function of surface free energy variations in the facets available at different angles.[244,246,247]

Whether self-assembly occurs via the SK or VW growth modes is due to the interplay between the strain and free surface energies of a particular QD material system.[68] For the Ge/InAlAs(111)A TSQD system, the tensile strain and surface energies of the InAlAs buffer and the Ge/InAlAs interface are constant regardless of T_{SUB}. It is therefore likely that, consistent with the case for offcut substrates,[247] the observed SK-to-VW transition is linked to the higher surface free energy of Ge crystal facets that become accessible when T_{SUB} increases.[245] Although outside of the scope of the work presented here, a future study using scanning tunneling microscopy will help clarify this point.

Figure 3.3 also provides some insight into the surface diffusivity of Ge adatoms on InAlAs(111)A. The fact that >80% of TSQDs form at step edges on the InAlAs(111)A surface (e.g. Figure 3.1(b), Figure 3.3(c),(d)) is often taken as a signature of a high adatom diffusion length.[19] The average InAlAs(111)A terrace width is 86 ± 13 nm, so to reach the nearest step edge, the average Ge adatom must diffuse a distance ≥43 ± 7 nm. However, we expect Ge adatom diffusion lengths to be greater than 50 nm. On Si(001) surfaces, Ge adatoms diffuse more than 2 μm,[338] a value that should be even higher on (111) surfaces that are known to have longer diffusion lengths than (001) surfaces.[339]

We therefore conclude that the Ehrlich-Schwöbel (ES) barrier limiting adatom migration between neighboring terraces of the InAlAs(111)A surface must be larger than the kinetic energy of the Ge adatoms over the range of T_{SUB} used here. Although values for the ES barrier on InAlAs(111)A are unavailable in the literature, it is known that ES

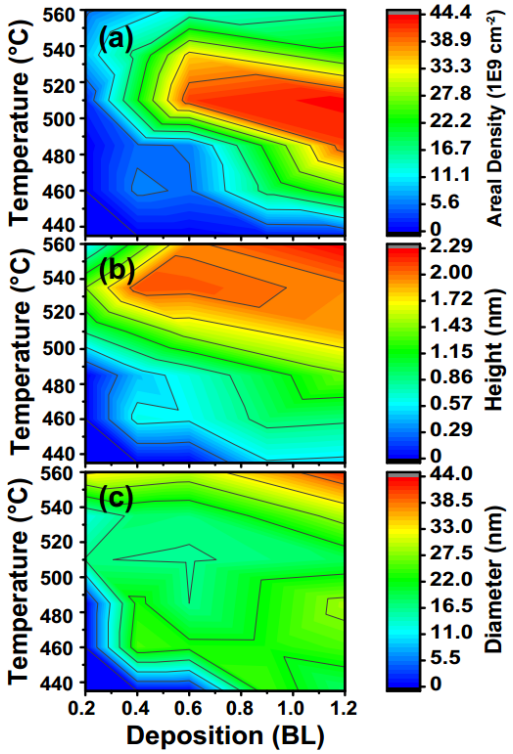

Figure 3.4 Contour plots summarizing changes in TSQD (a) areal density, (b) height, and (c) diameter as a function of Ge deposition amount and T_{SUB}.

barriers on (111)A surfaces of III-V compounds are typically large. A previous study estimated an ES barrier for Ga(Al)As(111)A of at least 100 meV.[340] We hence attribute the preferential nucleation of Ge/InAlAs(111)A TSQDs at step edges to a large ES barrier limiting Ge adatom diffusion.

2D contour plots of structural data from our 6×4 sample matrix reveal a local maximum in TSQD areal density for 0.6 BL Ge grown at T_{SUB} = 510–535 °C (Figure 3.4(a)). The local maximum for TSQD height occurs for 0.6 BL Ge grown at T_{SUB} = 535 °C (Figure 3.4(b)). As expected for mass conservation, we see a corresponding local minimum in TSQD diameter for 0.6 BL Ge grown at 510–535 °C (Figure 3.4(c)). If high-density, tall, narrow TSQDs are desirable, these growth conditions should be targeted.

The maximum areal density of 4.44×10^{10} cm^{-2} occurs for 1.2 BL Ge TSQDs grown at 510 °C.

At the highest values of T_{SUB} and deposition (upper righthand corners in Figure 3.4), there is a decrease in TSQD areal density, accompanied by a sharp increase in TSQD height and diameter to their maximum values over the range studied here. This behavior corresponds to Ostwald ripening of the TSQDs.[218] Raising T_{SUB} increases the Ge adatom diffusion length, allowing bigger TSQDs to grow at the expense of smaller ones nearby. This results in a lower density of larger Ge TSQDs that minimize the strain energy more efficiently than numerous small TSQDs.

We can also tailor TSQD self-assembly via the Ge growth rate. Holding total Ge deposition constant at 0.6 BL, we raised the Ge growth rate from 0.010 to 0.025 BL/s (Figure 3.6). TSQD areal density increases from 5.3 to 19.0×10^{9} cm^{-2}, with a simultaneous decrease in average TSQD diameter from 29.5 ± 4.3 to 23.1 ± 0.9nm, and a small increase in average height from 1.84 ± 0.46 to 2.59 ± 0.40 nm. Since adatom diffusion length decreases at higher growth rates, adatoms tend to cluster closer to where they land on the surface.[19,341] The result is a higher density of smaller dots.

The dependences of Ge TSQD size and areal density on the three MBE parameters explored here (T_{SUB}, deposition amount, and growth rate) are consistent with the self-assembly behavior of III-V QDs: both traditional compressively strained (001) QDs and tensile-strained QDs on (110) and (111) surfaces.[17–19,68] These similarities indicate that despite the introduction of Ge, a group IV semiconductor, the same physical processes underpin self-assembly. We can therefore apply the extensive body of

knowledge surrounding III-V QDs to hybrid group IV/III-V QD systems like this as we begin to develop them for specific applications.

3.4 Conclusions

We demonstrate the controllable growth of self-assembled Ge TSQDs on InAlAs(111)A. We can readily tune TSQD size and areal density in response to T_{SUB}, deposition amount, and growth rate. With Raman spectroscopy, we measure residual strains in the Ge TSQDs of 3.4% and observe indications of optical phonon confinement. We see compelling evidence for an unusual transition between the SK and VW growth modes for TSQD self-assembly. Self-assembly of Ge/InAlAs(111)A TSQDs provides the clearest evidence to date for a tunable transition between the SK and VW growth modes. The ability to select either the SK or VW growth mode for QD self-assembly, simply by controlling T_{SUB}, could be useful for certain applications. Its near ubiquity in III-V QD self-assembly means SK growth is very well-understood. On the other hand, VW growth eliminates the possibility of QD-wetting layer interactions,[342] while the lack of a wetting layer could help minimize antiphase disorder when capping Ge TSQDs with a III-V top barrier.[16] This work represents a robust starting point from which to use tensile-strained band engineering to investigate the transformation of Ge into a semimetal or direct band gap semiconductor.[4,324]

3.5 Supplemental Material

To explore the crystal quality of the Ge TSQDs we used a combination of (scanning) tunneling electron microscopy (S/TEM) and electron energy loss spectroscopy (EELS). Cross-sectional TEM (XTEM)-based analyses are time-consuming both in terms of sample preparation and imaging. However, for these samples that issue is compounded

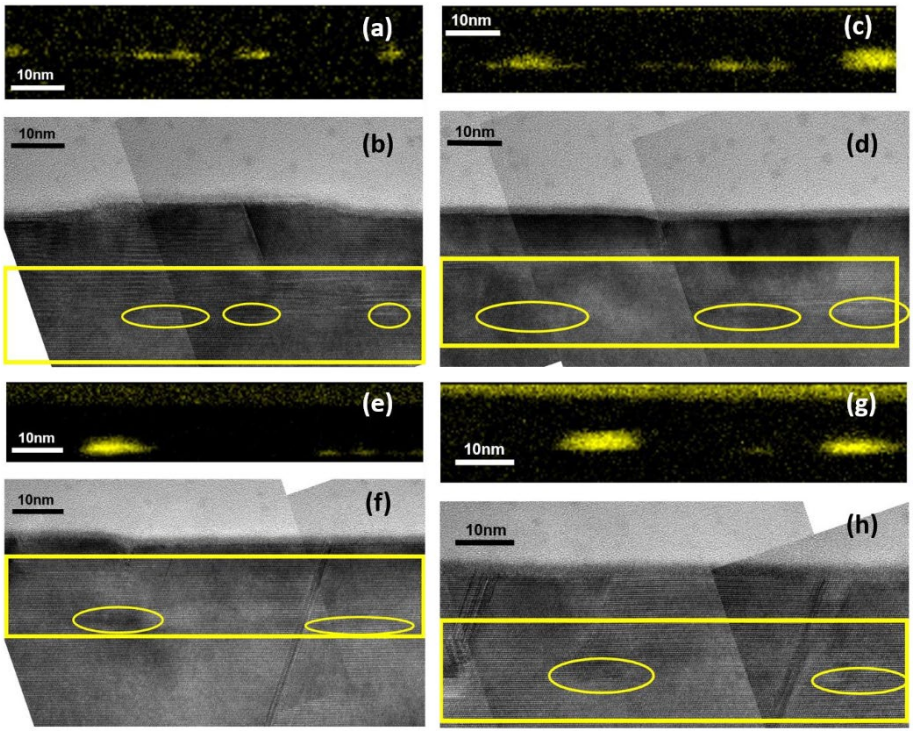

Figure 3.5 Analysis of Ge TSQD crystal quality using a combination of EELS maps of the Ge L signal ((a), (c), (e), and (g)) and corresponding BF TEM image montages in these same areas ((b), (d), (f), and (h)).

by the fact that the Ge TSQD areal densities are low (10^9 – 10^{10} cm^{-2}) and the field of view of each XTEM image is small, meaning that a large number of images are needed to capture enough TSQDs to say anything statistically meaningful. Furthermore, the Ge/InAlAs TSQDs show very low contrast relative to the InAlAs matrix in both bright-field (BF) TEM and annular dark-field (ADF) STEM, making it difficult to confirm the exact location of a TSQD without accompanying STEM/EELS compositional mapping. Once we had located a Ge TSQD in STEM/EELS, we then had to go back to that same location in the corresponding BF TEM image and look for evidence of dislocations or other defects in that region.

We examined 10–12 Ge TSQDs using this process of correlating QD locations in EELS mapping to BF TEM images. Uncertainty in the number of TSQDs is due to the

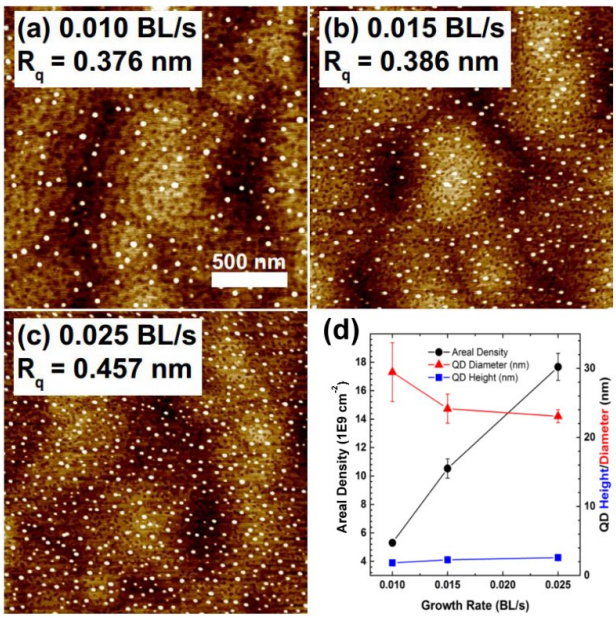

Figure 3.6 (a)–(c) 2 × 2 μm^2 AFM images showing evolution of Ge TSQD morphology and RMS roughness (R_q) with increasing Ge growth rate (0.6 BL Ge deposition; T_{SUB} = 535 °C). The z-scalebar is 1.5 nm. (d) Control of TSQD areal density, height, and diameter as a function of Ge growth rate.

close spacing of some of the TSQDs, which made it difficult to identify individual QDs. Figure 3.5 shows a representative subset of these: four BF TEM image montages and four corresponding Ge EELS maps. Of the 10–12 Ge TSQDs imaged, only two seemed to have linear defects originating in them (e.g., Figure 3.5(e)). This small survey suggests that 80–85% of Ge TSQDs are dislocation-free and are therefore coherently tensile-strained to the InAlAs(111)A matrix. Five of the Ge TSQDs surveyed overlap or are next to regions with triple-period (T-P) ordering in the InAlAs, but are not the obvious source that T-P ordering (e.g., Figure 3.5(a)). We notice that several of the Ge TSQDs are located close to through-stack threading dislocations originating in the InAlAs barrier below the TSQDs (e.g., Figure 3.5(f),(h)). The preferential location of TSQDs next to existing dislocations implies that localized strain compensation effects may increase the

probability of TSQD nucleation. This effect is consistent with the stacking of Ge TSQDs in consecutive layers that we see in Figure 3.2(f).

Acknowledgements

This material is based upon work supported by the Air Force Office of Scientific Research under award number FA9550-16-1-0278.

CHAPTER FOUR: SELF-ASSEMBLY OF Ge AND GaAs QUANTUM DOTS UNDER TENSILE STRAIN ON InAlAs(111)A

Kathryn E. Sautter,[1] Christopher F. Schuck,[1] Justin C. Smith,[2] Kevin D. Vallejo,[1] Trent A. Garrett,[3] Jake Soares,[1] Hunter J. Coleman,[3] Michael M. Henry,[1] Eric Jankowski,[1] Christian Ratsch,[2,4] and Paul J. Simmonds[1,3,a)]

[1] Micron School of Materials Science & Engineering, Boise State University, Boise, ID, 83725 USA

[2] Department of Mathematics, University of California, Los Angeles, CA 90095 USA

[3] Department of Physics, Boise State University, Boise, ID, 83725 USA

[4] Institute for Pure and Applied Mathematics, University of California, Los Angeles, CA 90095 USA

a) Corresponding author: paulsimmonds@boisestate.edu

Reproduced from K.E. Sautter, C.F. Schuck, J.C. Smith, K.D. Vallejo, T.A. Garrett, J. Soares, H.J. Coleman, M.M. Henry, E. Jankowski, C. Ratsch, and P.J. Simmonds, Cryst. Growth. Des. **21**(3), 1674-1682 (2021), with the permission of ACS publishing. See https://pubs.acs.org/doi/full/10.1021/acs.cgd.0c01528. Further permissions related to the material excerpted should be directed to the ACS.

DOI: https://doi.org/10.1021/acs.cgd.0c01528

Abstract

Quantum dots that store large tensile strains represent an emerging research area. We combine experiments and computational modeling to investigate the self-assembly of Ge and GaAs tensile-strained quantum dots (TSQDs) on $In_{0.52}Al_{0.48}As$(111)A. Comparing these two nominally similar material systems highlights how differences in adatom kinetics leads to distinct features of Ge and GaAs TSQD self-assembly. The energy barrier to diffusion of Ge adatoms is higher than that for Ga adatoms, while forming a stable island requires six Ge atoms and four Ga atoms. Unusually, these critical cluster sizes do not increase as we raise the substrate temperature. Radial distribution scaling shows that both Ge and GaAs TSQDs preferentially nucleate at a particular distance from their neighbors. This deeper understanding of the physics of Ge(111) and GaAs(111)A TSQD self-assembly will enable researchers to more effectively tailor these nanostructures to specific optoelectronic applications.

Synopsis

Germanium and gallium arsenide both spontaneously form quantum dot nanostructures when grown on InAlAs(111)A by molecular beam epitaxy. Despite experiencing similar tensile strains, the resulting Ge and GaAs quantum dots differ in shape, size, and areal density. Potential energy surface calculations help us understand how differences in adatom diffusion give rise to these structural variations.

4.1 Introduction

Demand is growing for high-quality semiconductor materials with a (111) crystallographic orientation. The structural and electronic characteristics of (111) surfaces give rise to properties that are inaccessible to semiconductors with the traditional (001)

orientation. (111)-Oriented semiconductor heterostructures are attractive for applications including topological insulators,[325,343,344] transition metal dichalcogenides and other 2D materials,[194,327,345] optoelectronics based on strain-induced piezoelectric effects,[346,347] and next-generation field-effect transistors.[326,348]

Quantum nanostructures grown on (111) surfaces exhibit some unique characteristics. Since tensile rather than conventional compressive strain is required to drive their self-assembly, these quantum dots (QDs) and quantum dashes derive their properties from both an unusual strain state and an unusual surface orientation.[18,19,21,23,25,26,154] For example, we can create defect-free Ge QDs on InAlAs(111)A (hereafter Ge(111)) under tensile strains ≥3.5%,[26] an important step toward future direct band gap Ge-based light emitting devices.[6,22,26,322,324] Tensile strain lifts the valence band degeneracy, pushing the light-hole states of a tensile-strained QD (TSQD) above its heavy-hole states, with important implications for quantum media conversion.[317,318] Meanwhile, the high symmetry of the (111) surface produces GaAs QDs with low fine-structure splitting, ideally suited to entangled photon generation via the biexciton–exciton decay cascade.[23,349,350]

However, the ability to grow these nanostructures is still in its infancy. A solid physical foundation for this emerging research field is needed to provide a clearer understanding of how TSQDs form and grow on (111) surfaces. By comparing the Ge(111) and GaAs(111)A TSQD systems, we have an opportunity to explore this developing growth technique at the atomic level. Ge and GaAs TSQDs are grown on $In_{0.52}Al_{0.48}As$(111)A (hereafter InAlAs), lattice-matched to InP.[21,26,154] The substrate temperatures and growth rates used during molecular beam epitaxy (MBE) are broadly

similar for Ge and GaAs TSQDs. The major difference between the two materials is polarity: Ge is nonpolar, while GaAs is a polar, compound semiconductor. However, from the point of view of the underlying InAlAs(111)A surface structure and tensile strain, these two TSQD systems are analogous. The almost identical lattice constants of Ge (5.6579 Å) and GaAs (5.6533 Å) mean that both materials experience ~3.7% tensile lattice mismatch with InAlAs. Removing these commonalities of surface structure and strain from the equation gives us a clearer view of the other physical factors influencing how TSQDs form and grow.

In this paper we show that TSQD self-assembly in these nominally similar Ge/InAlAs(111)A and GaAs/InAlAs(111)A materials systems exhibits some interesting and important differences. Density-functional theory (DFT) calculations reveal enhanced surface mobility for Ga adatoms compared to Ge. This study provides insight into the underlying kinetic processes that govern tensile-strained self-assembly during TSQD nucleation and growth. By comparing the scaled size and radial distributions of Ge and GaAs TSQDs, we see opportunities to enhance the size uniformity and spatial ordering of these nanostructures for future device applications.

4.2 Experimental Methods

We used Fe-doped, nominally on-axis (±0.5°) InP(111)A substrates for all sample growth. We grew samples via solid-source MBE, using As_4 as the group V source. We started by growing 50 nm of lattice-matched $In_{0.52}Ga_{0.48}As$ (hereafter InGaAs) at 169 nm/h to promote smoother InAlAs epitaxy.[52] We then grew 200 nm InAlAs at 172 nm/h as a bottom barrier for the Ge and GaAs TSQDs. We grew both InGaAs and InAlAs at a substrate temperature (T_{SUB}) of 510 °C, with a V/III beam equivalent pressure (BEP)

ratio of 160. Optimized MBE growth conditions for InGaAs and InAlAs on InP(111)A are discussed elsewhere.[21,52,320]

To grow the Ge TSQDs, we adjusted T_{SUB} for TSQD growth under As_4, closed the arsenic shutter and valve, waited 1 min, and then opened the Ge shutter.[26] Previous studies have shown that the InAlAs(111)A surface is thermally stable at these temperatures, even when the arsenic flux is removed for a short time.[26,90] For the GaAs TSQDs, we adjusted the sample to the desired T_{SUB} for TSQD growth under an As_4 flux and then opened the Ga shutter.[21]

In this study, we looked at four sets of samples: Ge TSQDs consisting of 0.2–0.6 bilayers (BL) of Ge grown at T_{SUB} = 535 and 560 °C, and GaAs TSQDs consisting of 3.5–4.5 monolayers (ML) of GaAs grown at T_{SUB} = 485 and 535 °C. The Ge growth rate was 0.020 BL/s. The GaAs growth rate was 0.075 ML/s, with an As_4/Ga BEP ratio of 75. After TSQD growth, we immediately cooled the samples; for the GaAs TSQDs, sample cooling took place under As_4.

We imaged the Ge and GaAs TSQDs with atomic force microscopy (AFM), using Nanoscope software to measure the height and diameter of 100–200 individual TSQDs on each sample. From these measurements, we compiled sample-dependent statistics of TSQD size distribution and areal density, which we used for island size scaling analysis. We used ImageJ software[351] to identify the TSQD coordinate positions on each AFM image. From these coordinates, we used a Python script and the *freud* analysis library[352] to extract interdot distances and plot the radial distribution of TSQDs on each sample.

4.3 Computational Methods

All electronic structure calculations were performed using DFT,[353,354] as implemented in the Fritz Haber Institute *ab initio* molecular simulations (FHI-aims) code.[355–358] FHI-aims uses numeric atom-centered orbitals for its basis set and by default includes scalar relativistic corrections. For all calculations, we used the Perdew–Burke–Ernzerhof generalized gradient approximation for the exchange-correlation (XC) approximation.[359] FHI-aims implements "light" and "tight" versions of its basis functions. We use the light settings throughout. Tight settings yield more accurate energies but do not change energy differences, which is our interest here.

To simulate a bulk random alloy such as InAlAs, a method such as special quasirandom structures (SQS) must be used.[360,361] However, we found that our calculations can be simplified by using InAs that is compressed 3.13% to the lattice constant of $In_{0.52}Al_{0.48}As$ (i.e., 5.8687 Å). We justify this simplification with DFT calculations for InAs and AlAs strained to have the same lattice constant as $In_{0.52}Al_{0.48}As$(111)A. We calculate that the InAs(111)A surface energy is lower than that of AlAs(111)A by ∼70 meV/Å^2, which corresponds to ∼1.2 eV per surface atom. We also ran a series of calculations for $In_{0.5}Al_{0.5}As$(111)A in three scenarios: (i) we fixed the top two group III layers as In; (ii) we fixed the top two group III layers as Al; and (iii) we maintained a 50–50 mix of In and Al in the top two layers. In all cases, the remaining group III atoms in the lower layers were randomized as In or Al (maintaining overall stoichiometry). These tests again show that the In-terminated surfaces are lower in energy than the Al-terminated surfaces by approximately 70 meV/Å^2. The In-terminated surfaces were also lower in energy than the surfaces with a 50–50 mix of In and Al by

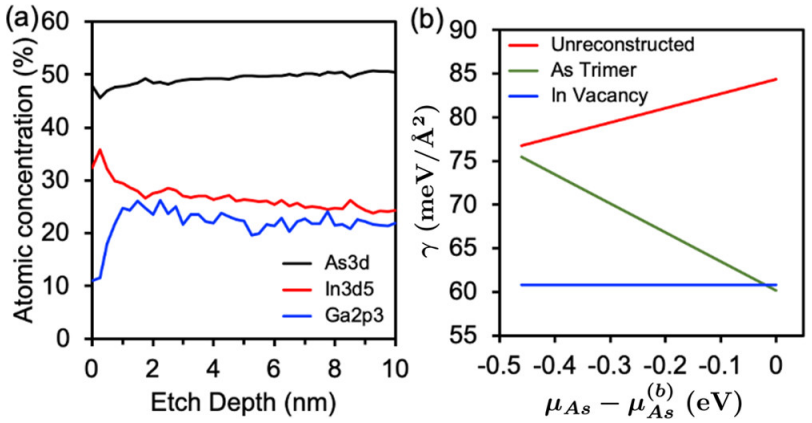

Figure 4.1 (a) XPS depth profile of bulk $In_{0.53}Ga_{0.47}As$(111)A showing enrichment (depletion) of indium (gallium) at the surface. (b) Surface energy of 3.13% compressively strained InAs versus arsenic chemical potential for both 2 × 2 reconstructions and the unreconstructed surface. The *x*-axis is equivalent to controlling the arsenic overpressure but is by no means one-to-one with an experimental knob.

approximately 10–15 meV/Å^2. For all three cases, run-to-run variations between the different randomizations were 2–3 meV/Å^2. Furthermore, we find that the difference in adsorption energy for an adatom on these three surfaces is very small. Even for the extreme case with only Al atoms in the layers below the top two InAs layers, the adsorption energy changes by ≤60 meV, and adsorption energy differences (i.e., diffusion barriers) change by even less. As a result of these calculations, we therefore conclude that InAs not only surface segregates, but the atomic composition of the bulk InAlAs below the top few layers has minimal bearing on the results at the surface.

Supporting our simulations is the fact that, during epitaxial growth of InAlAs(001) and InGaAs(001), the propensity for surface segregation of group III species increases with atomic size (i.e., In > Ga > Al).[362,363] To confirm this effect in our (111)A-oriented alloys, we use X-ray photoelectron spectroscopy (XPS) to construct elemental depth profiles for samples of InGaAs(111)A and observe a clear increase (decrease) in the surface concentration of indium (gallium) over the first 1–2 ML of the sample (Figure

4.1(a)). Equivalent XPS measurements for the InAlAs(111)A surface are complicated by oxidation in uncapped aluminum-containing alloys. However, since the observed effect is expected to be even stronger in $In_{0.52}Al_{0.48}As$ than in $In_{0.53}Ga_{0.47}As$,[362] we have little doubt that the results of our simulations are correct and that In surface segregation occurs in InAlAs(111)A.

The InAs(111)A surface is indium-terminated and has an AB–AB–AB pattern. Two stable reconstructions exist for the InAs(111)A surface: an indium-vacancy and an arsenic-trimer reconstruction, both of which have a 2 × 2 unit cell (Figure 4.1(b)). We limit our calculations to these two surface reconstructions. All our results are converged with respect to layers of vacuum (30 Å), k points (6 × 6 × 1 k points for 2 × 2 supercells and 12 × 12 × 1 k points for regular 1 × 1 cells) and slab thickness (five BL). We cap the final bottom layer with pseudohydrogen to minimize interaction with the top surface. Each bilayer contains 8 atoms in a 2 × 2 cell, and a typical calculation with a 2 × 2 cell for an adatom on the indium-vacancy (arsenic-trimer) reconstruction contains 43 (47) atoms total.

In Figure 4.1(b), we plot the phase diagram for the compressively strained InAs(111)A surface energy versus the arsenic chemical potential, which one can interpret physically as the arsenic overpressure during MBE (albeit with a nonlinear scaling to experimental settings). We find that the In-vacancy reconstruction is stable for lower arsenic overpressures, while the As-trimer reconstruction is stable for higher arsenic overpressures. These results are consistent with similar calculations for GaAs(111)A.[364]

The first step for understanding QD formation and growth is to understand the mobility of adatoms on a given surface reconstruction. For example, a higher adatom

mobility implies that the spacing between nuclei (that evolve into QDs) will increase. Although it seems reasonable to assume we have an As-trimer surface reconstruction given the high V/III flux ratio during MBE growth (Figure 4.1(b)), we could not confirm experimentally which reconstruction was present in all of our growths. We therefore calculated potential energy surfaces (PESs) for Ge and Ga adatoms on both the In-vacancy and As-trimer reconstructions of the InAs(111)A surface. As we will show, our conclusions regarding relative adatom mobility are qualitatively the same for both surface reconstructions. We obtained each PES by sampling a sufficiently large number of sites guided by test calculations that used the growing string,[365] and climbing image methods,[366] implemented in aimsChain, a Python package included with FHI-aims.

4.4 Results and Discussion

4.4.1 Key Differences between Ge and GaAs TSQDs

Despite self-assembling on nominally identical InAlAs(111)A surfaces, under similar MBE conditions, Ge and GaAs TSQDs exhibit major differences in size, shape, and areal density (Figure 4.2). Ge(111) TSQDs are lens shaped (Figure 4.2(a)) and are typically 0.5–3 nm high and 15–45 nm in diameter, with areal densities of 5×10^9 to 5×10^{10} cm^{-2} (Figure 4.2(b)).[26] In contrast, GaAs TSQDs grown at the same T_{SUB} self-assemble as equilateral triangles, reflecting the 3-fold symmetry of the (111)A surface (Figure 4.2(c)).[21,23,90,154] GaAs TSQDs form as stacked, concentric monolayer-high islands terminated by "A-steps" perpendicular to the $[2\bar{1}\bar{1}]$, $[\bar{1}2\bar{1}]$, and $[\bar{1}\bar{1}2]$ directions,[90] rather than the high-index side-facets typical of InAs/GaAs(001) QDs.(45) The GaAs TSQDs are 0.7–2 nm high and 45–60 nm in diameter, with areal densities of 2×10^8 to 2×10^9 cm^{-2} (Figure 4.2(d)).[21,154]

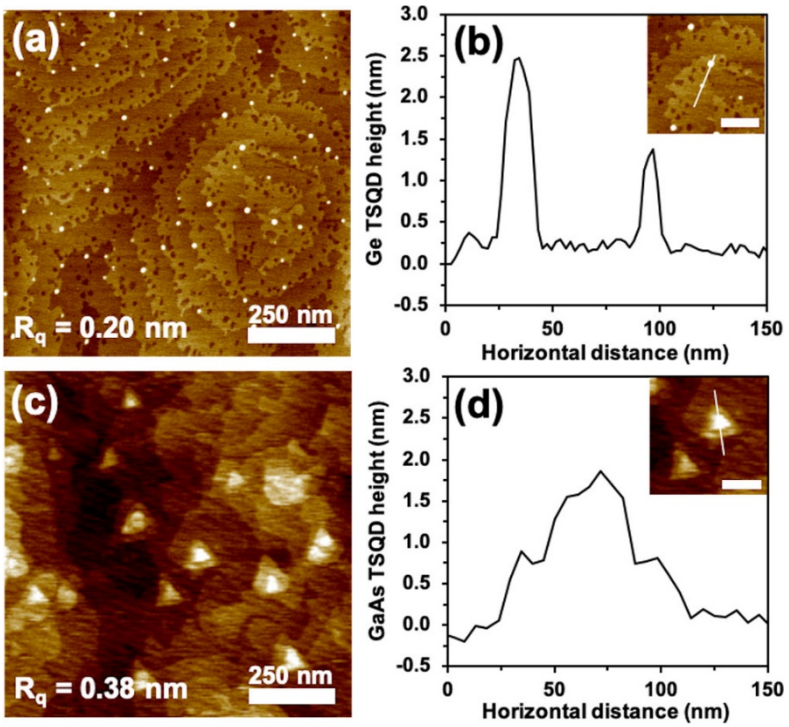

Figure 4.2 (a) AFM image showing typical Ge/InAlAs(111)A TSQDs, here grown from 0.2 BL Ge at T_{SUB} = 535 °C. (b) Cross section showing height and diameter of two representative Ge(111) TSQDs. (c) AFM image showing typical GaAs/InAlAs(111)A TSQDs here grown from 4 ML GaAs at T_{SUB} = 535 °C. (d) Cross section showing height and diameter of a representative GaAs(111)A TSQD. (insets b and d) AFM cross sections, where the white scale bars are 100 nm. The z-scale in all AFM images is 2.5 nm.

At $T_{SUB} \geq 535$ °C, Ge TSQDs self-assemble directly on the InAlAs(111)A buffer via the Volmer–Weber (VW) growth mode.[26] The InAlAs surface consists of rounded wedding cake-like terraces, 86 ± 13 nm wide (Figure 4.2(a)), with root mean squared roughness, $R_q \sim 2.0$ Å. The Ge TSQDs preferentially nucleate at the step edges connecting these terraces, as discussed in a previous report.[26] Since the areal density of the Ge TSQDs is related to the number of available step edges, the use of off-cut substrates to adjust the step edge density represents a potential route to controlling TSQD density. In addition, TSQD density along a step edge is a function of the adatom diffusivity along that step edge, and the stability of small clusters (or the adatom binding energy) at the step edge. DFT studies of edge atom diffusion, binding energies, and

cluster stability at step edges are computationally demanding and will form the subject of future work.

At comparable substrate temperatures, GaAs TSQDs self-assemble via an anomalous Stranski–Krastanov (SK) growth mode, where the tensile-strained GaAs wetting layer continues to grow even after the critical thickness for TSQD formation has occurred.[154] The tensile-strained GaAs wetting layer exhibits angular terraces, 85 ± 26 nm wide, with $R_q \sim 3.8$ Å (Figure 4.2(c)). After the 2D-to-3D SK transition, the GaAs TSQDs nucleate randomly across the wetting layer surface, without preference for particular locations.[21,154]

4.4.2 DFT Results for Surface Diffusion

To help us understand these differences in Ge and GaAs TSQD self-assembly, we use DFT calculations to compare adatom diffusion in the two material systems. Figure 4.3 shows the PES for Ge and Ga adatoms on the In-vacancy reconstruction. The energy barrier for surface diffusion, E_D, is given by the difference between the deepest energy well and the highest energy barrier as determined from exploring the PES. The adsorption site for both Ge and Ga atoms on the In-vacancy reconstruction is the vacancy site, labeled A_1. For both systems, diffusion occurs via a path that passes through a shallow secondary minimum (labeled A_2) and two transition sites (T_1 and T_2). We hence calculate the energy barrier to diffusion as $E_D = T_1 - A_1$. The adsorption energies and diffusion barriers for Ge and Ga on the In-vacancy reconstruction are summarized in Table 4.1. Since E_D is lower for Ga than Ge, Ga adatoms will diffuse faster than Ge adatoms on the In-vacancy surface.

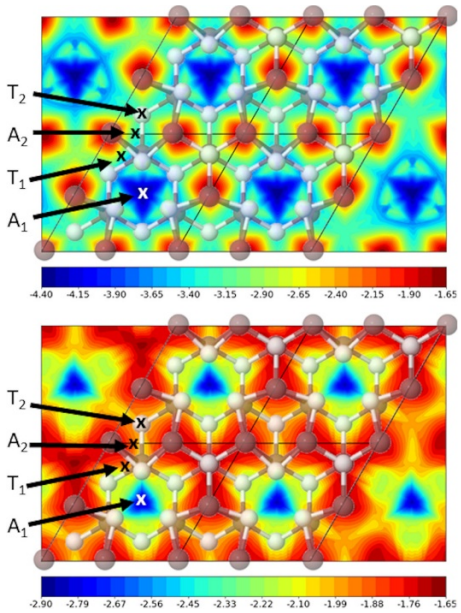

Figure 4.3 Potential energy surfaces for Ge (top) and Ga (bottom) adsorbed on the compressed In-vacancy reconstruction. The dark atoms are In, and the light atoms are As. The main adsorption site A_1, a secondary shallow minimum A_2, and the two transition sites T_1 and T_2 are shown.

Table 4.1 Adsorption Parameters for Ge and Ga on the In-Vacancy Reconstruction of the (Compressed) InAs(111)A Surface

Adatom	A_1	A_2	T_1	T_2	E_D
Ge	-4.36	-3.59	-3.09	-3.23	1.27
Ga	-2.82	-2.04	-1.92	-1.97	0.90

Figure 4.4 shows the PES for Ge and Ga adatoms on the As-trimer reconstruction. For this surface, there are two almost degenerate adsorption sites, labeled A_1 and A_2, in the region centered between three adjacent As trimers. There is almost no barrier for diffusion between A_1 and A_2 for Ga, and only a small diffusion barrier for Ge. We therefore refer to this region as a *superbasin*. Both Ge and Ga adatoms diffuse to the next superbasin by passing over an As trimer, but the details for Ge and Ga are slightly different. For Ge, the transition site T_1 is in the center of the As trimer. For Ga, on the other hand, there is a secondary adsorption site A_3 in the center of the trimer, and the

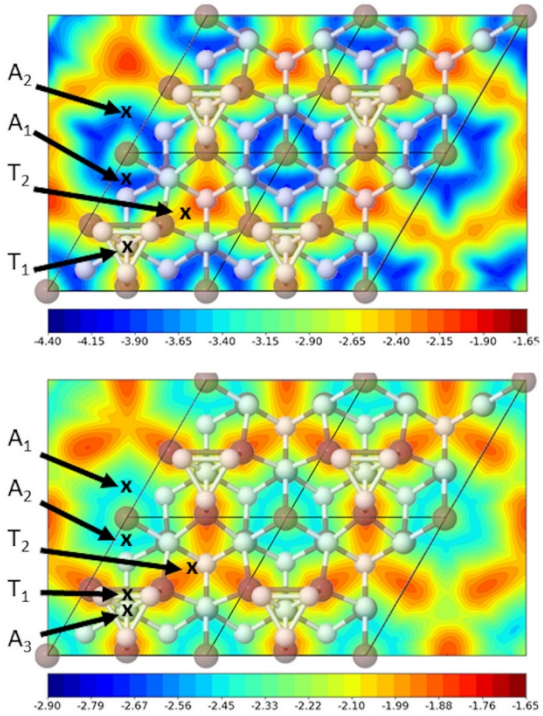

Figure 4.4 Potential energy surfaces for Ge (top) and Ga (bottom) adsorbed on the compressed As-trimer reconstruction. The dark atoms are In, and the light atoms are As. The main adsorption sites A_1 and A_2, a secondary shallow minimum A_3, and the transition sites T_1 and T_2 are shown.

transition site T_1 is on top of an As dimer bond within the As trimer. For both Ge and Ga, a secondary transition site T_2 provides an alternative path for diffusion. For Ge, the two diffusion paths are almost degenerate, while for Ga, the path via T_2 is 0.15 eV higher than T_1. The numerical values for Ge and Ga for all these sites and the barrier for surface diffusion are summarized in Table 4.2. The lower E_D for Ga means that Ga diffusion is again much faster than Ge diffusion on the As-trimer surface.

We note that due to the SK growth mode, the GaAs TSQDs begin to form only after the deposition of a few 2D layers of GaAs. Diffusion of Ga adatoms on this tensile-strained GaAs wetting layer (i.e., its in-plane lattice constant expanded to that of the underlying InAlAs) is hence the relevant process in this case. We therefore performed corresponding DFT calculations for Ga on 1 ML (2 ML) of tensile-strained GaAs on

Table 4.2 Adsorption Parameters for Ge and Ga on the As-Trimer Reconstruction of the (Compressed) InAs(111)A Surface

Adatom	A_1	A_2	A_3	T_1	T_2	E_D
Ge	-4.18	-3.90	n/a	-2.72	-2.69	1.46
Ga	-2.72	-2.71	-2.48	-2.44	-2.29	0.28

InAs(111)A (compressed to have the InAlAs lattice constant as before). We find that the Ga adatom diffusion barrier is then 1.10 eV (1.24 eV) for the In-vacancy reconstruction (which is now a Ga-vacancy reconstruction),[364] and 0.10 eV (0.10 eV) for the As-trimer reconstruction. Comparing these barriers with those in Tables 4.1 and 4.2 tells us that Ga diffusion on a thin GaAs(111)A wetting layer is still faster than Ge, and so our conclusions remain unchanged. We also note that these diffusion barriers for Ga on 1–2 ML of tensile-strained GaAs(111)A are similar to values we have obtained previously for Ga on unstrained GaAs(111)A, suggesting that the presence of strain does not modify the differences between Ga and Ge diffusion behavior to a great extent.[77]

The fact that for a given T_{SUB}, Ga diffuses faster than Ge means that diffusivity arguments alone are unable to explain our experimental observation that Ge TSQDs form predominantly at the step edges, while GaAs TSQDs form on the terraces (Figure 4.2). We speculate that small GaAs clusters are more stable than small Ge clusters. GaAs clusters are sufficiently stable that they can form directly on the terraces, while dangling bonds available at the step edges are needed to help stabilize Ge clusters. Step edges play a more important role for Ge since unlike GaAs it can fill both group III and group V sites and still satisfy electron counting rules. We believe that this difference in bonding between group III and group IV atoms is ultimately the main reason for the distinct self-

assembly behaviors of Ge and GaAs TSQDs. However, future experiments to compare other group IV and III–V TSQD systems, for example Si and GaP TSQDs grown on GaAs(111)A,[18] could allow us to definitively rank the relative importance to self-assembly of differences in adatom diffusion vs differences in bonding.

4.4.3 Scaling of Ge and GaAs TSQD Size Distributions

To experimentally test this hypothesis of differences in cluster stability, we studied the scaled island size distribution functions for Ge and GaAs TSQDs. This scaling analysis allows one to identify how many atoms are required to stabilize a cluster and nucleate a TSQD during the self-assembly process. We define a critical cluster size i as being one less than the number of atoms needed to form a stable nucleus. Lower stability means that more atoms are needed to form the TSQD nucleus and so i will be larger.

For homoepitaxial growth, the island size distribution scales according to a scaling function, f_i, given by [76,91,92].

$$f_i\left(\frac{s}{\langle s\rangle}\right) = \frac{N_s\langle s\rangle^2}{\theta}$$

where s is the size of the island, N_s is the number of islands of size s, $\langle s\rangle$ is the average island size, and θ is the coverage. The shape of f_i depends on the degree of reversibility of the adatom aggregation process, as well as on the value of i in a given system, which can take noninteger values.[76] Explicit analytic expressions for the functions f_i for integer values of i were given in Reference [91]. While this scaling behavior was studied in detail in the submonolayer regime, we now know that it also holds for heteroepitaxial QDs after the deposition of multiple layers.[18,367] Researchers speculate that the scaling also holds in these cases because the heteroepitaxial TSQDs do not coalesce and, in that sense, are

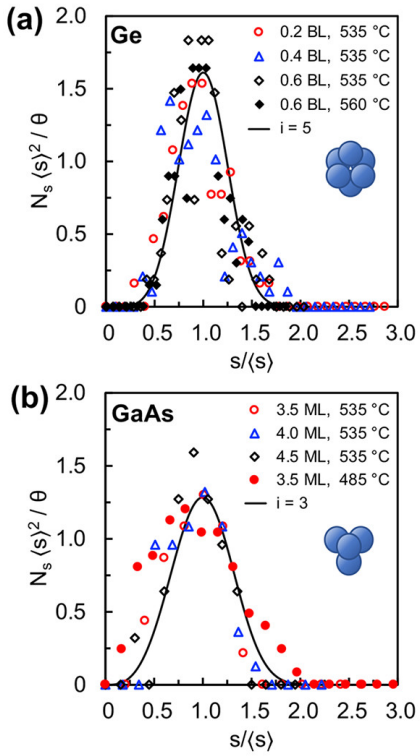

Figure 4.5 (a) Scaled 3D Ge/InAlAs(111)A TSQD size distributions with different Ge deposition amounts grown at T_{SUB} = 535 and 560 °C. (b) Scaled 3D GaAs/InAlAs(111)A TSQD size distributions with different GaAs deposition amounts grown at T_{SUB} = 485 and 535 °C. Solid lines are analytic expressions for critical cluster sizes i = 5 in a and i = 3 in b.[91] The schematics suggest how six atoms (i = 5) and four atoms (i = 3) can be arranged into clusters with 3-fold symmetry.

somewhat similar to islands during homoepitaxy in the submonolayer, precoalescence regime.

In Figure 4.5 we show the scaled size distributions for Ge and GaAs TSQDs grown at T_{SUB} = 535 °C, with different deposition amounts. In these plots, θ represents the effective surface coverage of the TSQDs, rather than their volume. The individual island size distributions for both the Ge and GaAs TSQDs collapse onto single curves after scaling, confirming that in each case we can describe the tensile self-assembly process with a single scaling function f_i (Figure 4.5(a),(b)).

For Ge TSQDs grown at T_{SUB} = 535 °C, the best fits to the data come from the analytic expressions for i = 5–6 (Figure 4.5(a) shows the fit for i = 5).[91] This range of values for i comes from the spread in the scaled data. When we also include scaled size distribution data for a similar Ge TSQD sample grown at T_{SUB} = 560 °C, we see that they too lie on the i = 5 curve, and are essentially indistinguishable from the T_{SUB} = 535 °C data. Therefore, at both temperatures the smallest stable cluster size (given by i + 1) for the Ge TSQDs consists of six atoms. That the critical cluster size appears to be insensitive to T_{SUB} over this range is somewhat surprising. Previous studies of QD critical cluster sizes have found that the value of i tends to increase with T_{SUB}.[18,367] As T_{SUB} rises, the additional thermal energy means that atoms are able to detach from previously stable clusters, and so for an atom to become irreversibly attached to a cluster, more atom-to-nearest-neighbor bonds are required.[91] The fact that i is the same in Figure 4.5(a) despite an increase in T_{SUB} of 25 °C suggests that the six-membered TSQD nucleus is particularly stable.

Similar analysis for GaAs TSQDs grown at T_{SUB} = 535 and 485 °C results in scaled island size distributions that, regardless of T_{SUB}, are best fitted with the analytic expressions for i = 2–3 (Figure 4.5(b) shows the fit for i = 3).[91] The fact that the critical cluster size for GaAs TSQD nucleation remains constant at four atoms, once again reveals that this specific arrangement is particularly stable over this 50 °C range of T_{SUB}.

It is worth noting that nuclei consisting of six atoms (Ge) and four atoms (GaAs) can both be arranged into clusters with 3-fold symmetries (see schematics in Figure 4.5(a),(b)). For a triangular lattice, Joyce and Vvedensky referred to clusters with 3-fold symmetry as “magic” islands.[68] Like them, we speculate whether clusters containing

these specific numbers of Ge and Ga atoms gain additional stability by mirroring the symmetry of the underlying (111)A surface reconstruction.

4.4.4 Scaling of Ge and GaAs TSQD Radial Distributions

Our DFT calculations predict differences in Ge and Ga adatom diffusion that we can observe experimentally. As diffusion length increases, we expect to see larger, lower density TSQDs (i.e., spaced farther apart).[68] We used radial distribution analysis to explore Ge and GaAs interdot spacings and find the scaling relation $N(r)$ for their separation as a function of distance r. The radial distribution function $g(r/\langle R\rangle)$ describes the normalized probability of finding a TSQD whose center is a distance r away from the center of another[72,92] and is given by

$$g\left(\frac{r}{\langle R\rangle}\right) = \frac{N(r)}{N}$$

where N is the TSQD areal density and $\langle R\rangle = 1/\sqrt{N}$ is the average distance between TSQDs if we assume uniform separation. Table 4.3 summarizes our results for $\langle R\rangle$ and the average TSQD radius (r_0) for Ge and GaAs TSQDs grown from different deposition amounts. The values for the four samples grown at 535 °C are entirely consistent with the results from our DFT calculations. At this same T_{SUB}, the faster diffusion of Ga adatoms compared to Ge results in bigger GaAs TSQDs with larger average interdot separation.

For the 0.2 BL Ge TSQDs we see overlap between $\langle R\rangle = 107 \pm 14$ nm and the average InAlAs terrace width in Figure 4.2(a) of 86 ± 13 nm. The similarity between these values indicates that, at low Ge coverage, the interstep separation has a stronger influence on TSQD separation than the distance between Ge TSQDs along a given step edge. Raising the Ge coverage to 0.6 BL increases the TSQD areal density.[26] As a result, $\langle R\rangle$ is reduced to 61 ± 6 nm, and so average TSQD separation along the step-edges is now

Table 4.3 Experimental Values for ⟨*R*⟩ and Average TSQD Radius (r_0) for the Ge and GaAs Samples in Figure 4.6(a),(b)

Sample	⟨*R*⟩ (nm)	r_0 (nm)
0.2 BL Ge, 535 °C	107 ± 14	6.4 ± 0.8
0.6 BL Ge, 535 °C	61 ± 6	8.2 ± 0.7
0.6 BL Ge, 560 °C	73.3 ± 0.4	14.9 ± 1.2
3.5 ML GaAs, 485 °C	358 ± 8	23.2 ± 5.4
4.0 ML GaAs, 535 °C	241 ± 13	32.0 ± 4.5
4.5 ML GaAs, 535 °C	360 ± 41	35.7 ± 5.3

less than the average InAlAs terrace width. Indeed, this is what we see from AFM images (e.g., Figure 1(c) in Reference [26]), where "chains" of QDs, often separated by less than 50 nm, decorate the step-edges. Increasing T_{SUB} to 560 °C enhances adatom diffusion, which increases the average size of the 0.6 BL Ge TSQDs but reduces their density.[26] As a result, ⟨*R*⟩ increases slightly to 73.3 ± 0.4 nm, but this separation is still less than the average terrace width.

Table 4.3 shows that raising the GaAs coverage from 3.5–4.0 ML while also raising T_{SUB} from 485–535 °C has the expected combined effect of increasing average GaAs TSQD size.[21] That ⟨*R*⟩ simultaneously decreases from 358–241 nm tells us that depositing an additional 0.5 ML of GaAs has a stronger effect on TSQD separation than the 50 °C increase in T_{SUB} which would tend to decrease areal density.[21] Interestingly, raising the GaAs coverage by a further 0.5 ML at 535 °C has the opposite effect on ⟨*R*⟩ of *increasing* the average TSQD separation from 241–360 nm. This decrease in TSQD areal

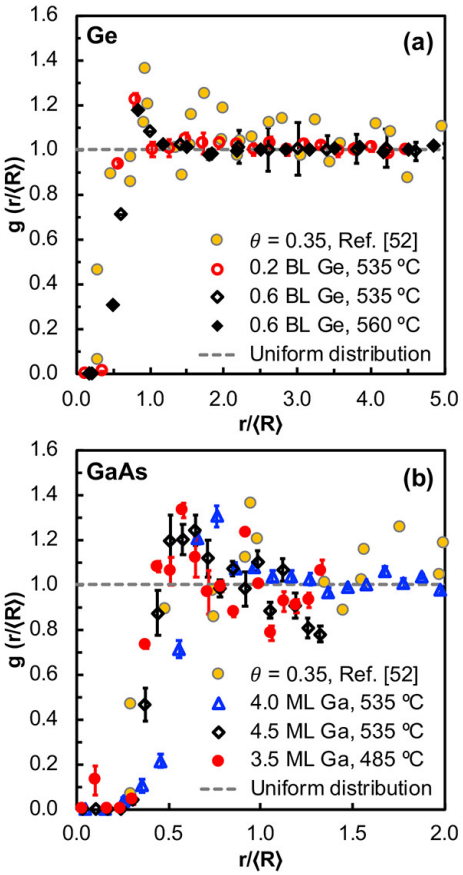

Figure 4.6 (a) Scaled Ge/InAlAs(111)A TSQD radial distributions with different Ge coverages grown at T_{SUB} = 535 and 560 °C. (b) Scaled GaAs/InAlAs(111)A TSQD radial distributions with different Ga coverages grown at T_{SUB} = 485 and 535 °C. In each data series, the standard errors are calculated using averages from at least three independent samples over an area of ≥33 μm^2. Dashed lines show the uniform radial distribution for a noninteracting system. Parts a and b include comparative radial distribution data from Reference [72].

density at high GaAs coverage is consistent with the onset of Ostwald ripening where the smallest TSQDs disappear, their material consumed by larger neighboring dots.[21]

Figure 4.6(a),(b) show the radial distribution functions for the samples in Table 4.3. If TSQD nucleation was perfectly uniform, their radial distributions would fall on the dashed lines at $g(r/\langle R\rangle) = 1$ in Figure 4.6(a),(b). Indeed, at long-range as $r \rightarrow \infty$ we do see $g(r/\langle R\rangle) \rightarrow 1$ as the data converge to these dashed lines. However, the fact that at short-

range we see significant deviation both below and above the dashed lines indicates that the nucleation and growth of Ge and GaAs TSQDs is not uniform.

Data falling below the dashed lines tell us we have a reduced probability of finding a Ge or GaAs TSQD in very close proximity to another. At very short-range, existing TSQDs act as local sinks for adatoms, preventing new TSQDs from nucleating nearby. Therefore, as $r \rightarrow r_0$ in Figure 4.6(a),(b), $g(r/\langle R \rangle) \rightarrow 0$.

In contrast, at slightly longer range, we see peaks in the data at $r/\langle R \rangle \sim 1$ for the Ge TSQDs, and $r/\langle R \rangle \sim 0.75$ for the GaAs TSQDs (Figure 4.6(a),(b). Data above the dashed lines at $g(r/\langle R \rangle) > 1$ are a measure of how many times more likely a TSQD is to be found at distance $r/\langle R \rangle$ from the center of any other TSQD. The peaks in the data therefore reveal spatial correlations for both Ge and GaAs TSQDs. We attribute the appearance of these peaks to the fact that existing TSQDs are surrounded by a capture zone for adatoms within which new TSQDs cannot nucleate. The result is an effective "repulsion" between the TSQD centers above a critical nucleus size. This is supported by simulation results for strained island growth in the submonolayer regime.[75,368] The island size distribution narrows and sharpens as a function of strain, because the island capture zones become more regular.

After sampling at least 31 1 μm^2 areas for each radial distribution function, these peaks of height $g(r/\langle R \rangle) = 1.2–1.4$ for Ge and GaAs TSQDs show good agreement with the correlation peaks of ~1.4 observed by Bressler-Hill et al. for distributions of InAs/GaAs(001) QDs (see yellow circles in Figure 4.6(a),(b)).[72] It is noteworthy that despite the opposite sign of strain, these similarities suggest tensile-strained Ge and GaAs QDs exhibit nearly identical spatial distributions and capture zones of comparable

strength to traditional compressively strained InAs/GaAs(001) QDs.[72] This is the first demonstration of tensile-strained QDs distributed with a preferred separation. In the future, the use of similar studies to tune short-range separations of Ge and GaAs TSQDs could be quite attractive for tailoring quantum dot densities to specific optoelectronic applications.

It is noteworthy that we do not observe temperature-dependent differences in the radial distribution functions for either Ge or GaAs TSQDs. The general agreement (to within error) of the various data sets in Figure 4.6(a),(b) suggest that the observed spatial correlations of the Ge and GaAs TSQDs persist across the T_{SUB} ranges explored here.

4.5 Conclusions

Although Ge and GaAs TSQDs both self-assemble on $In_{0.52}Al_{0.48}As$(111)A surfaces, their structural characteristics (size, shape, and areal density) are quite different. Formation of these TSQDs can be reproduced reliably over a fairly broad range of substrate temperatures. It appears that the critical island size for both Ge and GaAs TSQD nucleation is unchanged over the temperature windows explored here, enabling robust control of TSQD size uniformity and areal density. Our DFT calculations predict that regardless of the surface reconstruction, Ga diffuses much faster on the $In_{0.52}Al_{0.48}As$(111)A surface than Ge. These DFT results are borne out experimentally, as we show that Ge TSQDs are smaller and higher density than GaAs TSQDs grown at the same substrate temperature. We speculate that while GaAs clusters are stable enough to form on the terraces, most Ge clusters form at step-edges as a result of the extra stability provided by the additional dangling bonds. We find experimental support for this hypothesis from island size scaling analysis of our TSQD data, which shows that more

atoms are required to form a stable Ge nucleus than a GaAs nucleus. The spatial distributions of Ge and GaAs TSQDs are not uniform. Instead we see that the TSQDs are distributed such that they have a preferred separation from one another and that these spatial correlations are independent of substrate temperature over the ranges studied here. To build on these results, we are planning a more detailed DFT study of the binding energies and stability of step edges. The insights gained from this study will assist researchers interested in designing Ge(111) and GaAs(111)A TSQD arrays for a range of applications from novel infrared emitters to entangled photon sources.

Author Contributions

K.E.S. and C.F.S. contributed equally to this work.

Acknowledgements

This material is based upon work supported by the Air Force Office of Scientific Research under award number FA9550-16-1-0278 and by the National Science Foundation under NSF CAREER Grant No. 1555270. We acknowledge Elton Graugnard and Steven M. Hues (Boise State University) for valuable assistance with XPS. AFM was done at the Boise State Surface Science Laboratory.

CHAPTER FIVE: DIRECT BAND GAP LIGHT EMISSION FROM TENSILE-STRAINED Ge QUANTUM DOTS ON InAlAs(110)

Kathryn E. Sautter,[1] Aaron J. Muhowski,[2] Kevin A. Grossklaus,[3] Ashton E. Enrriques,[1] Paul H. Davis,[1] Alessia M. Molino,[4] Trent A. Garrett,[4] Kevin Saythavy,[1] Hunter J. Coleman,[4] Dmitri A. Tenne,[4] Eric Jankowski,[1] Christian Ratsch,[5,6] Daniel M. Wasserman,[2] and Paul J. Simmonds[1,4]

[1] Micron School of Materials Science & Engineering, Boise State University, Boise, ID, 83725, USA

[2] Department of Electrical and Computer Engineering, University of Texas at Austin, Austin, TX 78758, USA

[3] Department of Electrical and Computer Engineering, Tufts University, Medford, MA 02155, USA

[4] Department of Physics, Boise State University, Boise, ID, 83725, USA

[5] Department of Mathematics, University of California, Los Angeles, CA 90095, USA

[6] Institute for Pure and Applied Mathematics, University of California, Los Angeles, CA 90095, USA

In Progress for Publication.

Abstract

Recent reports show that defect-free, optically active quantum dots can store tensile strains large enough to transform germanium (Ge) into a direct band gap semiconductor. These tensile-strained quantum dots (TSQDs) self-assemble during molecular beam epitaxy (MBE) on (111) and (110) surfaces. We adopt this approach to synthesize defect-free Ge TSQDs on InAlAs(110) via the Volmer-Weber growth mode. This surface orientation allows us to avoid introducing antiphase domains in the InAlAs capping layer. The Ge(110) TSQDs grow as rectangular prisms oriented parallel to the $[\bar{1}10]$ direction, with flat tops and short-range ordering. We report room temperature light emission from Ge(110) TSQDs at 2.8 μm (~0.44 eV). This work paves the way to future edge-emitting infrared LEDs and lasers based on highly tunable, direct band gap Ge TSQDs.

5.1 Introduction

Researchers are searching for ways to turn the technologically vital element Ge into an effective light-emitter, and take advantage of this semiconductor's high gain coefficient and narrow band gap.[7,12–16] Ordinarily, Ge has an indirect semiconductor band gap making it unsuitable for light-emitting applications. Theory predicts however, that Ge should become a direct band gap semiconductor when grown on (001) and (110) surfaces, under ~1.9% and ~3% biaxial tensile strain respectively.[4,6,8,9] Direct band gap Ge could have important implications for future mid-infrared (IR) optoelectronic devices useful in environmental monitoring, *in vivo* diagnostics, and trace gas detection.[22,369,370]

Researchers have hence explored numerous approaches to induce these large tensile strains in Ge. The challenge is that such large tensile strains are quickly relaxed in

bulk Ge by the formation of dislocations that are detrimental to optoelectronic performance. For this reason, approaches that rely on mechanical stretching or differences in thermal expansion coefficients are typically limited to tensile strains of ~1%.[12,14,15,371]

However, by localizing the tensile strain at the nanoscale, we may be able to store the large strains needed without generating crystallographic defects. Groups have explored phase separation to form nanocomposites of highly tensile-strained Ge/InAlAs and Ge/AlAs, although these approaches have yet to report the strong mid-IR light emission we anticipate for direct band gap Ge.[13,16]

Quantum dot (QD) self-assembly offers an alternative route to highly tensile-strained Ge. We have known since the 1990s that QDs storing compressive strains in excess of 7% can have excellent crystal and optical quality.[80,81,137] More recently, groups have extended self-assembly techniques to produce defect-free, optically active QDs under large tensile strains.[21–26] Ge tensile-strained QDs (TSQDs) have been demonstrated on both InAlAs(001) and (111)A surfaces.[26,27] Indeed, for the Ge(001) TSQDs, photoluminescence (PL) at ~1550 nm (~0.8 eV) was reported below 100 K. Interestingly, the authors attributed this light emission to electron-heavy hole recombination (Γ_0–HH_0).[27] Given that tensile strain should induce a light hole valence band ground state, longer wavelength emission PL from Γ_0–LH_0 recombination was perhaps expected.[318] In fact, the authors saw only a weak spectral feature at ~2580 nm (~0.48 eV) that seemed to correspond to that transition.[27]

In this paper, we apply tensile-strained self-assembly to enable the growth of Ge TSQDs within $In_{0.52}Al_{0.48}As$(110) barriers. This material system is beneficial for several

reasons. The 3.7% lattice mismatch between Ge and InAlAs should generate tensile strains in excess of what is predicted for an indirect-to-direct band gap transition in Ge(110).[4,6] The (110) surface orientation is better suited than (001) to the accommodation of large tensile strains without plastic relaxation via dislocation formation.[19] Capping of the Ge TSQDs with the InAlAs top barrier should be simplified since antiphase disorder should be minimized at III-V/IV interfaces with a (110) orientation.[59]

We explore the impact of MBE parameters on Ge(110) TSQD self-assembly. We report the unusual formation of flat-topped TSQDs, and discuss the relationship between their rectangular shape and anisotropic adatom diffusion on the (110) surface. As a result of their large residual tensile strains and optical quality, for the first time we demonstrate room temperature light emission from direct band gap Ge(110) TSQDs.

5.2 Methodology

We grew the Ge/$In_{0.52}Al_{0.48}As$(110) samples with solid-source MBE. We used nominally on-axis (±0.5˚) Fe-doped InP(110) substrates and standard effusion cells for ultra-high purity Ge, In, and Al. We kept our valved-source As cracker at 600 °C to produce As_4, for consistency with previous TSQD studies on (110) surfaces.[22] To find the beam equivalent pressure (BEP) for each source, we used a flux monitor at the substrate position. We calibrate pyrometer and thermocouple measurements of the substrate temperature (T_{SUB}) against known surface reconstruction changes via reflection high-energy electron diffraction (RHEED).

We determined InAs and AlAs growth rates from RHEED intensity oscillations and calibrated the $In_{0.52}Al_{0.48}As$ (hereafter InAlAs) composition for lattice-matching to InP using *ex-situ* x-ray diffraction. We calibrated the Ge growth rate by growing Ge on

GaAs(001) at T_{SUB} = 535 °C for 1 hour and using *ex-situ* ellipsometry to determine the resulting layer thickness.

To grow the TSQD samples, we first removed the substrate surface oxide by heating the InP(110) substrate to 500 °C and degassing at this temperature for 30 min under an As_4 overpressure. We then cooled the sample to 300 °C at 50 °C/min, waited four minutes for the substrate temperature to stabilize, and then deposited a 500 nm InAlAs bottom barrier.[52] The InAlAs was grown at 0.5 μm/h under an As_4/III BEP ratio of ~80 (As_4 BEP ~2E-5 Torr). We finished the InAlAs bottom barrier by heating the substrate to 500 °C at 25 °C/min and annealing for 15 min under the same As_4 overpressure.

For TSQD growth, we brought the substrate temperature to 520–550 °C and closed the As valve. We waited 60 s for the As overpressure to drop and deposited 0.4, 1.4, 1.9, or 2.4 monolayers (ML) Ge at 0.025 ML/s. The RHEED pattern immediately changed from a streaky to a spotty pattern, indicative of 3D growth. This completed the growths for surface studies of the TSQDs, which were then promptly cooled and removed from the growth chamber.

For the photoluminescence (PL) samples, we continued growth by immediately opening the As valve to 100%; reducing T_{SUB} to 300 °C at 50 °C/min; waiting 4 min for the substrate temperature to stabilize; and growing a 50 nm InAlAs top barrier under the same growth conditions as the bottom barrier. We then deposited a 5 nm InAs cap to prevent oxidation. We rapidly cooled and then removed the sample from the growth chamber.

We used Raman spectroscopy to determine residual tensile strain in the Ge TSQDs. To increase the signal from the Ge TSQDs for Raman we grew a sample under the same

conditions as above, but containing four buried Ge TSQD layers grown at 520 °C, separated by 30 nm InAlAs layers, and finished with a 10 nm InAlAs cap. For this specific sample, we omitted the 15 min anneal step for the InAlAs barriers separating the Ge layers. We compared the Raman spectrum from this Ge(110) TSQD sample with both a bulk Ge(110) substrate and a control sample consisting of 500 nm InAlAs on InP(110) without Ge TSQDs. We took care to avoid sample heating during Raman spectroscopy.

We used atomic force microscopy (AFM) imaging and analysis to determine the TSQD areal density, and average height, length, width, and aspect ratio of surface TSQDs. Imaging details for high-resolution AFM appear in Section 5.5.

To explore whether Ge(110) TSQDs form at some preferred separation we used a custom radial distribution function (RDF) code written previously to compare Ge and GaAs TSQDs grown on InAlAs(111)A.[43] We adapted this RDF code to look for preferred clustering in TSQD separation parallel to $[\bar{1}10]$ and $[001]$. For these linear distribution functions (LDFs) we looked at 10 nm strip intervals and counted TSQD centers with a parallel histogram scheme,[372] using a 5 nm bin size. We obtained averaged plots and their corresponding error bars from using the LDF program on four 500 nm × 500 nm AFM scans for each sample (roughly 275 TSQDs per AFM scan).

We used scanning transmission electron microscopy (STEM) to investigate the internal structure of our Ge TSQDs and identify their bounding crystallographic facets. We also used electron energy loss spectroscopy (EELS) to map the compositional distribution of our samples in the region close to the Ge TSQDs. Additional detail regarding the STEM-based identification of the edge facets on our TSQDs appears in Section 5.5.

Details regarding our setup for PL spectroscopy can be found in one of our recent articles,[373] with the exception of a few key differences. Specifically, here we used a cooled InSb detector, together with either a Ge window or a GaAs wafer to act as a long pass filter.[373]

To better understand the physical origin of the asymmetric shape of the Ge(110) TSQDs we performed density-functional theory (DFT) calculations. All DFT calculations were completed with the Fritz-Haber Institute *ab initio* molecular simulations code (FHI-aims).[355–358] This code uses numeric atom-centered orbitals for its basis set and by default includes scalar relativistic corrections. For all calculations, we used the Perdew-Burke-Ernzerhof approximation for the exchange-correlation functional.[359] FHI-aims implements "light" and "tight" versions of its basis functions. We used the "light" setting, but only after testing that the results are essentially the same with the "tight" setting. All computational calculations reported here are for compressed InAs. This is justified since we have shown in earlier work on the (111)A surface that $In_{0.52}Al_{0.48}As$ can be approximated with InAs that is compressed by 3.13% (i.e., to the $In_{0.52}Al_{0.48}As$ lattice constant).[43] We do supercell calculations with a 2 × 2 cell size and 8 atomic layers. The bottom layer is capped with pseudo-hydrogen to minimize the interactions between the bottom and the top layer. The dimensions of the supercell are 8.65 Å × 12.24 Å × 50.0 Å (ensuring a vacuum thickness that is slightly larger than 30 Å). We have carefully tested that our results are converged with respect to the cell dimensions. We chose a k-grid that corresponds to (8 × 8 × 1) k-points for a 1 × 1 cell. In total there are 73 atoms in most calculations (72 plus the adatom).

5.3 Results & Discussion

5.3.1 Ge(110) TSQD Structure

We demonstrate for the first time that Ge TSQDs self-assemble on InAlAs(110). Figure 5.1 shows the evolution of the InAlAs(110) surface with increasing Ge deposition at 550 °C. The bare InAlAs(110) surface (i.e., 0 ML Ge) exhibits a streaky (1 × 1) RHEED pattern along the $[\bar{1}10]$ direction, confirming a smooth unreconstructed surface prior to Ge deposition (Figure 5.1(a)). AFM of the InAlAs(110) surface shows small hill-like features roughly 0.5-1.0 nm high extending parallel to $[\bar{1}10]$. After growing 0.4 ML Ge, the RHEED pattern immediately develops spotty features consistent with 3D self-assembly (Figure 5.1(b)). We confirm the spontaneous formation of these 0.4 ML Ge TSQDs using AFM. That these Ge(110) TSQDs form from sub-monolayer Ge coverage indicates that self-assembly takes place via the Volmer-Weber (VW) growth mode (i.e. without a wetting layer) (Figure 5.1(b),(d)). We have previously observed the VW-based self-assembly of Ge TSQDs on InAlAs(111)A grown at similar values of T_{SUB}.[26] Although 0.4 ML Ge TSQDs are elongated towards $[\bar{1}10]$, the elongation becomes more obvious with higher deposition amounts (Figure 5.1(c),(e)).

0.4 ML Ge on InAlAs(110) results in areal densities of ~2.7×10^{10} cm^{-2}, heights of 1.1 ± 0.04 nm, lengths of 15.2 ± 3.6 nm, and widths of 9.5 ± 2.1 nm. At the same T_{SUB} of 550 °C, we see all of these values increase at 2.4 ML: these QDs present with areal densities of ~1.1×10^{11} cm^{-2}, heights of 2.0 ± 0.6 nm, lengths of 24.7 ± 6.1 nm, and widths of 12.1 ± 3.1 nm (Table 5.1). Interestingly for this series, both the 0.4 ML and 2.4 ML series have the same average length/width ($[\bar{1}10]/[001]$) ratio of 1.6 ± 0.3 (0.4 ML) and 2.0 ±

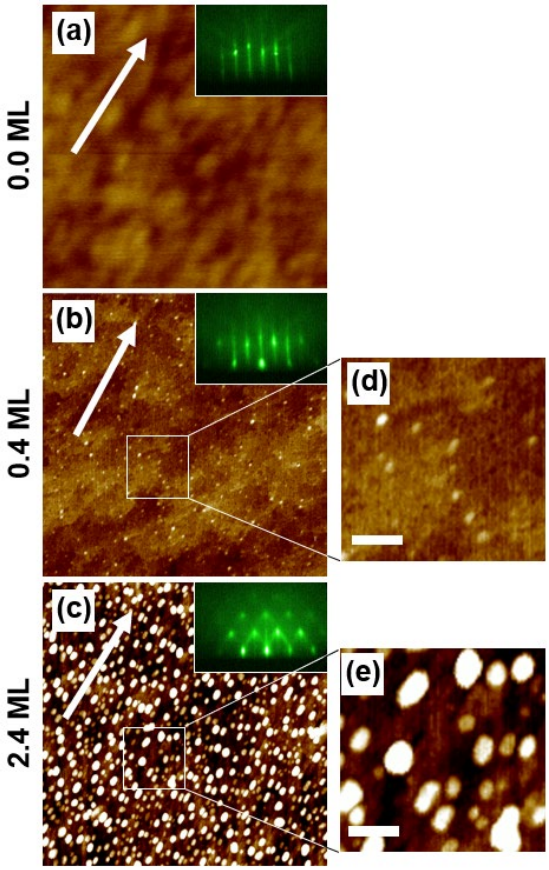

Figure 5.1 (a)-(c) 1 × 1 μm² AFM images showing how the surface changes with Ge deposition and (insets) the images' corresponding RHEED patterns seen down the [$\bar{1}10$] direction (later presented in greater detail). The arrows indicate the [$\bar{1}10$] direction. For (b) and (c), the Ge TSQDs grew at a substrate temperature of 550 °C. (d) and (e) are expanded sections of (b) and (c) respectively with a scalebar of 50 nm. For each image, the z-scale is 3 nm.

0.60, indicating that the Ge(110) TSQD shape does not change considerably with increasing deposition amounts.

In Figure 5.2 we compare the Raman spectrum from an InAlAs(110) sample containing four layers of Ge TSQDs to that from a bulk InAlAs(110) control sample. In the former, we see a weak feature at 290.8 cm^{-1} that we attribute to the presence of the Ge TSQD layers. This Ge-related feature appears at smaller wavenumbers than the LO phonon line for bulk Ge(110) at 303.4 cm^{-1} (dashed line in Figure 5.2), which tells us that the Ge TSQDs are under tensile strain.[45]

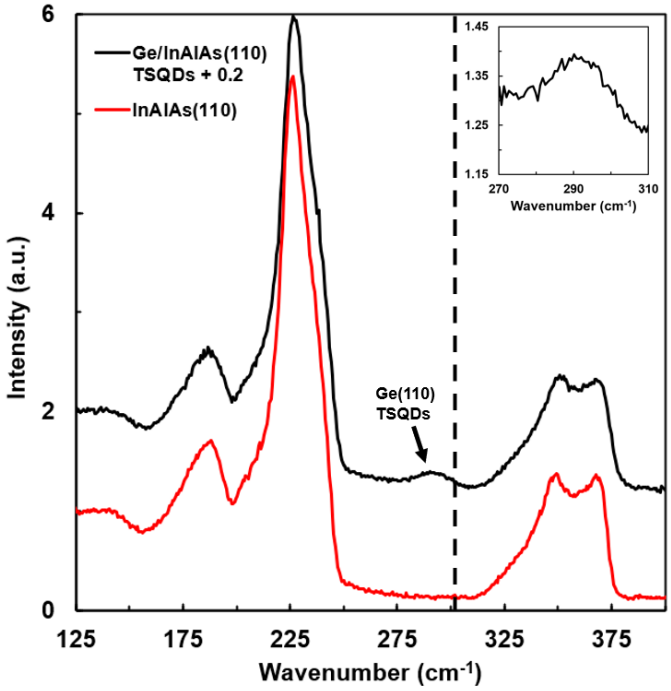

Figure 5.2 Raman spectra of Ge/InAlAs(110) TSQDs (black) and bulk InAlAs(110) (red). The Ge/InAlAs(110) TSQDs spectrum has been vertically offset for clarity. The vertical dashed black line is the peak position for bulk Ge(110). Inset: enlarged section showing the Ge emission peak.

Dividing the shift in the phonon line by the Ge phonon strain coefficient of –415±40 cm^{-1} (Ref. [45]), we calculate that the Ge TSQDs experience 3.0 ± 0.3% tensile strain. Theory suggests tensile strains in excess of 3% will transform Ge(110) into a direct band gap semiconductor.[4,6,8,9] This measured value reflects the average tensile strain for the four layers of TSQDs in our Raman sample. It is slightly lower than expected from the 3.7% lattice mismatch between Ge and InAlAs, which we attribute to the fact that some of the TSQDs are strain relaxed from threading dislocations (compare Figure 5.3(a) and 5.3(b)). Figure 5.3 shows that dislocations form at the InAlAs/Ge/InAlAs interface (Figure 5.3(a)) and that some Ge TSQDs have these dislocations next to them (left TSQD in Figure 5.3(b)) or within them (central TSQD in Figure 5.3(b)), with some TSQDs being free of defects entirely (rightmost TSQD in

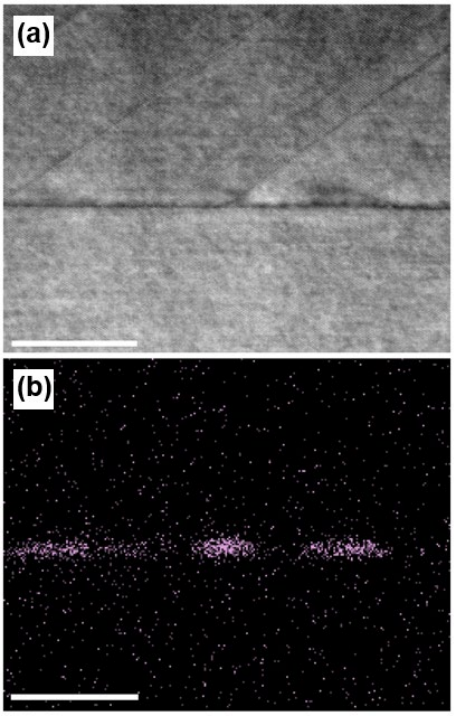

Figure 5.3 (a) STEM high angle annular dark field (HAADF) image of a 1.4 ML Ge/InAlAs(110) TSQD sample grown at 525 °C. (b) corresponding EELS map from the area in (a) showing the spatial distribution of Ge counts in pink. The white scalebars are 20 nm. The zone axis is $[\bar{1}10]$.

Figure 5.3(b)). As with our previous work on Ge/InAlAs(111)A TSQDs, we see asymmetric broadening of the Ge(110) TSQD phonon peak towards lower wavenumbers, which occurs due to optical phonon confinement in the TSQD arrays (Figure 5.2).[26,333–335]

EELS shows no evidence of As or group III desorption differences at this interface, nor any interdiffusion between the Ge TSQDs and surrounding InAlAs crystal (Figure 5.3(b)). There is no evidence of anti-phase boundary formation (Figure 5.3(a)); this is a result we expect to see on this surface orientation.[59,60]

The AFM images in Figure 5.1 suggest that Ge(110) TSQDs are preferentially elongated parallel to $[\bar{1}10]$. To explore this structural asymmetry, we grew a series of 2.4 ML Ge(110) TSQD samples at different values of T_{SUB} for imaging with high resolution AFM (Figure 5.4). These samples were grown with increased substrate temperature

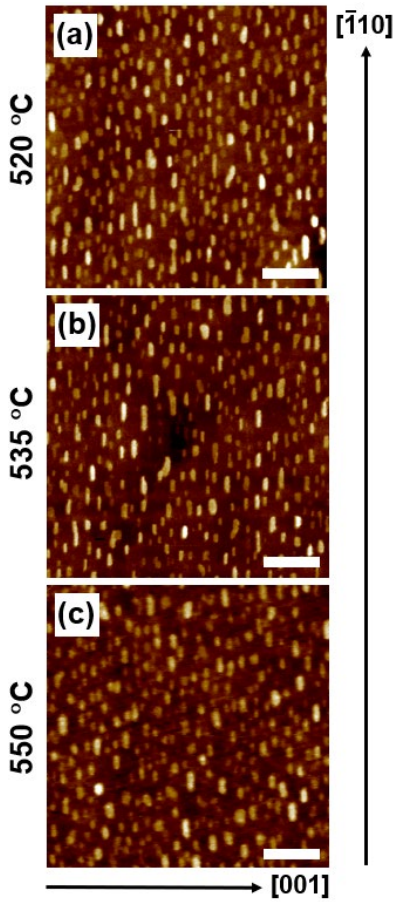

Figure 5.4 500 × 500 nm^2 AFM images showing the evolution of 2.4 ML Ge/InAlAs(110) surface morphology with substrate temperature. The arrows indicate the directions for the [$\bar{1}$10] and [001] directions. The scalebar is 100 nm. For all images, the z-scale is 5 nm.

precision after routine MBE maintenance and thus the 550 °C series completed for Figure 5.1 is similar but slightly different than the 550 °C sample in Figure 5.4(c). As we increase T_{SUB} from 520–550 °C, we show that we can control the size, areal density and shape of the Ge(110) TSQDs (Table 5.1).[19,21,26,43,90] A slight decrease in average TSQD areal density at higher substrate temperature is consistent with longer adatom diffusion lengths.[18,19,21,26,374,375] Since we deposit the same 2.4 ML of Ge in each case, a decrease in areal density must be accompanied by an increase in average TSQD size.[18,21,26,43,375]

Table 5.1 Substrate temperature dependence of particle analysis and aspect ratio data for 2.4 ML Ge(110) TSQDs.

Substrate Temperature (°C)	Areal Density (1E11 cm^{-2})	Avg. Height (nm)	Avg. [001] Length (nm)	Avg. [$\bar{1}$10] Length (nm)	Avg. QD Aspect Ratio [$\bar{1}$10]/ [001]
520	1.25	1.6 ± 0.61	9.1 ± 1.8	28.2 ± 9.3	3.18 ± 1.09
535	1.09	1.9 ± 0.62	9.3 ± 2.0	25.7 ± 8.4	2.86 ± 1.05
550	1.09	2.0 ± 0.60	12.1 ± 3.1	24.7 ± 6.1	2.10 ± 0.43

Indeed, as we raise T_{SUB} from 520–550 °C, the average TSQD height increases from 1.6±0.6 nm to 2.0±0.6 nm (Table 5.1).

The overall shape of the Ge(110) TSQDs in Figure 5.4 is rather unusual. They are discrete "fin-like" nanostructures, the vast majority of which have seemingly straight edges parallel to (001) and $(\bar{1}10)$. The longer edge of these rectangular prisms is consistently aligned parallel to the $[\bar{1}10]$ direction, reflecting 2-fold rotational and mirror symmetries.

Elongated self-assembled nanostructures are seen in other material systems, for example compressively strained InAs/InAlAs(001), InAs/AlAsSb(001), and InP/InGaP(001).[236,277,285] However the morphology of those elongated compressively strained nanostructures on (001) surfaces is typically quite different from what we see for the Ge(110) TSQDs in Figure 5.4. Most notably, the discrete nature of the Ge(110) TSQDs contrasts with the compressively strained nanostructures that tend to cluster together such that they almost touch (Figure 5.5(a)). The compressive (001) nanostructures can be hundreds of nanometers long, with widths that, though similar in

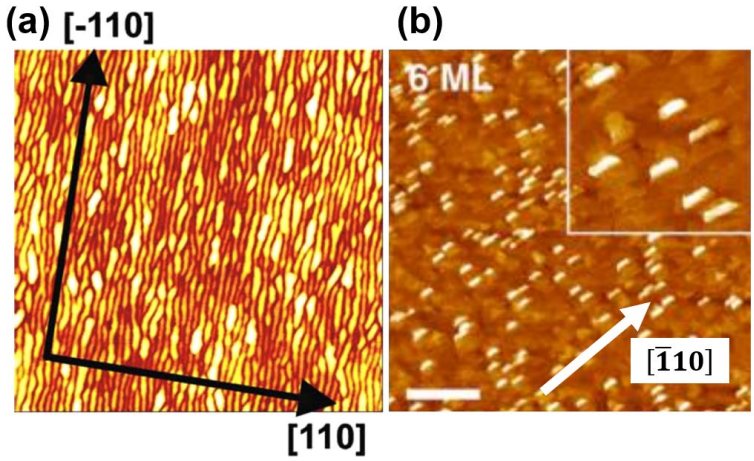

Figure 5.5 (a) 1 × 1 µm^2 AFM image of compressively-strained, self-assembled InAs/InAlAs(001) nanostructures. From Reference [236]. (b) AFM image of 6 ML GaAs TSQDs on InAlAs(110), where the white scalebar is 1 µm, the inset is 1 × 1 µm^2, and the z-scale is 4 nm. Adapted from Reference [22]. Both (a) and (b) show QD alignment parallel to [$\bar{1}$10].

scale to the Ge(110) TSQDs in Figure 5.4, vary along the length of the nanostructure, removing any symmetry (Figure 5.5(a)).[236,277,280,282,285,376]

Perhaps the closest resemblance to these Ge(110) TSQDs are the discrete GaAs TSQDs that self-assemble on InAlAs(110), which adopt a trapezoidal-like asymmetry (Figure 5.5(b)).[22]

As we increase T_{SUB} from 520–550 °C, the ratio between the length/width of these fin-like Ge(110) TSQDs, changes measurably (Figure 5.4). With high resolution AFM (Figure 5.6(a)), we can build up reliable statistics for average length (along [$\bar{1}$10]) and width (along [001]) by accurately measuring a large number of individual TSQDs on each sample (Table 5.1). At 520 °C, the Ge(110) TSQDs are less uniform in size and have an aspect ratio ([$\bar{1}$10]/[001]) of 3.18±1.09. As we increase T_{SUB}, the TSQD aspect ratio decreases, indicating that they are becoming less elongated and more symmetric. At 550 °C, the average TSQD aspect ratio is reduced to 2.10±0.43 (Table

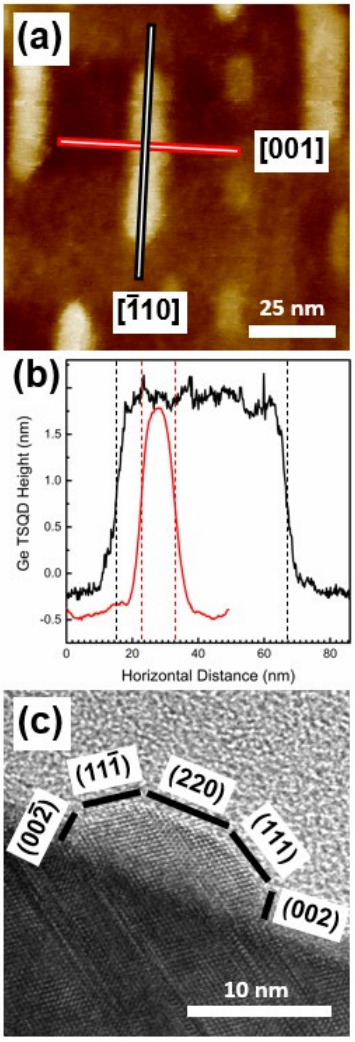

Figure 5.6 (a) 100 × 100 nm^2 AFM image of a 2.4 ML Ge TSQD grown at 535 °C and 0.025 ML/s. The z-scale is 5 nm. (b) Height profiles along [$\bar{1}$10] (black) and [001] (red) for a Ge TSQD shown in (a). The vertical dashed lines indicate the approximate FWHM limits used to determine QD lengths along each direction. (c) High-resolution STEM image of the cross-section of a single Ge(110) TSQD with identifiable facets labelled.

5.1). Figure 5.6(c) reveals a similar, flat-topped TSQD shape to that seen in Figure 5.6(b), a discussion for which is described later in this section.

We attribute the elongation of the Ge TSQDs to the natural anisotropy in adatom diffusion on a (110) zinc-blende surface.[19,375] Figure 5.7 depicts the two dominant pathways for Ge adatom movement on an InAlAs(110) surface according to our computational model. We calculated overall diffusion barriers of 0.36 eV for Ge

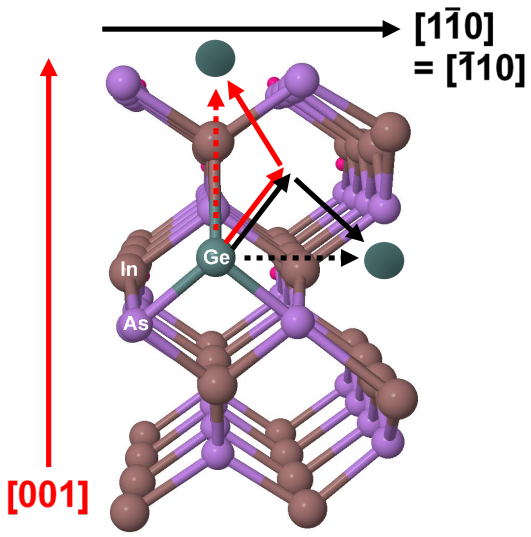

Figure 5.7 InAlAs(110) crystal structure with a Ge adatom and its accompanying paths of lowest energy diffusion (solid black and red arrows). The dashed arrows indicate the total distance moved by a Ge adatom along [1$\bar{1}$0] (black) or [001] (red).

diffusion in the [$\bar{1}$10] direction, and 0.72 eV for diffusion towards [001]. The fact that the diffusion of adatoms will be faster in the [$\bar{1}$10] direction for the T_{SUB} range studied here leads to the elongated TSQDs we observe. The ratio of the orthogonal adatom diffusion coefficients, $D_{[\bar{1}10]/[001]}$, is shown in Equation 5.1:

Equation 5.1

$$D_{\frac{[\bar{1}10]}{[001]}} = \frac{D_0 \exp\left[\frac{-0.36\ eV}{k_B T_{SUB}}\right]}{D_0 \exp\left[\frac{-0.72\ eV}{k_B T_{SUB}}\right]} = \exp\left[\frac{0.36\ eV}{k_B T_{SUB}}\right]$$

Where D_0 is the adatom diffusion constant, and k_B is the Boltzmann constant. At 520°C we calculate $D_{[\bar{1}10]/[001]}$ = 194, which reduces to 160 at 550 °C. The decreasing value of this ratio suggests reduced anisotropy in Ge adatom diffusion at higher T_{SUB}, and hence more symmetric TSQDs, in agreement with what we observe experimentally in Figure 5.4. By this analysis, the aspect ratio should approach unity at a high enough growth temperature, allowing us to produce highly symmetric TSQDs. In reality

however, 550 °C serves as a practical limit to how hot we can take the InAlAs(110) surface before detrimental effects begin to occur.[26]

This is obviously a simplistic analysis, however. A more comprehensive model would need to account for differences in adatom detachment and diffusion rates at step edges parallel to $[\bar{1}10]$ and $[001]$, as well as anisotropic corner diffusion between them.[90,368,377] We see that areal density decreases with substrate temperature; however, a lower density also means that the islands should increase in size.[18,21,26,43,375] Instead, we see a decrease in QD length/width along both $[\bar{1}10]$ and $[001]$, indicating that there is another adatom diffusion consideration at play. The resolution to this contradiction is that more mass diffuses to higher layers, which we see in the increase of TSQD height at 550 °C. The other factor is that at higher T_{SUB}, the probability that an adatom can diffuse up a step edge to the top of an island increases. This is borne out in the data of Table 5.1, which shows that even as the average in-plane area of the TSQDs is decreasing with higher temperature, average TSQD height increases. Research shows that in kinetically-driven processes, QDs avoid each other by increasing their height,[378] which is what we see in Ge(110) TSQDs. Additional diffusion factors, such as adatom diffusion along the $(\bar{1}10)$ and (001) QD edges and around other QD facets/corners, adatom detachment, and adatom desorption complicate the diffusion analysis.[285,368,377] Anisotropy in surface diffusion lengths likely has a significant influence on the QD shapes we see here.[285,377] For this reason, it is very complicated to directly relate the aspect ratio to the diffusion constants.

We were interested to see if anisotropic adatom diffusion also led to differences in TSQD separation in different directions on the sample surface. We used radial

distribution functions (RDFs) to look for clustering of the Ge TSQDs at some preferred distance (Figure 5.8(a)), following similar analyses of Ge and GaAs TSQDs on InAlAs(111)A.[43] Small peaks above one (i.e. the expected curve for a uniform distribution) show a weak preference for clustering of the TSQDs with a separation of ~27 nm, with no clear change as a function of T_{SUB}. However, the circular symmetry of the RDF analysis obscures any anisotropy we see in TSQD separation along the $[\bar{1}10]$ and $[001]$ directions. We therefore constructed a linear distribution function (LDF) approach for analyzing TSQD separations specifically in the $[\bar{1}10]$ and $[001]$ directions as a function of T_{SUB} (Figure 5.8(b),(c)). Similar to previous studies, the first peaks are directly related to capture zone width and thus the adatom diffusion lengths along the investigated directions.[43,379] In the $[001]$ direction we see a shift in preferred separation distance as T_{SUB} varies (Figure 5.8(b)). At T_{SUB} = 550 °C, there are possible peaks at 15, 30, and 45 nm along $[001]$, but these are not particularly distinct. RDF analysis at this temperature also indicates that there is a reduced chance of finding TSQD centers between 15-30 nm at higher temperatures compared to lower temperatures (Figure 5.8 (a)). This is indicated by the slight decrease in peak height at 550 °C compared to 520 °C (Figure 5.8(a)). Reducing T_{SUB} to 535 °C gives similar nearest neighbor distances as the 550 °C sample, but the nearest neighbor correlations increase, particularly at 15 nm and 45 nm (Figure 5.8(b)). This means that compared to the 550 °C sample, the 535 °C sample has more short-range order, i.e. periodicity, between TSQDs along $[001]$. Further reducing T_{SUB} to 520 °C reveals a stronger shift in spacing with peaks at ~27 nm and 55 nm (Figure 5.8(b)), meaning that the QDs are not as close together for the low temperatures along $[001]$. We attribute this to mass conservation: the increased

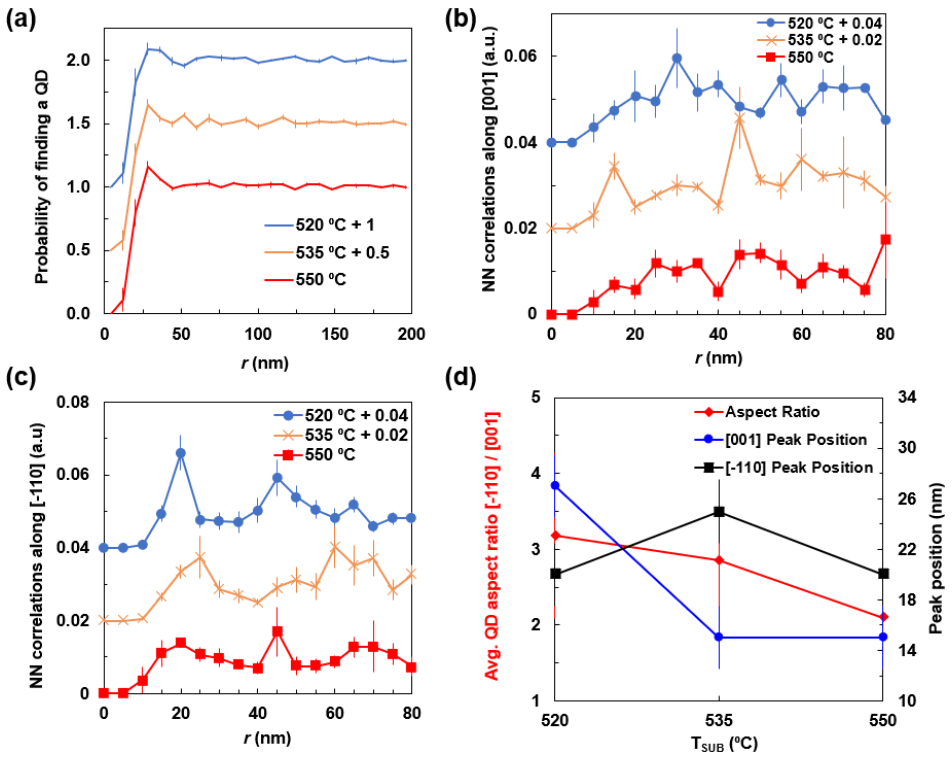

Figure 5.8 (a) Radial distribution functions indicating the most probable distance between the radii of Ge(110) TSQD centers. (b),(c) Linear distribution functions illustrating nearest neighbor (NN) correlations along (b) [001] and (c) [-110] directions for Ge(110) TSQDs. (d) Plot comparing average QD aspect ratios to the first peak positions from (b) and (c) for Ge(110) TSQDs. All plots compare these quantities to the substrate temperature, T_{SUB}.

elongation towards $[\bar{1}10]$ at low temperatures increases the separation distance towards [001].

In contrast, LDF data along $[\bar{1}10]$ does not show a significant change in preferred separation distance between temperatures (Figure 5.8(c)). We see that between 520-550 °C most peaks are at ~20-25 nm with echoing peaks at ~45 nm and ~65 nm (Figure 5.8(c)). Focusing on the first, ~20 nm peaks, the nearest neighbor correlations decrease with increasing temperature (Figure 5.8(c)). In general, we see that at T_{SUB} = 520 °C the QDs have lower uniformity in size and shape (see Table 5.1), but their spacing is more ordered along $[\bar{1}10]$ than [001]. This contrasts with the sample grown at 550 °C, which

has broader, less distinct peaks along both directions (Figure 5.8(c)). We attribute this effect to longer adatom diffusion lengths at higher growth temperatures, which reduce the uniformity in TSQD spacings by giving adatoms more energy to move further on the surface.[21,26,43,72]

LDF data appears to inversely reflect the TSQD aspect ratio with changing T_{SUB} (Figure 5.8(d)). The aspect ratio decreases from 3.18±1.09 at 550 °C to 2.10±0.43 at 520 °C. The LDF shows that while the preferred separation distance between TSQD centers along $[\bar{1}10]$ remains approximately the same across the T_{SUB} range studied, the preferred separation distance along $[001]$ increases with decreasing temperature (Figure 5.8(d)). This change indicates that the QD aspect ratio changes with temperature, but it also shows that mass conservation plays an important part in the overall separation distances for elongated TSQDs.

The integer increase in peaks along each direction indicates short range periodicity between the TSQDs (Figure 5.8(b),(c)). These echoing peaks disappear after about 80 nm, indicating no long-range periodicity in TSQD arrangements. Research on compressively strained InP QDs grown on $In_xGa_{1-x}P(001)$ and InAs QDs grown on $In_{0.52}Al_{0.48}As(001)$ shows that growth parameters have a strong impact on self-assembled quantum dot periodicity/arrangement.[236,280–282,285] We see this strong dependence of TSQD arrangement on growth parameters reflected similarly in this Ge/InAlAs(110) system.

Interestingly, despite the inherent differences between Ge(110) TSQDs and compressively strained InP/$In_xGa_{1-x}P(001)$ QDs, these two systems both have flat-topped quantum dots (Figure 5.6).[281,285,376]

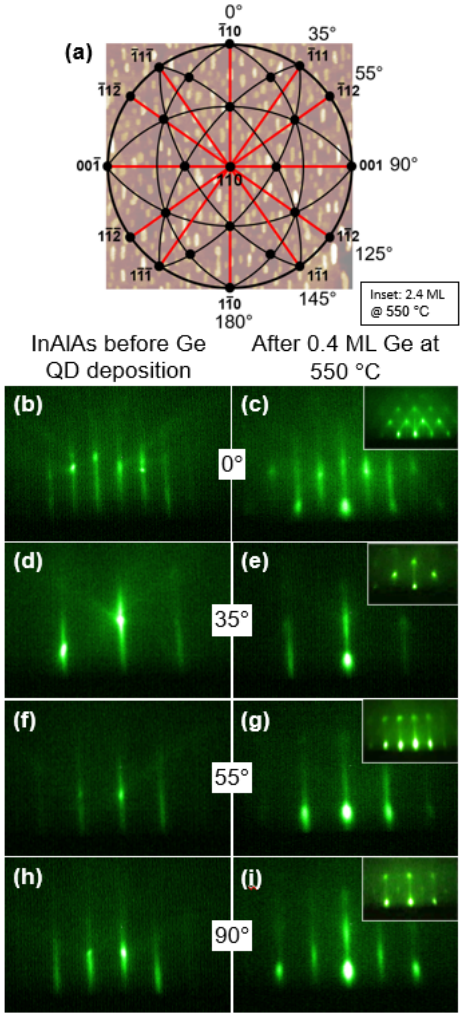

Figure 5.9 (a) A (110) stereographic projection labelled with important directions and angles, overlaying a 500 × 500 nm^2 AFM image of a 2.4 ML Ge TSQD sample grown at 520 °C. The z-scalebar for this AFM image is 5 nm. (b)-(i) RHEED images taken before (b, d, f, h) and after (c, e, g, i) Ge deposition at different angles: (b, c) at 0°, (d, e) at 35°, (f, g) at 55°, and (h, i) at 90°. For (c, e, g, i), we deposited 0.4 ML Ge at 550 °C. The RHEED insets in (c, e, g, i) were screen-captured from a video taken while rotating a 2.4 ML Ge sample grown at 550 °C.

Upon deposition, the RHEED immediately changes from streaky to spotty, but with depositions greater than 0.4 ML, we see a few interesting details form (Figure 5.9). Along [$\bar{1}$10], our 0° position, we see diagonal reciprocal lattice rods (hereafter rel-rods) form at approximately a 45° angle from the original streak, orthogonal to the incident beam (Figure 5.9(c)). These orthogonal streaks may be indicative of {112} and {111}

facets. FFT analysis of our high-resolution STEM images indicates that looking along $[\bar{1}10]$ shows (111) and $(11\bar{1})$ facets (see Figure 5.6(c)). This does not mean that $\{112\}$ facets are not present, but we were not able to find them using a $[\bar{1}10]$ zone axis in STEM.

We continue to see streaks in these RHEED patterns at 2.4 ML Ge deposition (Figure 5.9). In a typical InAs/GaAs(001) growth, the streaks completely disappear as the spotty QD signature dominates.[80] However, InAs QDs on GaAs(001) form highly-faceted dome-like structures.[80] The streaky-spotty combination seen on the Ge(110) RHEED pattern thus provides additional evidence that the QDs themselves have flat tops. Flat-topped QDs are unusual, because strain acts against flattened islands.[378] Research indicates that there is an interplay between kinetics and surface energy that significantly complicates interpreting QD shape.[227,378]

We can consider surface energy effects on Volmer-Weber QD shape in terms of the wetting angle.[378] Adjusting the square Figure 5.6(a) x- and y-axes to the same scale, we determined the approximate wetting angle for these Ge(110) TSQDs to be about 140-150° along both $[\bar{1}10]$ and $[001]$. The STEM image in Figure 5.6(c) reveals a much sharper wetting angle of 90-100° along the elongated $[\bar{1}10]$ QD direction, between the $\{110\}$ and $\{002\}$ facets. When looking at the angles between the $\{110\}$ and the $\{111\}$ facets, we again measure 140-150°, which matches up well with the AFM profile angles extracted from Figure 5.6(a). Since these two samples grown 30 °C apart appear to have similar wetting angles, we suggest that the surface energy does not change significantly in this temperature difference. This statement is supported by research showing that QD facets are not typically impacted by a change in substrate temperature.[380] Since surface

energy does not appear to change, we can contribute much of this unusual flattening affect to kinetics.[378] Müller and Kern suggest that QD shapes governed by kinetics will be flatter than those governed by thermodynamics.[378] We see from AFM profiles and cross-sectional STEM images that Ge(110) TSQDs do not share the same dome-like shape of typical InAs/GaAs QDs (see Figure 5.6).[80] Instead, they reveal flat-topped QDs.

5.3.2 Ge(110) Light Emission

The residual tensile strain in the Ge/InAlAs(110) TSQDs appears to have transformed Ge into a direct band gap semiconductor. We grew three samples at different deposition amounts (1.4, 1.9, and 2.4 ML) at the lowest T_{SUB} in our range, 520 °C.

When we compare PL from these three samples, we see a distinct emission peak at 2.8 μm appear for the 2.4 ML TSQD sample spectrum (Figure 5.10). We can assign all other peaks in the spectra and so we attribute this unaccounted-for peak to emission from the Ge(110) TSQDs. No similar peak is present for either the 1.4 ML or 1.9 ML TSQD samples. We believe that the smaller TSQDs of the 1.4-1.9 ML samples may lead to a loss of confined states. Other peaks in Figure 5.10 at 1.0 μm (~1.3 eV) and 1.25 μm (~1.0 eV) can be attributed to the InP and InAlAs-Ge top interface, respectively.[27,381] We also see a broad peak at 3.6-4 μm, which is from Fe^{2+} deep-level recombination in the semi-insulating InP(110) substrates.[382]

The Ge-related light emission at 2.8 μm (~0.44 eV) is 0.45 eV lower than the bulk Ge direct band gap of 0.89 eV.[27] This red shift is consistent with previous research demonstrating that tensile strain reduces a materials' band gap,[4,6,8,9,27] and this band gap energy is close to Tahini *et al.*'s calculated value of 0.47 eV.[4] Experimentally, these values also align well with the PL emission value of ~0.48 eV in Ge(001) TSQDs from

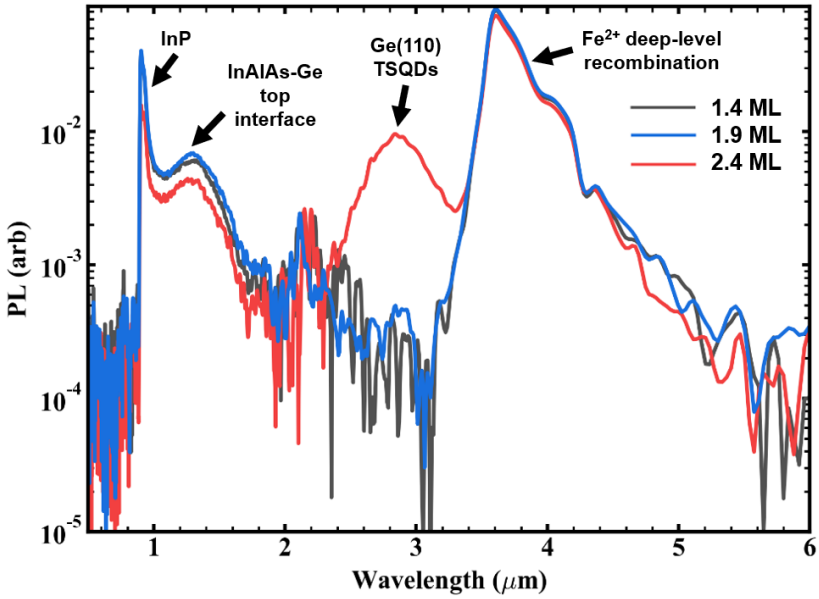

Figure 5.10 77 K PL spectra from three Ge/InAlAs(110) TSQD samples grown with different Ge coverages.

the work by Chen *et al*.[27] Although Chen *et al*. show that their 0.48 eV peak is relatively weak, ours is comparatively bright (Figure 5.10).[27] This is likely due to the fact that (001)-oriented zinc-blende semiconductors emit in-plane.[383] Since in-plane directions for (001) are related to the ⟨110⟩ family of directions,[383] we anticipate that our (110) TSQDs will be brighter, which we see in Figure 5.10. This 0.44 eV peak can be attributed to a conduction band (CB) to light hole (LH) transition.[27]

We discovered that the 2.4 ML Ge TSQD sample emits light only in locations where the sample is scratched (see Figure 5.11). Shiny regions free of scratches, (e.g., "dim regions") do not appear to have any TSQD light emission. We plan to soon test whether this is the reason we do not see light emission from smaller deposition amounts (Figure 5.10). These scratches indicate that Ge(110) TSQDs emit light laterally, which could be important for developing edge-emitting lasers or LEDs. This is particularly interesting for practical applications such as fiber optic communications that would benefit from the more singularly directed light of edge-emitters.[384]

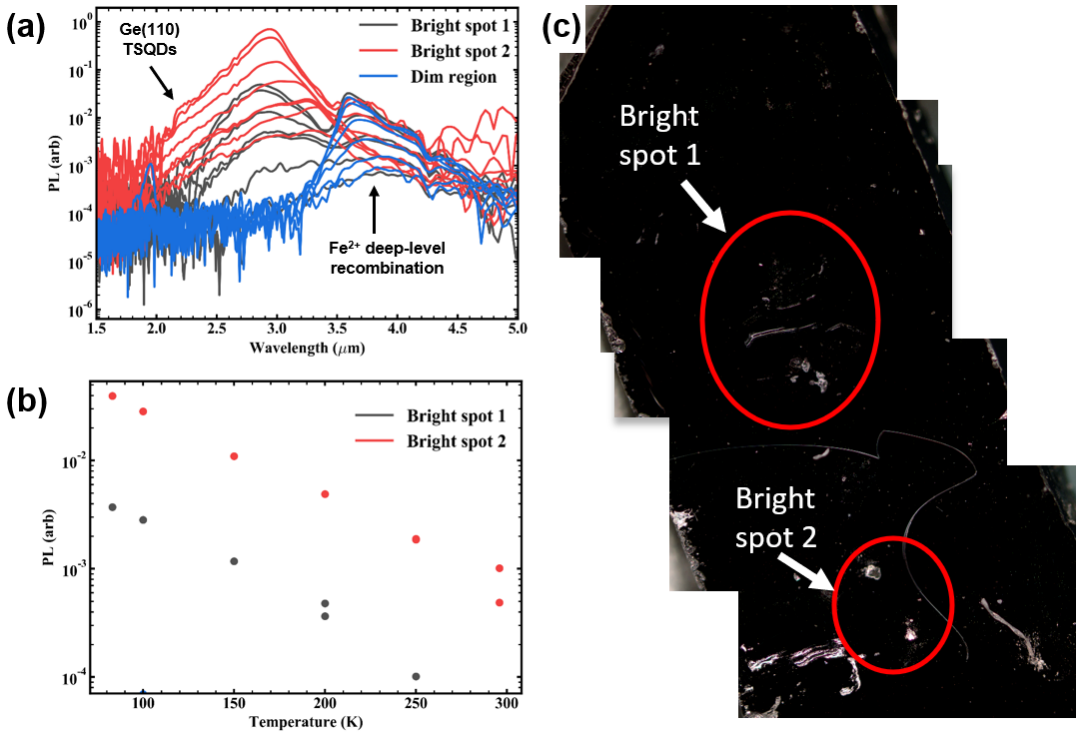

Figure 5.11 (a) Temperature-dependent PL spectra on 2.4 ML Ge TSQDs, where (b) shows the corresponding emission efficiency decrease with increasing temperature. The bright spot locations are defined in (c), which are close-up photographs of the sample surface. The blue spectra (i.e., the "dim region") is from shiny locations on the sample surface, whereas the bright spots originate from scratches.

Although PL emission intensity decreases with increasing temperature as expected due to increased phonon interaction,[27,141,385] Figure 5.11 shows that emission from the Ge(110) TSQDs persists up to room temperature, indicating excellent optical quality. Room temperature emission from Ge(110) TSQDs is a big improvement over the emission from the Ge(001) TSQDs reported by Chen *et al*. which was quenched above 100 K. Further optimization is needed to improve room-temperature light emission, but this initial finding is promising for the development of edge-emitting LEDs and lasers based on direct band gap Ge TSQDs.

5.4 Conclusions

Defect-free Ge/InAlAs(110) TSQDs grow via the Volmer-Weber growth mode in symmetrical, elongated shapes with unusual flat tops. These TSQDs are distinctly separated along the major axes of the substrate so that short-range ordering in TSQD arrangement exists. We attributed the shapes and growth behavior of the TSQDs to a high anisotropy in adatom diffusion lengths, owing to the surface symmetry. Importantly, we demonstrate the first room-temperature, direct-band gap light emission from tensile-strained Ge quantum dots grown on InAlAs(110). These TSQDs could lead to novel edge-emitting infrared lasers and LEDs for a wide range of optoelectronic applications in communication, medicine, and defense.

5.5 Supplemental Information

5.5.1 Atomic Force Microscopy (AFM)

A Bruker Dimension FastScan AFM operating in Bruker's proprietary Peakforce Tapping mode, which utilizes rapid force curve acquisition to image sample topography, was used for AFM imaging. All images were obtained with a Bruker PeakForce-HIRS-F-A probe (k = 0.35 N/m, f_0 = 165 kHz) with a 1 nm radius of curvature and 15°/25° front/back angle. Sequentially smaller image sizes of 5 μm x 5 μm and 1 μm x 1 μm were acquired for each sample to enable identification of areas of interest for high resolution 500 nm x 500 nm and 100 nm x 100 nm imaging. Typical parameters representative for a 500 nm x 500 nm scan included a low PeakForce Setpoint of ~650 pN to minimize damage to the sample or dulling of the probe tip, and a PeakForce frequency of 2 kHz coupled with a 1 Hz scan rate and 512 samples/line to ensure at least 2 force curves/data point (i.e., 2 tip-sample interactions per pixel) and ~1 nm pixel resolution (i.e.,

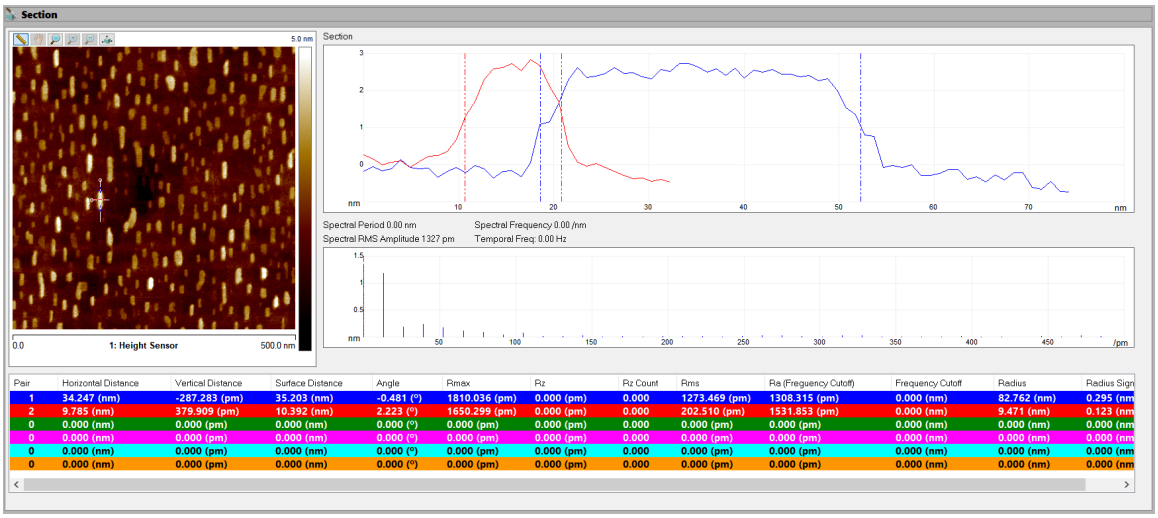

Figure 5.12 Representative lateral dimensions measurement of a Ge TSQD using the rotating line section tool along $[\bar{1}10]$ (i.e., the 'y' direction) and $[001]$ (i.e., the 'x' direction).

approximately equal to the nominal probe radius). Due to the extremely small heights of the TSQDs and overall low surface roughness of the samples, a reduced Z limit of 1 μm or less was employed to maximize the Z resolution of the A/D board.

Prior to imaging, each sample was carefully oriented to ensure the $(\bar{1}10)$ plane was perpendicular to the scanning direction of the probe. AFM image processing and analysis were conducted using NanoScope Analysis Version 2.0 (Bruker). Prior to quantitative analysis, raw image files were processed using a first order plane fit to remove sample tip and tilt, followed by a first order flatten if necessary. After image processing, TSQD dimensions were determined using a cross-section tool as shown in Figure 5.12. For consistency and to minimize the effects of AFM tip dilation (which will artificially increase the apparent TSQD length and width due to the finite probe diameter and geometry), lateral dimensions were calculated as full width at half maximum (FWHM), while TSQD heights were measured relative to the baseline (i.e., surrounding substrate) using NanoScope Analysis's built-in particle analysis tool. TSQD aspect ratios

were calculated by measuring the TSQD FWHM dimensions along both the major and minor axes in the X-Y plane. To generate statistics, fifty (50) TSQDs per sample were analyzed in this way, with the results summarized in Table 5.1.

5.5.2 Scanning Transmission Electron Microscopy (STEM)

The sample imaged with STEM contained one buried layer of 1.4 ML Ge TSQDs grown at 525 °C, and a second layer of Ge TSQDs grown on the surface under identical MBE conditions. The zone axis for STEM was $[\bar{1}10]$. We performed a 2D fast Fourier transform (FFT) of cross-sectional STEM images and indexed the resulting spots. We masked the FFT to select a single set or single family of spots and took the inverse FFT (IFFT) of this mask to create an image showing only the periodicity captured in the masked portion of the FFT. We then zoomed in on the real space and IFFT images to compare specific regions, identifying crystallographic planes in the real image. We confirmed this quantitatively by taking careful angle measurements between selected planes. We repeated these steps for all planes of interest.

Acknowledgements

The authors thank Dr. Elton Graugnard and the Boise State Surface Science Laboratory for AFM imaging of TSQDs and helpful discussions regarding image processing and analysis. The authors also thank Dr. M. Larry Lee for the help understanding our RHEED patterns. Many thanks also to Matthew B. Abramson and Patrick D. Eusepi for their assistance with AFM analysis.

This material is based upon work supported by the Air Force Office of Scientific Research under award number FA9550-16-1-0278.

CHAPTER SIX: FUTURE WORK

Abstract

Since the work within this dissertation is so new, the area of self-assembled tensile-strained germanium quantum dots (Ge TSQDs) offers many unexplored areas for continued research and development. In this chapter, I provide several avenues for exploration in this exciting area of materials science. Since we only recently discovered that Ge(110) TSQDs emit light at room temperature, that is the first system I would choose to investigate, with the eventual goal of creating a Ge-based light-emitting diode (LED) or laser. I would also be interested to study the semimetallic behavior we anticipate for the Ge/InAlAs(111)A TSQDs, which could be used to increase the efficiency of multijunction solar cell and thermoelectric devices for renewable energy applications.[10,102,104] In addition, I provide a few other ideas, for example using (211), (111)B, and offcut substrates to develop novel semiconductor devices based on tensile-strained Ge, or adopting migration-enhanced epitaxy (MEE) at the onset of the InAlAs cap growth to reduce top barrier defects, thus increasing the emitted light intensity from our Ge TSQDs. I hope that this chapter acts as a roadmap for future optoelectronic devices based on Ge TSQDs.

6.1 Exploring Ge's direct band gap light emission and its applications

In Chapter 5, we demonstrated the first-ever light emission from direct band gap Ge(110) TSQDs. We showed that 2.4 ML Ge(110) TSQDs grown at 520 °C emit light with a wavelength of 2.8 μm, even at room temperature. We noted that the light came out

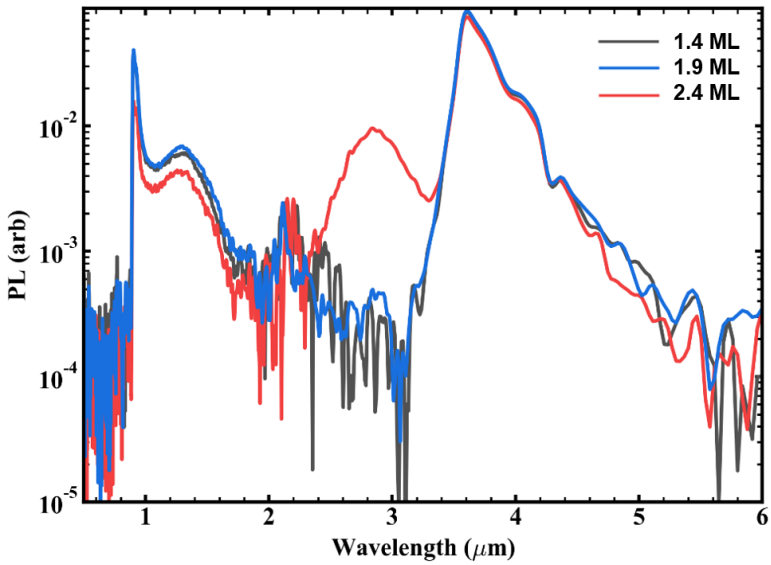

Figure 6.1 PL spectra of three different Ge TSQD samples grown with different deposition amounts. We obtained all PL spectra at ~77K.

of scratches and areas where there was indium metal on the surface. One thing we were unable to do prior to submitting this dissertation was test the other two samples grown at 1.4 ML and 1.9 ML for these scratch- and/or indium-related emission peaks (Figure 6.1). The metal on the surface may be causing out-coupling of light from in-plane transverse-magnetic polarized light-hole exciton recombination, possibly due to plasmonic waveguiding at the surface.[27,373,386,387] If so, we will want to fabricate metal structures, such as gratings, in a cleanroom to enable out-coupling in an efficient way. We can then use this approach to collect polarization-dependent emission along different crystal axes by making grating arrays at different angles.

In addition, we should grow samples with larger TSQD amounts, starting at 2.6 ML and increasing until we see plastic deformations. Knowing the min-to-max deposition amounts and their accompanying PL will tell us the range of possible IR emission wavelengths, which will increase light emission tunability for optoelectronic devices based on these Ge(110) TSQDs. I expect that larger TSQDs will be further red-

shifted due to the increased quantum confinement well size.[3,21,22,98] For this reason, we should perform these growths on undoped InP(110) substrates. Using undoped InP(110) will be important at higher deposition amounts, because we want to prevent the 3.5-4 μm Fe^{2+} deep-level recombination (Figure 6.1) from obscuring light emission from larger TSQDs. Since TSQDs will be increasingly red-shifted by quantum confinement effects as we grow the TSQDs bigger (see Chapter 1, Section 1.2.5 for more information on this),[3] ensuring there is no Fe^{2+} emission is important for this future work.

Once we show the dependence of the Ge(110) TSQD light emission on deposition amount, we should also explore how other MBE growth parameters affect the emitted light. Based on GaAs(111)A TSQD research, optimizing the MBE growth parameters is the natural next step for enhanced light emission.[21,90] Exploring how substrate temperature (T_{SUB}) and Ge growth rate impact the intensity of emitted light will be crucial for optimizing TSQD growth conditions for future optoelectronic devices based on this material system. Understanding how growth parameters affect light polarization, room temperature emission intensity, and quantum efficiency are all important for the successful integration of Ge(110) TSQDs into LEDs and lasers. An additional step will be optimizing the initiation of the InAlAs capping layer, which I discuss in more detail in Section 6.4. Once we optimize these parameters, we should build LEDs and lasers with these TSQDs and see how they perform compared to analogous compressively strained systems, such as one of the most well-studied systems, $In_xGa_{1-x}As/GaAs(001)$.[114]

I want to emphasize that mid-IR lasers based on self-assembled Volmer-Weber TSQDs will be much easier, quicker, and cheaper to grow than many other current devices used for producing light in this IR range. For example, quantum cascade laser

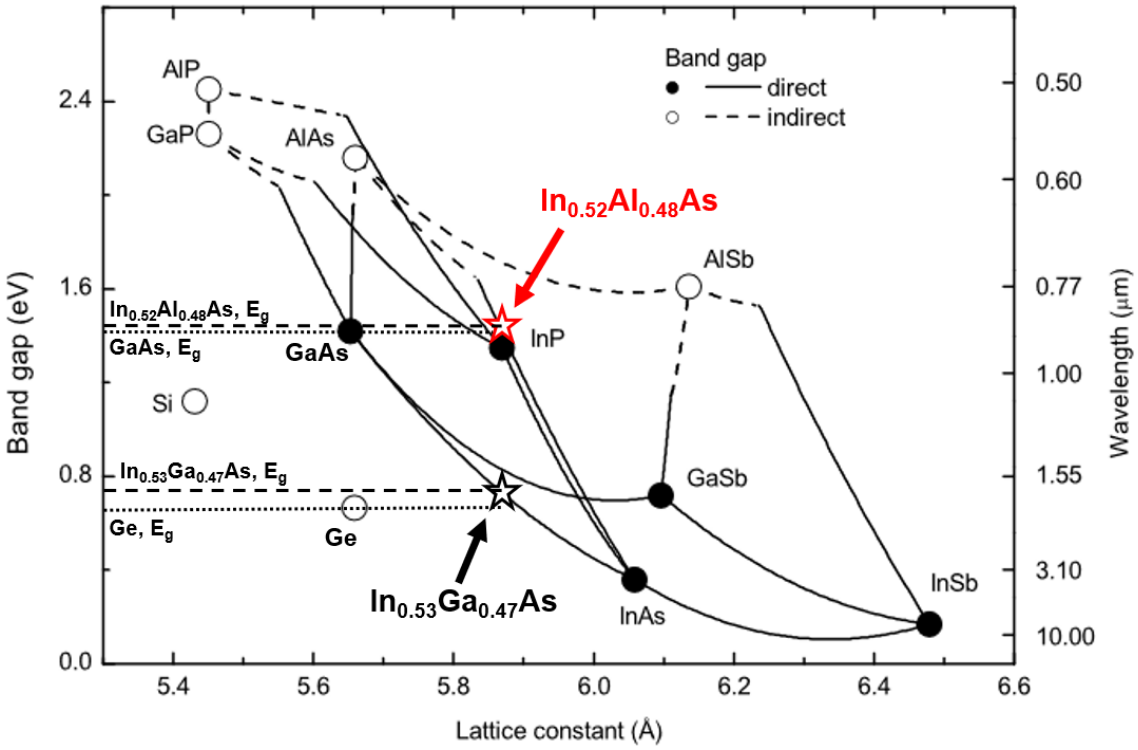

Figure 6.2 Lattice constant vs. band gap energy/wavelength for various group IV and III-V semiconductors. The lines connecting III-V semiconductors indicate ternary alloys. Solid lines and filled-in circles illustrate direct band gap semiconductors while dashed lines and open circles indicate indirect band gap semiconductors. The red star and black star indicate where $In_{0.52}Al_{0.48}As$ and $In_{0.53}Ga_{0.47}As$ lie on this diagram, respectively. The dashed line helps define where the bulk $In_{0.52}Al_{0.48}As$ and $In_{0.53}Ga_{0.47}As$ band gaps (E_g) are relative to the dotted line, which points out the E_g for bulk GaAs and Ge. Adapted from Reference [20].

approaches rely on many hundreds of quantum wells (QWs) with very specific widths that can take tens of hours to grow epitaxially.[388,389] Additionally, QD-based lasers have other benefits due to their delta-function density of states: they offer excellent temperature stability and comparatively low threshold currents than QWs.[156,157,201]

Finally, I suggest growing Ge TSQDs in $In_{0.53}Ga_{0.47}As(110)$. Since the $In_{0.53}Ga_{0.47}As$ band gap is larger than Ge's, quantum confinement should still occur (see Figure 6.2), plus InGaAs is much easier to grow via MBE than InAlAs.[52] Since this surface is different than InAlAs, Ge TSQDs on this surface may form in a different growth pattern. Depending on how the Ge TSQDs grow, the direct band gap emission

along different directions could change due to the TSQDs' symmetry. Although the confinement would not be as deep, GaAs(111)A TSQDs still experience Type I quantum confinement in InAlAs(111)A[21] even though the band gap difference is small between these two materials (Figure 6.2).[20]

6.2 Examining Ge/InAlAs(111)A TSQDs

While direct band gap Ge(110) TSQDs will be important for building novel, edge-emitting devices, semimetallic Ge on InAlAs(111)A could potentially improve the efficiency of an entirely different group of devices. In Chapter 3, I discussed several applications for Ge TSQDs grown on InAlAs(111)A. We could embed them in tunnel junctions for both surface-emitting lasers[103] and improved multijunction solar cell efficiency.[102] We could also embed them in thermoelectric energy conversion devices for an increased thermoelectric figure of merit.[104]

We first need to learn more about Ge/InAlAs(111)A TSQD semimetallic properties, then we can embed them into these devices for testing. An idea I have for testing whether or not the Ge TSQDs are semimetallic is based on the work by Zide *et al.*[102] I would grow two InAlAs(111)A samples, each with a p-n junction, where one of the samples contains Ge TSQDs inside the p-n junction while the other does not. We would need to deposit a simple front and back metal contact for the sample in a cleanroom, and then we could perform a current density vs. bias test on each. If we see a decrease in required forward bias to get the same current density as with the Ge-free p-n junction (e.g., for 10 mA/cm^2 we only need 0.3 V forward bias for the Ge TSQD-containing junction while the Ge-free junction needs 0.7 V to get the same current

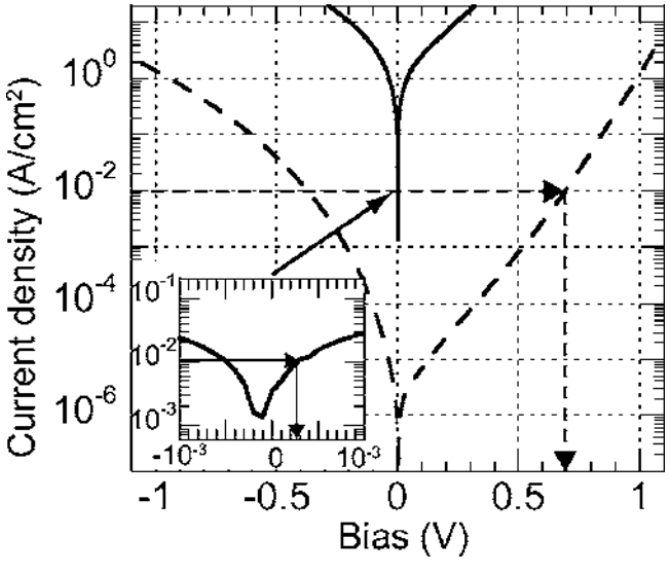

Figure 6.3 A current density vs. bias curve for a semimetallic ErAs nanoparticle-filled p-n junction (solid line) compared to the same p-n junction without ErAs (dashed line). The arrows point out the differences between the two junctions: the p-n junction with the ErAs nanoparticles needs far less forward (+) bias than the ErAs-free p-n junction to get the same current density. From Reference [102].

density[102]), then that would be indicative of semimetallic nanoparticles. An example for this is found in Figure 6.3.

After this initial testing, I want to replace the semimetallic nanoparticles from the aforementioned device references[10,102,104] with Ge/InAlAs(111)A. This way, we can see if Ge affects the tunnel junctions and thermoelectric devices differently than the ErAs and GaAs nanoparticles from these references.[10,102,104]

6.3 Investigating other substrates for novel tensile-strained Ge devices

I discovered how to grow Ge on nominally flat (i.e., on-axis, ±0.5°) InAlAs(111)A and (110) surfaces for the semimetallic and direct band gap transitions, respectively. However, these are not the only viable substrates we can use. We could explore several other surface orientations to see how they change Ge TSQD growth and band structure.

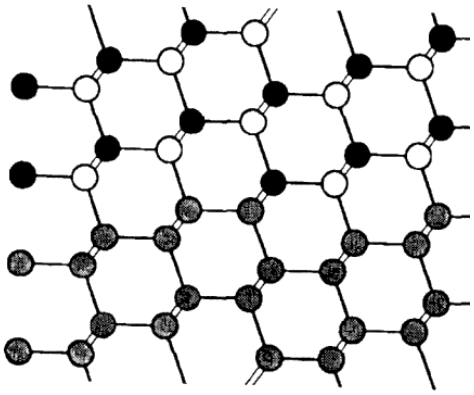

Figure 6.4 A cross-sectional diagram of ZB growth on a DC crystal with a (211) orientation. Despite step edges, there are no antiphase domains. The group III element is black, the group IV element is a mottled dark grey, and the group V element is white. Singly back-bonded group IV sites bond preferentially to group III atoms whereas doubly back-bonded group IV sites prefer bonding to group V atoms. Adapted from Reference [53].

One interesting surface we could investigate is the InAlAs(211) surface. Research suggests that it might be possible to grow zinc-blende (ZB) crystals that are free from APDs on diamond cubic (DC) materials with a (211) surface orientation.[53,390] The symmetry of the ZB/DC interface allows for only two types of bonding sites: singly back-bonded sites and doubly back-bonded sites (Figure 6.4).[53,390] These bonding types depend on the sublattice orientation of the two interpenetrating FCC lattices that make up the DC crystal.[53] This means that each possible site is not equivalent energetically or chemically.[53,390] As a result, in a GaAs/Ge system, As and Ga atoms will preferentially bond to the doubly or singly back-bonded Ge sites, respectively (Figure 6.4).[53,390] This means that even in the presence of single-height step edges, APD formation is unlikely.[53,390] For this reason, depositing Ge on InAlAs(211) may be successful. The caveat is that although we know tensile-strained self-assembly works on (110) and (111) surfaces,[19] the (211) surface has not yet been investigated.

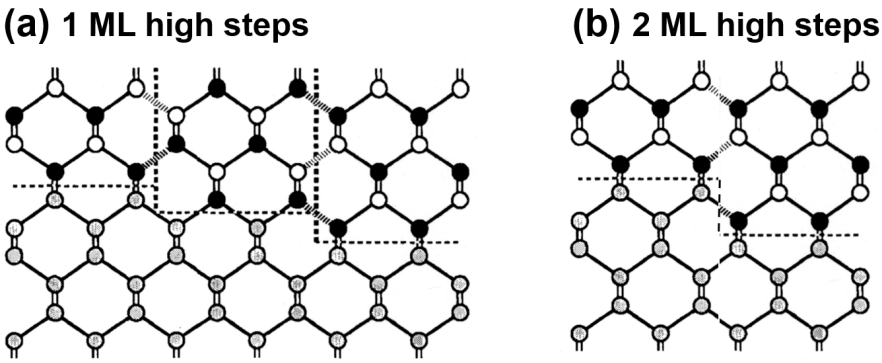

Figure 6.5 2D crystal representations showing a III-V material (black and white atoms) grown on a diamond cubic structure's (001) interface (grey atoms). In general, the dashed lines represent interfaces, but in (a), the vertical dashed lines separate APDs. (b) shows how increasing the step height from one to two monolayers (ML) eliminates APDs. Adapted from Reference [53].

Although tensile-strained self-assembly on (211) has not yet been tested, the effects this surface will have on the Ge band structure are remarkably similar to that seen on (111) surfaces: it should become semimetallic.[391] Thus, self-assembled, Ge TSQDs on this surface could be used in applications like those for Ge/InAlAs(111)A TSQDs: embedded in multijunction solar cells or for thermoelectric devices.[10,102,104] The key difference is that this surface orientation is relatively unexplored, and thus is a rich new area for developing novel electronic devices based on self-assembled Ge or even GaAs TSQDs.

Offcut substrates are another possibility for continued development of novel electronic devices based on self-assembled, tensile-strained Ge. Carefully choosing the offcut angle and its crystallographic direction can result in a terraced surface with steps two ML high. Polar materials (i.e., ZB crystals like InAlAs) grown on nonpolar materials (i.e., DC crystals like Ge) with a double-stepped surface have no opportunity to form APDs (Figure 6.5).[53] Therefore, we could use offcut substrates to create terraced InAlAs buffers on which we will synthesize the tensile Ge TSQDs. During subsequent capping of

the Ge TSQDs with InAlAs, the double-height steps will encourage formation of a top InAlAs barrier that is APD-free. Although we did not find APDs in our Ge TSQDs (see Chapters 3 and 5),[26] offcut substrates have the benefit of being easier to grow on than exactly-oriented substrates for the (110) and (111) surfaces.[19] Researchers used offcut substrates with great success to promote smooth, step-flow growth on non-(001) surfaces.[392,393]

One specific offcut substrate example could be for developing novel Ge/InAlAs(111)B devices. This surface might be interesting, because tensile-strained self-assembly of GaP on 2° offcut GaAs(111)B showed quantum wire (QWr) formation.[19] QWrs have different electronic properties than QDs, because unlike QDs, QWrs confine carriers in only two directions instead of three.[394] This makes QWrs particularly useful for electron waveguides and switchable high-speed lasers.[394] Growing tensile-strained Ge QWrs could open up novel devices in these areas. Additionally, since (111)-oriented tensile-strained Ge should be semimetallic,[4,6] the QWrs may be useful as embedded structures in solar cell tunnel junctions[10,102] and thermoelectric devices[104] while offering a different geometry than lens-shaped Ge/InAlAs(111)A TSQDs.[26]

6.4 Optimizing the capping layer for improved TSQD properties

While offcut (111) and (110) substrates may offer reduced dislocation formation in the InAlAs capping layer, this is not the only method we should consider for further optimizing the capping layer above the Ge TSQDs. The capping layer quality is essential for improved light emission, since this capping layer acts as the top barrier to our TSQDs (see also: light-emitting GaAs/InAlAs TSQDs).[21,22,26] Since dislocations act as

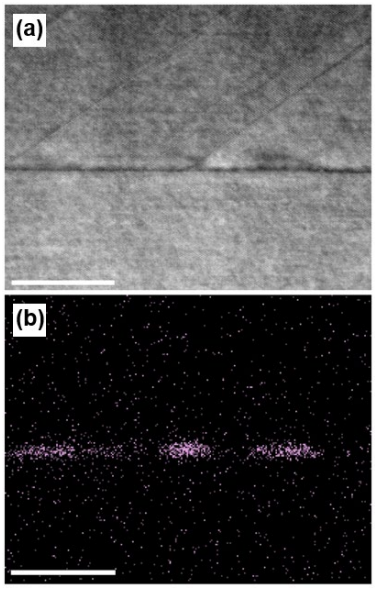

Figure 6.6 (a) STEM high angle annular dark field (HAADF) image and (b) accompanying EELS map showing the Ge counts in pink. The white scalebar is 20 nm. These are discrete, 1.4 ML Ge(110) TSQDs grown at 525 °C. From Chapter 5.

recombination locations, they reduce the overall emitted light and quantum efficiency of the system.[28]

Using offcut substrates may eventually be useful, but they do not improve the Ge TSQDs I already grew on nominally on-axis substrates. Instead for these on-axis systems, migration-enhanced epitaxy (MEE) may be particularly useful for reducing the dislocations we see in STEM (Figure 6.6). As I discussed in Chapter 1, Section 1.2.3.3, MEE enables the smooth, low-defect growth of III-V materials by increasing the adatom diffusion lengths for both the group III and group V elements.[61,65,66] MEE does this by alternating the deposition of the group III and group V elemental components, separated by short, annealing pauses.[61,65,66] Thus, performing MEE to initiate the growth of the InAlAs capping layer after Ge TSQD deposition could allow us to greatly improve its material quality. Due to its pulsed nature, MEE is slow, but it does not need to be used throughout the entire capping layer. Since the dislocations form at the InAlAs/Ge/InAlAs

interfaces (Figure 6.6), MEE will be most beneficial at the onset of capping layer growth. Once the Ge TSQDs are completely encapsulated, I suggest continuing the capping layer growth with traditional MBE to save time. Improving the capping layer quality will increase the emitted light intensity by reducing detrimental recombination centers, enhancing the efficiency of light-emitting devices based on Ge TSQDs.

6.5 Summary

I suggest that we continue the work found in this dissertation by: further investigating Ge(110) TSQD light emission; exploring the semimetallic properties of Ge/InAlAs(111)A TSQDs in tunnel junctions and thermoelectric devices; discovering how Ge self-assembles on (211), offcut, and (111)B substrates; optimizing the InAlAs capping layer formation; and finally making novel LEDs and lasers based on Ge TSQDs. This new and exciting area of research has the potential to unlock novel optoelectronic devices based on self-assembled Ge TSQDs. This chapter provides a roadmap for continued research in tensile-strained Ge self-assembly.

AUTHOR CONTRIBUTIONS TO PUBLISHED WORK

Chapter 2

This chapter had equal contributions from both myself and Kevin D. Vallejo. Dr. Paul J. Simmonds was the primary author for Sections 2.1 and 2.2. Kevin D. Vallejo was the primary author for Sections 2.3, 2.4, 2.5.7, 2.5.8, 2.5.9, and 2.5.10. I was the primary author for Sections 2.5, 2.6, and 2.7. All authors contributed to writing and editing each section.

Chapter 3

I wrote the majority of the article. I also grew all of the samples for the project, analyzed atomic force microscopy (AFM) images using line section and particle analysis tools, and researched possible reasons for the unusual Stranski-Krastinov to Volmer-Weber transition. I also performed Raman spectroscopy measurements and analysis. I coordinated with the authors of this chapter. Dr. Christopher F. Schuck pioneered the ideal InGaAs/InAlAs buffer conditions needed for tensile strained quantum dot (TSQD) growth and trained me on molecular beam epitaxy. Trent A. Garrett acquired the AFM images. Garrett and Ariel E. Weltner helped me with particle analysis for all samples used in Figure 3.4. Kevin D. Vallejo conducted rocking curve x-ray diffraction (XRD) on some of the samples in this project to test for lattice-matching between the substrate and buffer materials. Vallejo also performed transmission electron microscopy (TEM) to get the Ge growth rate measurements for the project. Dr. Dingkun Ren and Dr. Baolai Liang helped us with energy dispersive x-ray spectroscopy (EDS) imaging on cross-sectional

TEM images for the Raman spectroscopy Ge TSQD sample. Dr. Kevin A. Grossklaus and Dr. Thomas E. Vandervelde carried out the high-resolution scanning TEM (STEM) and electron energy-loss spectroscopy (EELS) imaging. Dr. Paul J. Simmonds, the principal investigator (PI), oversaw the entirety of this work and contributed greatly to its flow and success. Dr. Simmonds came up with the idea for this project, and he initiated the collaborations with the authors in other universities/departments. All authors contributed to writing and editing each section.

Chapter 4

Dr. Christopher F. Schuck and I contributed equally to this work. We both grew and analyzed the AFM images for both GaAs and Ge TSQDs on InAlAs(111)A. We contributed equally to writing the experimental methods and results sections, Sections 4.2 4.4.1, 4.4.3, and 4.4.4. I coordinated with the authors of this chapter. Dr. Justin C. Smith and Dr. Christian Ratsch performed all density functional theory (DFT) and potential energy surface calculations. Dr. Smith and Dr. Ratsch wrote about their computational methods and analysis, or sections 4.3 and 4.4.2. Kevin D. Vallejo performed the same tasks as mentioned for Chapter 3. Trent A. Garrett acquired the AFM images and performed both island scaling analysis. Garrett, Hunter J. Coleman, Dr. Michael M. Henry, and Dr. Eric Jankowski took the AFM images and created a program to collect radial distribution scaling (RDS) plots for this paper. Dr. Jankowski wrote much of the RDS analysis. Jake Soares collected x-ray photoelectron spectra (XPS) to determine the indium segregation at the surface. Dr. Paul J. Simmonds, the principal investigator (PI), oversaw the entirety of this work and contributed greatly to its flow and success. All authors contributed to writing and editing each section.

Chapter 5

I wrote the majority of this chapter and grew all of the samples used within this work. I performed XRD and the AFM analysis for the Ge(110) TSQDs. I coordinated with the authors of this chapter. Dr. Aaron J. Muhowski and Dr. Daniel M. Wasserman executed and analyzed the photoluminescence spectroscopy and analyzed the resulting spectra. Dr. Kevin A. Grossklaus acquired and analyzed the STEM and EELS images. Ashton E. Enrriques performed high-resolution AFM on the temperature variation series samples and, with Dr. Paul H. Davis, wrote the AFM methodology in section 5.5.1. I used these high-resolution AFM images for the majority of TSQD structural analysis. Dr. Davis advised Enrriques and I on ideal AFM conditions for these samples in addition to analyzing TSQD diameters without the particle analysis tool. Alessia M. Molino helped me create Figure 5.8 and aided in analysis. Hunter J. Coleman created the plot used in Figure 5.6(b). Trent A. Garrett and Kevin Saythavy performed AFM imaging on all other Ge(110) samples. Dr. Dmitri A. Tenne acquired the Raman spectra that I used to calculate the tensile strain within Ge(110) TSQDs. Dr. Eric Jankowski collected the data used in Figure 5.8 and created a new program for finding linear distribution function (LDF) plots. Dr. Jankowski helped myself and Molino understand our results from the radial distribution function (RDF) and LDF plots. Dr. Christian Ratsch did the computational analysis and helped me form a discussion on adatom diffusion processes for Ge(110) TSQDs. Dr. Paul J. Simmonds, the principal investigator (PI), oversaw the entirety of this work and contributed greatly to its flow and success. Dr. Simmonds came up with the idea for this project. All authors contributed to writing and editing each section.

REFERENCES

(1) Wadhwani, P.; Saha, P. Consumer Electronics Market Forecast 2026 | Global Report https://www.gminsights.com/industry-analysis/consumer-electronics-market (accessed Apr 26, 2021).

(2) Callister, W. D.; Rethwisch, D. G. *Materials Science and Engineering - An Introduction*, 9th ed.; John Wiley & Sons, Inc.: Hoboken, New Jersey, 2014.

(3) Simon, S. H. *The Oxford Solid State Basics*, 1st ed.; Oxford University Press: Oxford, United Kingdom, 2013.

(4) Tahini, H.; Chroneos, A.; Grimes, R. W.; Schwingenschlögl, U.; Dimoulas, A. Strain-Induced Changes to the Electronic Structure of Germanium. *J. Phys. Condens. Matter* **2012**, *24*, 195802. https://doi.org/10.1088/0953-8984/24/19/195802.

(5) Fadaly, E. M. T.; Dijkstra, A.; Suckert, J. R.; Ziss, D.; van Tilburg, M. A. J.; Mao, C.; Ren, Y.; van Lange, V. T.; Korzun, K.; Kölling, S.; Verheijen, M. A.; Busse, D.; Rödl, C.; Furthmüller, J.; Bechstedt, F.; Stangl, J.; Finley, J. J.; Botti, S.; Haverkort, J. E. M.; Bakkers, E. P. A. M. Direct-Bandgap Emission from Hexagonal Ge and SiGe Alloys. *Nature* **2020**, *580* (7802), 205–209. https://doi.org/10.1038/s41586-020-2150-y.

(6) El Kurdi, M.; Fishman, G.; Sauvage, S.; Boucaud, P. Band Structure and Optical Gain of Tensile-Strained Germanium Based on a 30 Band K·p Formalism. *J. Appl. Phys.* **2010**, *107*, 013710. https://doi.org/10.1063/1.3279307.

(7) Xiong, W.; Wang, J.-W.; Fan, W.-J.; Song, Z.-G.; Tan, C.-S. The Theoretical Direct-Band-Gap Optical Gain of Germanium Nanowires. *Sci. Rep.* **2020**, *10* (32). https://doi.org/10.1038/s41598-019-56765-5.

(8) Aldaghri, O.; Ikonić, Z.; Kelsall, R. W. Optimum Strain Configurations for Carrier Injection in near Infrared Ge Lasers. *J. Appl. Phys.* **2012**, *111*, 053106. https://doi.org/10.1063/1.3691790.

(9) Lan, H. S.; Chan, S. T.; Cheng, T. H.; Chen, C. Y.; Jan, S. R.; Liu, C. W. Biaxial Tensile Strain Effects on Photoluminescence of Different Orientated Ge Wafers. *Appl. Phys. Lett.* **2011**, *98*, 101106. https://doi.org/10.1063/1.3562589.

(10) Zhao, M.; Chen, X.; Li, L.; Zhang, X. Driving a GaAs Film to a Large-Gap Topological Insulator by Tensile Strain. *Sci. Rep.* **2015**, *5*, 8441. https://doi.org/10.1038/srep08441.

(11) Chang, G.-E.; Cheng, H. H. Optical Gain of Germanium Infrared Lasers on Different Crystal Orientations. *J. Phys. Appl. Phys.* **2013**, *46*, 065103. https://doi.org/10.1088/0022-3727/46/6/065103.

(12) Sánchez-Pérez, J. R.; Boztug, C.; Chen, F.; Sudradjat, F. F.; Paskiewicz, D. M.; Jacobson, R. B.; Lagally, M. G.; Paiella, R. Direct-Bandgap Light-Emitting Germanium in Tensilely Strained Nanomembranes. *Proc. Natl. Acad. Sci. U. S. A.* **2011**, *108* (47), 18893–18898. https://doi.org/10.1073/pnas.1107968108.

(13) Jung, D.; Faucher, J.; Mukherjee, S.; Akey, A.; Ironside, D. J.; Cabral, M.; Sang, X.; Lebeau, J.; Bank, S. R.; Buonassisi, T.; Moutanabbir, O.; Lee, M. L. Highly Tensile-Strained Ge/InAlAs Nanocomposites. *Nat. Commun.* **2017**, *8*, 14204. https://doi.org/10.1038/ncomms14204.

(14) Greil, J.; Lugstein, A.; Zeiner, C.; Strasser, G.; Bertagnolli, E. Tuning the Electro-Optical Properties of Germanium Nanowires by Tensile Strain. *Nano Lett.* **2012**, *12* (12), 6230–6234. https://doi.org/10.1021/nl303288g.

(15) Ghrib, A.; El Kurdi, M.; de Kersauson, M.; Prost, M.; Sauvage, S.; Checoury, X.; Beaudoin, G.; Sagnes, I.; Boucaud, P. Tensile-Strained Germanium Microdisks. *Appl. Phys. Lett.* **2013**, *102*, 221112. https://doi.org/10.1063/1.4809832.

(16) Qi, M.; Stephenson, C. A.; Protasenko, V.; O'Brien, W. A.; Mintairov, A.; Xing, H.; Wistey, M. A. Ge Quantum Dots Encapsulated by AlAs Grown by Molecular Beam Epitaxy on GaAs without Extended Defects. *Appl. Phys. Lett.* **2014**, *104*, 073113. https://doi.org/10.1063/1.4866278.

(17) Simmonds, P. J.; Lee, M. L. Tensile Strained Island Growth at Step-Edges on GaAs(110). *Appl. Phys. Lett.* **2010**, *97*, 153101. https://doi.org/10.1063/1.3498676.

(18) Simmonds, P. J.; Lee, M. L. Self-Assembly on (111)-Oriented III-V Surfaces. *Appl. Phys. Lett.* **2011**, *99*, 123111. https://doi.org/10.1063/1.3640501.

(19) Simmonds, P. J.; Lee, M. L. Tensile-Strained Growth on Low-Index GaAs. *J. Appl. Phys.* **2012**, *112*, 054313. https://doi.org/10.1063/1.4749407.

(20) Aierken, A. Passivation of GaAs Surfaces and Fabrication of Self-Assembled In (Ga) As/GaAs Quantum Ring Structures. PhD Dissertation, Helsinki University of Technology, Espoo, Finland, 2008.

(21) Schuck, C. F.; McCown, R. A.; Hush, A.; Mello, A.; Roy, S.; Spinuzzi, J. W.; Liang, B.; Huffaker, D. L.; Simmonds, P. J. Self-Assembly of (111)-Oriented Tensile-Strained Quantum Dots by Molecular Beam Epitaxy. *J. Vac. Sci. Technol. B* **2018**, *36* (3), 031803. https://doi.org/10.1116/1.5018002.

(22) Simmonds, P. J.; Yerino, C. D.; Sun, M.; Liang, B.; Huffaker, D. L.; Dorogan, V. G.; Mazur, Y.; Salamo, G.; Lee, M. L. Tuning Quantum Dot Luminescence Below the Bulk Band Gap Using Tensile Strain. *ACS Nano* **2013**, *7* (6), 5017–5023. https://doi.org/10.1021/nn400395y.

(23) Yerino, C. D.; Simmonds, P. J.; Liang, B.; Jung, D.; Schneider, C.; Unsleber, S.; Vo, M. V.; Huffaker, D. L.; Höfling, S.; Kamp, M.; Lee, M. L. Strain-Driven Growth of GaAs(111) Quantum Dots with Low Fine Structure Splitting. *Appl. Phys. Lett.* **2014**, *105*, 251901. https://doi.org/10.1063/1.4904944.

(24) Simmonds, P. J. Quantum Dot Growth on (111) and (110) Surfaces Using Tensile-Strained Self-Assembly. In *Quantum Dots and Nanostructures: Growth, Characterization, and Modeling XV*; International Society for Optics and Photonics, 2018; Vol. 10543, p 105430L. https://doi.org/10.1117/12.2299676.

(25) Yerino, C. D.; Simmonds, P. J.; Liang, B.; Dorogan, V. G.; Ware, M. E.; Mazur, Y. I.; Jung, D.; Huffaker, D. L.; Salamo, G. J.; Lee, M. L. Tensile GaAs(111) Quantum Dashes with Tunable Luminescence below the Bulk Bandgap. *Appl. Phys. Lett.* **2014**, *105*, 071912. https://doi.org/10.1063/1.4893747.

(26) Sautter, K. E.; Schuck, C. F.; Garrett, T. A.; Weltner, A. E.; Vallejo, K. D.; Ren, D.; Liang, B.; Grossklaus, K. A.; Vandervelde, T. E.; Simmonds, P. J. Self-Assembly of Tensile-Strained Ge Quantum Dots on InAlAs(111)A. *J. Cryst. Growth* **2020**, *533* (125468). https://doi.org/10.1016/j.jcrysgro.2019.125468.

(27) Chen, Q.; Zhang, L.; Song, Y.; Chen, X.; Koelling, S.; Zhang, Z.; Li, Y.; Koenraad, P. M.; Shao, J.; Tan, C. S.; Wang, S.; Gong, Q. Highly Tensile-Strained Self-Assembled Ge Quantum Dots on InP Substrates for Integrated Light Sources. *ACS Appl. Nano Mater.* **2021**, *4* (1), 897–906. https://doi.org/10.1021/acsanm.0c03373.

(28) Shockley, W.; Read, W. T. Statistics of the Recombinations of Holes and Electrons. *Phys. Rev.* **1952**, *87* (5), 835–842. https://doi.org/10.1103/PhysRev.87.835.

(29) Morresi, L. Molecular Beam Epitaxy. In *Silicon Based Thin Film Solar Cells*; Murri, R., Ed.; Bentham Science Publishers, 2013; Vol. 1, pp 81–107.

(30) LaBella, V. P.; Bullock, D. W.; Emery, C.; Ding, Z.; Thibado, P. M. Enabling Electron Diffraction as a Tool for Determining Substrate Temperature and Surface Morphology. *Appl. Phys. Lett.* **2001**, *79* (19), 3065. https://doi.org/10.1063/1.1416477.

(31) Neave, J. H.; Joyce, B. A.; Dobson, P. J.; Norton, N. Dynamics of Film Growth of GaAs by MBE from Rheed Observations. *Appl. Phys. A* **1983**, *31* (1), 1–8. https://doi.org/10.1007/BF00617180.

(32) Neave, J. H.; Dobson, P. J.; Joyce, B. A.; Zhang, J. Reflection High-energy Electron Diffraction Oscillations from Vicinal Surfaces—a New Approach to Surface Diffusion Measurements. *Appl. Phys. Lett.* **1985**, *47* (2), 100–102. https://doi.org/10.1063/1.96281.

(33) Sakamoto, T. Rheed Oscillations in MBE and Their Applications to Precisely Controlled Crystal Growth. In *Physics, Fabrication, and Applications of Multilayered Structures*; Dhez, P., Weisbuch, C., Eds.; Springer: Boston, MA, 1988; pp 93–110. https://doi.org/10.1007/978-1-4757-0091-6_5.

(34) Maksym, P. A. Fast Monte Carlo Simulation of MBE Growth. *Semicond. Sci. Technol.* **1988**, *3* (6), 594–596.

(35) Davuluri, P. An Introduction to Electron Microscopy - The Scanning Transmission Electron Microscope https://www.fei.com/introduction-to-electron-microscopy/stem/#gsc.tab=0 (accessed Mar 10, 2021).

(36) Woollam Co., J. A. What is Ellipsometry? https://www.jawoollam.com/resources/ellipsometry-tutorial/what-is-ellipsometry (accessed Mar 12, 2021).

(37) Tompkins, H. G.; Hilfiker, J. N. *Spectroscopic Ellipsometry: Practical Application to Thin Film Characterization*; Momentum Press: New York, NY, 2015.

(38) Kuo, Y.-K.; Liou, B.-T.; Yen, S.-H.; Chu, H.-Y. Vegard's Law Deviation in Lattice Constant and Band Gap Bowing Parameter of Zincblende InxGa1−xN. *Opt. Commun.* **2004**, *237* (4), 363–369. https://doi.org/10.1016/j.optcom.2004.04.012.

(39) Egerton, R. F. *Electron Energy-Loss Spectroscopy in the Electron Microscope*, 3rd ed.; Springer Science & Business Media: New York City, New York, 2011.

(40) Shindo, D.; Oikawa, T. Energy Dispersive X-Ray Spectroscopy. In *Analytical Electron Microscopy for Materials Science*; Shindo, D., Oikawa, T., Eds.; Springer: Tokyo, Japan, 2002; pp 81–102. https://doi.org/10.1007/978-4-431-66988-3_4.

(41) Eaton, P.; West, P. *Atomic Force Microscopy*; Oxford University Press: Oxford, United Kingdom, 2010.

(42) Hassani, S. S.; Tasharrofi, S.; Sobat, Z. Kelvin Probe: Kelvin Probe Force Microscopy as a Tool for the Characterization of Nanomaterials. In *CRC Concise Encyclopedia of Nanotechnology*; Kharisov, B. I., Kharissova, O. V., Ortiz-Mendez, U., Eds.; CRC Press, 2015; pp 391–396.

(43) Sautter, K. E.; Schuck, C. F.; Smith, J. C.; Vallejo, K. D.; Garrett, T. A.; Soares, J.; Coleman, H. J.; Henry, M. M.; Jankowski, E.; Ratsch, C.; Simmonds, P. J. Self-Assembly of Ge and GaAs Quantum Dots under Tensile Strain on InAlAs(111)A. *Cryst. Growth Des.* **2021**, *21* (3), 1674–1682. https://doi.org/10.1021/acs.cgd.0c01528.

(44) Ferraro, J. R.; Nakamoto, K.; Brown, C. W. *Introductory Raman Spectroscopy*, 2nd ed.; Academic Press: San Diego, California, 2002.

(45) Fang, Y. Y.; Tolle, J.; Roucka, R.; Chizmeshya, A. V. G.; Kouvetakis, J.; D'Costa, V. R.; Menéndez, J. Perfectly Tetragonal, Tensile-Strained Ge on Ge1-YSny Buffered Si(100). *Appl. Phys. Lett.* **2007**, *90*, 061915. https://doi.org/10.1063/1.2472273.

(46) Vuong, P. Optical Spectroscopy of Boron Nitride Heterostructures. phdthesis, Université Montpellier, Montpellier, France, 2018.

(47) Fornari, R. 1 - Epitaxy for Energy Materials. In *Handbook of Crystal Growth (Second Edition)*; Kuech, T. F., Ed.; Handbook of Crystal Growth; North-Holland: Boston, 2015; pp 1–49. https://doi.org/10.1016/B978-0-444-63304-0.00001-9.

(48) Rivoire, K.; Buckley, S.; Song, Y.; Lee, M. L.; Vučković, J. Photoluminescence from In0.5Ga0.5As/GaP Quantum Dots Coupled to Photonic Crystal Cavities. *Phys. Rev. B* **2012**, *85* (4), 045319.

(49) Temkin, H.; Dolan, G. J.; Panish, M. B.; Chu, S. N. G. Low-temperature Photoluminescence from InGaAs/InP Quantum Wires and Boxes. *Appl. Phys. Lett.* **1987**, *50* (7), 413–415. https://doi.org/10.1063/1.98159.

(50) Lefebvre, J.; Maruyama, S.; Finnie, P. Photoluminescence: Science and Applications. In *Carbon Nanotubes: Advanced Topics in the Synthesis, Structure, Properties and Applications*; Jorio, A., Dresselhaus, G., Dresselhaus, M. S., Eds.; Topics in Applied Physics; Springer: Berlin, Heidelberg, 2007; Vol. 111, pp 287–319. https://doi.org/10.1007/978-3-540-72865-8_9.

(51) Cohen, M. L.; Chelikowsky, J. R. *Electronic Structure and Optical Properties of Semiconductors*, 1st ed.; Springer Series in Solid-State Sciences; Springer-Verlag: Berlin Heidelberg, 1988. https://doi.org/10.1007/978-3-642-97080-1.

(52) Yerino, C. D.; Liang, B.; Huffaker, D. L.; Simmonds, P. J.; Lee, M. L. Review Article: Molecular Beam Epitaxy of Lattice-Matched InAlAs and InGaAs Layers on InP (111)A, (111)B, and (110). *J. Vac. Sci. Technol. B* **2017**, *35*, 010801. https://doi.org/10.1116/1.4972049.

(53) Kroemer, H. Polar-on-Nonpolar Epitaxy. *J. Cryst. Growth* **1987**, *81*, 193–204. https://doi.org/10.1016/0022-0248(87)90391-5.

(54) Lide, D. R. *CRC Handbook of Chemistry and Physics*, 84th ed.; CRC Press LLC: Boca Raton, FL, 2003; Vol. 53.

(55) Neave, J. H.; Larsen, P. K.; Joyce, B. A.; Gowers, J. P.; van der Veen, J. F. Some Observations on Ge:GaAs(001) and GaAs:Ge(001) Interfaces and Films. *J. Vac. Sci. Technol. B Microelectron. Process. Phenom.* **1983**, *1* (3), 668–674. https://doi.org/10.1116/1.582574.

(56) Strite, S.; Ünlü, M. S.; Adomi, K.; Gao, G. -B.; Agarwal, A.; Rockett, A.; Morkoç, H.; Li, D.; Nakamura, Y.; Otsuka, N. GaAs/Ge/GaAs Heterostructures by Molecular Beam Epitaxy. *J. Vac. Sci. Technol. B Microelectron. Process. Phenom.* **1990**, *8* (5), 1131–1140. https://doi.org/10.1116/1.584931.

(57) Sieg, R. M.; Ringel, S. A.; Ting, S. M.; Fitzgerald, E. A.; Sacks, R. N. Anti-Phase Domain-Free Growth of GaAs on Offcut (001) Ge Wafers by Molecular Beam Epitaxy with Suppressed Ge Outdiffusion. *J. Electron. Mater.* **1998**, *27* (7), 900–907. https://doi.org/10.1007/s11664-998-0116-1.

(58) Grassman, T. J.; Brenner, M. R.; Rajagopalan, S.; Unocic, R.; Dehoff, R.; Mills, M.; Fraser, H.; Ringel, S. A. Control and Elimination of Nucleation-Related Defects in GaP/Si(001) Heteroepitaxy. *Appl. Phys. Lett.* **2009**, *94* (232106). https://doi.org/10.1063/1.3154548.

(59) Kroemer, H.; Polasko, K. J.; Wright, S. C. On the (110) Orientation as the Preferred Orientation for the Molecular Beam Epitaxial Growth of GaAs on Ge, GaP on Si, and Similar Zincblende-on-Diamond Systems. *Appl. Phys. Lett.* **1980**, *36* (9), 763–765. https://doi.org/10.1063/1.91643.

(60) Hudait, M. K.; Zhu, Y.; Jain, N.; Hunter, J. L. Structural, Morphological, and Band Alignment Properties of GaAs/Ge/GaAs Heterostructures on (100), (110), and (111)A GaAs Substrates. *J. Vac. Sci. Technol. B* **2012**, *31* (1), 011206. https://doi.org/10.1116/1.4770070.

(61) Horikoshi, Y. Chapter 5 - Migration-Enhanced Epitaxy for Low-Dimensional Structures. In *Molecular Beam Epitaxy*; Henini, M., Ed.; Elsevier, 2013; pp 113–120. https://doi.org/10.1016/B978-0-12-387839-7.00005-1.

(62) Miller, D. L.; Harris, J. S. Molecular Beam Epitaxial GaAs Heteroface Solar Cell Grown on Ge. *Appl. Phys. Lett.* **1980**, *37* (12), 1104–1106. https://doi.org/10.1063/1.91889.

(63) Chand, N.; Klem, J.; Henderson, T.; Morkoç, H. Diffusion of As and Ge during Growth of GaAs on Ge Substrate by Molecular-beam Epitaxy: Its Effect on the Device Electrical Characteristics. *J. Appl. Phys.* **1986**, *59* (10), 3601–3604. https://doi.org/10.1063/1.336790.

(64) Andre, C. L.; Carlin, J. A.; Boeckl, J. J.; Wilt, D. M.; Smith, M. A.; Pitera, A. J.; Lee, M. L.; Fitzgerald, E. A.; Ringel, S. A. Investigations of High-Performance GaAs Solar Cells Grown on Ge-Si(1-x)Ge(x)-Si Substrates. *IEEE Trans. Electron Devices* **2005**, *52* (6), 1055–1060. https://doi.org/10.1109/TED.2005.848117.

(65) Horikoshi, Y.; Kawashima, M.; Yamaguchi, H. Migration-Enhanced Epitaxy of GaAs and AlGaAs. *Jpn. J. Appl. Phys.* **1988**, *27* (2R), 169. https://doi.org/10.1143/JJAP.27.169.

(66) Lu, H.; Schaff, W. J.; Hwang, J.; Wu, H.; Yeo, W.; Pharkya, A.; Eastman, L. F. Improvement on Epitaxial Grown of InN by Migration Enhanced Epitaxy. *Appl. Phys. Lett.* **2000**, *77* (16), 2548–2550. https://doi.org/10.1063/1.1318235.

(67) Kegel, I.; Metzger, T. H.; Lorke, A.; Peisl, J.; Stangl, J.; Bauer, G.; García, J. M.; Petroff, P. M. Nanometer-Scale Resolution of Strain and Interdiffusion in Self-Assembled $\mathrm{InAs}/\mathrm{GaAs}$ Quantum Dots. *Phys. Rev. Lett.* **2000**, *85* (8), 1694–1697. https://doi.org/10.1103/PhysRevLett.85.1694.

(68) Joyce, B. A.; Vvedensky, D. D. Self-Organized Growth on GaAs Surfaces. *Mater. Sci. Eng. R Rep.* **2004**, *46*, 127–176. https://doi.org/10.1016/j.mser.2004.10.001.

(69) Baskaran, A.; Smereka, P. Mechanisms of Stranski-Krastanov Growth. *J. Appl. Phys.* **2012**, *111*, 044321. https://doi.org/10.1063/1.3679068.

(70) Eaglesham, D. J.; Cerullo, M. Dislocation-Free Stranski-Krastanow Growth of Ge on Si(100). *Phys. Rev. Lett.* **1990**, *64* (16), 1943–1946. https://doi.org/10.1103/PhysRevLett.64.1943.

(71) Zheng, H. Molecular Dynamic Simulation of Thin Film Growth Stress Evolution, Lehigh University, Bethlehem, Pennsylvania, USA, 2011.

(72) Bressler-Hill, V.; Varma, S.; Lorke, A.; Nosho, B. Z.; Petroff, P. M.; Weinberg, W. H. Island Scaling in Strained Heteroepitaxy: InAs/GaAs(001). *Phys. Rev. Lett.* **1995**, *74* (16), 3209–3212. https://doi.org/10.1103/PhysRevLett.74.3209.

(73) Patel, H. A.; Byun, J.; Yavuz, C. T. Carbon Dioxide Capture Adsorbents: Chemistry and Methods. *ChemSusChem* **2017**, *10* (7), 1303–1317. https://doi.org/10.1002/cssc.201601545.

(74) Zangwill, A. *Physics at Surfaces*; Cambridge University Press: Cambridge, 1988. https://doi.org/10.1017/CBO9780511622564.

(75) Ratsch, C.; Zangwill, A.; Šmilauer, P. Scaling of Heteroepitaxial Island Sizes. *Surf. Sci.* **1994**, *314* (3), L937–L942. https://doi.org/10.1016/0039-6028(94)90231-3.

(76) Ratsch, C.; Šmilauer, P.; Zangwill, A.; Vvedensky, D. D. Submonolayer Epitaxy Without A Critical Nucleus. *Surf. Sci.* **1995**, *Surface Science* (329), L599–L604. https://doi.org/10.1016/0039-6028(95)00353-3.

(77) Shapiro, J. N.; Lin, A.; Huffaker, D. L.; Ratsch, C. Potential Energy Surface of In and Ga Adatoms above the (111)A and (110) Surfaces of a GaAs Nanopillar. *Phys. Rev. B* **2011**, *84* (8), 085322. https://doi.org/10.1103/PhysRevB.84.085322.

(78) Barabási, A.-L. Thermodynamic and Kinetic Mechanisms in Self-Assembled Quantum Dot Formation. *Mater. Sci. Eng. B* **1999**, *67* (1), 23–30. https://doi.org/10.1016/S0921-5107(99)00205-6.

(79) Ohring, M. *Materials Science of Thin Films*, 2nd ed.; Academic Press: Hoboken, New Jersey, 2002. https://doi.org/10.1016/B978-0-12-524975-1.X5000-9.

(80) Sautter, K. E.; Vallejo, K. D.; Simmonds, P. J. Strain-Driven Quantum Dot Self-Assembly by Molecular Beam Epitaxy. *J. Appl. Phys.* **2020**, *128* (3), 031101. https://doi.org/10.1063/5.0012066.

(81) Leonard, D.; Krishnamurthy, M.; Reaves, C. M.; Denbaars, S. P.; Petroff, P. M. Direct Formation of Quantum-sized Dots from Uniform Coherent Islands of InGaAs on GaAs Surfaces. *Appl. Phys. Lett.* **1993**, *63* (23), 3203–3205. https://doi.org/10.1063/1.110199.

(82) Schuck, C. F.; Roy, S. K.; Garrett, T. A.; Yuan, Q.; Wang, Y.; Cabrera, C. I.; Grossklaus, K. A.; Vandervelde, T. E.; Liang, B.; Simmonds, P. J. Anomalous Stranski-Krastanov Growth of (111)-Oriented Quantum Dots with Tunable Wetting Layer Thickness. **2019**, *In Review*.

(83) Sanguinetti, S.; Watanabe, K.; Tateno, T.; Gurioli, M.; Werner, P.; Wakaki, M.; Koguchi, N. Modified Droplet Epitaxy GaAs/AlGaAs Quantum Dots Grown on a Variable Thickness Wetting Layer. *J. Cryst. Growth* **2003**, *253* (1–4), 71–76. https://doi.org/10.1016/S0022-0248(03)01016-9.

(84) Shahzadeh, M.; Sabaeian, M. The Effects of Wetting Layer on Electronic and Optical Properties of Intersubband P-to-S Transitions in Strained Dome-Shaped InAs/GaAs Quantum Dots. *AIP Adv.* **2014**, *4* (6), 067113. https://doi.org/10.1063/1.4881980.

(85) Sun, C.; Lu, P.; Yu, Z.; Cao, H.; Zhang, L. Wetting Layers Effect on InAs/GaAs Quantum Dots. *Phys. B Condens. Matter* **2012**, *407* (22), 4440–4445. https://doi.org/10.1016/j.physb.2012.07.039.

(86) Tersoff, J.; LeGoues, F. K. Competing Relaxation Mechanisms in Strained Layers. *Phys. Rev. Lett.* **1994**, *72* (22), 3570–3573. https://doi.org/10.1103/PhysRevLett.72.3570.

(87) Simon, J.; Tomasulo, S.; Simmonds, P. J.; Romero, M.; Lee, M. L. Metamorphic GaAsP Buffers for Growth of Wide-Bandgap InGaP Solar Cells. *J. Appl. Phys.* **2011**, *109*, 013708. https://doi.org/10.1063/1.3525599.

(88) Pachinger, D.; Groiss, H.; Lichtenberger, H.; Stangl, J.; Hesser, G.; Schäffler, F. Stranski-Krastanow Growth of Tensile Strained Si Islands on Ge (001). *Appl. Phys. Lett.* **2007**, *91* (23), 233106. https://doi.org/10.1063/1.2820605.

(89) Thompson, N. Dislocation Nodes in Face-Centred Cubic Lattices. *Proc. Phys. Soc. Sect. B* **1953**, *66* (6), 481–492. https://doi.org/10.1088/0370-1301/66/6/304.

(90) Schuck, C. F.; Vallejo, K. D.; Garrett, T.; Yuan, Q.; Wang, Y.; Liang, B.; Simmonds, P. J. Impact of Arsenic Species on Self-Assembly of Triangular and Hexagonal Tensile-Strained GaAs(111)A Quantum Dots. *Semicond. Sci. Technol.* **2020**, *35* (10), 105001. https://doi.org/10.1088/1361-6641/aba6e0.

(91) Amar, J. G.; Family, F. Critical Cluster Size: Island Morphology and Size Distribution in Submonolayer Epitaxial Growth. *Phys. Rev. Lett.* **1995**, *74* (11), 2066–2069. https://doi.org/10.1103/PhysRevLett.74.2066.

(92) Bartelt, M. C.; Evans, J. W. Scaling Analysis of Diffusion-Mediated Island Growth in Surface Adsorption Processes. *Phys. Rev. B* **1992**, *46* (19), 12675–12687. https://doi.org/10.1103/PhysRevB.46.12675.

(93) Syaranamual, G. J.; Sasangka, W. A.; Made, R. I.; Arulkumaran, S.; Ng, G. I.; Foo, S. C.; Gan, C. L.; Thompson, C. V. Role of Two-Dimensional Electron Gas (2DEG) in AlGaN/GaN High Electron Mobility Transistor (HEMT) ON-State Degradation. *Microelectron. Reliab.* **2016**, *64*, 589–593. https://doi.org/10.1016/j.microrel.2016.07.012.

(94) Dimroth, F.; Kurtz, S. High-Efficiency Multijunction Solar Cells. *MRS Bull.* **2007**, *32* (3), 230–235. https://doi.org/10.1557/mrs2007.27.

(95) Brault, J.; Al Khalfioui, M.; Matta, S.; Damilano, B.; Leroux, M.; Chenot, S.; Korytov, M.; Nkeck, J.; Vennéguès, P.; Duboz, J.; others. UVA and UVB Light Emitting Diodes with Al y Ga1- y N Quantum Dot Active Regions Covering the 305–335 Nm Range. *Semicond. Sci. Technol.* **2018**, *33* (7), 075007.

(96) Müller, T.; Skiba-Szymanska, J.; Krysa, A. B.; Huwer, J.; Felle, M.; Anderson, M.; Stevenson, R. M.; Heffernan, J.; Ritchie, D. A.; Shields, A. J. A Quantum Light-Emitting Diode for the Standard Telecom Window around 1,550 Nm. *Nat. Commun.* **2018**, *9* (1), 862. https://doi.org/10.1038/s41467-018-03251-7.

(97) Griffiths, D. J. *Introduction to Quantum Mechanics*, 2nd ed.; Cambridge University Press: Cambridge, 2016.

(98) Amin, G. ZnO and CuO Nanostructures: Low Temperature Growth, Characterization, Their Optoelectronic and Sensing Applications. PhD Thesis, Linköping University, Linköping, Sweden, 2012.

(99) Ashcroft, N. W.; Mermin-Brooks Cole, N. D. *Solid State Physics*; Saunders College: Philadelphia, Pennsylvania, 1976.

(100) Streetman, B. G.; Banerjee, S. *Solid State Electronic Devices*, 5th ed.; Prentice Hall: Upper Saddle River, New Jersey, 2000.

(101) Kittel, C. *Introduction to Solid State Physics*, 8th ed.; Johnson, S., Ed.; John Wiley & Sons, Inc.: Hoboken, New Jersey, 1996.

(102) Zide, J. M. O.; Kleiman-Schwasctein, A.; Strandwitz, N. C.; Zimmerman, J. D.; Steenblock-Smith, T.; Gossard, A. C.; Forman, A.; Ivanovskaya, A.; Stucky, G. D. Increased Efficiency in Multijunction Solar Cells through the Incorporation of Semimetallic ErAs Nanoparticles into the Tunnel Junction. *Appl. Phys. Lett.* **2006**, *88*, 162103. https://doi.org/10.1063/1.2196059.

(103) Crook, A. M.; Nair, H. P.; Bank, S. R. High-Performance Nanoparticle-Enhanced Tunnel Junctions for Photonic Devices. *Phys. Status Solidi C* **2010**, *7* (10), 2544–2547. https://doi.org/10.1002/pssc.200983914.

(104) Kim, W.; Zide, J.; Gossard, A.; Klenov, D.; Stemmer, S.; Shakouri, A.; Majumdar, A. Thermal Conductivity Reduction and Thermoelectric Figure of Merit Increase by Embedding Nanoparticles in Crystalline Semiconductors. *Phys. Rev. Lett.* **2006**, *96*, 045901. https://doi.org/10.1103/PhysRevLett.96.045901.

(105) Cho, A. Y. Film Deposition by Molecular-Beam Techniques. *J. Vac. Sci. Technol.* **1971**, *8*, S31.

(106) Chang, L. L.; Esaki, L.; Tsu, R. Resonant Tunneling in Semiconductor Double Barriers. *Appl. Phys. Lett.* **1974**, *24* (12), 593–595. https://doi.org/10.1063/1.1655067.

(107) Dingle, R.; Wiegmann, W.; Henry, C. H. Quantum States of Confined Carriers in Very Thin Al$_x$Ga$_{1-x}$As-GaAs-Al$_x$Ga$_{1-x}$As Heterostructures. *Phys. Rev. Lett.* **1974**, *33* (14), 827–830. https://doi.org/10.1103/PhysRevLett.33.827.

(108) Kash, K.; Scherer, A.; Worlock, J. M.; Craighead, H. G.; Tamargo, M. C. Optical Spectroscopy of Ultrasmall Structures Etched from Quantum Wells. *Appl. Phys. Lett.* **1986**, *49* (16), 1043–1045. https://doi.org/10.1063/1.97466.

(109) Reed, M.; Randall, J.; Aggarwal, R.; Matyi, R.; Moore, T.; Wetsel, A. Observation of Discrete Electronic States in a Zero-Dimensional Semiconductor Nanostructure. *Phys. Rev. Lett.* **1988**, *60* (6), 535.

(110) Thornton, T.; Pepper, M.; Ahmed, H.; Andrews, D.; Davies, G. One-Dimensional Conduction in the 2D Electron Gas of a GaAs-AlGaAs Heterojunction. *Phys. Rev. Lett.* **1986**, *56* (11), 1198.

(111) Wharam, D.; Thornton, T. J.; Newbury, R.; Pepper, M.; Ahmed, H.; Frost, J.; Hasko, D.; Peacock, D.; Ritchie, D.; Jones, G. One-Dimensional Transport and the Quantisation of the Ballistic Resistance. *J. Phys. C Solid State Phys.* **1988**, *21* (8), L209.

(112) Van Wees, B.; Van Houten, H.; Beenakker, C.; Williamson, J. G.; Kouwenhoven, L.; Van der Marel, D.; Foxon, C. Quantized Conductance of Point Contacts in a Two-Dimensional Electron Gas. *Phys. Rev. Lett.* **1988**, *60* (9), 848.

(113) Simmonds, P.; Sfigakis, F.; Beere, H.; Ritchie, D.; Pepper, M.; Anderson, D.; Jones, G. Quantum Transport in $In_{0.75}Ga_{0.25}As$ Quantum Wires. *Appl. Phys. Lett.* **2008**, *92* (15), 152108.

(114) Grundmann, M.; Christen, J.; Ledentsov, N. N.; Böhrer, J.; Bimberg, D.; Ruvimov, S. S.; Werner, P.; Richter, U.; Gösele, U.; Heydenreich, J.; Ustinov, V. M.; Egorov, A. Yu.; Zhukov, A. E.; Kop'ev, P. S.; Alferov, Zh. I. Ultranarrow Luminescence Lines from Single Quantum Dots. *Phys. Rev. Lett.* **1995**, *74* (20), 4043–4046. https://doi.org/10.1103/PhysRevLett.74.4043.

(115) Meirav, U.; Kastner, M.; Wind, S. Single-Electron Charging and Periodic Conductance Resonances in GaAs Nanostructures. *Phys. Rev. Lett.* **1990**, *65* (6), 771.

(116) Johnson, A.; Kouwenhoven, L.; De Jong, W.; Van der Vaart, N.; Harmans, C.; Foxon, C. Zero-Dimensional States and Single Electron Charging in Quantum Dots. *Phys. Rev. Lett.* **1992**, *69* (10), 1592.

(117) Ashoori, R. Electrons in Artificial Atoms. *Nature* **1996**, *379* (6564), 413–419.

(118) Schaffer, W. J.; Lind, M. D.; Kowalczyk, S. P.; Grant, R. W. Nucleation and Strain Relaxation at the InAs/GaAs(100) Heterojunction. *J. Vac. Sci. Technol. B Microelectron. Process. Phenom.* **1983**, *1*, 688–695. https://doi.org/10.1116/1.582579.

(119) Elman, B.; Koteles, E. S.; Melman, P.; Jagannath, C.; Lee, J.; Dugger, D. In Situ Measurements of Critical Layer Thickness and Optical Studies of InGaAs Quantum Wells Grown on GaAs Substrates. *Appl. Phys. Lett.* **1989**, *55* (16), 1659–1661.

(120) Kataoka, Y.; Ueba, H.; Tatsuyama, C. Structural Properties of Heteroepitaxial Ge Films on a Si (100)-2x1 Surface. *J. Appl. Phys.* **1988**, *63* (3), 749–759.

(121) Copel, M.; Reuter, M.; Kaxiras, E.; Tromp, R. Surfactants in Epitaxial Growth. *Phys. Rev. Lett.* **1989**, *63* (6), 632.

(122) LeGoues, F.; Copel, M.; Tromp, R. Novel Strain-Induced Defect in Thin Molecular-Beam Epitaxy Layers. *Phys. Rev. Lett.* **1989**, *63* (17), 1826.

(123) Nakao, H.; Yao, T. Surface Lattice Strain Relaxation at the Initial Stage of Heteroepitaxial Growth of In$_x$$Ga_{1-x}As on GaAs by Molecular Beam Epitaxy. *Jpn. J. Appl. Phys.* **1989**, *28* (3A), L352.

(124) Reithmaier, J.-P.; Cerva, H.; Lösch, R. Investigation of the Critical Layer Thickness in Elastically Strained InGaAs/GaAlAs Quantum Wells by Photoluminescence and Transmission Electron Microscopy. *Appl. Phys. Lett.* **1989**, *54* (1), 48–50.

(125) Snyder, C.; Orr, B.; Kessler, D.; Sander, L. Effect of Strain on Surface Morphology in Highly Strained InGaAs Films. *Phys. Rev. Lett.* **1991**, *66* (23), 3032.

(126) Guha, S.; Madhukar, A.; Rajkumar, K. Onset of Incoherency and Defect Introduction in the Initial Stages of Molecular Beam Epitaxial Growth of Highly Strained In$_x$$Ga_{1-x}As on GaAs(100). *Appl. Phys. Lett.* **1990**, *57* (20), 2110–2112.

(127) Krishnamurthy, M.; Drucker, J.; Venables, J. Microstructural Evolution during the Heteroepitaxy of Ge on Vicinal Si(100). *J. Appl. Phys.* **1991**, *69* (9), 6461–6471.

(128) Moison, J.; Houzay, F.; Barthe, F.; Leprince, L.; Andre, E.; Vatel, O. Self-Organized Growth of Regular Nanometer-Scale InAs Dots on GaAs. *Appl. Phys. Lett.* **1994**, *64* (2), 196–198.

(129) Marzin, J.; Gerard, J. Optical Properties of Some III–V Strained-Layer Superlattices. *Superlattices Microstruct.* **1989**, *5* (1), 51–58.

(130) Mukai, K.; Ohtsuka, N.; Sugawara, M.; Yamazaki, S. Self-Formed $In_{0.5}Ga_{0.5}As$ Quantum Dots on GaAs Substrates Emitting at 1.3 Mm. *Jpn. J. Appl. Phys.* **1994**, *33* (12A), L1710.

(131) Nabetani, Y.; Ishikawa, T.; Noda, S.; Sasaki, A. Initial Growth Stage and Optical Properties of a Three-Dimensional InAs Structure on GaAs. *J. Appl. Phys.* **1994**, *76* (1), 347–351.

(132) Leonard, D.; Krishnamurthy, M.; Fafard, S.; Merz, J.; Petroff, P. Molecular Beam Epitaxy Growth of Quantum Dots from Strained Coherent Uniform Islands of InGaAs on GaAs. *J. Vac. Sci. Technol. B* **1994**, *12* (2), 1063–1066.

(133) Xie, Q.; Chen, P.; Kalburge, A.; Ramachandran, T.; Nayfonov, A.; Konkar, A.; Madhukar, A. Realization of Optically Active Strained InAs Island Quantum Boxes on GaAs (100) via Molecular Beam Epitaxy and the Role of Island Induced Strain Fields. *J. Cryst. Growth* **1995**, *150*, 357–363.

(134) Gérard, J.-M.; Genin, J.; Lefebvre, J.; Moison, J.; Lebouche, N.; Barthe, F. Optical Investigation of the Self-Organized Growth of InAs/GaAs Quantum Boxes. *J. Cryst. Growth* **1995**, *150*, 351–356.

(135) Bimberg, D.; Grundmann, M.; Ledentsov, N.; Ruvimov, S.; Werner, P.; Richter, U.; Heydenreich, J.; Ustinov, V.; Kop'ev, P.; Alferov, Z. I. Self-Organization Processes in MBE-Grown Quantum Dot Structures. *Thin Solid Films* **1995**, *267* (1–2), 32–36.

(136) Ledentsov, N.; Shchukin, V.; Grundmann, M.; Kirstaedter, N.; Böhrer, J.; Schmidt, O.; Bimberg, D.; Ustinov, V.; Egorov, A. Y.; Zhukov, A.; others. Direct Formation of Vertically Coupled Quantum Dots in Stranski-Krastanow Growth. *Phys. Rev. B* **1996**, *54* (12), 8743.

(137) Hatami, F.; Ledentsov, N. N.; Grundmann, M.; Böhrer, J.; Heinrichsdorff, F.; Beer, M.; Bimberg, D.; Ruvimov, S. S.; Werner, P.; Gösele, U.; Heydenreich, J.; Richter, U.; Ivanov, S. V.; Meltser, B. Ya.; Kop'ev, P. S.; Alferov, Zh. I. Radiative Recombination in Type-II GaSb/GaAs Quantum Dots. *Appl. Phys. Lett.* **1995**, *67* (5), 656–658. https://doi.org/10.1063/1.115193.

(138) Glaser, E. R.; Bennett, B. R.; Shanabrook, B. V.; Magno, R. Photoluminescence Studies of Self-assembled InSb, GaSb, and AlSb Quantum Dot Heterostructures. *Appl. Phys. Lett.* **1996**, *68* (25), 3614–3616. https://doi.org/10.1063/1.115747.

(139) Junno, B.; Junno, T.; Miller, M. S.; Samuelson, L. A Reflection High-Energy Electron Diffraction and Atomic Force Microscopy Study of the Chemical Beam Epitaxial Growth of InAs and InP Islands on (001) GaP. *Appl. Phys. Lett.* **1998**, *72* (8), 954. https://doi.org/10.1063/1.120883.

(140) Gerhard, S.; Baumann, V.; Höfling, S.; Forchel, A. The Structural and Optical Characterization of High Areal Density GaxIn1-XP Quantum Dots on GaP. *Nanotechnology* **2009**, *20* (43), 434016. https://doi.org/10.1088/0957-4484/20/43/434016.

(141) Hatami, F.; Masselink, W. T.; Schrottke, L. Radiative Recombination from InP Quantum Dots on (100) GaP. *Appl. Phys. Lett.* **2001**, *78* (15), 2163. https://doi.org/10.1063/1.1361277.

(142) Fafard, S.; Wasilewski, Z.; McCaffrey, J.; Raymond, S.; Charbonneau, S. InAs Self-Assembled Quantum Dots on InP by Molecular Beam Epitaxy. *Appl. Phys. Lett.* **1996**, *68* (7), 991–993. https://doi.org/10.1063/1.116122.

(143) Ustinov, V. M.; Weber, E. R.; Ruvimov, S.; Liliental-Weber, Z.; Zhukov, A. E.; Egorov, A. Yu.; Kovsh, A. R.; Tsatsul'nikov, A. F.; Kop'ev, P. S. Effect of Matrix on InAs Self-Organized Nanostructures on InP Substrate. *Appl. Phys. Lett.* **1998**, *72* (3), 362–364.

(144) Lambert, B.; Le Corre, A.; Drouot, V.; L'Haridon, H.; Loualiche, S. High Photoluminescence Efficiency of InAs/InP Self-Assembled Quantum Dots Emitting at 1.5-1.6 Mm. *Semicond. Sci. Technol.* **1998**, *13* (1), 143–145. https://doi.org/10.1088/0268-1242/13/1/001.

(145) Song, Y.; Simmonds, P. J.; Lee, M. L. Self-Assembled In0.5Ga0.5As Quantum Dots on GaP. *Appl. Phys. Lett.* **2010**, *97* (22), 223110. https://doi.org/10.1063/1.3522647.

(146) Huang, D.; Reshchikov, M. A.; Morkoç, H. Growth, Structures, and Optical Properties of III-Nitride Quantum Dots. *Int. J. High Speed Electron. Syst.* **2002**, *12* (01), 79–110.

(147) Shen, X.-Q.; Tanaka, S.; Iwai, S.; Aoyagi, Y. The Formation of GaN Dots on Al$_x$$Ga_{1-x}N Surfaces Using Si in Gas-Source Molecular Beam Epitaxy. *Appl. Phys. Lett.* **1998**, *72* (3), 344–346.

(148) Minor, S. P. Growth of Indium Nitride Quantum Dots by Molecular Beam Epitaxy. PhD Thesis, University of Arkansas, Fayetteville, 2019.

(149) Adelmann, C.; Simon, J.; Feuillet, G.; Pelekanos, N.; Daudin, B.; Fishman, G. Self-Assembled InGaN Quantum Dots Grown by Molecular-Beam Epitaxy. *Appl. Phys. Lett.* **2000**, *76* (12), 1570–1572.

(150) Xin, S.; Wang, P.; Yin, A.; Kim, C.; Dobrowolska, M.; Merz, J.; Furdyna, J. Formation of Self-Assembling CdSe Quantum Dots on ZnSe by Molecular Beam Epitaxy. *Appl. Phys. Lett.* **1996**, *69* (25), 3884–3886.

(151) Hernaīndez-Calderoīn, I. Epitaxial Growth of Thin Films and Quantum Structures of IIeVI Visible-Bandgap Semiconductors. *Mol. Beam Epitaxy Res. Mass Prod.* **2012**, 311.

(152) Wojnar, P.; K\lopotowski, \Lukasz; Kossut, J. Molecular Beam Epitaxy of Semi-Magnetic Quantum Dots. *Mol. Beam Epitaxy Res. Mass Prod.* **2013**.

(153) Karczewski, G.; Maćkowski, S.; Kutrowski, M.; Wojtowicz, T.; Kossut, J. Photoluminescence Study of CdTe/ZnTe Self-Assembled Quantum Dots. *Appl. Phys. Lett.* **1999**, *74* (20), 3011–3013.

(154) Schuck, C. F.; Roy, S. K.; Garrett, T.; Yuan, Q.; Wang, Y.; Cabrera, C. I.; Grossklaus, K. A.; Vandervelde, T. E.; Liang, B.; Simmonds, P. J. Anomalous Stranski-Krastanov Growth of (111)-Oriented Quantum Dots with Tunable Wetting Layer Thickness. *Sci. Rep.* **2019**, *9*, 18179. https://doi.org/10.1038/s41598-019-54668-z.

(155) Pryor, C. E.; Pistol, M.-E. Band-Edge Diagrams for Strained III-V Semiconductor Quantum Wells, Wires, and Dots. *Phys. Rev. B* **2005**, *72* (20), 205311. https://doi.org/10.1103/PhysRevB.72.205311.

(156) Eliseev, P. G.; Li, H.; Liu, G. T.; Stintz, A.; Newell, T. C.; Lester, L. F.; Malloy, K. J. Ground-State Emission and Gain in Ultralow-Threshold InAs-InGaAs Quantum-Dot Lasers. *IEEE J. Sel. Top. Quantum Electron.* **2001**, *7* (2), 135–142. https://doi.org/10.1109/2944.954121.

(157) Ellis, B.; Mayer, M. A.; Shambat, G.; Sarmiento, T.; Harris, J.; Haller, E. E.; Vučković, J. Ultralow-Threshold Electrically Pumped Quantum-Dot Photonic-Crystal Nanocavity Laser. *Nat. Photonics* **2011**, *5* (5), 297–300. https://doi.org/10.1038/nphoton.2011.51.

(158) Zhou, T.; Tang, M.; Xiang, G.; Fang, X.; Liu, X.; Xiang, B.; Hark, S.; Martin, M.; Touraton, M.-L.; Baron, T.; Lu, Y.; Chen, S.; Liu, H.; Zhang, Z. Ultra-Low Threshold InAs/GaAs Quantum Dot Microdisk Lasers on Planar on-Axis Si (001) Substrates. *Optica* **2019**, *6* (4), 430–435.

(159) Bennet, C. H.; Brassard, G. Quantum Cryptography: Public Key Distribution and Coin Tossing. In *Proceedings IEEE International Conference on Computers, Systems and Signal Processing*; IEEE, New York: Bangalore, India, 1984; p 175.

(160) Schliwa, A.; Winkelnkemper, M.; Lochmann, A.; Stock, E.; Bimberg, D. In(Ga)As/GaAs Quantum Dots Grown on a (111) Surface as Ideal Sources of Entangled Photon Pairs. *Phys. Rev. B* **2009**, *80* (16), 161307(R).

(161) Shields, A. Quantum Logic with Light, Glass, and Mirrors. *Science* **2002**, *297* (5588), 1821. https://doi.org/10.1126/science.1075871.

(162) Shields, A. J. Semiconductor Quantum Light Sources. *Nat. Photonics* **2007**, *1* (4), 215–223.

(163) Gisin, N.; Ribordy, G.; Tittel, W.; Zbinden, H. Quantum Cryptography. *Rev. Mod. Phys.* **2002**, *74* (1), 145.

(164) Gisin, N.; Thew, R. Quantum Communication. *Nat. Photonics* **2007**, *1* (3), 165–171.

(165) Eisaman, M. D.; Fan, J.; Migdall, A.; Polyakov, S. V. Invited Review Article: Single-Photon Sources and Detectors. *Rev. Sci. Instrum.* **2011**, *82* (7), 071101. https://doi.org/10.1063/1.3610677.

(166) Kim, J.-H.; Aghaeimeibodi, S.; Carolan, J.; Englund, D.; Waks, E. Hybrid Integration Methods for On-Chip Quantum Photonics. *Optica* **2020**, *7* (4), 291–308. https://doi.org/10.1364/optica.384118.

(167) Santori, C.; Pelton, M.; Solomon, G.; Dale, Y.; Yamamoto, Y. Triggered Single Photons from a Quantum Dot. *Phys. Rev. Lett.* **2001**, *86* (8), 1502–1505. https://doi.org/10.1103/PhysRevLett.86.1502.

(168) Claudon, J.; Bleuse, J.; Malik, N. S.; Bazin, M.; Jaffrennou, P.; Gregersen, N.; Sauvan, C.; Lalanne, P.; Gérard, J.-M. A Highly Efficient Single-Photon Source Based on a Quantum Dot in a Photonic Nanowire. *Nat. Photonics* **2010**, *4* (March), 174–177. https://doi.org/10.1038/nphoton.2009.287.

(169) Paul, H. Photon Antibunching. *Rev. Mod. Phys.* **1982**, *54* (4), 1061–1102. https://doi.org/10.1103/RevModPhys.54.1061.

(170) Mirin, R. P. Photon Antibunching at High Temperature from a Single InGaAs/GaAs Quantum Dot. *Appl. Phys. Lett.* **2004**, *84* (8), 1260–1262. https://doi.org/10.1063/1.1650032.

(171) Hanbury Brown, R.; Twiss, R. Q. Correlation between Photons in Two Coherent Beams of Light. *Nature* **1956**, *177* (4497), 27–29. https://doi.org/10.1038/177027a0.

(172) Unsleber, S.; Deppisch, M.; Krammel, C. M.; Vo, M.; Yerino, C. D.; Simmonds, P. J.; Lee, M. L.; Koenraad, P. M.; Schneider, C.; Höfling, S. Bulk AlInAs on InP(111) as a Novel Material System for Pure Single Photon Emission. *Opt Express* **2016**, *24* (20), 23198–23206. https://doi.org/10.1364/OE.24.023198.

(173) Ekert, A. K. Quantum Cryptography Based on Bell's Theorem. *Phys. Rev. Lett.* **1991**, *67*, 661–663.

(174) Rarity, J. G.; Owens, P. C. M.; Tapster, P. R. Quantum Random-Number Generation and Key Sharing. *J. Mod. Opt.* **1994**, *41* (12), 2435–2444. https://doi.org/10.1080/09500349414552281.

(175) Motes, K. R.; Olson, J. P.; Rabeaux, E. J.; Dowling, J. P.; Olson, S. J.; Rohde, P. P. Linear Optical Quantum Metrology with Single Photons: Exploiting Spontaneously Generated Entanglement to Beat the Shot-Noise Limit. *Phys Rev Lett* **2015**, *114* (17), 170802. https://doi.org/10.1103/PhysRevLett.114.170802.

(176) Gobby, C.; Yuan, Z. L.; Shields, A. J. Quantum Key Distribution over 122 Km of Standard Telecom Fiber. *Appl. Phys. Lett.* **2004**, *84* (19), 3762–3764. https://doi.org/10.1063/1.1738173.

(177) Jaspan, M. A.; Habif, J. L.; Hadfield, R. H.; Nam, S. W. Heralding of Telecommunication Photon Pairs with a Superconducting Single Photon Detector. *Appl. Phys. Lett.* **2006**, *89* (3), 031112. https://doi.org/10.1063/1.2219411.

(178) Hadfield, R. H. Single-Photon Detectors for Optical Quantum Information Applications. *Nat. Photonics* **2009**, *3* (12), 696–705. https://doi.org/10.1038/nphoton.2009.230.

(179) Natarajan, C. M.; Tanner, M. G.; Hadfield, R. H. Superconducting Nanowire Single-Photon Detectors: Physics and Applications. *Supercond. Sci. Technol.* **2012**, *25*, 063001. https://doi.org/10.1088/0953-2048/25/6/063001.

(180) Komiyama, S.; Astafiev, O.; Antonov, V.; Kutsuwa, T.; Hirai, H. A Single-Photon Detector in the Far-Infrared Range. *Nature* **2000**, *403* (6768), 405–407. https://doi.org/10.1038/35000166.

(181) Shields, A. J.; O'Sullivan, M. P.; Farrer, I.; Ritchie, D. A.; Leadbeater, M. L.; Patel, N. K.; Hogg, R. A.; Norman, C. E.; Curson, N. J.; Pepper, M. Single Photon Detection with a Quantum Dot Transistor. *Jpn. J. Appl. Phys.* **2001**, *40* (3 B), 2058–2064. https://doi.org/10.1143/jjap.40.2058.

(182) Kardynal, B. E.; Shields, A. J.; O'Sullivan, M. P.; Beattie, N. S.; Farrer, I.; Ritchie, D. A.; Cooper, K. Detection of Single Photons Using a Field Effect Transistor with a Layer of Quantum Dots. *Meas. Sci. Technol.* **2002**, *13* (11), 1721–1726. https://doi.org/10.1088/0957-0233/13/11/308.

(183) Blakesley, J. C.; See, P.; Shields, A. J.; Kardynal, B. E.; Atkinson, P.; Farrer, I.; Ritchie, D. A. Efficient Single Photon Detection by Quantum Dot Resonant Tunneling Diodes. *Phys. Rev. Lett.* **2005**, *94* (6), 067401. https://doi.org/10.1103/PhysRevLett.94.067401.

(184) Rowe, M. A.; Gansen, E. J.; Greene, M.; Hadfield, R. H.; Harvey, T. E.; Su, M. Y.; Nam, S. W.; Mirin, R. P.; Rosenberg, D. Single-Photon Detection Using a Quantum Dot Optically Gated Field-Effect Transistor with High Internal Quantum Efficiency. *Appl. Phys. Lett.* **2006**, *89*, 253505.

(185) Li, H. W.; Kardyna\l, B. E.; See, P.; Shields, A. J.; Simmonds, P.; Beere, H. E.; Ritchie, D. A. Quantum Dot Resonant Tunneling Diode for Telecommunication Wavelength Single Photon Detection. *Appl. Phys. Lett.* **2007**, *91* (7), 073516.

(186) Weng, Q.; An, Z.; Zhang, B.; Chen, P.; Chen, X.; Zhu, Z.; Lu, W. Quantum Dot Single-Photon Switches of Resonant Tunneling Current for Discriminating-Photon-Number Detection. *Sci. Rep.* **2015**, *5*, 9389. https://doi.org/10.1038/srep09389.

(187) Bouwmeester, D.; Pan, J.-W.; Mattle, K.; Eibl, M.; Weinfurter, H.; Zeilinger, A. Experimental Quantum Teleportation. *Nature* **1997**, *390*, 575–579.

(188) Benson, O.; Santori, C.; Pelton, M.; Yamamoto, Y. Regulated and Entangled Photons from a Single Quantum Dot. *Phys. Rev. Lett.* **2000**, *84* (11), 2513–2516.

(189) Kwiat, P. G.; Mattle, K.; Weinfurter, H.; Zeilinger, A.; Sergienko, Alexander, V.; Shih, Y. New High-Intensity Source of Polarization-Entangled Photon Pairs. *Phys. Rev. Lett.* **1995**, *75*, 4337–4341.

(190) Edamatsu, K.; Oohata, G.; Shimizu, R.; Itoh, T. Generation of Ultraviolet Entangled Photons in a Semiconductor. *Nature* **2004**, *431*, 167–170. https://doi.org/10.1038/nature02838.

(191) Thompson, J. K.; Simon, J.; Loh, H.; Vuletić, V. A High-Brightness Source of Narrowband, Identical-Photon Pairs. *Science* **2006**, *313*, 74–77.

(192) Fulconis, J.; Alibart, O.; O'Brien, J. L.; Wadsworth, W. J.; Rarity, J. G. Nonclassical Interference and Entanglement Generation Using a Photonic Crystal Fiber Pair Photon Source. *Phys. Rev. Lett.* **2007**, *99*, 120501.

(193) Hacker, B.; Welte, S.; Rempe, G.; Ritter, S. A Photon-Photon Quantum Gate Based on a Single Atom in an Optical Resonator. *Nature* **2016**, *536* (7615), 193–196. https://doi.org/10.1038/nature18592.

(194) Yuan, Z.; Kardynal, B. E.; Stevenson, R. M.; Shields, A. J.; Lobo, C. J.; Cooper, K.; Beattie, N. S.; Ritchie, D. A.; Pepper, M. Electrically Driven Single-Photon Source. *Science* **2002**, *295*, 102–105.

(195) Heindel, T.; Schneider, C.; Lermer, M.; Kwon, S. H.; Braun, T.; Reitzenstein, S.; Höfling, S.; Kamp, M.; Forchel, A. Electrically Driven Quantum Dot-Micropillar Single Photon Source with 34% Overall Efficiency. *Appl. Phys. Lett.* **2010**, *96*, 011107.

(196) Stevenson, R. M.; Young, R. J.; Atkinson, P.; Cooper, K.; Ritchie, D. A.; Shields, A. J. A Semiconductor Source of Triggered Entangled Photon Pairs. *Nature* **2006**, *439*, 179–182.

(197) Akopian, N.; Lindner, N. H.; Poem, E.; Berlatzky, Y.; Avron, J.; Gershoni, D.; Gerardot, B. D.; Petroff, P. M. Entangled Photon Pairs from Semiconductor Quantum Dots. *Phys. Rev. Lett.* **2006**, *96*, 130501.

(198) Hafenbrak, R.; Ulrich, S. M.; Michler, P.; Wang, L.; Rastelli, A.; Schmidt, O. G. Triggered Polarization-Entangled Photon Pairs from a Single Quantum Dot up to 30 K. *New J. Phys.* **2007**, *9*, 315.

(199) Seguin, R.; Schliwa, A.; Rodt, S.; Pötschke, K.; Pohl, U. W.; Bimberg, D. Size-Dependent Fine-Structure Splitting in Self-Organized InAs/GaAs Quantum Dots. *Phys. Rev. Lett.* **2005**, *95* (25), 257402.

(200) Gammon, D.; Snow, E. S.; Shanabrook, B. V.; Katzer, D. S.; Park, D. Fine Structure Splitting in the Optical Spectra of Single GaAs Quantum Dots. *Phys. Rev. Lett.* **1996**, *76* (16), 3005–3008.

(201) Ellis, D. J. P.; Stevenson, R. M.; Young, R. J.; Shields, A. J.; Atkinson, P.; Ritchie, D. A. Control of Fine-Structure Splitting of Individual InAs Quantum Dots by Rapid Thermal Annealing. *Appl. Phys. Lett.* **2007**, *90*, 011907.

(202) Pooley, M. A.; Bennett, A. J.; Farrer, I.; Ritchie, D. A.; Shields, A. J. Engineering Quantum Dots for Electrical Control of the Fine Structure Splitting. *Appl. Phys. Lett.* **2013**, *103* (3), 031105.

(203) Varnava, C.; Stevenson, R. M.; Nilsson, J.; Skiba-Szymanska, J.; Dzurňák, B.; Lucamarini, M.; Penty, R. V.; Farrer, I.; Ritchie, D. A.; Shields, A. J. An Entangled-LED-Driven Quantum Relay over 1 Km. *Npj Quantum Inf.* **2016**, *2*, 16006. https://doi.org/10.1038/npjqi.2016.6.

(204) Ha, N.; Mano, T.; Kuroda, T.; Sakuma, Y.; Sakoda, K. Current-Injection Quantum-Entangled-Pair Emitter Using Droplet Epitaxial Quantum Dots on GaAs(111)A. *Appl. Phys. Lett.* **2019**, *115* (8), 083106. https://doi.org/10.1063/1.5103217.

(205) Koguchi, N.; Takahashi, S.; Chikyow, T. New MBE Growth Method for InSb Quantum Well Boxes. *J. Cryst. Growth* **1991**, *111*, 688–692.

(206) Ratto, F.; Rosei, F. Order and Disorder in the Heteroepitaxy of Semiconductor Nanostructures. *Mater. Sci. Eng. R Rep.* **2010**, *70* (3–6), 243–264.

(207) *Lateral Alignment of Epitaxial Quantum Dots*; Schmidt, O. G., Ed.; Springer-Verlag: Berlin-Heidelberg, 2007.

(208) Koguchi, N.; Ishige, K. Growth of GaAs Epitaxial Microcrystals on an S-Terminated GaAs Substrate by Successive Irradiation of Ga and As Molecular Beams. *Jpn. J. Appl. Phys.* **1993**, *32*, 2052.

(209) Watanabe, K.; Koguchi, N.; Gotoh, Y. Fabrication of GaAs Quantum Dots by Modified Droplet Epitaxy. *Jpn. J. Appl. Phys.* **2000**, *39*, L79-81.

(210) Heyn, C.; Stemmann, A.; Schramm, A.; Welsch, H.; Hansen, W.; Nemcsics, Á. Regimes of GaAs Quantum Dot Self-Assembly by Droplet Epitaxy. *Phys. Rev. B* **2007**, *76* (7), 075317.

(211) Liang, B.; Lin, A.; Pavarelli, N.; Reyner, C.; Tatebayashi, J.; Nunna, K.; He, J.; Ochalski, T. J.; Huyet, G.; Huffaker, D. L. GaSb/GaAs Type-II Quantum Dots Grown by Droplet Epitaxy. *Nanotechnology* **2009**, *20* (45), 455604. https://doi.org/10.1088/0957-4484/20/45/455604.

(212) Wang, Z. M.; Liang, B.; Sablon, K. A.; Lee, J.; Mazur, Y. I.; Strom, N. W.; Salamo, G. J. Self-Organization of InAs Quantum-Dot Clusters Directed by Droplet Homoepitaxy. *Small* **2007**, *3* (2), 235–238.

(213) Gurioli, M.; Wang, Z.; Rastelli, A.; Kuroda, T.; Sanguinetti, S. Droplet Epitaxy of Semiconductor Nanostructures for Quantum Photonic Devices. *Nat. Mater.* **2019**, *18* (8), 799–810. https://doi.org/10.1038/s41563-019-0355-y.

(214) Wu, J.; Wang, Z. M. Droplet Epitaxy for Advanced Optoelectronic Materials and Devices. *J. Phys. Appl. Phys.* **2014**, *47* (17), 173001.

(215) Bauer, E. Phänomenologische Theorie Der Kristallabscheidung an Oberflächen. i. *Z. Für Krist. Mater.* **1958**, *110* (1–6), 372–394.

(216) Heckingbottom, R. The Application of Thermodynamics to Molecular Beam Epitaxy. In *Molecular Beam Epitaxy and Heterostructures*; Chang, L. L., Ploog, K., Eds.; Springer Netherlands: Dordrecht, 1985; pp 71–104. https://doi.org/10.1007/978-94-009-5073-3_3.

(217) Vesselinov, M. I. *Crystal Growth for Beginners: Fundamentals of Nucleation, Crystal Growth and Epitaxy*; World scientific, 2016.

(218) Krzyzewski, T. J.; Jones, T. S. Ripening and Annealing Effects in InAs/GaAs(001) Quantum Dot Formation. *J. Appl. Phys.* **2004**, *96*, 668. https://doi.org/10.1063/1.1759788.

(219) Evans, J. W.; Thiel, P. A.; Bartelt, M. C. Morphological Evolution during Epitaxial Thin Film Growth: Formation of 2D Islands and 3D Mounds. *Surf. Sci. Rep.* **2006**, *61* (1–2), 1–128. https://doi.org/10.1016/j.surfrep.2005.08.004.

(220) Schwoebel, R. L.; Shipsey, E. J. Step Motion on Crystal Surfaces. *J. Appl. Phys.* **1966**, *37* (10), 3682–3686. https://doi.org/10.1063/1.1707904.

(221) Pohl, U. W. *Epitaxy of Semiconductors: Introduction to Physical Principles*; Graduate Texts in Physics; Springer Berlin Heidelberg, 2013.

(222) Mutaftschiev, B. *The Atomistic Nature of Crystal Growth*; Springer Series in Materials Science; Springer Berlin Heidelberg, 2013.

(223) Nakajima, K. Equilibrium Phase Diagrams for Stranski-Krastanov Structure Mode of III–V Ternary Quantum Dots. *Jpn. J. Appl. Phys.* **1999**, *38* (Part 1, No. 4A), 1875–1883. https://doi.org/10.1143/jjap.38.1875.

(224) Moustakas, T.; Xu, T.; Thomidis, C.; Nikiforov, A. Y.; Zhou, L.; Smith, D. J. Growth of III-Nitride Quantum Dots and Their Applications to Blue-Green LEDs. *Phys. Status Solidi A* **2008**, *205* (11), 2560–2565.

(225) Biegelsen, D. K.; Ponce, F. A.; Smith, A. J.; Tramontana, J. C. Initial Stages of Epitaxial Growth of GaAs on (100) Silicon. *J. Appl. Phys.* **1987**, *61* (5), 1856–1859. https://doi.org/10.1063/1.338029.

(226) Hull, R.; Fischer-Colbrie, A. Nucleation of GaAs on Si: Experimental Evidence for a Three-Dimensional Critical Transition. *Appl. Phys. Lett.* **1987**, *50* (13), 851–853. https://doi.org/10.1063/1.98011.

(227) Raviswaran, A.; Liu, C.-P.; Kim, J.; Cahill, D. G.; Gibson, J. M. Evolution of Coherent Islands during Strained-Layer Volmer-Weber Growth of Si on Ge(111). *Phys. Rev. B* **2001**, *63* (12), 125314. https://doi.org/10.1103/PhysRevB.63.125314.

(228) Ponchet, A.; Patriarche, G.; Rodriguez, J. B.; Cerutti, L.; Tournié, E. Interface Energy Analysis of III-V Islands on Si (001) in the Volmer-Weber Growth Mode. *Appl. Phys. Lett.* **2018**, *113* (19), 191601. https://doi.org/10.1063/1.5055056.

(229) Lozovoy, K.; Kokhanenko, A.; Voitsekhovskii, A. Comparative Analysis of Germanium–Silicon Quantum Dots Formation on Si (100), Si (111) and Sn/Si (100) Surfaces. *Nanotechnology* **2018**, *29* (5), 054002.

(230) Petroff, P. M. Epitaxial Growth and Electronic Structure of Self-Assembled Quantum Dots. In *Single Quantum Dots*; Springer, 2003; pp 1–24.

(231) Cullis, A. G.; Norris, D. J.; Walther, T.; Migliorato, M. A.; Hopkinson, M. Stranski-Krastanow Transition and Epitaxial Island Growth. *Phys. Rev. B* **2002**, *66* (8), 081305(R). https://doi.org/10.1103/PhysRevB.66.081305.

(232) Tu, Y.; Tersoff, J. Origin of Apparent Critical Thickness for Island Formation in Heteroepitaxy. *Phys. Rev. Lett.* **2004**, *93* (21), 216101. https://doi.org/10.1103/PhysRevLett.93.216101.

(233) Walther, T.; Cullis, A. G.; Norris, D. J.; Hopkinson, M. Nature of the Stranski-Krastanow Transition during Epitaxy of InGaAs on GaAs. *Phys. Rev. Lett.* **2001**, *86* (11), 2381–2384. https://doi.org/10.1103/PhysRevLett.86.2381.

(234) Brune, H. *Growth Modes*; Pergamon, 2001.

(235) Li, H.; Wu, J.; Xu, B.; Liang, J.; Wang, Z. Ordered InAs Quantum Dots in InAlAs Matrix on (001) InP Substrates Grown by Molecular Beam Epitaxy. *Appl. Phys. Lett.* **1998**, *72* (17), 2123–2125.

(236) Simmonds, P. J.; Beere, H. E.; Li, H. W.; See, P.; Shields, A. J.; Ritchie, D. A. Growth by Molecular Beam Epitaxy of Self-Assembled InAs Quantum Dots on InAlAs and InGaAs Lattice-Matched to InP. *J. Vac. Sci. Technol. B* **2007**, *25* (3), 1044–1048.

(237) Eisele, H.; Dähne, M. Critical Thickness of the 2-Dimensional to 3-Dimensional Transition in GaSb/GaAs(001) Quantum Dot Growth. *J. Cryst. Growth* **2012**, *338* (1), 103–106. https://doi.org/10.1016/j.jcrysgro.2011.10.037.

(238) Voigtländer, B. Fundamental Processes in Si/Si and Ge/Si Epitaxy Studied by Scanning Tunneling Microscopy during Growth. *Surf. Sci. Rep.* **2001**, *43* (5), 127–254. https://doi.org/10.1016/S0167-5729(01)00012-7.

(239) Mo, Y.-W.; Savage, D. E.; Swartzentruber, B. S.; Lagally, M. G. Kinetic Pathway in Stranski-Krastanov Growth of Ge on Si(001). *Phys. Rev. Lett.* **1990**, *65* (8), 1020–1023. https://doi.org/10.1103/PhysRevLett.65.1020.

(240) Teichert, C. Self-Organization of Nanostructures in Semiconductor Heteroepitaxy. *Phys. Rep.* **2002**, *365* (5), 335–432. https://doi.org/10.1016/S0370-1573(02)00009-1.

(241) Lee, M. L.; Leitz, C. W.; Cheng, Z.; Pitera, A. J.; Langdo, T.; Currie, M. T.; Taraschi, G.; Fitzgerald, E. A.; Antoniadis, D. A. Strained Ge Channel P-Type Metal-Oxide-Semiconductor Field-Effect Transistors Grown on Si1 - XGex/Si Virtual Substrates. *Appl. Phys. Lett.* **2001**, *79* (20), 3344–3346.

(242) Lee, M. L.; Fitzgerald, E. A.; Bulsara, M. T.; Currie, M. T.; Lochtefeld, A. Strained Si, SiGe, and Ge Channels for High-Mobility Metal-Oxide-Semiconductor Field-Effect Transistors. *J. Appl. Phys.* **2005**, *97* (1), 011101. https://doi.org/10.1063/1.1819976.

(243) Ross, F. M.; Tromp, R. M.; Reuter, M. C. Transition States Between Pyramids and Domes During Ge/Si Island Growth. *Science* **1999**, *286* (5446), 1931–1934. https://doi.org/10.1126/science.286.5446.1931.

(244) Spencer, B. J.; Tersoff, J. Asymmetry and Shape Transitions of Epitaxially Strained Islands on Vicinal Surfaces. *Appl. Phys. Lett.* **2010**, *96*, 073114. https://doi.org/10.1063/1.3318256.

(245) Daruka, I.; Tersoff, J.; Barabási, A.-L. Shape Transition in Growth of Strained Islands. *Phys. Rev. Lett.* **1999**, *82* (13), 2753–2756. https://doi.org/10.1103/PhysRevLett.82.2753.

(246) Persichetti, L.; Sgarlata, A.; Fanfoni, M.; Balzarotti, A. Shaping Ge Islands on Si(001) Surfaces with Misorientation Angle. *Phys. Rev. Lett.* **2010**, *104*, 036104. https://doi.org/10.1103/PhysRevLett.104.036104.

(247) Zhou, T.; Zhong, Z. Dramatically Enhanced Self-Assembly of GeSi Quantum Dots with Superior Photoluminescence Induced by the Substrate Misorientation. *APL Mater.* **2014**, *2*, 022108. https://doi.org/10.1063/1.4866356.

(248) Copel, M.; Reuter, M. C.; Horn von Hoegen, M.; Tromp, R. M. Influence of Surfactants in Ge and Si Epitaxy on Si(001). *Phys. Rev. B* **1990**, *42* (18), 11682–11689. https://doi.org/10.1103/PhysRevB.42.11682.

(249) Brunner, K. Si/Ge Nanostructures. *Rep. Prog. Phys.* **2001**, *65* (1), 27–72. https://doi.org/10.1088/0034-4885/65/1/202.

(250) Yano, M.; Nogami, M.; Matsushima, Y.; Kimata, M. Molecular Beam Epitaxial Growth of InAs. *Jpn. J. Appl. Phys.* **1977**, *16* (12), 2131. https://doi.org/10.1143/JJAP.16.2131.

(251) Houzay, F.; Guille, C.; Moison, J. M.; Henoc, P.; Barthe, F. First Stages of the MBE Growth of InAs on (001)GaAs. *J. Cryst. Growth* **1987**, *81* (1–4), 67–72. https://doi.org/10.1016/0022-0248(87)90367-8.

(252) Brandt, O.; Tapfer, L.; Ploog, K.; Bierwolf, R.; Hohenstein, M.; Phillipp, F.; Lage, H.; Heberle, A. InAs Quantum Dots in a Single-Crystal GaAs Matrix. *Phys. Rev. B* **1991**, *44* (15), 8043–8053. https://doi.org/10.1103/PhysRevB.44.8043.

(253) Wang, G.; Liang, B.; Juang, B.-C.; Das, A.; Debnath, M. C.; Huffaker, D. L.; Mazur, Y. I.; Ware, M. E.; Salamo, G. J. Comparative Study of Photoluminescence from In0.3Ga0.7As/GaAs Surface and Buried Quantum Dots. *Nanotechnology* **2016**, *27* (46), 465701. https://doi.org/10.1088/0957-4484/27/46/465701.

(254) Ji, H.-M.; Liang, B.; Simmonds, P. J.; Juang, B.-C.; Yang, T.; Young, R. J.; Huffaker, D. L. Hybrid Type-I InAs/GaAs and Type-II GaSb/GaAs Quantum Dot Structure with Enhanced Photoluminescence. *Appl. Phys. Lett.* **2015**, *106*, 103104. https://doi.org/10.1063/1.4914895.

(255) Joyce, P. B.; Krzyzewski, T. J.; Bell, G. R.; Joyce, B. A.; Jones, T. S. Composition of InAs Quantum Dots on GaAs(001): Direct Evidence for (In,Ga)As Alloying. *Phys. Rev. B* **1998**, *58* (24), R15981–R15984. https://doi.org/10.1103/PhysRevB.58.R15981.

(256) Sun, C. -K.; Wang, G.; Bowers, J. E.; Brar, B.; Blank, H. -R.; Kroemer, H.; Pilkuhn, M. H. Optical Investigations of the Dynamic Behavior of GaSb/GaAs Quantum Dots. *Appl. Phys. Lett.* **1996**, *68* (11), 1543–1545. https://doi.org/10.1063/1.115693.

(257) Schliwa, A.; Hönig, G. M. O.; Bimberg, D. Electronic Properties of III-V Quantum Dots. In *Multi-Band Effective Mass Approximations. Lecture Notes in Computational Science and Engineering*; Springer, Cham, 2014; Vol. 94, pp 57–85. https://doi.org/10.1007/978-3-319-01427-2.

(258) Grandjean, N.; Massies, J.; Etgens, V. H. Delayed Relaxation by Surfactant Action in Highly Strained III-V Semiconductor Epitaxial Layers. *Phys. Rev. Lett.* **1992**, *69* (5), 796–799. https://doi.org/10.1103/PhysRevLett.69.796.

(259) Jacobi, K. Atomic Structure of InAs Quantum Dots on GaAs. *Prog. Surf. Sci.* **2003**, *71* (5–8), 185–215.

(260) Heyn, C.; Hansen, W. Desorption of InAs Quantum Dots. *J. Cryst. Growth* **2003**, *251* (1), 218–222. https://doi.org/10.1016/S0022-0248(02)02379-5.

(261) Ilahi, B.; Sfaxi, L.; Hassen, F.; Salem, B.; Bremond, G.; Marty, O.; Bouzaiene, L.; Maaref, H. Optimizing the Spacer Layer Thickness of Vertically Stacked InAs/GaAs Quantum Dots. *Mater. Sci. Eng. C* **2006**, *26* (2), 374–377. https://doi.org/10.1016/j.msec.2005.10.034.

(262) Laghumavarapu, R.; Moscho, A.; Khoshakhlagh, A.; El-Emawy, M.; Lester, L.; Huffaker, D. GaSb/GaAs Type II Quantum Dot Solar Cells for Enhanced Infrared Spectral Response. *Appl. Phys. Lett.* **2007**, *90* (17), 173125.

(263) Gradkowski, K.; Pavarelli, N.; Ochalski, T. J.; Williams, D. P.; Tatebayashi, J.; Huyet, G.; O'Reilly, E. P.; Huffaker, D. L. Complex Emission Dynamics of Type-II GaSb/GaAs Quantum Dots. *Appl. Phys. Lett.* **2009**, *95* (6), 061102. https://doi.org/10.1063/1.3202419.

(264) Suzuki, K.; Hogg, R. A.; Arakawa, Y. Structural and Optical Properties of Type II GaSb/GaAs Self-Assembled Quantum Dots Grown by Molecular Beam Epitaxy. *J. Appl. Phys.* **1999**, *85* (12), 8349–8352.

(265) Sun, M.; Simmonds, P. J.; Babu Laghumavarapu, R.; Lin, A.; Reyner, C. J.; Duan, H.-S.; Liang, B.; Huffaker, D. L. Effects of GaAs(Sb) Cladding Layers on InAs/AlAsSb Quantum Dots. *Appl. Phys. Lett.* **2013**, *102* (2), 023107. https://doi.org/10.1063/1.4776221.

(266) Kim, J. S.; Lee, J. H.; Hong, S. U.; Han, W. S.; Kwack, H.-S.; Lee, C. W.; Oh, D. K. Room-Temperature Operation of InP-Based InAs Quantum Dot Laser. *IEEE Photonics Technol. Lett.* **2004**, *16* (7), 1607–1609. https://doi.org/10.1109/LPT.2004.828494.

(267) Paranthoen, C.; Bertru, N.; Dehaese, O.; Le Corre, A.; Loualiche, S.; Lambert, B.; Patriarche, G. Height Dispersion Control of InAs/InP Quantum Dots Emitting at 1.55 Mm. *Appl. Phys. Lett.* **2001**, *78* (12), 1751–1753. https://doi.org/10.1063/1.1356449.

(268) Brault, J.; Gendry, M.; Grenet, G.; Hollinger, G.; Desières, Y.; Benyattou, T. Role of Buffer Surface Morphology and Alloying Effects on the Properties of InAs Nanostructures Grown on InP(001). *Appl. Phys. Lett.* **1998**, *73* (20), 2932–2934. https://doi.org/10.1063/1.122634.

(269) Brault, J.; Gendry, M.; Grenet, G.; Hollinger, G.; Olivares, J.; Salem, B.; Benyattou, T.; Bremond, G. Surface Effects on Shape, Self-Organization and Photoluminescence of InAs Islands Grown on InAlAs/InP(001). *J. Appl. Phys.* **2002**, *92* (1), 506–510. https://doi.org/10.1063/1.1481959.

(270) Rudra, A.; Houdré, R.; Carlin, J. F.; Ilegems, M. Dynamics of Island Formation in the Growth of InAs/InP Quantum Wells. *J. Cryst. Growth* **1994**, *136* (1–4), 278–281. https://doi.org/10.1016/0022-0248(94)90424-3.

(271) González, L.; García, J. M.; García, R.; Briones, F.; Martínez-Pastor, J.; Ballesteros, C. Influence of Buffer-Layer Surface Morphology on the Self-Organized Growth of InAs on InP(001) Nanostructures. *Appl. Phys. Lett.* **2000**, *76* (9), 1104–1106. https://doi.org/10.1063/1.125952.

(272) Weber, A.; Gauthier-Lafaye, O.; Julien, F. H.; Brault, J.; Gendry, M.; Désieres, Y.; Benyattou, T. Strong Normal-Incidence Infrared Absorption in Self-Organized InAs/InAlAs Quantum Dots Grown on InP(001). *Appl. Phys. Lett.* **1999**, *74* (3), 413–415. https://doi.org/10.1063/1.123045.

(273) Parry, H. J.; Ashwin, M. J.; Neave, J. H.; Jones, T. S. Growth of InAs/InP(001) Nanostructures: The Transition from Quantum Wires to Quantum Dots. *J. Cryst. Growth* **2005**, *278* (1–4), 131–135. https://doi.org/10.1016/j.jcrysgro.2005.01.100.

(274) Wang, R. H.; Stintz, A.; Varangis, P. M.; Newell, T. C.; Li, H.; Malloy, K. J.; Lester, L. F. Room-Temperature Operation of InAs Quantum-Dash Lasers on InP [001]. *IEEE Photonics Technol. Lett.* **2001**, *13* (8), 767–769.

(275) Bierwagen, O.; Masselink, W. T. Self-Organized Growth of InAs Quantum Wires and Dots on InP(001): The Role of Vicinal Substrates. *Appl. Phys. Lett.* **2005**, *86* (11), 113110. https://doi.org/10.1063/1.1884762.

(276) García, J. M.; González, L.; González, M. U.; Silveira, J. P.; González, Y.; Briones, F. InAs/InP(001) Quantum Wire Formation Due to Anisotropic Stress Relaxation: In Situ Stress Measurements. *J. Cryst. Growth* **2001**, *227–228*, 975–979. https://doi.org/10.1016/S0022-0248(01)00962-9.

(277) Simmonds, P. J.; Laghumavarapu, R. B.; Sun, M.; Lin, A.; Reyner, C. J.; Liang, B.; Huffaker, D. L. Structural and Optical Properties of InAs/AlAsSb Quantum Dots with GaAs(Sb) Cladding Layers. *Appl. Phys. Lett.* **2012**, *100*, 243108. https://doi.org/10.1063/1.4729419.

(278) Ponchet, A.; Le Corre, A.; L'Haridon, H.; Lambert, B.; Salaün, S. Relationship between Self-organization and Size of InAs Islands on InP(001) Grown by Gas-source Molecular Beam Epitaxy. *Appl. Phys. Lett.* **1995**, *67* (13), 1850. https://doi.org/10.1063/1.114353.

(279) Zhang, Z. P.; Song, Y. X.; Chen, Q. M.; Wu, X. Y.; Zhu, Z. Y. S.; Zhang, L. Y.; Li, Y. Y.; Wang, S. M. Growth Mode of Tensile-Strained Ge Quantum Dots Grown by Molecular Beam Epitaxy. *J. Phys. Appl. Phys.* **2017**, *50*, 465301. https://doi.org/10.1088/1361-6463/aa8bcf.

(280) Bortoleto, J. R. R.; Gazoto, A.; Brasil, M. J. S. P.; Meneses, E. A.; Cotta, M. A. Nucleation and Growth Evolution of InP Dots on InGaP/GaAs. *J. Phys. Appl. Phys.* **2010**, *43* (28), 285301. https://doi.org/10.1088/0022-3727/43/28/285301.

(281) Bortoleto, J. R. R.; Gutiérrez, H. R.; Cotta, M. A.; Bettini, J. Mechanism of Lateral Ordering of InP Dots Grown on InGaP Layers. *Appl. Phys. Lett.* **2005**, *87*, 013105. https://doi.org/10.1063/1.1953875.

(282) Bortoleto, J. R. R.; Gutiérrez, H. R.; Cotta, M. A.; Bettini, J.; Cardoso, L. P.; de Carvalho, M. M. G. Spatial Ordering in InP/InGaP Nanostructures. *Appl. Phys. Lett.* **2003**, *82* (20), 3523–3525. https://doi.org/10.1063/1.1572553.

(283) Häusler, K.; Eberl, K.; Noll, F.; Trampert, A. Strong Alignment of Self-Assembling InP Quantum Dots. *Phys. Rev. B* **1996**, *54* (7), 4913. https://doi.org/10.1103/PhysRevB.54.4913.

(284) Jevasuwan, W.; Boonpeng, P.; Panyakeow, S.; Ratanathammaphan, S. Growth and Characterization of InP Ringlike Quantum-Dot Molecules Grown by Solid-Source Molecular Beam Epitaxy. *J. Nanosci. Nanotechnol.* **2010**, *10* (11), 7291–7294. https://doi.org/10.1166/jnn.2010.2860.

(285) Schmidbauer, M.; Hatami, F.; Hanke, M.; Schäfer, P.; Braune, K.; Masselink, W. T.; Köhler, R.; Ramsteiner, M. Shape-Mediated Anisotropic Strain in Self-Assembled InP/In0.48Ga0.52P Quantum Dots. *Phys. Rev. B* **2002**, *65* (12), 125320. https://doi.org/10.1103/PhysRevB.65.125320.

(286) Wan, Y.; Jung, D.; Norman, J.; Shang, C.; MacFarlane, I.; Li, Q.; Kennedy, M. J.; Gossard, A. C.; Lau, K. M.; Bowers, J. E. O-Band Electrically Injected Quantum Dot Micro-Ring Lasers on on-Axis (001) GaP/Si and V-Groove Si. *Opt. Express* **2017**, *25* (22), 26853–26860. https://doi.org/10.1364/OE.25.026853.

(287) Jung, D.; Norman, J.; Kennedy, M. J.; Shang, C.; Shin, B.; Wan, Y.; Gossard, A. C.; Bowers, J. E. High Efficiency Low Threshold Current 1.3 Mm InAs Quantum Dot Lasers on on-Axis (001) GaP/Si. *Appl. Phys. Lett.* **2017**, *111* (12), 122107. https://doi.org/10.1063/1.4993226.

(288) Damilano, B.; Grandjean, N.; Dalmasso, S.; Massies, J. Room-Temperature Blue-Green Emission from InGaN/GaN Quantum Dots Made by Strain-Induced Islanding Growth. *Appl. Phys. Lett.* **1999**, *75* (24), 3751–3753.

(289) Bürger, M.; Lindner, J.; Reuter, D.; As, D. Investigation of Cubic GaN Quantum Dots Grown by the Stranski-Krastanov Process. *Phys. Status Solidi C* **2015**, *12* (4–5), 452–455.

(290) Gačević, Ž.; Das, A.; Teubert, J.; Kotsar, Y.; Kandaswamy, P.; Kehagias, T.; Koukoula, T.; Komninou, P.; Monroy, E. Internal Quantum Efficiency of III-Nitride Quantum Dot Superlattices Grown by Plasma-Assisted Molecular-Beam Epitaxy. *J. Appl. Phys.* **2011**, *109* (10), 103501.

(291) Schupp, T.; Meisch, T.; Neuschl, B.; Feneberg, M.; Thonke, K.; Lischka, K.; As, D. Growth of Cubic GaN Quantum Dots. In *AIP Conference Proceedings*; American Institute of Physics, 2010; Vol. 1292, pp 165–168.

(292) As, D.; Potthast, S.; Fernandez, J.; Schörmann, J.; Lischka, K.; Nagasawa, H.; Abe, M. Ni Schottky Diodes on Cubic GaN. *Appl. Phys. Lett.* **2006**, *88* (15), 152112.

(293) Blumenthal, S.; Reuter, D.; As, D. J. Optical Properties of Cubic GaN Quantum Dots Grown by Molecular Beam Epitaxy. *Phys. Status Solidi B* **2018**, *255* (5), 1700457.

(294) Brault, J.; Matta, S.; Ngo, T.-H.; Al Khalfioui, M.; Valvin, P.; Leroux, M.; Damilano, B.; Korytov, M.; Brändli, V.; Vennegues, P.; others. Internal Quantum Efficiencies of AlGaN Quantum Dots Grown by Molecular Beam Epitaxy and Emitting in the UVA to UVC Ranges. *J. Appl. Phys.* **2019**, *126* (20), 205701.

(295) Verma, J.; Kandaswamy, P. K.; Protasenko, V.; Verma, A.; Grace Xing, H.; Jena, D. Tunnel-Injection GaN Quantum Dot Ultraviolet Light-Emitting Diodes. *Appl. Phys. Lett.* **2013**, *102* (4), 041103.

(296) Daudin, B.; Widmann, F.; Feuillet, G.; Samson, Y.; Arlery, M.; Rouvière, J. Stranski-Krastanov Growth Mode during the Molecular Beam Epitaxy of Highly Strained GaN. *Phys. Rev. B* **1997**, *56* (12), R7069.

(297) Wang, X.; Yoshikawa, A. Molecular Beam Epitaxy Growth of GaN, AlN and InN. *Prog. Cryst. Growth Charact. Mater.* **2004**, *48–49*, 42–103. https://doi.org/10.1016/j.pcrysgrow.2005.03.002.

(298) Gogneau, N.; Jalabert, D.; Monroy, E.; Shibata, T.; Tanaka, M.; Daudin, B. Structure of GaN Quantum Dots Grown under "Modified Stranski–Krastanow" Conditions on AlN. *J. Appl. Phys.* **2003**, *94* (4), 2254–2261.

(299) Tinjod, F.; Gilles, B.; Moehl, S.; Kheng, K.; Mariette, H. II–VI Quantum Dot Formation Induced by Surface Energy Change of a Strained Layer. *Appl. Phys. Lett.* **2003**, *82* (24), 4340–4342. https://doi.org/10.1063/1.1583141.

(300) Robin, I.; André, R.; Mariette, H.; Tatarenko, S.; Dang, L. S.; Bleuse, J.; Bellet-Amalric, E.; Gérard, J. Control of the Two-Dimensional–Three-Dimensional Transition of Self-Organized CdSe/ZnSe Quantum Dots. *Nanotechnology* **2005**, *16* (8), 1116.

(301) Robin, I.-C.; Andre, R.; Bougerol, C.; Aichele, T.; Tatarenko, S. Elastic and Surface Energies: Two Key Parameters for CdSe Quantum Dot Formation. *Appl. Phys. Lett.* **2006**, *88* (23), 233103.

(302) Merz, J. L.; Lee, S.; Furdyna, J. K. Self-Organized Growth, Ripening, and Optical Properties of Wide-Bandgap II–VI Quantum Dots. *J. Cryst. Growth* **1998**, *184–185*, 228–236. https://doi.org/10.1016/S0022-0248(98)80050-X.

(303) Lee, J.; Wang, Z. M.; Liang, B.; Black, W.; Kunets, V. P.; Mazur, Y. I.; Salamo, G. Selective Growth of InGaAs/GaAs Quantum Dot Chains on Pre-Patterned GaAs (100). *Nanotechnology* **2006**, *17* (9), 2275.

(304) Daruka, I.; Barabási, A.-L. Equilibrium Phase Diagrams for Dislocation Free Self-Assembled Quantum Dots. *Appl. Phys. Lett.* **1998**, *72* (17), 2102–2104.

(305) Rabe, M.; Lowisch, M.; Henneberger, F. LenzSelf-Assembled CdSe Quantum Dots Formation by Thermally Activated Surface Reorganization. *J. Cryst. Growth* **1998**, *184*, 248–253.

(306) Lee, S.; Daruka, I.; Kim, C.; Barabási, A.-L.; Merz, J.; Furdyna, J. Dynamics of Ripening of Self-Assembled II-VI Semiconductor Quantum Dots. *Phys. Rev. Lett.* **1998**, *81* (16), 3479.

(307) Kratzert, P.; Rabe, M.; Henneberger, F. Self-Organized Formation of Wide-Bandgap II–VI Quantum Dots. Thermally Activated Surface Re-Organization versus 2D Stabilization. *Phys. Status Solidi B* **2001**, *224* (1), 179–183.

(308) Maćkowski, S.; Lee, S.; Furdyna, J.; Dobrowolska, M.; Prechtl, G.; Heiss, W.; Kossut, J.; Karczewski, G. Growth and Optical Properties of Mn-Containing II–VI Quantum Dots. *Phys. Status Solidi B* **2002**, *229* (1), 469–472.

(309) Kurtz, E.; Shen, J.; Schmidt, M.; Grün, M.; Hong, S.; Litvinov, D.; Gerthsen, D.; Oka, T.; Yao, T.; Klingshirn, C. Formation and Properties of Self-Organized II–VI Quantum Islands. *Thin Solid Films* **2000**, *367* (1–2), 68–74.

(310) Wojnar, P.; Karczewski, G.; Wojtowicz, T.; Kossut, J. Changing the Properties of the CdTe/ZnTe Quantum Dots by in Situ Annealing during the Growth. *Acta Phys. Pol.-Ser. Gen. Phys.* **2007**, *112* (2), 283–288.

(311) Sorokin, S.; Sedova, I.; Gronin, S.; Klimko, G.; Belyaev, K.; Rakhlin, M.; Mukhin, I.; Toropov, A.; Ivanov, S. CdTe/Zn (Mg)(Se) Te Quantum Dots for Single Photon Emitters Grown by MBE. *J. Cryst. Growth* **2017**, *477*, 127–130.

(312) Sorokin, S.; Sedova, I.; Belyaev, K.; Rakhlin, M.; Yagovkina, M.; Toropov, A.; Ivanov, S. Nanoheterostructures with CdTe/ZnMgSeTe Quantum Dots for Single-Photon Emitters Grown by Molecular Beam Epitaxy. *Tech. Phys. Lett.* **2018**, *44* (3), 267–270.

(313) Toropov, A. A.; Lyublinskaya, O. G.; Meltser, B. Ya.; Solov'ev, V. A.; Sitnikova, A. A.; Nestoklon, M. O.; Rykhova, O. V.; Ivanov, S. V.; Thonke, K.; Sauer, R. Tensile-Strained GaAs Quantum Wells and Quantum Dots in a GaAsxSb1-x Matrix. *Phys. Rev. B* **2004**, *70* (20), 205314. https://doi.org/10.1103/PhysRevB.70.205314.

(314) Meltser, B. Ya.; Solov'ev, V. A.; Lyublinskaya, O. G.; Toropov, A. A.; Terent'ev, Ya. V.; Semenov, A. N.; Sitnikova, A. A.; Ivanov, S. V. Molecular Beam Epitaxy, Photoluminescence and Lasing of GaAs/GaSbAs QD Nanostructures. *J. Cryst. Growth* **2005**, *278*, 119–124. https://doi.org/10.1016/j.jcrysgro.2004.12.120.

(315) Taliercio, T.; Gassenq, A.; Luna, E.; Trampert, A.; Tournié, E. Highly Tensile-Strained, Type-II, Ga1−xInxAs/GaSb Quantum Wells. *Appl. Phys. Lett.* **2010**, *96* (6), 062109. https://doi.org/10.1063/1.3303821.

(316) Lenz, A.; Tournié, E.; Schuppang, J.; Dähne, M.; Eisele, H. Atomic Structure of Tensile-Strained GaAs/GaSb(001) Nanostructures. *Appl. Phys. Lett.* **2013**, *102* (10), 102105. https://doi.org/10.1063/1.4795020.

(317) Vrijen, R.; Yablonovitch, E. A Spin-Coherent Semiconductor Photo-Detector for Quantum Communication. *Phys. E* **2001**, *10* (4), 569–575. https://doi.org/10.1016/S1386-9477(00)00296-4.

(318) Huo, Y. H.; Witek, B. J.; Kumar, S.; Cardenas, J. R.; Zhang, J. X.; Akopian, N.; Singh, R.; Zallo, E.; Grifone, R.; Kriegner, D.; Trotta, R.; Ding, F.; Stangl, J.; Zwiller, V.; Bester, G.; Rastelli, A.; Schmidt, O. G. A Light-Hole Exciton in a Quantum Dot. *Nat. Phys.* **2013**, *10* (1), 46–51.

(319) Vallejo, K. D.; Garrett, T. A.; Sautter, K. E.; Saythavy, K.; Liang, B.; Simmonds, P. J. InAs(111)A Homoepitaxy with Molecular Beam Epitaxy. *J. Vac. Sci. Technol. B* **2019**, *37* (6), 061810. https://doi.org/10.1116/1.5127857.

(320) Sadeghi, I.; Tam, M. C.; Wasilewski, Z. R. On the Optimum Off-Cut Angle for the Growth on InP(111)B Substrates by Molecular Beam Epitaxy. *J. Vac. Sci. Technol. B* **2019**, *37* (3), 031210. https://doi.org/10.1116/1.5089919.

(321) Schuck, C. F. (111)-Oriented Gallium Arsenide Tensile-Strained Quantum Dots Tailored for Entangled Photon Emission. Dissertation, Boise State University, Boise, ID, 2019.

(322) Yang, C. H.; Yu, Z. Y.; Liu, Y. M.; Lu, P. F.; Gao, T.; Li, M.; Manzoor, S. Dependence of Electronic Properties of Germanium on the In-Plane Biaxial Tensile Strains. *Phys. B Condens. Matter* **2013**, *427*, 62–67. https://doi.org/10.1016/j.physb.2013.06.015.

(323) Huo, Y.; Lin, H.; Chen, R.; Rong, Y.; Kamins, T. I.; Harris, J. S. MBE Growth of Tensile-Strained Ge Quantum Wells and Quantum Dots. *Front. Optoelectron.* **2012**, *5* (1), 112–116. https://doi.org/10.1007/s12200-012-0193-x.

(324) Niquet, Y. M.; Rideau, D.; Tavernier, C.; Jaouen, H.; Blase, X. Onsite Matrix Elements of the Tight-Binding Hamiltonian of a Strained Crystal: Application to Silicon, Germanium, and Their Alloys. *Phys. Rev. B* **2009**, *79*, 245201. https://doi.org/10.1103/PhysRevB.79.245201.

(325) Guo, X.; Xu, Z. J.; Liu, H. C.; Zhao, B.; Dai, X. Q.; He, H. T.; Wang, J. N.; Liu, H. J.; Ho, W. K.; Xie, M. H. Single Domain Bi2Se3 Films Grown on InP(111)A by Molecular-Beam Epitaxy. *Appl. Phys. Lett.* **2013**, *102*, 151604. https://doi.org/10.1063/1.4802797.

(326) Mehrotra, S. R.; Povolotskyi, M.; Elias, D. C.; Kubis, T.; Law, J. J. M.; Rodwell, M. J. W.; Klimeck, G. Simulation Study of Thin-Body Ballistic n-MOSFETs Involving Transport in Mixed Γ-L Valleys. *IEEE Electron Device Lett.* **2013**, *34* (9), 1196–1198. https://doi.org/10.1109/LED.2013.2273072.

(327) May, B. J.; Hettiaratchy, E. C.; Myers, R. C. Controlled Nucleation of Monolayer MoSe2 Islands on Si (111) by MBE. *J. Vac. Sci. Technol. B* **2019**, *37*, 021211. https://doi.org/10.1116/1.5087212.

(328) Masuda, T.; Faucher, J.; Simmonds, P. J.; Okumura, K.; Lee, M. L. Device and Material Characteristics of GaInP Solar Cells Grown on Ge Substrates by Molecular Beam Epitaxy. In *2016 IEEE 43rd Photovoltaic Specialists Conference*; 2016; pp 2344–2348. https://doi.org/10.1109/PVSC.2016.7750058.

(329) Simmonds, P. J.; Sun, M.; Laghumavarapu, R. B.; Liang, B.; Norman, A. G.; Luo, J.-W.; Huffaker, D. L. Improved Quantum Dot Stacking for Intermediate Band Solar Cells Using Strain Compensation. *Nanotechnology* **2014**, *25* (44). https://doi.org/10.1088/0957-4484/25/44/445402.

(330) Milekhin, A. G.; Kalagin, A. K.; Vasilenko, A. P.; Toropov, A. I.; Surovtsev, N. V.; Zahn, D. R. T. Vibrational Spectroscopy of InAlAs Epitaxial Layers. *J. Appl. Phys.* **2008**, *104*, 073516. https://doi.org/10.1063/1.2980344.

(331) Kim, H.; Rho, H.; Lee, E. H.; Song, J. D. Polarized and Spatially Resolved Raman Scattering from Composition-Graded Wurtzite InGaAs Nanowires. *J. Phys. Appl. Phys.* **2016**, *49*, 175105. https://doi.org/10.1088/0022-3727/49/17/175105.

(332) Tenne, D. A.; Bakarov, A. K.; Toropov, A. I.; Zahn, D. R. T. Raman Study of Self-Assembled InAs Quantum Dots Embedded in AlAs: Influence of Growth Temperature. *Phys. E Low-Dimens. Syst. Nanostructures* **2002**, *13* (2–4), 199–202. https://doi.org/10.1016/S1386-9477(01)00519-7.

(333) Richter, H.; Wang, Z. P.; Ley, L. The One Phonon Raman Spectrum in Microcrystalline Silicon. *Solid State Commun.* **1981**, *39* (5), 625–629. https://doi.org/10.1016/0038-1098(81)90337-9.

(334) Arora, A. K.; Rajalakshmi, M.; Ravindran, T. R.; Sivasubramanian, V. Raman Spectroscopy of Optical Phonon Confinement in Nanostructured Materials. *J. Raman Spectrosc.* **2007**, *38* (6), 604–617. https://doi.org/10.1002/jrs.1684.

(335) Rolo, A. G.; Vasilevskiy, M. I. Raman Spectroscopy of Optical Phonons Confined in Semiconductor Quantum Dots and Nanocrystals. *J. Raman Spectrosc.* **2007**, *38* (6), 618–633. https://doi.org/10.1002/jrs.1746.

(336) Zhang, H.; Chen, Y.; Zhou, G.; Tang, C.; Wang, Z. Wetting Layer Evolution and Its Temperature Dependence during Self-Assembly of InAs/GaAs Quantum Dots. *Nanoscale Res. Lett.* **2012**, *7*, 600. https://doi.org/10.1186/1556-276X-7-600.

(337) Riposan, A.; Millunchick, J. M.; Pearson, C. Critical Film Thickness Dependence on As Flux in In0.27Ga0.73As/GaAs(001) Films. *Appl. Phys. Lett.* **2007**, *90*, 091902. https://doi.org/10.1063/1.2476259.

(338) Jiang, Y.; Mo, D.; Hu, X.; Wang, S.; Chen, Y.; Lin, D.; Fan, Y.; Yang, X.; Zhong, Z.; Jiang, Z. Investigation on Ge Surface Diffusion via Growing Ge Quantum Dots on Top of Si Pillars. *AIP Adv.* **2016**, *6*, 085120. https://doi.org/10.1063/1.4961992.

(339) Takebe, T.; Fujii, M.; Yamamoto, T.; Fujita, K.; Watanabe, T. Orientation-Dependent Ga Surface Diffusion in Molecular Beam Epitaxy of GaAs on GaAs Patterned Substrates. *J. Appl. Phys.* **1997**, *81*, 7273–7281. https://doi.org/10.1063/1.365548.

(340) Esposito, L.; Bietti, S.; Fedorov, A.; Nötzel, R.; Sanguinetti, S. Ehrlich-Schwöbel Effect on the Growth Dynamics of GaAs(111)A Surfaces. *Phys. Rev. Mater.* **2017**, *1* (2), 024602. https://doi.org/10.1103/PhysRevMaterials.1.024602.

(341) Joyce, P. B.; Krzyzewski, T. J.; Bell, G. R.; Jones, T. S.; Malik, S.; Childs, D.; Murray, R. Effect of Growth Rate on the Size, Composition, and Optical Properties of InAs/GaAs Quantum Dots Grown by Molecular-Beam Epitaxy. *Phys. Rev. B* **2000**, *62* (16), 10891–10895. https://doi.org/10.1103/PhysRevB.62.10891.

(342) Hopfer, F.; Mutig, A.; Fiol, G.; Kuntz, M.; Shchukin, V.; Ledentsov, N. N.; Bimberg, D.; Mikhrin, S. S.; Krestnikov, I. L.; Livshits, D. A.; Kovsh, A. R.; Bornholdt, C. 20 Gb/s 85 °C Error Free Operation of VCSEL Based on Submonolayer Deposition of Quantum Dots. In *2006 IEEE 20th International Semiconductor Laser Conference*; IEEE, 2006; pp 119–120. https://doi.org/10.1109/islc.2006.1708115.

(343) Richardella, A.; Zhang, D. M.; Lee, J. S.; Koser, A.; Rench, D. W.; Yeats, A. L.; Buckley, B. B.; Awschalom, D. D.; Samarth, N. Coherent Heteroepitaxy of Bi2Se3 on GaAs (111)B. *Appl. Phys. Lett.* **2010**, *97* (26), 262104. https://doi.org/10.1063/1.3532845.

(344) He, L.; Xiu, F.; Wang, Y.; Fedorov, A. V.; Huang, G.; Kou, X.; Lang, M.; Beyermann, W. P.; Zou, J.; Wang, K. L. Epitaxial Growth of Bi2Se3 Topological Insulator Thin Films on Si (111). *J. Appl. Phys.* **2011**, *109* (10), 103702. https://doi.org/10.1063/1.3585673.

(345) Vishwanath, S.; Liu, X.; Rouvimov, S.; Basile, L.; Lu, N.; Azcatl, A.; Magno, K.; Wallace, R. M.; Kim, M.; Idrobo, J.-C.; Furdyna, J. K.; Jena, D.; Xing, H. G. Controllable Growth of Layered Selenide and Telluride Heterostructures and Superlattices Using Molecular Beam Epitaxy. *J. Mater. Res.* **2016**, *31* (7), 900–910. https://doi.org/10.1557/jmr.2015.374.

(346) Caridi, E. A.; Chang, T. Y.; Goossen, K. W.; Eastman, L. F. Direct Demonstration of a Misfit Strain-generated Electric Field in a [111] Growth Axis Zinc-blende Heterostructure. *Appl. Phys. Lett.* **1990**, *56* (7), 659–661. https://doi.org/10.1063/1.102729.

(347) David, J. P. R.; Sale, T. E.; Pabla, A. S.; Rodríquez-Gironés, P. J.; Woodhead, J.; Grey, R.; Rees, G. J.; Robson, P. N.; Skolnick, M. S.; Hogg, R. A. Photoluminescence of Piezoelectric Strained InGaAs□GaAs Multi-Quantum Well p-i-n Structures. *Mater. Sci. Eng. B* **1995**, *35* (1–3), 42–46. https://doi.org/10.1016/0921-5107(95)01384-9.

(348) Alam, K.; Takagi, S.; Takenaka, M. Strain-Modulated L-Valley Ballistic-Transport in (111) GaAs Ultrathin-Body NMOSFETs. *IEEE Trans. Electron Devices* **2014**, *61* (5), 1335–1340. https://doi.org/10.1109/TED.2014.2311840.

(349) Juska, G.; Dimastrodonato, V.; Mereni, L. O.; Gocalinska, A.; Pelucchi, E. Towards Quantum-Dot Arrays of Entangled Photon Emitters. *Nat. Photonics* **2013**, *7* (7), 527–531. https://doi.org/10.1038/nphoton.2013.128.

(350) Stock, E.; Warming, T.; Ostapenko, I.; Rodt, S.; Schliwa, A.; Töfflinger, J. A.; Lochmann, A.; Toropov, A. I.; Moshchenko, S. A.; Dmitriev, D. V.; Haisler, V. A.; Bimberg, D. Single-Photon Emission from InGaAs Quantum Dots Grown on (111) GaAs. *Appl. Phys. Lett.* **2010**, *96* (9), 093112. https://doi.org/10.1063/1.3337097.

(351) Schneider, C. A.; Rasband, W. S.; Eliceiri, K. W. NIH Image to ImageJ: 25 Years of Image Analysis. *Nat. Methods* **2012**, *9* (7), 671–675. https://doi.org/10.1038/nmeth.2089.

(352) Ramasubramani, V.; Dice, B. D.; Harper, E. S.; Spellings, M. P.; Anderson, J. A.; Glotzer, S. C. Freud: A Software Suite for High Throughput Analysis of Particle Simulation Data. *Comput. Phys. Commun.* **2020**, *254*, 107275. https://doi.org/10.1016/j.cpc.2020.107275.

(353) Hohenberg, P.; Kohn, W. Inhomogeneous Electron Gas. *Phys. Rev.* **1964**, *136* (3B), B864–B871. https://doi.org/10.1103/PhysRev.136.B864.

(354) Kohn, W.; Sham, L. J. Self-Consistent Equations Including Exchange and Correlation Effects. *Phys. Rev.* **1965**, *140* (4A), A1133–A1138. https://doi.org/10.1103/PhysRev.140.A1133.

(355) Blum, V.; Gehrke, R.; Hanke, F.; Havu, P.; Havu, V.; Ren, X.; Reuter, K.; Scheffler, M. Ab Initio Molecular Simulations with Numeric Atom-Centered Orbitals. *Comput. Phys. Commun.* **2009**, *180* (11), 2175–2196. https://doi.org/10.1016/j.cpc.2009.06.022.

(356) Havu, V.; Blum, V.; Havu, P.; Scheffler, M. Efficient O(N) Integration for All-Electron Electronic Structure Calculation Using Numeric Basis Functions. *J. Comput. Phys.* **2009**, *228* (22), 8367–8379. https://doi.org/10.1016/j.jcp.2009.08.008.

(357) Marek, A.; Blum, V.; Johanni, R.; Havu, V.; Lang, B.; Auckenthaler, T.; Heinecke, A.; Bungartz, H.-J.; Lederer, H. The ELPA Library: Scalable Parallel Eigenvalue Solutions for Electronic Structure Theory and Computational Science. *J. Phys. Condens. Matter* **2014**, *26* (21), 213201. https://doi.org/10.1088/0953-8984/26/21/213201.

(358) Yu, V. W.; Corsetti, F.; García, A.; Huhn, W. P.; Jacquelin, M.; Jia, W.; Lange, B.; Lin, L.; Lu, J.; Mi, W.; Seifitokaldani, A.; Vázquez-Mayagoitia, Á.; Yang, C.; Yang, H.; Blum, V. ELSI: A Unified Software Interface for Kohn–Sham Electronic Structure Solvers. *Comput. Phys. Commun.* **2018**, *222*, 267–285. https://doi.org/10.1016/j.cpc.2017.09.007.

(359) Perdew, J. P.; Burke, K.; Ernzerhof, M. Generalized Gradient Approximation Made Simple. *Phys. Rev. Lett.* **1996**, *77* (18), 3865–3868. https://doi.org/10.1103/PhysRevLett.77.3865.

(360) Zunger, A.; Wei, S.-H.; Ferreira, L. G.; Bernard, J. E. Special Quasirandom Structures. *Phys. Rev. Lett.* **1990**, *65* (3), 353–356. https://doi.org/10.1103/PhysRevLett.65.353.

(361) Wei, S.-H.; Ferreira, L. G.; Bernard, J. E.; Zunger, A. Electronic Properties of Random Alloys: Special Quasirandom Structures. *Phys. Rev. B* **1990**, *42* (15), 9622–9649. https://doi.org/10.1103/PhysRevB.42.9622.

(362) Moison, J. M.; Guille, C.; Houzay, F.; Barthe, F.; Van Rompay, M. Surface Segregation of Third-Column Atoms in Group III-V Arsenide Compounds: Ternary Alloys and Heterostructures. *Phys. Rev. B* **1989**, *40* (9), 6149–6162. https://doi.org/10.1103/PhysRevB.40.6149.

(363) Houzay, F.; Moison, J. M.; Guille, C.; Barthe, F.; Van Rompay, M. Surface Segregation of Third-Column Atoms in III–V Ternary Arsenides. *J. Cryst. Growth* **1989**, *95* (1–4), 35–37. https://doi.org/10.1016/0022-0248(89)90345-X.

(364) Moll, N.; Kley, A.; Pehlke, E.; Scheffler, M. GaAs Equilibrium Crystal Shape from First Principles. *Phys. Rev. B* **1996**, *54* (12), 8844–8855. https://doi.org/10.1103/PhysRevB.54.8844.

(365) Peters, B.; Heyden, A.; Bell, A. T.; Chakraborty, A. A Growing String Method for Determining Transition States: Comparison to the Nudged Elastic Band and String Methods. *J. Chem. Phys.* **2004**, *120* (17), 7877–7886. https://doi.org/10.1063/1.1691018.

(366) Henkelman, G.; Uberuaga, B. P.; Jónsson, H. A Climbing Image Nudged Elastic Band Method for Finding Saddle Points and Minimum Energy Paths. *J. Chem. Phys.* **2000**, *113* (22), 9901–9904. https://doi.org/10.1063/1.1329672.

(367) Krzyzewski, T. J.; Joyce, P. B.; Bell, G. R.; Jones, T. S. Scaling Behavior in InAs/GaAs(001) Quantum-Dot Formation. *Phys. Rev. B* **2002**, *66* (20), 201302. https://doi.org/10.1103/PhysRevB.66.201302.

(368) Ratsch, C.; DeVita, J.; Smereka, P. Level-Set Simulation for the Strain-Driven Sharpening of the Island-Size Distribution during Submonolayer Heteroepitaxial Growth. *Phys. Rev. B* **2009**, *80* (15), 155309. https://doi.org/10.1103/PhysRevB.80.155309.

(369) Guo, B.; Wang, Y.; Peng, C.; Zhang, H. L.; Luo, G. P.; Le, H. Q.; Gmachl, C.; Sivco, D. L.; Peabody, M. L.; Cho, A. Y. Laser-Based Mid-Infrared Reflectance Imaging of Biological Tissues. *Opt. Express* **2004**, *12* (1), 208–219. https://doi.org/10.1364/OPEX.12.000208.

(370) Bakhirkin, Y. A.; Kosterev, A. A.; Roller, C.; Curl, R. F.; Tittel, F. K. Mid-Infrared Quantum Cascade Laser Based off-Axis Integrated Cavity Output Spectroscopy for Biogenic Nitric Oxide Detection. *Appl. Opt.* **2004**, *43* (11), 2257–2266. https://doi.org/10.1364/AO.43.002257.

(371) Liu, J.; Michel, J.; Giziewicz, W.; Pan, D.; Wada, K.; Cannon, D. D.; Jongthammanurak, S.; Danielson, D. T.; Kimerling, L. C.; Chen, J.; Ilday, F. Ö.; Kärtner, F. X.; Yasaitis, J. High-Performance, Tensile-Strained Ge p-i-n Photodetectors on a Si Platform. *Appl. Phys. Lett.* **2005**, *87* (10), 103501. https://doi.org/10.1063/1.2037200.

(372) Levine, B. G.; Stone, J. E.; Kohlmeyer, A. Fast Analysis of Molecular Dynamics Trajectories with Graphics Processing Units—Radial Distribution Function Histogramming. *J. Comput. Phys.* **2011**, *230* (9), 3556–3569. https://doi.org/10.1016/j.jcp.2011.01.048.

(373) Nordin, L.; Petluru, P.; Muhowski, A. J.; Shaner, E. A.; Wasserman, D. All-Epitaxial Long-Range Surface Plasmon Polariton Structures with Integrated Active Materials. *J. Appl. Phys.* **2021**, *129* (11), 113102. https://doi.org/10.1063/5.0041509.

(374) Bietti, S.; Esposito, L.; Fedorov, A.; Ballabio, A.; Martinelli, A.; Sanguinetti, S. Characterization and Effect of Thermal Annealing on InAs Quantum Dots Grown by Droplet Epitaxy on GaAs(111)A Substrates. *Nanoscale Res. Lett.* **2015**, *10*, 247. https://doi.org/10.1186/s11671-015-0930-3.

(375) Joyce, B. A.; Vvedensky, D. D. Self-Organized Growth on GaAs Surfaces. *Mater. Sci. Eng. R Rep.* **2004**, *46* (6), 127–176. https://doi.org/10.1016/j.mser.2004.10.001.

(376) Hatami, F.; Müller, U.; Kissel, H.; Braune, K.; Blum, R.-P.; Rogaschewski, S.; Niehus, H.; Kirmse, H.; Neumann, W.; Schmidbauer, M.; Köhler, R.; Masselink, W. T. Planar Ordering of InP Quantum Dots on (100)In0.48Ga0.52P. *J. Cryst. Growth* **2000**, *216* (1–4), 26–32. https://doi.org/10.1016/S0022-0248(00)00422-X.

(377) Heyn, Ch. Anisotropic Island Growth during Submonolayer Epitaxy. *Phys. Rev. B* **2001**, *63* (3), 033403. https://doi.org/10.1103/PhysRevB.63.033403.

(378) Müller, P.; Kern, R. Equilibrium Shape of Epitaxially Strained Crystals (Volmer–Weber Case). *J. Cryst. Growth* **1998**, *193* (1–2), 257–270. https://doi.org/10.1016/S0022-0248(98)00508-9.

(379) Tuktamyshev, A.; Fedorov, A.; Bietti, S.; Tsukamoto, S.; Sanguinetti, S. Temperature Activated Dimensionality Crossover in the Nucleation of Quantum Dots by Droplet Epitaxy on GaAs(111)A Vicinal Substrates. *Sci. Rep.* **2019**, *9*, 14520. https://doi.org/10.1038/s41598-019-51161-5.

(380) Jacobi, K. Atomic Structure of InAs Quantum Dots on GaAs. *Prog. Surf. Sci.* **2003**, *71* (5), 185–215. https://doi.org/10.1016/S0079-6816(03)00007-8.

(381) Kasap, S.; Capper, P. *Springer Handbook of Electronic and Photonic Materials*; Springer: Germany, 2006.

(382) Schmidt, J.; Macdonald, D. Recombination Activity of Iron-Gallium and Iron-Indium Pairs in Silicon. *J. Appl. Phys.* **2005**, *97* (11), 113712. https://doi.org/10.1063/1.1929096.

(383) Huo, Y. H.; Witek, B. J.; Kumar, S.; Cardenas, J. R.; Zhang, J. X.; Akopian, N.; Singh, R.; Zallo, E.; Grifone, R.; Kriegner, D.; Trotta, R.; Ding, F.; Stangl, J.; Zwiller, V.; Bester, G.; Rastelli, A.; Schmidt, O. G. A Light-Hole Exciton in a Quantum Dot. *Nat. Phys.* **2013**, *10*, 46–51. https://doi.org/10.1038/nphys2799.

(384) Bhattacharya, A.; Baten, Z.; Frost, T.; Bhattacharya, P. Room Temperature GaN-Based Edge-Emitting Spin-Polarized Light Emitting Diode. *IEEE Photonics Technol. Lett.* **2017**, *29* (3), 338–341. https://doi.org/10.1109/LPT.2017.2650866.

(385) Schuck, C. F.; Roy, S. K.; Garrett, T. A.; Yuan, Q.; Wang, Y.; Cabrera, C. I.; Grossklaus, K. A.; Vandervelde, T. E.; Liang, B.; Simmonds, P. J. Anomalous Stranski-Krastanov Growth of (111)-Oriented Quantum Dots with Tunable Wetting Layer Thickness. *Sci. Rep.* **2019**, *9*, 18179. https://doi.org/10.1038/s41598-019-54668-z.

(386) Senanayake, P.; Hung, C.-H.; Shapiro, J.; Lin, A.; Liang, B.; Williams, B. S.; Huffaker, D. L. Surface Plasmon-Enhanced Nanopillar Photodetectors. *Nano Lett.* **2011**, *11* (12), 5279–5283. https://doi.org/10.1021/nl202732r.

(387) Zhang, Y.; Zheng, Y.; Meng, R.; Sun, C.; Tian, K.; Geng, C.; Zhang, Z.-H.; Liu, G.; Bi, W. Enhancing Both TM- and TE-Polarized Light Extraction Efficiency of AlGaN-Based Deep Ultraviolet Light-Emitting Diode via Air Cavity Extractor With Vertical Sidewall. *IEEE Photonics J.* **2018**, *10* (4), 1–9. https://doi.org/10.1109/JPHOT.2018.2849747.

(388) Lee, B. G.; Belkin, M. A.; Audet, R.; MacArthur, J.; Diehl, L.; Pflügl, C.; Capasso, F.; Oakley, D. C.; Chapman, D.; Napoleone, A.; Bour, D.; Corzine, S.; Höfler, G.; Faist, J. Widely Tunable Single-Mode Quantum Cascade Laser Source for Mid-Infrared Spectroscopy. *Appl. Phys. Lett.* **2007**, *91* (23), 231101. https://doi.org/10.1063/1.2816909.

(389) Chen, S.; Liao, M.; Tang, M.; Wu, J.; Martin, M.; Baron, T.; Seeds, A.; Liu, H. Electrically Pumped Continuous-Wave 1.3 Micrometer InAs/GaAs Quantum Dot Lasers Monolithically Grown on on-Axis Si (001) Substrates. *Opt. Express* **2017**, *25* (5), 4632–4639. https://doi.org/10.1364/OE.25.004632.

(390) Mazur, A.; Pollmann, J. Electronic Properties of (211) Surfaces of Group-IV and III-V Semiconductors. *Phys. Rev. B* **1984**, *30* (4), 2084–2089. https://doi.org/10.1103/PhysRevB.30.2084.

(391) Tan, C.-S.; Huang, M. H. Density Functional Theory Calculations Revealing Metal-like Band Structures for Ultrathin Germanium (111) and (211) Surface Layers. *Chem. – Asian J.* **2018**, *13* (15), 1972–1976. https://doi.org/10.1002/asia.201800765.

(392) Chin, A.; Martin, P.; Ho, P.; Ballingall, J.; Yu, T.; Mazurowski, J. High Quality (111)B GaAs, AlGaAs, AlGaAs/GaAs Modulation Doped Heterostructures and a GaAs/InGaAs/GaAs Quantum Well. *Appl. Phys. Lett.* **1991**, *59* (15), 1899–1901. https://doi.org/10.1063/1.106182.

(393) Yeo, W.; Dimitrov, R.; Schaff, W. J.; Eastman, L. F. Material Properties of Bulk InGaAs and InAlAs/InGaAs Heterostructures Grown on (111)B and (111)B Misoriented by 1° towards 〈211〉 InP Substrates. *Appl. Phys. Lett.* **2000**, *77* (26), 4292–4294. https://doi.org/10.1063/1.1332836.

(394) Band, Y. B.; Avishai, Y. Low-Dimensional Quantum Systems. In *Quantum Mechanics with Applications to Nanotechnology and Information Science*; Band, Y. B., Avishai, Y., Eds.; Academic Press: Amsterdam, 2013; pp 749–823. https://doi.org/10.1016/B978-0-444-53786-7.00013-7.